Université du Québec

INRS Institut national de la recherche scientifique

Centre Énergie Matériaux Télecommunications

STUDY AND DESIGN OF RECONFIGURABLE ANTENNA USING METAMATERIALS FOR WIRELESS COMMUNICATION SYSTEMS, OPERATING AT MM-WAVE FREQUENCY BAND

Par

Noureddine Melouki

Thèse présentée pour l'obtention du grade de
Philosophiae Doctor, Ph.D.
en Télécommunications

Jury d'évaluation

Président du jury et examinateur interne	Prof. Serioja O. Tatu Institut National de la Recherche Scientifique
Examinateur externe	Prof. Niamat Hussain University of Glasgow
Examinateur externe	Dr. Gijo Augustin Ultra Intelligence & Communications
Directeur de recherche	Prof. Tayeb A. Denidni Institut National de la Recherche Scientifique

REMERCIEMENTS

Avant tout, je rends grâce à Dieu, le Tout-Puissant, pour m'avoir accordé la santé, la patience et la persévérance nécessaires pour mener à bien ce travail. Sans Sa guidance et Sa bénédiction, rien de tout cela n'aurait été possible.

Je tiens à exprimer ma profonde gratitude à mon épouse bien-aimée, **Houda**, pour son amour, sa compréhension et son soutien inébranlable tout au long de ces années. Sa présence constante, son encouragement et ses sacrifices m'ont donné la force d'aller toujours plus loin. À ma famille, je dédie également une grande part de ce travail : à mes parents, pour leurs prières, leur sagesse et leurs valeurs qui ont façonné mon parcours.

Je souhaite exprimer ma reconnaissance la plus sincère à mon directeur de recherche, le Professeur **Tayeb A. Denidni**, pour sa confiance, son encadrement attentif et ses précieux conseils scientifiques. Sa rigueur, sa vision et son exigence intellectuelle ont profondément marqué ma façon de concevoir la recherche. J'ai énormément appris à ses côtés, tant sur le plan scientifique que personnel.

Je remercie également l'ensemble de mes collègues et amis du laboratoire de recherche à l'INRS pour leur bienveillance, leur esprit d'équipe et les nombreuses discussions enrichissantes que nous avons partagées. Leur soutien technique et moral a grandement contribué à la réussite de ce travail.

Enfin, j'exprime ma gratitude à tous ceux et celles qui, de près ou de loin, ont contribué à ce parcours doctoral. À chacun d'entre vous, je dis simplement : merci du fond du cœur.

RÉSUMÉ

Cette thèse présente une étude complète sur la conception, l'optimisation et la validation expérimentale d'antennes transmitarray et lentilles conformes 3D destinées aux applications de formation de faisceaux et de frontaux reconfigurables à ondes millimétriques. Le travail établit une continuité entre les structures passives optimisées par algorithme, les lentilles diélectriques imprimées en 3D, et les architectures reconfigurables basées sur la transition CPW-vers-slotline, permettant un contrôle de faisceau agile et efficace dans la bande Ka.

La première partie met en évidence les limites des systèmes à commande mécanique ou entièrement active en termes de complexité et de rendement. Une transmitarray multi-bits à commande indépendante de phase et d'amplitude est ensuite proposée et optimisée au moyen d'un algorithme génétique (GA). Grâce à une cellule unitaire bi-couche et à une pondération d'amplitude adaptée, l'antenne atteint des lobes secondaires réduits tout en conservant un gain élevé et une large bande passante, confirmés expérimentalement sur un prototype de 20$\times$20 éléments.

La deuxième partie introduit des lentilles diélectriques conformes imprimées en 3D exploitant le principe hauteur-phase pour un pilotage de faisceau entièrement passif et la génération de modes à moment angulaire orbital (OAM). Réalisées en filament PLA à faibles pertes, ces lentilles démontrent des fonctions de bipolarisation, de double faisceau et de balayage mécanique sur 360°, adaptées aux communications embarquées sur drones et aux plateformes légères.

Enfin, la recherche se concentre sur une cellule unitaire CPW-vers-slotline assurant une inversion binaire de phase (0°/180°) grâce à la symétrie intrinsèque du champ. Cette approche évolue d'une structure bi-couche compatible PIN-diodes vers une architecture uniplanaire à simple métal, maintenant une transmission stable et uniforme. Une extension géométrique à 3 bits améliore encore la résolution sans complexité supplémentaire, ouvrant la voie à des arrays reconfigurables efficaces et industrialisables.

Dans son ensemble, cette thèse propose un cadre complet reliant optimisation algorithmique, fabrication additive et reconfigurabilité électronique, offrant une solution évolutive, performante et à faible coût pour les systèmes mm-wave de communication, de détection et de véhicules intelligents.

Mots-clés : ondes millimétriques, antenne réseau transmetteur, lentille 3D imprimée, transition CPW-slotline, optimisation phase-amplitude, algorithme génétique, commande de faisceau, bande Ka.

ABSTRACT

This dissertation presents a comprehensive investigation into the design, optimization, and experimental realization of millimeter-wave (mm-wave) transmitarray and lens antennas for advanced beam-forming and reconfigurable front-end applications. The research establishes a unified progression from passive, algorithmically optimized apertures, through 3D-printed conformal dielectric lenses, to electronically reconfigurable CPW-to-slotline transmitarrays that enable agile and efficient beam control at Ka-band frequencies.

The study begins by revisiting conventional beam-steering techniques and identifies the inherent trade-offs between efficiency, complexity, and cost in mechanical and fully active phased arrays. Building on this foundation, a multi-bit wideband transmitarray with independent phase and amplitude control is proposed and optimized using a Genetic Algorithm (GA)-based synthesis framework. By coupling a dual-layer unit-cell topology with algorithmic amplitude tapering, the array achieves markedly lower sidelobe levels and broadband high-gain performance, validated experimentally through 20×20 prototypes.

Expanding this concept into spatially continuous designs, the next stage introduces 3D-printed conformal dielectric lenses that exploit the height-to-phase conversion principle for fully passive beam steering and orbital angular momentum (OAM) generation. Fabricated using low-loss PLA substrates, these lenses demonstrate single- and dual-beam steering, multi-mode OAM formation, and mechanical 360° scanning for UAV-assisted communication scenarios, bridging the gap between rigid planar antennas and lightweight conformal architectures.

The final stage focuses on a CPW-to-slotline-based unit-cell architecture, enabling binary (0°/180°) phase inversion through intrinsic mode symmetry rather than external networks. This topology evolves from a dual-layer diode-ready configuration to a uni-planar single-metal implementation, maintaining high transmission magnitude and scalability. A 3-bit geometric extension further enhances resolution without added complexity, paving the way for electronically steerable and manufacturable arrays.

Collectively, this work delivers a complete framework—from algorithmic optimization to additive manufacturing and electronic reconfiguration—for efficient, low-cost, and scalable mm-wave front-ends applicable to future vehicular, satellite, and 5G/6G communication systems.

Keywords : millimeter-wave, transmitarray, 3D-printed lens, CPW-slotline transition, phase–amplitude optimization, genetic algorithm, beam steering, Ka-band.

SOMMAIRE RECAPITULATIF

0.1 Titre de la Thèse en Français

ÉTUDE ET CONCEPTION D'ANTENNE RECONFIGURABLE UTILISANT DES MÉTAMATÉRIAUX POUR DES SYSTÈMES DE COMMUNICATION SANS FIL FONCTIONNANT DANS LA BANDE DE FRÉQUENCES DES ONDES MILLIMÉTRIQUES

0.2 Introduction

Chaque nouvelle génération de réseaux sans fil apporte des vitesses de transmission plus élevées et de nouvelles fonctionnalités à nos appareils connectés. Par exemple, la 1G a introduit le premier téléphone cellulaire, la 2G a permis l'envoi de messages texte, la 3G nous a donné accès à Internet, tandis que la 4G a offert les vitesses que nous utilisons aujourd'hui. Cependant, à mesure que le nombre d'utilisateurs augmente, les réseaux 4G atteignent leurs limites de capacité alors même que la demande en données ne cesse de croître. Nous sommes ainsi à l'aube de la 5G, la prochaine génération de systèmes de communication sans fil, capable de gérer mille fois plus de trafic que les réseaux actuels et jusqu'à dix fois plus rapide que la 4G. Dans ce contexte, les opérateurs cherchent à offrir des applications multimédias et vidéo de haute qualité, à faible latence, pour les appareils mobiles [1].

Actuellement, cinq technologies émergentes constituent la base du déploiement de la 5G : les ondes millimétriques, les petites cellules, le MIMO massif, la formation de faisceaux (*beamforming*) et le duplex intégral. La technologie des ondes millimétriques vise à résoudre le problème de la bande passante limitée des fréquences inférieures à 6 GHz, aujourd'hui saturées. L'utilisation de fréquences plus élevées permet non seulement d'augmenter la capacité spectrale, mais aussi de réduire la taille des antennes et circuits RF, rendant les transcepteurs plus compacts et économiques [2–4]. Cependant, ces ondes millimétriques se propagent mal à travers les obstacles et sont fortement atténuées par la pluie ou la végétation. Pour surmonter ces limites, les réseaux à petites cellules constituent une solution efficace : ils reposent sur des stations de base miniatures et peu puissantes, placées de manière dense afin de relayer le signal autour des obstacles. Ces antennes peuvent être pilotées par des systèmes intelligents intégrant des stations MIMO massives comportant plusieurs dizaines de ports, augmentant la capacité du réseau par un facteur supérieur à 20. Toutefois, le MIMO massif introduit de nouvelles contraintes, notamment des interférences entre canaux, d'où l'importance du *beamforming*, une technique permettant de concentrer le signal dans une direction spécifique, réduisant ainsi les interférences et améliorant l'efficacité énergétique.

Ainsi, il devient nécessaire de concevoir des antennes capables d'intégrer plusieurs fonctions dans un même élément [5–7]. Afin de limiter les interférences de rayonnement, cet élément doit pouvoir orienter son faisceau dans des directions spécifiques tout en supprimant les lobes indésirables. Les antennes à balayage ou à commutation de faisceau suscitent donc un intérêt croissant dans les systèmes de communication modernes. Ces antennes permettent d'ajouter des fonctionnalités supplémentaires et une flexibilité accrue tout en occupant un volume réduit par rapport aux réseaux d'antennes intelligentes classiques [8].

De plus, pour répondre aux exigences technologiques futures, les sous-systèmes de formation de faisceaux doivent combiner faible perte, compacité et simplicité de fabrication. Ils doivent également relever les défis liés à la conception d'antennes à faible coût fonctionnant aux fréquences millimétriques. L'objectif principal de cette recherche est donc de concevoir et développer des antennes à balayage de faisceau, basées sur des métamatériaux, capables d'être intégrées dans les systèmes 5G et au-delà.

0.3 Motivation

Face à la congestion croissante du spectre sub-6 GHz, les chercheurs et ingénieurs se tournent désormais vers la bande des ondes millimétriques (mm-Wave), encore peu exploitée. Les technologies 5G reposent sur ces fréquences élevées pour répondre à l'augmentation massive du nombre d'appareils connectés et pour permettre le déploiement de technologies émergentes telles que les villes intelligentes, la réalité virtuelle et les véhicules autonomes. Ces systèmes nécessiteront inévitablement des antennes reconfigurables, des réseaux MIMO massifs et des réseaux de petites cellules interconnectés.

Cependant, le passage aux fréquences millimétriques pose de nouveaux défis en matière de propagation. Il devient donc crucial de proposer des solutions rentables permettant d'améliorer la couverture. Dans cette optique, la technologie du *beamforming* apparaît comme une solution prometteuse pour accroître la performance des systèmes existants et garantir la couverture des réseaux futurs. Ainsi, des antennes à gain élevé, à large bande et à faisceau dynamique sont indispensables pour les applications millimétriques. Le présent travail vise donc à concevoir une antenne reconfigurable basée sur des métamatériaux, offrant un haut gain et un balayage de faisceau à large bande afin de répondre à ces exigences.

0.4 Problématique

L'objectif du *beamforming* et du balayage électronique est de surmonter les principales limites des systèmes actuels en matière de couverture et de fiabilité. Pour ce faire, les antennes électroniquement reconfigurables jouent un rôle central. Une antenne reconfigurable est capable de modifier dynamiquement ses caractéristiques de rayonnement — fréquence de fonctionnement, diagramme de rayonnement ou polarisation — afin d'ajouter de nouvelles fonctionnalités et d'améliorer les performances du système. Cette reconfigurabilité peut être obtenue par l'ajout de composants actifs ou de matériaux à propriétés variables au sein de la structure rayonnante.

Les antennes à lentille intégrée (ILA) [10–12], les antennes à onde progressive [13, 14], les réseaux adaptatifs [15], les réseaux phasés [16], ou encore les structures photoniques actives (AMPBG) [17], sont autant de solutions permettant de diriger le faisceau rayonné. Toutefois, chacune présente ses propres avantages et inconvénients. Par exemple, les antennes à onde progressive sont volumineuses, tandis que les réseaux phasés nécessitent un contrôle précis d'amplitude et de phase, rendant leur conception complexe et coûteuse. De même, les structures AMPBG restent encombrantes et génèrent des lobes secondaires élevés.

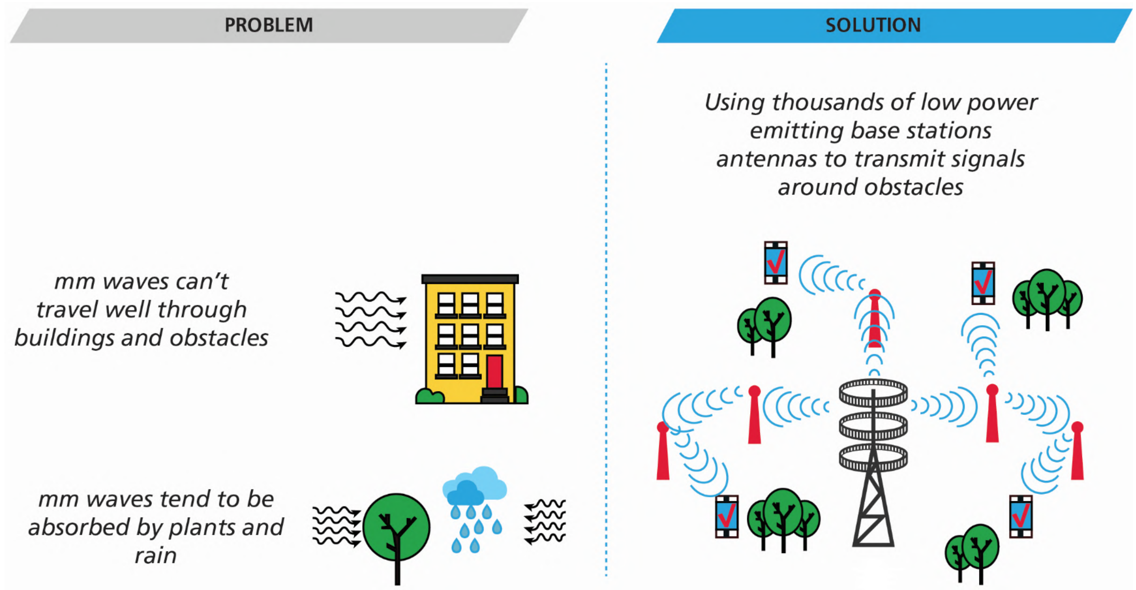

FIGURE 1 : Amélioration de la couverture dans un système de communication 5G.

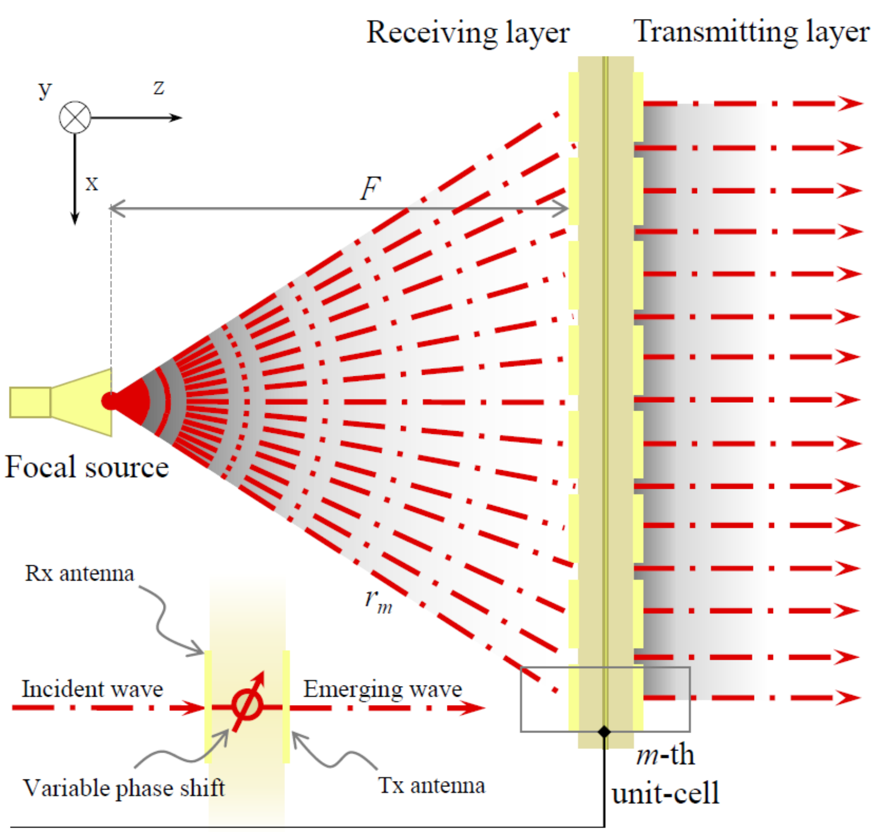

FIGURE 2 : Schéma du principe de fonctionnement d'une antenne à réseau transmetteur [9].

Pour surmonter ces contraintes de taille, de coût et de complexité, les chercheurs se sont tournés vers les antennes réseaux transmetteurs à base de métamatériaux (M-TAs). Ces structures reposent sur des réseaux multi-couches de cellules unitaires capables de contrôler localement la phase du signal transmis, afin de focaliser ou de collimater le rayonnement d'une source. Chaque cellule effectue successivement les fonctions de réception, déphasage et transmission du signal.

La majorité des antennes réseaux transmetteurs modernes utilisent des technologies planaires peu coûteuses, basées sur les procédés standards de fabrication PCB. Ces antennes se distinguent par l'absence de blocage du faisceau d'alimentation et par une distance focale réduite, ce qui les rend idéales pour les plateformes mobiles telles que les avions ou trains à grande vitesse.

En contrôlant électroniquement la phase de chaque cellule, il devient possible de modifier dynamiquement la direction du faisceau principal. Divers mécanismes permettent de réaliser ce déphasage : par exemple, l'utilisation d'une diode varactor dans une cellule sélective en fréquence (*FSS*) [18], ou encore la méthode de renversement du courant, qui assure une modulation binaire (0°/180°) du signal transmis à l'aide de diodes PIN [9]. Cette dernière approche offre une large bande passante au prix d'une légère perte de gain de crête et d'un niveau de lobe secondaire plus élevé. La technique de rotation de polarisation représente une autre alternative pratique.

0.5 Objectifs

L'objectif général de cette recherche est de développer une nouvelle génération d'antennes reconfigurables basées sur des métamatériaux, capables de former et de diriger le faisceau dans la bande millimétrique à 28 GHz pour les systèmes 5G. Les objectifs spécifiques sont les suivants :

- Obtenir une capacité de balayage de faisceau de $\pm 30°$ dans le plan azimutal (soit 60° au total).
- Atteindre un gain minimal de 16 dBi pour chaque direction de faisceau.
- Réduire le niveau des lobes secondaires, notamment pour les angles de déflexion élevés.

Pour atteindre ces objectifs, une approche innovante est proposée, combinant une antenne H à base de guide d'onde intégré au substrat (SIW) avec une Transmitarray à métamatériaux reconfigurable, commandée électroniquement.

0.6 Méthodologie

La méthodologie adoptée repose sur trois volets principaux : la conception de l'élément d'alimentation, le développement de la cellule unitaire reconfigurable, et la mise en œuvre d'une carte de commande. Ces trois composantes forment un système complet de commande de faisceau, décrit ci-dessous.

0.6.1 Volet de Travail 1 : Élément d'alimentation

Une alimentation efficace, à haut rendement de rayonnement et à faible niveau de lobe secondaire, est essentielle. La technologie SIW s'impose comme une solution adaptée pour les antennes planaires millimétriques. Différentes configurations (mono-secteur et octogonale) seront étudiées afin d'assurer une couverture azimutale complète de 360°, un gain élevé et une large bande passante.

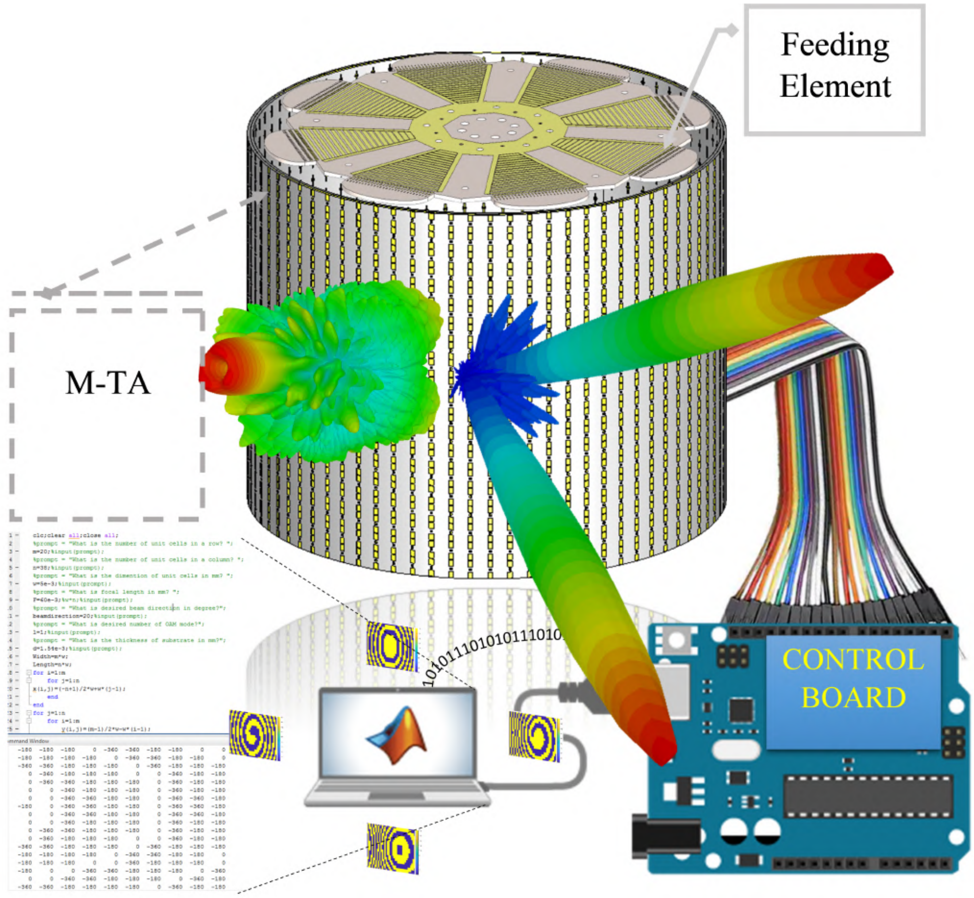

FIGURE 3 : Système proposé de balayage de faisceau à couverture 360°.

0.6.2 Volet de Travail 2 : Cellule unitaire reconfigurable

Ce second volet se concentre sur l'étude des techniques de manipulation du faisceau électromagnétique servant de base à l'antenne à réseau transmetteur reconfigurable. Les métamatériaux, structures périodiques 2D ou 3D capables de manipuler la phase, la polarisation ou la direction d'ondes EM, sont utilisés pour contrôler la propagation du champ et améliorer les caractéristiques de rayonnement. Ces structures offrent un fort potentiel pour la conception d'antennes compactes à faisceau dynamique [18–22].

0.6.3 Volet de Travail 3 : Carte de commande

Le troisième volet consiste en la conception de la carte logique permettant de piloter les diodes PIN intégrées dans les cellules unitaires. Cette carte génère les signaux de polarisation nécessaires aux lignes de commande, tout en évitant toute perturbation du diagramme de rayonnement. Un code MATLAB a été développé pour générer les séquences binaires de commande, transmises ensuite aux registres à décalage assurant la conversion série-parallèle, afin d'activer sélectivement les diodes PIN de l'antenne à réseau transmetteur. .

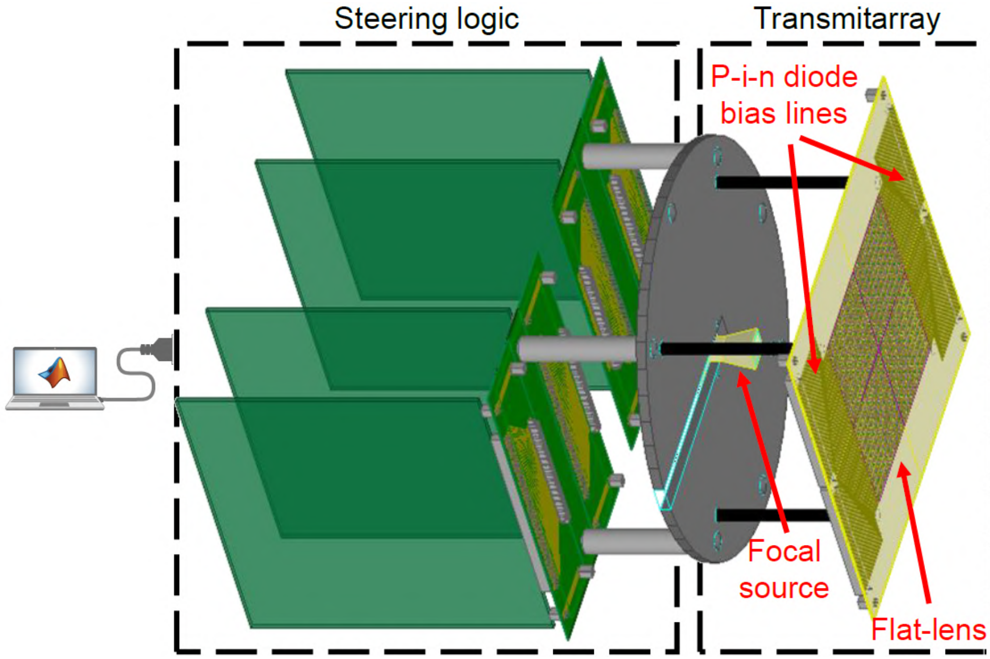

FIGURE 4 : Carte logique de commande [9].

0.7 Contributions

Les principales contributions de cette thèse peuvent être résumées comme suit :

1. **Cadre méthodologique unifié pour les antennes réseaux transmetteurs reconfigurables :** Un cadre de conception intégré a été élaboré pour d'antennes réseaux transmetteurs (TA) à haut gain, large bande et reconfigurables en bande Ka. Ce cadre combine modélisation électromagnétique, optimisation algorithmique, fabrication additive et reconfigurabilité électronique, afin de lever les limitations clés des réseaux phasés et des réflectarrays traditionnels.

2. **Commande multi-bit d'amplitude et de phase optimisée par algorithme génétique :** Une architecture de TA à base de métamatériaux, capable d'ajuster indépendamment la phase et l'amplitude, a été proposée et optimisée. La cellule unitaire exploite la torsion de polarisation et le renversement de courant pour réaliser un contrôle binaire (1-bit) de la phase, tandis qu'une rotation de la couche émettrice assure une modulation multi-bit de l'amplitude. Une stratégie d'optimisation par algorithme génétique (GA) a été mise en œuvre pour accroître l'efficacité d'ouverture et réduire les lobes secondaires, aboutissant à des performances large bande et à haut gain, validées expérimentalement sur prototypes.

3. **Lentilles diélectriques conformes imprimées en 3D pour le façonnage passif du faisceau :** Le concept d'ouverture continue a été concrétisé par la conception et la fabrication de lentilles diélectriques légères imprimées en 3D. En exploitant la conversion hauteur–phase, ces lentilles ont démontré le balayage passif, la formation bi-faisceau et la génération de moment angulaire orbital (OAM), confirmant le potentiel de la fabrication additive pour des systèmes front-end mm-onde conformes, modulaires et à faible coût.

4. **Architecture Transmitarray reconfigurable CPW–slotline :** Une TA uniplanaire reconfigurable 1-bit a été développée à partir d'une transition compacte CPW–slotline intégrant deux diodes PIN par cellule. L'inversion binaire de phase résulte d'une symétrie de modes intrinsèque,

sans hybrides externes ni réseaux multicouches. Des panneaux modulaires de 16 cellules ont été conçus et simulés, montrant une conversion de mode efficace, une transmission large bande et un balayage électronique en bande Ka.

5. **Validation expérimentale et intégration système :** Plusieurs prototypes de TA ont été fabriqués et caractérisés. Les résultats mesurés confirment la large bande de transmission, la précision du balayage et la forte corrélation simulation–mesure, validant la démarche proposée. Des lignes directrices sont également établies pour l'extension vers des architectures multipanneaux, conformes et hybrides.

Dans leur ensemble, ces contributions font progresser l'état de l'art des systèmes d'antennes reconfigurables millimétriques, en proposant des solutions compactes, faiblement dissipatives et économiques pour les communications 5G/6G, la détection véhiculaire et les charges utiles satellites, tout en posant les bases d'architectures de *beamforming* intelligentes et pilotées par algorithmes.

0.8 Contributions

0.8.1 Revues Scientifiques

1. **Melouki, N.**, Ahmed, F., Pourmohammadi, P., Naseri, H., & Denidni, T. A. (2025). Wideband transmitarray with independent phase/amplitude control for millimeter-wave vehicular sensing and communication. AEU-International Journal of Electronics and Communications, 195, 155771.
2. **Melouki, N.**, Ahmed, F., PourMohammadi, P., Naseri, H., Bizan, M. S., Iqbal, A., & Denidni, T. A. (2024) 3D-Printed Conformal Meta-Lens with Multiple Beam-Shaping Functionalities for Mm-Wave Sensing Applications. Sensors. 24 : 2826.
3. **Melouki, N.**, PourMohammadi, P., Nasseri, H., Ahmed, F., Iqbal, A., Hocini, A., & Denidni, T. A. (2023) Ultra-compact Quarter-Mode SIW Self-Hexaplexing Antenna for C-band and X-band Applications. IEEE Antennas and Wireless Propagation Letters. 23 : 995-999.
4. **Melouki, N.**, Hocini, A., & Denidni, T. A., "High gain and Wideband Fabry-Perot Resonator Antenna based on a compact single PRS layer, " in *IEEE Access*, 10, 96526-96537, 2022.
5. **Melouki, N.**, Hocini, A., & Denidni, T. A., "Performance enhancement of an ultra-wideband antenna using a compact topology optimized single frequency selective surface-layer as a reflector, " in *International Journal of RF and Microwave Computer-Aided Engineering*, 32(5), e23097, 2022.
6. **Melouki, N.**, Hocini, A., Fegriche, F. Z., PourMohammadi, P., Naseri, H., Iqbal, A., & Denidni, T. A., "High-gain wideband circularly polarised Fabry–Perot resonator array antenna using a single-layered pixelated PRS for millimetre-wave applications, " in *Micromachines*, 13(10), 1658, 2022.
7. Naseri, H., Pourmohammadi, P., Kamali, N., **Melouki, N.**, Ahmed, F., Iqbal, A., & Denidni, T. A. (2026). Introduction to BeamWave Matrix for beam-forming and wave manipulation applications. AEU-International Journal of Electronics and Communications, 203, 156062.
8. Naseri, H., Pourmohammadi, P., Barua, S., **Melouki, N.**, Ahmed, F., Iqbal, A., & Denidni, T. A. (2025). High-security antenna system with dual polarization and frequency tunability for driverless vehicles. AEU-International Journal of Electronics and Communications, 155928.

9. Naseri, H., Pourmohammadi, P., **Melouki, N.**, Ahmed, F., Iqbal, A., & Denidni, T. (2024). Frequency-adjustable OAM antenna with co-divergent beams for IoT applications. AEU-International Journal of Electronics and Communications, 177, 155188.
10. Naseri, H., PourMohammadi, P., **Melouki, N.**, Ahmed, F., Iqbal, A., & Denidni, T. A. (2024). Reconfigurable OAM antenna with flexibility on mode numbers, polarization, and frequency. IEEE Antennas and Wireless Propagation Letters, 23(6), 1710-1714.
11. Naseri, H., Pourmohammadi, P., Fei, P., **Melouki, N.**, Iqbal, A., & Denidni, T. (2023). Butler matrix-based beamforming with polarization reconfigurability for reducing electromagnetic interference. AEU-International Journal of Electronics and Communications, 170, 154833.
12. Naseri, H., PourMohammadi, P., **Melouki, N.**, Ahmed, F., Iqbal, A., & Denidni, T. A. (2023). Substrate integrated waveguide-based dual-polarized self-diplexing antenna array. IEEE Transactions on Circuits and Systems II : Express Briefs, 70(8), 2839-2843.
13. Naseri, H., PourMohammadi, P., **Melouki, N.**, Ahmed, F., Iqbal, A., & Denidni, T. A. (2023). Generation of mixed-OAM-carrying waves using huygens' metasurface for mm-wave applications. Sensors, 23(5), 2590.
14. Naseri, H., Pourmohammadi, P., **Melouki, N.**, Iqbal, A., & Denidni, T. A., "A low-profile antenna system for generating reconfigurable oam-carrying beams," in *IEEE Antennas and Wireless Propagation Letters*, vol. 22, no. 2, pp. 402-406, Feb. 2023.
15. Naseri, H., Pourmohammadi, P., **Melouki, N.**, Ahmed, F., Iqbal, A., & Denidni, T. A., "Substrate Integrated Waveguide Based Dual-Polarized Self-Diplexing Antenna Array," in *IEEE Transactions on Circuits and Systems II : Express Briefs*, 2023.
16. Naseri, H., Pourmohammadi, P., **Melouki, N.**, Ahmed, F., Iqbal, A., & Denidni, T. A., "Generation of mixed-oam-carrying waves using huygens' metasurface for mm-wave applications," in *Sensors*, vol. 23, no. 5, p. 2590, 2023.
17. Naseri, H., Pourmohammadi, P., Fei, P., **Melouki, N.**, Iqbal, A., & Denidni, T., "Butler matrix-based beamforming with polarization reconfigurability for reducing electromagnetic interference, " in *AEU-International Journal of Electronics and Communications*, 170, 154833, 2023.
18. Bizan, M. S., Naseri, H., Pourmohammadi, P., **Melouki, N.**, Iqbal, A., & Denidni, T. A., "Dual-Band Dielectric Resonator Antenna with Filtering Features for Microwave and Mm-Wave Applications, " in *Micromachines*, 14(6), 1236, 2023.
19. Khodja, K., Atia, S., Messaoudene, I., Belazzoug, M., Merabet, I., **Melouki, N.**, & Denidni, T. A. (2025). Novel High Efficiency V-Band Pure TEM D-PRGW Antenna for 5G mmWave Applications. International Journal of Communication Systems, 38(4), e6008.
20. Ksouri, E., Boufrioua, A., Belazzoug, M., Messaoudene, I., **Melouki, N.**, & Denidni, T. A. (2024). A gain enhancement of compact UWB antenna based on a single FSS layer. Microwave and Optical Technology Letters, 66(8), e34301.
21. Ahmed, F., **Melouki, N.**, PourMohammadi, P., Naseri, H., & Denidni, T. A. (2025). A Compact and Wideband Active Asymmetric Transmit Array Unit Cell for Millimeter-Wave Applications. Sensors, 25(16), 5168.
22. Ahmed, F., Ahmed, A., **Melouki, N.**, PourMohammadi, P., Naseri Gheisanab, H., Shoaib, N., & Denidni, T. A. (2024). A wideband bianisotropic FSS absorber with angular stable and polarization-insensitive properties. Waves in Random and Complex Media, 1-16.
23. Ahmed, F., Faisal, F., **Melouki, N.**, Ahmed, A., Naseri, H., PourMohammadi, P., & Denidni, T. A. (2024). A Multi-Functional Reflective Polarization Transforming Surface with In-Band and Out-Band Transmission Characteristics. IEEE Antennas and Wireless Propagation Letters.

24. Pourmohammadi, P., Naseri, H., **Melouki, N.**, Ahmed, F., Zheng, Q., Iqbal, A., & Denidni, T. A. (2025). A wideband beam steering transmitarray antenna for Ka-band applications. AEU-International Journal of Electronics and Communications, 193, 155720.
25. PourMohammadi, P., Naseri, H., **Melouki, N.**, Ahmed, F., Zheng, Q., Iqbal, A., ... & Denidni, T. A. (2024). Highly-isolated compact self-diplexing antenna. AEU-International Journal of Electronics and Communications, 173, 155025.
26. PourMohammadi, P., Naseri, H., **Melouki, N.**, Ahmed, F., and Iqbal, A., and & Denidni, T. A., “Substrate Integrated Waveguide Based Full-Duplex Antenna with Improved Out-of-Band Suppression,” in *IEEE Transactions on Circuits and Systems II : Express Briefs*, pp. 1–5, 2022.
27. PourMohammadi, P., Naseri, H., **Melouki, N.**, F. Ahmed, A. Iqbal, Vandenbosch, G. A., & Denidni, T. A., “Compact SIW-Based Self-Quadruplexing Antenna for Mm-wave and Microwave Communications, ” in *IEEE Transactions on Circuits and Systems II : Express Briefs*, 2023.
28. PourMohammadi, P., Naseri, H., **Melouki, N.**, Ahmed, F., Bizan, M. S., Iqbal, A., & Denidni, T. A., "A Fabry–Perot antenna using a frequency selective surface layer with wideband and Low RCS for Mm-wave applications, " in *AEU-International Journal of Electronics and Communications*, 169, 154736, 2023.

0.8.2 Conférences

1. **Melouki, N.**, & Denidni, T. A. (2024, December). AI-Driven Beam-Steering Metamaterial Lens for 5G and Autonomous Vehicles. In 2024 International Conference on Telecommunications and Intelligent Systems (ICTIS) (pp. 1-4). IEEE.
2. **Melouki, N.**, Ahmed, F., PourMohammadi, P., & Denidni, T. A. (2024, July). 3D-Printed Conformal Meta-Lens with Multi-Mode Orbital Angular Momentum (OAM) Generation and Beam-Steering Capabilities. In 2024 IEEE International Symposium on Antennas and Propagation and INC/USNC-URSI Radio Science Meeting (AP-S/INC-USNC-URSI) (pp. 419-420). IEEE.
3. **Melouki, N.**, Ahmed, F., Nasseri, H., Pourmohammadi, P., Iqbal, A., & Denidni, T. A. (2024, March). Multi-Bit Wideband Transmitarray Aperture with Independent Phase and Amplitude Control for High Gain with Low Sidelobe Mm-Wave Applications. In 2024 18th European Conference on Antennas and Propagation (EuCAP) (pp. 01-04). IEEE.
4. **Melouki, N.**, Ahmed, F., PourMohammadi, P., Naseri, H., Iqbal, A., & Denidni, T. A. (2023, July). 3D-printed conformal metamaterial lens with multiple beam steering functionalities. In 2023 IEEE International Symposium on Antennas and Propagation and USNC-URSI Radio Science Meeting (USNC-URSI) (pp. 791-792). IEEE.
5. **Melouki, N.**, Nasseri, H., Iqbal, A., & Denidni, T. A. (2023, March). Compact quarter-mode SIW self-triplexing antenna for C-band and X-band applications. In 2023 17th European Conference on Antennas and Propagation (EuCAP) (pp. 1-5). IEEE.
6. **Melouki, N.**, Hocini, A., & Denidni, T. A., "High-gain and Wideband Fabry-Perot Resonator Antenna based on a Pixelated single PRS layer for Ku-band Applications, " in *2022 IEEE International Symposium on Antennas and Propagation and USNC-URSI Radio Science Meeting (AP-S/URSI)*, pp. 988-989), July, 2022. (published).

7. **Melouki, N.**, Nasseri, H., Iqbal, A., & Denidni, T. A., "Compact Quarter-Mode SIW Self-triplexing Antenna for C-band and X-band Applications, " in *2023 17th European Conference on Antennas and Propagation (EuCAP)*, (pp. 1-5), March, 2023.
8. **Melouki, N.**, Ahmed, F., Pourmohammadi, P., Naseri, H., Iqbal, A., & Denidni, T. A., "Low-loss 2-bit Reflective Intelligent Surface for mm-wave Applications, " in *2023 URSI International Symposium on Electromagnetic Theory (EMTS)*, May, 2023.
9. **Melouki, N.**, Ahmed, F., Pourmohammadi, P., Naseri, H., Iqbal, A., & Denidni, T. A., "3D-Printed Conformal Metamaterial Lens with Multiple Beam Steering Functionalities, " in *2023 IEEE International Symposium on Antennas and Propagation and USNC-URSI Radio Science Meeting (AP-S/URSI)*, July, 2023.
10. PourMohammadi, P., Naseri, H., **Melouki, N.**, & Denidni, T. A. (2024, July). A 1-Bit Wideband Electronically Beam Steering Transmitarray for 5G Communication Systems. In 2024 IEEE International Symposium on Antennas and Propagation and INC/USNC-URSI Radio Science Meeting (AP-S/INC-USNC-URSI) (pp. 139-140). IEEE.
11. PourMohammadi, P., Naseri, H., **Melouki, N.**, Ahmed, F., Vandenbosch, G. A.E., Iqbal, A., and & Denidni, T. A., "A Low-profile Self-duplexing Antenna for Millimeter-wave and Microwave Frequency Bands, " in *2023 IEEE International Symposium on Antennas and Propagation and USNC-URSI Radio Science Meeting (AP-S/URSI)*, July, 2023.
12. PourMohammadi, P., Naseri, H., **Melouki, N.**, Ahmed, F., Bizan, M., Iqbal, A., and & Denidni, T. A., "A Wideband Fabry-Perot Antenna with a Bianisotropic FSS Layer, " in *2023 IEEE International Symposium on Antennas and Propagation and USNC-URSI Radio Science Meeting (AP-S/URSI)*, July, 2023.
13. PourMohammadi, P., Naseri, H., **Melouki, N.**, Ahmed, F., Bizan, M., Iqbal, A., and & Denidni, T. A., "A Wideband Anisotropic Metasurface for Cross-Polarization Applications, " in *2023 URSI International Symposium on Electromagnetic Theory (EMTS)*, May, 2023.
14. Naseri, H., Pourmohammadi, P., **Melouki, N.**, Ahmed, F., Iqbal, A., & Denidni, T. A. (2024, March). Dual-Polarized OAM Antenna with Frequency and Mode Agility for Intelligent OAM Communications. In 2024 18th European Conference on Antennas and Propagation (EuCAP) (pp. 1-4). IEEE.
15. Naseri, H., PourMohammadi, P., Bizan, M., **Melouki, N.**, Ahmed, F., Iqbal, A., and & Denidni, T. A., "Reconfigurable Dielectric Resonator OAM Antenna with Augmented Modes, " in *2023 IEEE International Symposium on Antennas and Propagation and USNC-URSI Radio Science Meeting (AP-S/URSI)*, July, 2023.
16. Naseri, H., PourMohammadi, P., Bizan, M., **Melouki, N.**, Ahmed, F., Iqbal, A., and & Denidni, T. A., "Triple-Mode OAM Generating Dielectric Resonator Antenna, " in *2023 URSI International Symposium on Electromagnetic Theory (EMTS)*, May, 2023.
17. Naseri, H., PourMohammadi, P., **Melouki, N.**, Iqbal, A., and & Denidni, T. A., ”Self-diplexing Antenna Operating at Sub-6 GHz and Milimeter wave Frequencies”, in *2023 17th European Conference on Antennas and Propagation (EuCAP)*, March, 2023.
18. Ahmed, F., **Melouki, N.**, PourMohammadi, P., & Denidni, T. A. (2024, July). A Multifunctional Bianisotropic Frequency Selective Surface for Microwave Applications. In 2024 IEEE International Symposium on Antennas and Propagation and INC/USNC-URSI Radio Science Meeting (AP-S/INC-USNC-URSI) (pp. 1823-1824). IEEE.
19. Ahmed, F., **Melouki, N.**, PourMohammadi, P., Naseri, H. & Denidni, T. A., "A 2-Bit Reconfigurable Reflecting Metasurface for Mm-wave Applications," in *2023 IEEE International Symposium on Antennas and Propagation and USNC-URSI Radio Science Meeting (AP-S/URSI)*, July, 2023.

20. Ahmed, F., **Melouki, N.**, PourMohammadi, P., Naseri, H. & Denidni, T. A., "4-Bit Reconfigurable Reflecting Metasurface for Sub-6 GHz Band," in *2023 URSI International Symposium on Electromagnetic Theory (EMTS)*, May, 2023.

0.9 Distinctions et prix

1. Reconnaissance pour la contribution en tant que mentor au programme *Apprentis chercheurs*, INRS, Université du Québec, Canada, 2023–2024.

2. 1er prix — meilleur poster étudiant, STARaCom, Université McGill, Canada, 2023.

0.10 Plan de la thèse

La thèse est organisée en six chapitres principaux, couvrant l'ensemble du parcours — des fondements théoriques à la validation expérimentale et aux perspectives futures.

Chapitre 1 (Introduction) : Ce chapitre présente la motivation pour le développement d'antennes Transmitarray (TA) et de lentilles pour la bande millimétrique, reconfigurables et extensibles. Il précise la problématique, les objectifs et la méthodologie, en situant le travail dans le contexte des communications 5G/6G, des applications satellitaires et véhiculaires. Il se conclut par un aperçu de la structure de la thèse et des contributions et publications associées.

Chapitre 2 (Revue de la littérature) : Une synthèse des avancées récentes sur les Transmitarrays à base de métasurfaces et les techniques de *beamforming*. L'évolution des réseaux phasés et réflectarrays vers les métasurfaces reconfigurables est discutée, en soulignant les défis liés à la quantification de phase, à l'élargissement de bande et à la complexité d'intégration. Les lacunes identifiées motivent des approches combinant optimisation algorithmique, fabrication additive et reconfigurabilité électrique.

Chapitre 3 (Transmitarray large bande multi-bit : conception et optimisation) : Développement d'une architecture TA capable de contrôler indépendamment phase et amplitude. Une cellule unitaire bi-couche, exploitant torsion de polarisation et renversement de courant, assure un contrôle de phase 1-bit et une modulation d'amplitude multi-bit. Un cadre d'optimisation par GA est mis en place pour réduire les lobes secondaires tout en préservant le haut gain. Le chapitre se termine par la fabrication et la mesure de prototypes 20×20 validant la large bande et le balayage.

Chapitre 4 (Lentilles diélectriques conformes imprimées en 3D) : Extension du concept de TA vers des ouvertures continues via la fabrication additive. De nouvelles lentilles diélectriques 3D sont conçues selon le principe hauteur–phase, réalisant un balayage passif, un bi-faisceau et la génération d'OAM. Les résultats expérimentaux confirment la faisabilité de structures conformes, légères et à faibles pertes, adaptées aux UAV et aux plateformes véhiculaires.

Chapitre 5 (Architecture Transmitarray reconfigurable CPW–slotline) : Présentation d'une TA reconfigurable 1-bit fondée sur une transition compacte CPW–slotline avec deux diodes PIN par cellule. L'inversion binaire de phase découle d'une symétrie de champ intrinsèque, sans réseaux de déphasage externes. Des panneaux modulaires de 16 cellules sont assemblés en matrice multipanneaux, montrant une transmission large bande, une conversion de mode efficace et un balayage électronique en bande Ka.

Chapitre 6 (Conclusion et perspectives) : Synthèse des principaux résultats et contributions. Mise en perspective de l'intégration conjointe modélisation EM, optimisation GA, fabrication additive et reconfigurabilité, au service d'antennes mm-onde à haut gain, large bande et faible coût. Les perspectives incluent la reconfigurabilité multi-bit avancée, le contrôle de faisceau intelligent, les systèmes hybrides lentille–métasurface et des architectures sobres énergétiquement pour les applications 5G/6G.

TABLE DES MATIÈRES

LISTE DES FIGURES

LISTE DES TABLEAUX

LISTE DES ABREVIATIONS

5G Fifth Generation Wireless Communication
6G Sixth Generation Wireless Communication
AI Artificial Intelligence
AMPBG Active Metallic Photonic Band Gap
CAD Computer-Aided Design
CPW Coplanar Waveguide
EM Electromagnetic
FSS Frequency Selective Surface
GA Genetic Algorithm
ILA Integrated Lens Antenna
Ka-band Frequency band from 26.5 GHz to 40 GHz
mm-Wave Millimeter Wave
MIMO Multiple Input Multiple Output
M-MIMO Massive Multiple Input Multiple Output
M-TA Metamaterial-Based Transmitarray
OAM Orbital Angular Momentum
PCB Printed Circuit Board
PBG Photonic Band Gap
PIN Diode P-type / Intrinsic / N-type Semiconductor Diode
PRS Partially Reflective Surface
RF Radio Frequency
RIS Reconfigurable Intelligent Surface
SIW Substrate Integrated Waveguide
TA Transmitarray
TRL Thru–Reflect–Line Calibration
UAV Unmanned Aerial Vehicle
WR-34 Standard Waveguide for 26.5–40 GHz Frequency Range

Symbols :

λ Wavelength (m)
ϵ_r Relative permittivity (dielectric constant)
μ_0 Permeability of free space (H/m)
ϵ_0 Permittivity of free space (F/m)
θ Elevation / incidence angle (degrees)
ϕ Azimuth angle (degrees)

S_{11}, S_{21}	Reflection and transmission coefficients
G	Antenna gain (dBi)
η	Efficiency
f	Frequency (Hz)
c	Speed of light in vacuum (3×10^8 m/s)

1 INTRODUCTION

Every new generation of wireless networks brings faster speeds and more features to our smartphones. For example, 1G brought us the first cell phone, 2G allowed us to text for the first time, 3G brought us online, and 4G brought us the speeds that we enjoy today. Nonetheless, as more users come online, 4G networks have reached their capacity at a time when users want even more data, and we are now on our way to 5G, the next generation of wireless communication system. This latter will be capable of handling a thousand times more traffic than current networks and will be up to ten times faster than 4G. To this end, cellular providers are striving to offer superior-quality, low-latency video and multimedia applications for wireless devices [1].

Currently, there are five brand new technologies emerging as a foundation of 5G, millimeter waves, small cells, massive MIMO, beam forming, and full duplex. Millimeter wave technology came to solve the issue of limited bandwidth, in the current frequencies typically those under 6 Gigahertz. They are starting to get more crowded, and the solution is to open new spectrum of frequencies, to bring more bandwidth for everyone. In addition, the utilization of higher frequencies results in the availability of smaller antennas and circuits, thus enabling RF transceivers to become more affordable [2–4], but there is a catch, millimeter waves can't travel well through obstacles and tend to be absorbed by plants and rain. To get around this problem, small cell network would solve this problem by using thousands of low-power mini base stations closer together, forming a sort of relay team to transmit signals around obstacles. These antennas can be operated by smart systems that incorporate Massive multiple-input multiple-output (M-MIMO) base stations supporting about a hundred ports. This could increase the capacity by a factor of 22 or more. Of course, massive MIMO comes with its own complications, namely the interference between crossing signals, which brings us to Beam forming technology, which is in a simplest form like a traffic signaling system for cellular signals, instead of broadcasting in every direction it would allow a base station to send a focus stream of data to a specific user. This precision prevents interference and it is much more efficient.

As a result, it is necessary to design an antenna capable of performing multiple functions by combining them into a single element [5–7]. To mitigate radiation interference, this element should be capable of manipulating the beam in specific deflection directions, while preventing unwanted beams from traveling in other ones. As a result, beam-switching/forming antennas have received a great deal of attention in wireless communication systems. Additional functionalities and more properties that are flexible can be achieved by using these antennas, while occupying the same or even less physical space than traditional smart antenna arrays [8].

Furthermore, in order to meet future consumer and technological needs, beamforming subsystems and components must meet certain criteria such as low-loss, compactness, and ease of manufacture. They must also address the difficulties associated with designing cost-effective systems working at higher Mm-wave frequencies. To that end, the primary goal of the proposed research is to improve and develop antennas with beamforming capabilities, using metamaterials to make such devices more easily implementable in current 5G applications and beyond.

1.1 Motivation

Researchers and engineers are now turning to the untapped millimeter wave (mm-Wave) spectrum of frequencies due to the congested, constrained bandwidth, and constrained channel capacity of the current wireless system. In addition to being able to handle the massive increase in the number of connected devices around us, 5G wireless communication technology is predicted to be able to fully realize the potential of cutting-edge new emerging technologies like smart cities, virtual reality, and autonomous cars, among other breath-taking applications. beamforming antennas, massive MIMO (M-MIMO), and multiple base stations (small cell network) will almost certainly be a part of these systems.

As previously stated, the ongoing challenge of congestion in Sub 6 GHz bands, and moving to Mm-wave frequencies, opens up more challenging propagation issues. Therefore, the challenge is to find cost efficient solutions to improve coverage; beamforming technology is on the radar in terms of providing improvements to existing systems and ensuring coverage of future systems. Thus, high gain antennas with wider operating frequencies and dynamic beam steering capabilities are required for Mm-wave applications, and the focus of our research project, is to have a reconfigurable metamaterial-based antenna with high gain and beam steering features over a wideband, to meet all of the aforementioned requirements.

1.2 Problematic

The intention for beam-forming/steering is to fill in the gaps for key challenges – one being around coverage enhancements, and to tackle this issue, electronically tunable antennas are the key player in this matter.

An antenna that can alter its radiation characteristics in order to add new features and improve wireless communication systems is known as a reconfigurable antenna. This antenna's classification is determined by its dynamically adjustable parameters, which are typically its operating frequency, radiation pattern, or polarization. By altering the material's properties or adding parasitic components to the primary antenna, the electric or magnetic currents of the radiating structure can be changed to alter the pattern. Integrated lens antennas (ILAs) [10–12], traveling-wave antennas [13, 14], adaptive arrays [15], phased arrays [16], and active metallic photonic bandgap (AMPBG) [17], are among the techniques that can be used to direct the radiation pattern beam. However, each of these technologies has pros and cons of its own. For instance, when used for

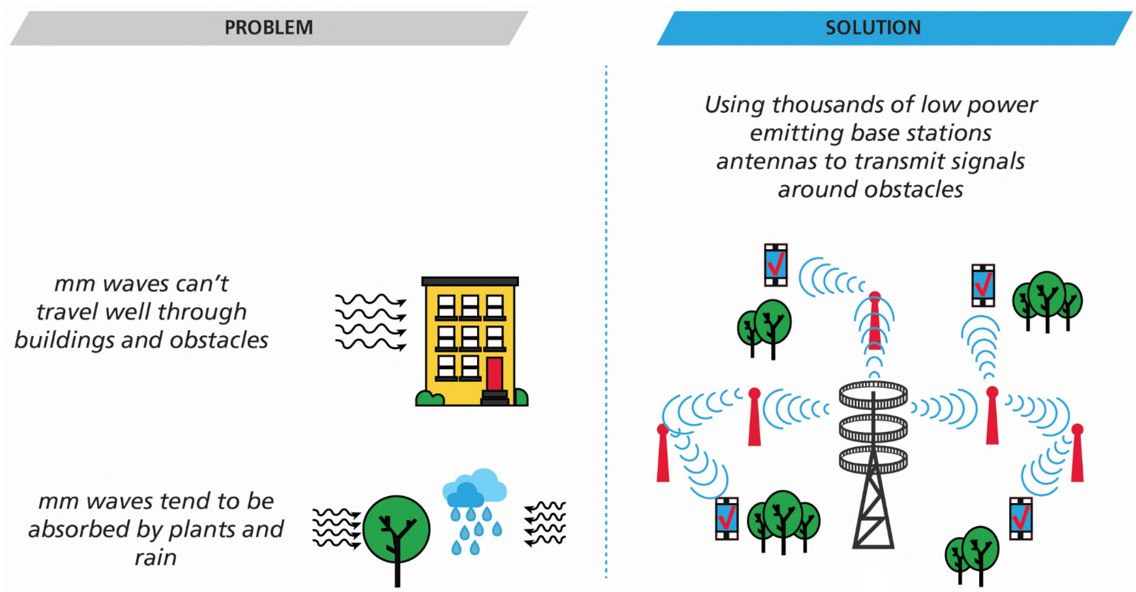

FIGURE 1.1 : 5G communication system coverage enhancement.

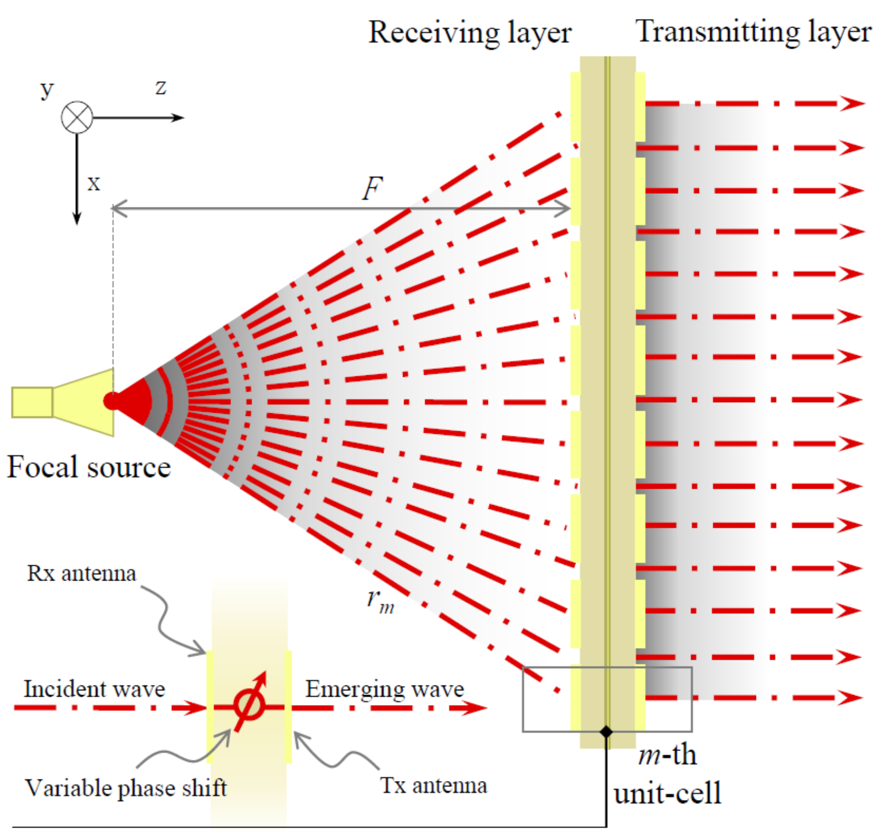

FIGURE 1.2 : Scheme of the working principle of a transmitarray [9].

beam steering, traveling wave antennas are typically large. In order to steer the beam, phased antenna arrays need to precisely control the amplitude and phase of each element, which complicates their structural design and raises the cost of production. In addition to the AMPBG which is a bulky structure with increased side-lobe levels and cross-polarization.

In order to address the complexities, large size, and high cost of the previously mentioned techniques, researchers have recently started using metamaterial-based Transmitarrays (M-TAs). So, what are those? Transmitarrays are based on a thin, multi-layer array of transmitting unit cells that locally adjust the transmitted signals' phase to focus or collimate the radiation toward or away from one or more focal sources. Each unit-cell includes at least three functions : receiving, phase shifting and transmitting the signal. A general scheme of a transmitarray antenna is shown in Fig. 1.2.

The vast majority of transmitarrays that have been proposed in recent years are based on a planar technology, which lowers the cost of fabrication by utilizing the common PCB (Printed Circuit Board) manufacturing method. Transmitarray antennas' main benefits include the lack of a feed blockage area and the ability to shorten the focal distance for compact systems that can be mounted on moving platforms like airplanes and high-speed trains.

The main beam direction and shape can be changed dynamically and the transmitarray becomes reconfigurable by controlling the phase shift provided by each unit-cell. There are numerous ways to implement this phase shifting functionality. For instance, by using a Varactor diode as an active element in an FSS-based spatial pass-band filter [18], it is possible to produce the necessary continuous phase shift while compensating for the differential path rm from the source position and generating the desired phase distribution. This approach, though, has a limited bandwidth.

Another method mentioned in the literature is the current reversal method, which creates a 1-Bit resolution (0 and 180 degrees) system by flipping the direction of the current coming from the receiving side of the TA and achieving a 180° phase shift through the transmitting side of it [9]. Pin diodes can be used to easily accomplish this in place of a varactor. This method offers a larger operating bandwidth but at the cost of peak gain quantization loss and side lobe levels. A practical option for achieving the desired phases is also the polarization-twisting technique.

1.3 Objectives

The aim of this project is to develop a new class of mm-wave metamaterials-based reconfigurable antennas with beam-forming/-steering capability, operating at 28 GHz for future mm-wave 5G wireless communication systems, with the following goals kept in mind :

- $\pm$ 30° beams-steering capability (60 ° in total) in the azimuth plane.
- Minimum of 16 dBi in peak gain for every beam-steering angles.
- Low Side-lobe levels, especially at larger deflection angles.

To acquire these objectives, we propose here a novel approach combining SIW H-horn antenna incorporated with an end-fire leaky-wave pattern, and a Fan-like one in the elevation plane, with a metamaterial-based Transmitarray (M-TA), electronically controlled.

This proposal aims to achieve :

— Design and development of SIW-based H-horn antenna operating at Mm-wave (26-32 GHz), with a minimum gain of 16 dBi, across the band of interest, with different configuration for single and multi-sectors coverage of 360° azimuth beam-steering capabilities.
— Design and development of tunable metamaterial-based Transmitarray (M-TA) with compactness ease of fabrication, and implementation in Mm-wave spectrum taken in consideration. The reconfigurable M-TA should be relatively small, comprising a sufficient number of unit cells (Meta-atom). The meta-atom unit cells must provide a whether a continuous phase tunability ranging from 0 to 360°, or a more simpler discretized form of it in terms of phase bits (1 Bit, 2 Bit, ...etc.), by employing Varactor or Pin diodes.
— A software based control board for all active components, for beam manipulating schemes is also needed to finalize a working prototype.

1.4 Methodology

Up until this point, our focus has been mostly on designing tunable M-TA antennas, and to achieve the aforementioned research goals, we divided the project into three distinct work packages, starting by the conception and design of the feeding element with specific properties, followed by the design and analysis of different techniques, for the meta-atom concept, and finishing by combining both these two crucial elements, in a full working beam-manipulating system, electronically controlled via a software based unit, as our final step of the project.

1.4.1 Work Package 1 : Feeding element

A reliable feeding method is needed with high radiation efficiency and low side-lobe levels. The Substrate Integrated Waveguide (SIW) technology is on the radar as an impressive method to feed planar antennas in the millimeter-wave band. To that end, different feeding elements based on the aforementioned technology, will used in a single and octagonal-shaped forms of feedings, covering the full 360° azimuth beam-steering requirement, as well as being able to provide high gain and wide band operation, making it a great candidate for the final project prototype (see Fig. 1.3).

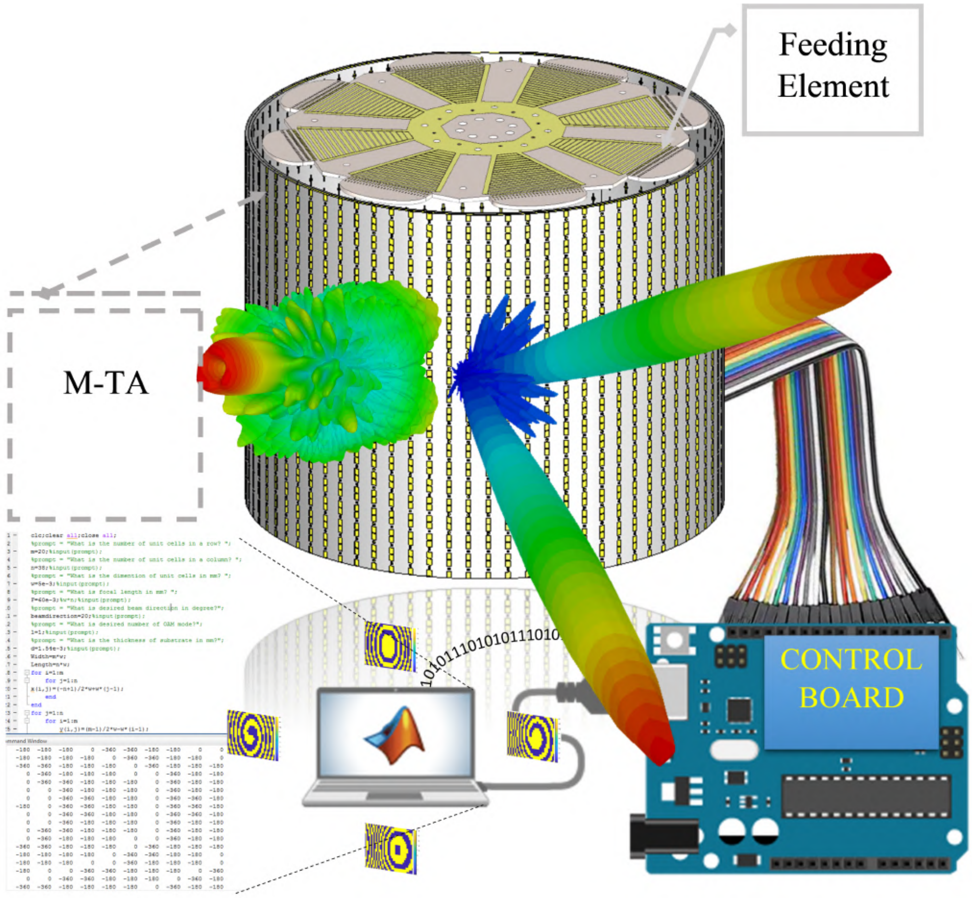

FIGURE 1.3 : Proposed 360° coverage beamsteering system.

1.4.2 Work Package 2 : Tunable Meta-atom

In the second step of the project, our focus will be on studying and investigating different electromagnetic (EM) beam manipulating techniques, as a foundation for the tunable metamaterial-based transmitarray, by exploring their EM properties to improve and alter the radiation characteristics, to a predefined functionality to meet the requirement of a mm-wave reconfigurable antenna with dynamic radiation pattern, as shown in Fig. 1.3.

Recently metamaterials have attracted a lot of interest in the antenna domain because of their ability to control and manipulate the electromagnetic properties of EM waves. These structures are periodical in nature. They can be dielectric or metallic, 2D or 3D structures, that can perform spectral, spatial, or polarization-wise twisting of the incident EM waves. Meaning, they can be used as spatial filters, polarization converters, and/or high impedance surfaces, to EM waves at specific frequency band, leading to an engineered sort of a control of EM wave propagation. This fascinating technology can provide innovative and highly efficient solutions for critical problems in antenna design. More specifically, for reconfigurable antennas with beam-forming/steering functionalities [18–22].

1.4.3 Work Package 3 : Control Board

The third and final part of the project is the steering logic boards, which are used to control the p-i-n diodes mounted on the transmitarray unit-cells. The board itself needs to generate the DC current for the control of n x m bias lines of the transmitarray. It will be placed behind the feeding antenna for the single-shaped form of M-TA, and in the bottom in the case of the octagonal-shaped one, so no interference is introduced to the direction of beam-steering. Furthermore, the code for the control unit has already been developed in Matlab, with different beam-manipulating schemes, to generate binary-programmable sequences, which then will be sent to each control board serially. This data stream is going to be saved on shift registers for a series-to-parallel conversion. These registers will be connected to several switches, and these latter are then connected to a specific bias line of the tunable transmitarray, giving whether a negative ($-$Vcc) or a positive (Vcc) voltage, switching on/off P-i-n diodes.

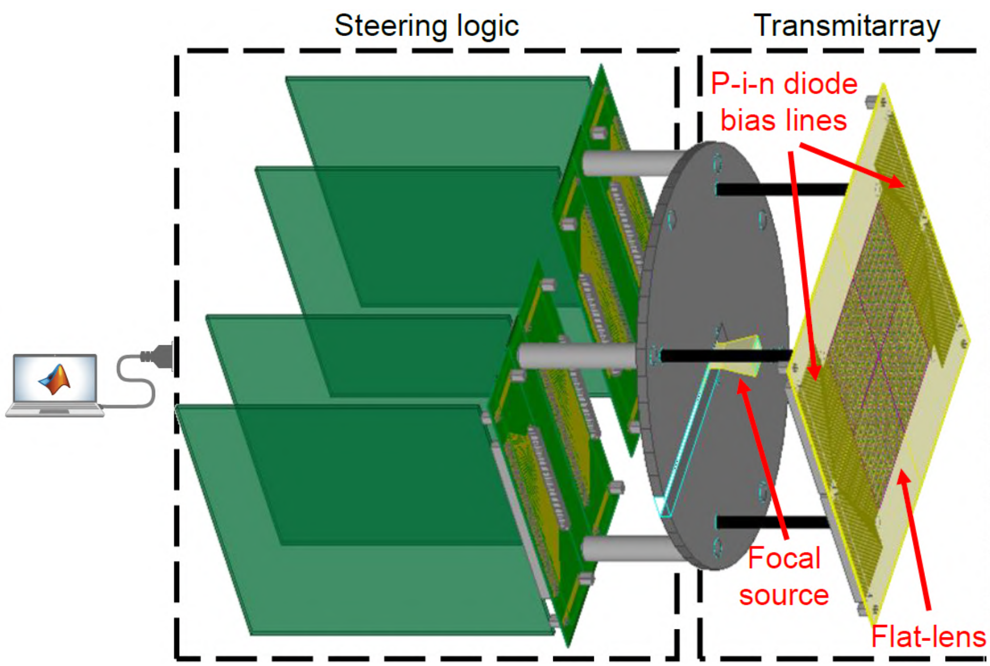

FIGURE 1.4 : The steering logic board [9].

1.5 Contributions

The primary contributions of this thesis can be summarized as follows :

1. **Comprehensive Framework for Reconfigurable Transmitarrays :** A unified design methodology was developed for high-gain, wideband, and reconfigurable transmitarray (TA) antennas operating at Ka-band frequencies. The framework combines electromagnetic modeling, algorithmic

optimization, additive manufacturing, and electronic reconfiguration to address the key limitations of traditional phased-array and reflectarray systems.

2. **Multi-bit Phase and Amplitude Control Using Genetic Algorithm Optimization :** A novel metamaterial-based TA architecture capable of independent phase and amplitude tuning was proposed and optimized. The design employs polarization twisting and current-reversal principles to achieve binary (1-bit) phase control, while a rotating transmitting layer provides multi-bit amplitude modulation. A Genetic Algorithm (GA)-based optimization strategy was implemented to enhance aperture efficiency and suppress sidelobe levels, yielding wideband and high-gain performance experimentally validated through fabricated prototypes.

3. **3D-Printed Conformal Dielectric Lenses for Passive Beam Shaping :** The concept of continuous-aperture beamforming was realized through the design and fabrication of lightweight 3D-printed dielectric lenses. By exploiting the height-to-phase conversion mechanism, these lenses demonstrated passive beam steering, dual-beam formation, and orbital angular momentum (OAM) generation. The results confirm the potential of additive manufacturing for scalable, conformal, and low-cost mm-wave front-end systems.

4. **Electrically Reconfigurable CPW-to-Slotline Transmitarray Architecture :** A novel uniplanar reconfigurable 1-bit transmitarray was developed using a compact CPW-to-slotline transition with dual PIN diodes per unit cell. The structure achieves binary phase inversion through intrinsic mode symmetry, eliminating the need for external hybrids or multi-layer networks. Modular 16-cell panels were designed and simulated, demonstrating efficient mode conversion, broadband transmission, and electronically steerable radiation patterns at Ka-band.

5. **Experimental Validation and System Integration :** Several transmitarray prototypes were fabricated and characterized through full-wave simulations and far-field measurements. The measured results confirmed broadband transmission, accurate beam steering, and strong correlation with simulation data, thereby validating the proposed design methodologies. The work also establishes clear guidelines for scaling toward multi-panel, conformal, and hybrid reconfigurable architectures.

Collectively, these contributions advance the state of the art in millimeter-wave reconfigurable antenna systems. The proposed approaches offer compact, low-loss, and cost-effective solutions for future 5G/6G communication, vehicular sensing, and satellite front-end applications, while providing a versatile foundation for intelligent, algorithmically controlled beamforming architectures.

1.6 Publications

1.6.1 Published journals

1. **Melouki, N.**, Ahmed, F., Pourmohammadi, P., Naseri, H., & Denidni, T. A. (2025). Wideband transmitarray with independent phase/amplitude control for millimeter-wave vehicular sensing and communication. AEU-International Journal of Electronics and Communications, 195, 155771.
2. **Melouki, N.**, Ahmed, F., PourMohammadi, P., Naseri, H., Bizan, M. S., Iqbal, A., & Denidni, T. A. (2024) 3D-Printed Conformal Meta-Lens with Multiple Beam-Shaping Functionalities for Mm-Wave Sensing Applications. Sensors. 24 : 2826.
3. **Melouki, N.**, PourMohammadi, P., Nasseri, H., Ahmed, F., Iqbal, A., Hocini, A., & Denidni, T. A. (2023) Ultra-compact Quarter-Mode SIW Self-Hexaplexing Antenna for C-band and X-band Applications. IEEE Antennas and Wireless Propagation Letters. 23 : 995-999.
4. **Melouki, N.**, Hocini, A., & Denidni, T. A., "High gain and Wideband Fabry-Perot Resonator Antenna based on a compact single PRS layer, " in *IEEE Access*, 10, 96526-96537, 2022.
5. **Melouki, N.**, Hocini, A., & Denidni, T. A., "Performance enhancement of an ultra-wideband antenna using a compact topology optimized single frequency selective surface-layer as a reflector, " in *International Journal of RF and Microwave Computer-Aided Engineering*, 32(5), e23097, 2022.
6. **Melouki, N.**, Hocini, A., Fegriche, F. Z., PourMohammadi, P., Naseri, H., Iqbal, A., & Denidni, T. A., "High-gain wideband circularly polarised Fabry–Perot resonator array antenna using a single-layered pixelated PRS for millimetre-wave applications, " in *Micromachines*, 13(10), 1658, 2022.
7. Naseri, H., Pourmohammadi, P., Kamali, N., **Melouki, N.**, Ahmed, F., Iqbal, A., & Denidni, T. A. (2026). Introduction to BeamWave Matrix for beam-forming and wave manipulation applications. AEU-International Journal of Electronics and Communications, 203, 156062.
8. Naseri, H., Pourmohammadi, P., Barua, S., **Melouki, N.**, Ahmed, F., Iqbal, A., & Denidni, T. A. (2025). High-security antenna system with dual polarization and frequency tunability for driverless vehicles. AEU-International Journal of Electronics and Communications, 155928.
9. Naseri, H., Pourmohammadi, P., **Melouki, N.**, Ahmed, F., Iqbal, A., & Denidni, T. (2024). Frequency-adjustable OAM antenna with co-divergent beams for IoT applications. AEU-International Journal of Electronics and Communications, 177, 155188.
10. Naseri, H., PourMohammadi, P., **Melouki, N.**, Ahmed, F., Iqbal, A., & Denidni, T. A. (2024). Reconfigurable OAM antenna with flexibility on mode numbers, polarization, and frequency. IEEE Antennas and Wireless Propagation Letters, 23(6), 1710-1714.

11. Naseri, H., Pourmohammadi, P., Fei, P., **Melouki, N.**, Iqbal, A., & Denidni, T. (2023). Butler matrix-based beamforming with polarization reconfigurability for reducing electromagnetic interference. AEU-International Journal of Electronics and Communications, 170, 154833.
12. Naseri, H., PourMohammadi, P., **Melouki, N.**, Ahmed, F., Iqbal, A., & Denidni, T. A. (2023). Substrate integrated waveguide-based dual-polarized self-diplexing antenna array. IEEE Transactions on Circuits and Systems II : Express Briefs, 70(8), 2839-2843.
13. Naseri, H., PourMohammadi, P., **Melouki, N.**, Ahmed, F., Iqbal, A., & Denidni, T. A. (2023). Generation of mixed-OAM-carrying waves using huygens' metasurface for mm-wave applications. Sensors, 23(5), 2590.
14. Naseri, H., Pourmohammadi, P., **Melouki, N.**, Iqbal, A., & Denidni, T. A., "A low-profile antenna system for generating reconfigurable oam-carrying beams," in *IEEE Antennas and Wireless Propagation Letters*, vol. 22, no. 2, pp. 402-406, Feb. 2023.
15. Naseri, H., Pourmohammadi, P., **Melouki, N.**, Ahmed, F., Iqbal, A., & Denidni, T. A., "Substrate Integrated Waveguide Based Dual-Polarized Self-Diplexing Antenna Array," in *IEEE Transactions on Circuits and Systems II : Express Briefs*, 2023.
16. Naseri, H., Pourmohammadi, P., **Melouki, N.**, Ahmed, F., Iqbal, A., & Denidni, T. A., "Generation of mixed-oam-carrying waves using huygens' metasurface for mm-wave applications," in *Sensors*, vol. 23, no. 5, p. 2590, 2023.
17. Naseri, H., Pourmohammadi, P., Fei, P., **Melouki, N.**, Iqbal, A., & Denidni, T., "Butler matrix-based beamforming with polarization reconfigurability for reducing electromagnetic interference, " in *AEU-International Journal of Electronics and Communications*, 170, 154833, 2023.
18. Bizan, M. S., Naseri, H., Pourmohammadi, P., **Melouki, N.**, Iqbal, A., & Denidni, T. A., "Dual-Band Dielectric Resonator Antenna with Filtering Features for Microwave and Mm-Wave Applications, " in *Micromachines*, 14(6), 1236, 2023.
19. Khodja, K., Atia, S., Messaoudene, I., Belazzoug, M., Merabet, I., **Melouki, N.**, & Denidni, T. A. (2025). Novel High Efficiency V-Band Pure TEM D-PRGW Antenna for 5G mmWave Applications. International Journal of Communication Systems, 38(4), e6008.
20. Ksouri, E., Boufrioua, A., Belazzoug, M., Messaoudene, I., **Melouki, N.**, & Denidni, T. A. (2024). A gain enhancement of compact UWB antenna based on a single FSS layer. Microwave and Optical Technology Letters, 66(8), e34301.
21. Ahmed, F., **Melouki, N.**, PourMohammadi, P., Naseri, H., & Denidni, T. A. (2025). A Compact and Wideband Active Asymmetric Transmit Array Unit Cell for Millimeter-Wave Applications. Sensors, 25(16), 5168.
22. Ahmed, F., Ahmed, A., **Melouki, N.**, PourMohammadi, P., Naseri Gheisanab, H., Shoaib, N., & Denidni, T. A. (2024). A wideband bianisotropic FSS absorber with angular stable and polarization-insensitive properties. Waves in Random and Complex Media, 1-16.

23. Ahmed, F., Faisal, F., **Melouki, N.**, Ahmed, A., Naseri, H., PourMohammadi, P., & Denidni, T. A. (2024). A Multi-Functional Reflective Polarization Transforming Surface with In-Band and Out-Band Transmission Characteristics. IEEE Antennas and Wireless Propagation Letters.
24. Pourmohammadi, P., Naseri, H., **Melouki, N.**, Ahmed, F., Zheng, Q., Iqbal, A., & Denidni, T. A. (2025). A wideband beam steering transmitarray antenna for Ka-band applications. AEU-International Journal of Electronics and Communications, 193, 155720.
25. PourMohammadi, P., Naseri, H., **Melouki, N.**, Ahmed, F., Zheng, Q., Iqbal, A., ... & Denidni, T. A. (2024). Highly-isolated compact self-diplexing antenna. AEU-International Journal of Electronics and Communications, 173, 155025.
26. PourMohammadi, P., Naseri, H., **Melouki, N.**, Ahmed, F., and Iqbal, A., and & Denidni, T. A., “Substrate Integrated Waveguide Based Full-Duplex Antenna with Improved Out-of-Band Suppression,” in *IEEE Transactions on Circuits and Systems II : Express Briefs*, pp. 1–5, 2022.
27. PourMohammadi, P., Naseri, H., **Melouki, N.**, F. Ahmed, A. Iqbal, Vandenbosch, G. A., & Denidni, T. A., “Compact SIW-Based Self-Quadruplexing Antenna for Mm-wave and Microwave Communications, ” in *IEEE Transactions on Circuits and Systems II : Express Briefs*, 2023.
28. PourMohammadi, P., Naseri, H., **Melouki, N.**, Ahmed, F., Bizan, M. S., Iqbal, A., & Denidni, T. A., "A Fabry–Perot antenna using a frequency selective surface layer with wideband and Low RCS for Mm-wave applications, " in *AEU-International Journal of Electronics and Communications*, 169, 154736, 2023.

1.6.2 Conferences

1. **Melouki, N.**, & Denidni, T. A. (2024, December). AI-Driven Beam-Steering Metamaterial Lens for 5G and Autonomous Vehicles. In 2024 International Conference on Telecommunications and Intelligent Systems (ICTIS) (pp. 1-4). IEEE.
2. **Melouki, N.**, Ahmed, F., PourMohammadi, P., & Denidni, T. A. (2024, July). 3D-Printed Conformal Meta-Lens with Multi-Mode Orbital Angular Momentum (OAM) Generation and Beam-Steering Capabilities. In 2024 IEEE International Symposium on Antennas and Propagation and INC/USNC-URSI Radio Science Meeting (AP-S/INC-USNC-URSI) (pp. 419-420). IEEE.
3. **Melouki, N.**, Ahmed, F., Nasseri, H., Pourmohammadi, P., Iqbal, A., & Denidni, T. A. (2024, March). Multi-Bit Wideband Transmitarray Aperture with Independent Phase and Amplitude Control for High Gain with Low Sidelobe Mm-Wave Applications. In 2024 18th European Conference on Antennas and Propagation (EuCAP) (pp. 01-04). IEEE.
4. **Melouki, N.**, Ahmed, F., PourMohammadi, P., Naseri, H., Iqbal, A., & Denidni, T. A. (2023, July). 3D-printed conformal metamaterial lens with multiple beam steering functionalities. In

2023 IEEE International Symposium on Antennas and Propagation and USNC-URSI Radio Science Meeting (USNC-URSI) (pp. 791-792). IEEE.

5. **Melouki, N.**, Nasseri, H., Iqbal, A., & Denidni, T. A. (2023, March). Compact quarter-mode SIW self-triplexing antenna for C-band and X-band applications. In 2023 17th European Conference on Antennas and Propagation (EuCAP) (pp. 1-5). IEEE.
6. **Melouki, N.**, Hocini, A., & Denidni, T. A., "High-gain and Wideband Fabry-Perot Resonator Antenna based on a Pixelated single PRS layer for Ku-band Applications, " in *2022 IEEE International Symposium on Antennas and Propagation and USNC-URSI Radio Science Meeting (AP-S/URSI)*, pp. 988-989), July, 2022. (published).
7. **Melouki, N.**, Nasseri, H., Iqbal, A., & Denidni, T. A., "Compact Quarter-Mode SIW Self-triplexing Antenna for C-band and X-band Applications, " in *2023 17th European Conference on Antennas and Propagation (EuCAP)*, (pp. 1-5), March, 2023.
8. **Melouki, N.**, Ahmed, F., Pourmohammadi, P., Naseri, H., Iqbal, A., & Denidni, T. A., "Low-loss 2-bit Reflective Intelligent Surface for mm-wave Applications, " in *2023 URSI International Symposium on Electromagnetic Theory (EMTS)*, May, 2023.
9. **Melouki, N.**, Ahmed, F., Pourmohammadi, P., Naseri, H., Iqbal, A., & Denidni, T. A., "3D-Printed Conformal Metamaterial Lens with Multiple Beam Steering Functionalities, " in *2023 IEEE International Symposium on Antennas and Propagation and USNC-URSI Radio Science Meeting (AP-S/URSI)*, July, 2023.
10. PourMohammadi, P., Naseri, H., **Melouki, N.**, & Denidni, T. A. (2024, July). A 1-Bit Wideband Electronically Beam Steering Transmitarray for 5G Communication Systems. In 2024 IEEE International Symposium on Antennas and Propagation and INC/USNC-URSI Radio Science Meeting (AP-S/INC-USNC-URSI) (pp. 139-140). IEEE.
11. PourMohammadi, P., Naseri, H., **Melouki, N.**, Ahmed, F., Vandenbosch, G. A.E., Iqbal, A., and & Denidni, T. A., "A Low-profile Self-duplexing Antenna for Millimeter-wave and Microwave Frequency Bands, " in *2023 IEEE International Symposium on Antennas and Propagation and USNC-URSI Radio Science Meeting (AP-S/URSI)*, July, 2023.
12. PourMohammadi, P., Naseri, H., **Melouki, N.**, Ahmed, F., Bizan, M., Iqbal, A., and & Denidni, T. A., "A Wideband Fabry-Perot Antenna with a Bianisotropic FSS Layer, " in *2023 IEEE International Symposium on Antennas and Propagation and USNC-URSI Radio Science Meeting (AP-S/URSI)*, July, 2023.
13. PourMohammadi, P., Naseri, H., **Melouki, N.**, Ahmed, F., Bizan, M., Iqbal, A., and & Denidni, T. A., "A Wideband Anisotropic Metasurface for Cross-Polarization Applications, " in *2023 URSI International Symposium on Electromagnetic Theory (EMTS)*, May, 2023.
14. Naseri, H., Pourmohammadi, P., **Melouki, N.**, Ahmed, F., Iqbal, A., & Denidni, T. A. (2024, March). Dual-Polarized OAM Antenna with Frequency and Mode Agility for Intelligent OAM Communications. In 2024 18th European Conference on Antennas and Propagation (EuCAP) (pp. 1-4). IEEE.

15. Naseri, H., PourMohammadi, P., Bizan, M., **Melouki, N.**, Ahmed, F., Iqbal, A., and & Denidni, T. A., "Reconfigurable Dielectric Resonator OAM Antenna with Augmented Modes, " in *2023 IEEE International Symposium on Antennas and Propagation and USNC-URSI Radio Science Meeting (AP-S/URSI)*, July, 2023.
16. Naseri, H., PourMohammadi, P., Bizan, M., **Melouki, N.**, Ahmed, F., Iqbal, A., and & Denidni, T. A., "Triple-Mode OAM Generating Dielectric Resonator Antenna, " in *2023 URSI International Symposium on Electromagnetic Theory (EMTS)*, May, 2023.
17. Naseri, H., PourMohammadi, P., **Melouki, N.**, Iqbal, A., and & Denidni, T. A., ”Self-diplexing Antenna Operating at Sub-6 GHz and Milimeter wave Frequencies”, in *2023 17th European Conference on Antennas and Propagation (EuCAP)*, March, 2023.
18. Ahmed, F., **Melouki, N.**, PourMohammadi, P., & Denidni, T. A. (2024, July). A Multifunctional Bianisotropic Frequency Selective Surface for Microwave Applications. In 2024 IEEE International Symposium on Antennas and Propagation and INC/USNC-URSI Radio Science Meeting (AP-S/INC-USNC-URSI) (pp. 1823-1824). IEEE.
19. Ahmed, F., **Melouki, N.**, PourMohammadi, P., Naseri, H. & Denidni, T. A., "A 2-Bit Reconfigurable Reflecting Metasurface for Mm-wave Applications," in *2023 IEEE International Symposium on Antennas and Propagation and USNC-URSI Radio Science Meeting (AP-S/URSI)*, July, 2023.
20. Ahmed, F., **Melouki, N.**, PourMohammadi, P., Naseri, H. & Denidni, T. A., "4-Bit Reconfigurable Reflecting Metasurface for Sub-6 GHz Band," in *2023 URSI International Symposium on Electromagnetic Theory (EMTS)*, May, 2023.

1.7 Honors and Awards

1. Recognition of contribution as a mentor for Apprentis chercheurs Program ,INRS, University du Quebec, Canada, 2023-2024.
2. 1st place best student poster award, STARaCom, McGill University, Canada, 2023.

1.8 Outline of the Thesis

The thesis is organized into six main chapters, each addressing a distinct stage of the research process, from theoretical foundation to experimental validation and future perspectives.

Chapter 1 (Introduction) : This chapter establishes the motivation behind developing efficient, reconfigurable, and scalable millimeter-wave transmitarray (TA) and lens antennas. It defines the research problem, objectives, and adopted methodology, while situating the work within the broader context of 5G/6G, satellite, and vehicular communication systems. The chapter concludes with an overview of the thesis structure, highlighting the key milestones, related publications, and scholarly contributions arising from this research.

Chapter 2 (Literature Review) : This chapter provides a comprehensive review of state-of-the-art metasurface-based transmitarrays and related beamforming techniques. It discusses the evolution from traditional phased arrays and reflectarrays to reconfigurable metasurfaces, emphasizing challenges in phase quantization, bandwidth enhancement, and integration complexity. The review identifies the existing research gaps and establishes the need for new approaches combining algorithmic optimization, additive manufacturing, and electrical reconfigurability.

Chapter 3 (Multi-bit Wideband Transmitarray Design and Optimization) : This chapter presents the development of a wideband transmitarray architecture capable of independent control of phase and amplitude. A dual-layer metamaterial unit cell is introduced, leveraging polarization twisting and current-reversal principles to achieve 1-bit phase control and multi-bit amplitude modulation. A Genetic Algorithm (GA)-based optimization framework is implemented to minimize sidelobe levels while maintaining high gain. The chapter concludes with the fabrication and measurement of 20×20 prototypes that validate the wideband and beam-steering capabilities of the design.

Chapter 4 (3D-Printed Conformal Dielectric Lenses) : This chapter extends the transmitarray concept to three-dimensional continuous apertures through the use of additive manufacturing. Novel 3D-printed dielectric lenses are designed using the height-to-phase conversion principle to realize passive beam steering, dual-beam formation, and orbital angular momentum (OAM) generation. Experimental results confirm the feasibility of low-loss, lightweight, and conformal lens structures suitable for UAV and vehicular applications.

Chapter 5 (Reconfigurable CPW-to-Slotline Transmitarray Architecture) : This chapter introduces a reconfigurable 1-bit transmitarray antenna based on a compact CPW-to-slotline transition employing dual PIN diodes per unit cell. The proposed structure achieves binary phase inversion through intrinsic field symmetry rather than external phase-shifting networks. Modular 16-cell panels are designed and assembled into a larger multi-panel array, demonstrating broadband transmission, efficient mode conversion, and electronically controlled beam steering at Ka-band frequencies.

Chapter 6 (Conclusion and Future Work) : The final chapter summarizes the major findings and original contributions of this research. It reflects on the integration of electromagnetic modeling, GA optimization, additive manufacturing, and reconfigurable design into a unified framework for high-gain, wideband, and low-cost mm-wave antennas. The chapter concludes by outlining prospective research directions involving multi-bit reconfigurability, intelligent beam control, hybrid lens-metasurface systems, and energy-efficient architectures for next-generation 5G/6G applications.

2 LITERATURE REVIEW

This chapter presents a comprehensive survey of metasurface-based reconfigurable transmitarray antennas, emphasizing their beamforming and radiation control capabilities at millimeter-wave frequencies. It begins with a discussion of conventional beam-steering techniques, outlining the inherent limitations of traditional mechanical, analog, and digital architectures in terms of efficiency, complexity, and scalability. The review then revisits the fundamental principles of transmitarray antennas, describing their evolution from passive configurations toward electronically reconfigurable metasurfaces. Particular attention is devoted to the incorporation of tunable elements—such as PIN diodes, varactors, and emerging active materials—that enable dynamic phase control and adaptive radiation. Furthermore, recent advancements in analog and digital phase quantization, material engineering, and hybrid reconfiguration schemes are examined in detail. Finally, the chapter surveys the latest application-oriented developments spanning satellite communications, vehicular sensing, millimeter-wave base stations, and unmanned aerial vehicle (UAV) platforms, establishing the technological context for the research directions pursued in subsequent chapters.

2.1 Introduction

The rapid evolution of wireless communications and sensing systems toward fifth-generation (5G) and beyond networks has intensified the demand for antennas that combine high gain, wide bandwidth, low profile, and agile beam-steering capability. Traditional phased arrays provide electronic beam control through distributed phase shifters, but their complexity, power consumption, and cost increase dramatically at millimeter-wave frequencies. Reflectarray antennas mitigate these limitations by transforming an incident field from a feed into a collimated beam through spatial phase compensation, yet they suffer from feed blockage and phase non-linearity effects.

Transmitarray antennas (TAs) have therefore emerged as an effective hybrid between lens and phased-array concepts—achieving directive transmission through spatially distributed subwavelength unit cells that control the transmitted phase of an impinging feed wave [1, 23]. Compared to conventional phased arrays, TAs offer a passive or semi-passive architecture with reduced feed loss, minimal mutual coupling, and mechanical simplicity. Over the last decade, a substantial body of research has advanced their design from early narrowband configurations toward broadband, polarization-flexible, and electronically reconfigurable implementations across the microwave and millimeter-wave spectrum [24, 25].

This chapter reviews the relevant literature underpinning the development of transmitarray technology, including static and reconfigurable architectures, metasurface-based realizations, beam-steering mechanisms, and enabling device technologies. The review concludes by identifying the remaining technical challenges motivating the present investigation into a compact, uniplanar reconfigurable approach suitable for Ka-band front-ends.

2.2 Foundations of Transmitarray Antenna Technology

The transmitarray concept evolved from the synthesis of phased-array and lens antenna principles, wherein the transmission phase of each element compensates for the spatial delay between the feed and aperture (see Fig. 2.1). Abdelrahman *et al.* [26] provided a comprehensive analytical framework describing field transformation, path compensation, and aperture efficiency optimization, establishing the theoretical baseline for contemporary designs. Guo and Ziolkowski [27] further extended these foundations by integrating advanced array engineering methods aimed at 6G and terahertz-band front-ends.

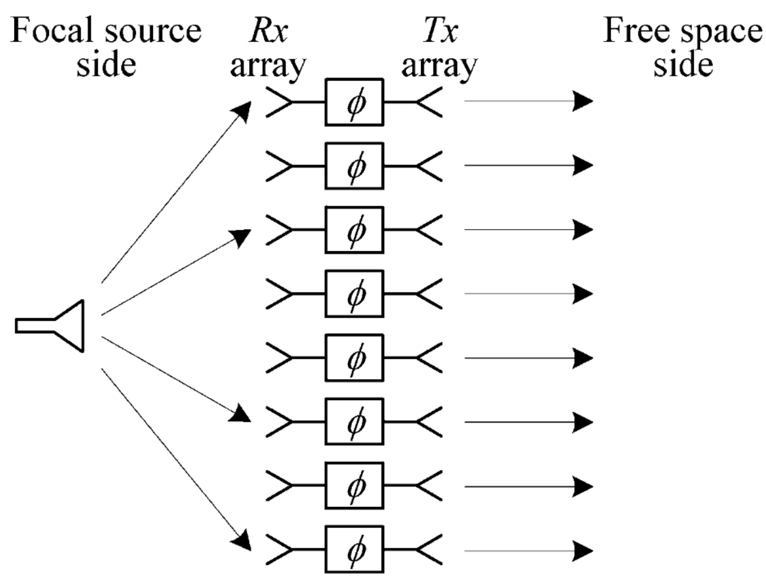

FIGURE 2.1 : Conceptual operation of a planar transmitarray [24].

Early passive transmitarrays employed resonant patch or ring elements to introduce discrete transmission phase delays [28]. Ryan *et al.* introduced a dual-resonant double-square-ring cell that achieved wideband phase coverage through the superposition of two resonances, thereby improving bandwidth and amplitude uniformity (see Fig. 2.2). Kaouach *et al.* [24] later implemented both linearly and circularly polarized low-loss transmitarrays in V-band using multilayer stacking and dual-resonant coupling apertures, demonstrating efficiencies exceeding 60 %.

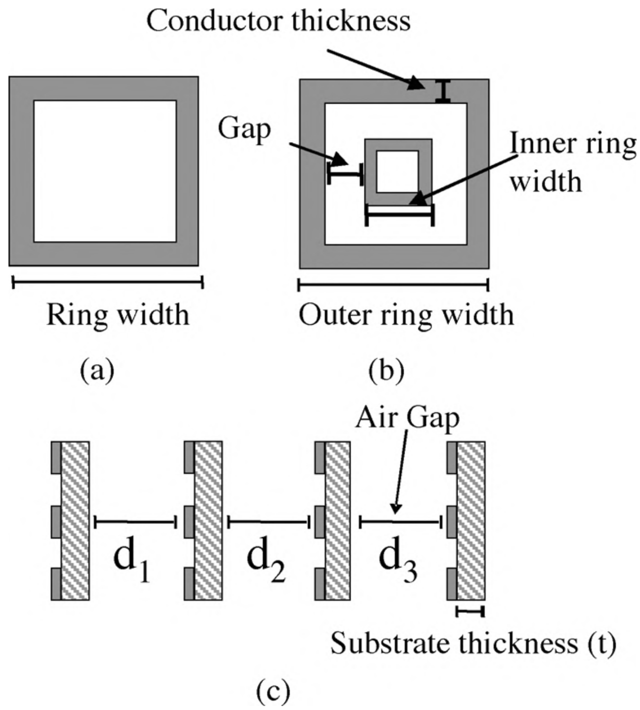

FIGURE 2.2 : (a) Single square ring element (b) double square ring element and (c) arrangement on multilayer transmitarray [28].

2.3 Metasurface and Huygens-Type Elements

The advent of metasurface engineering provided a new paradigm for transmitarray design. By employing sub-wavelength scatterers capable of simultaneously manipulating electric and magnetic responses, so-called *Huygens' metasurfaces* enable near-unity transmission with precise phase control [29, 30] as seen in Fig. 2.3. Pfeiffer and Grbic [29] demonstrated reflectionless Huygens' sheets capable of arbitrarily shaping transmitted wavefronts. Subsequent work by Eleftheriades *et al.* [30] examined their prospects for practical antenna implementations, emphasizing their capacity to realize highly efficient, polarization-controllable apertures.

Cao *et al.* [32] presented a broadband millimeter-wave transmitarray based on a metasurface-derived element providing smooth 360° phase variation, while Pourgholamhossein *et al.* [31] exploited an ultrathin Huygens' metasurface to design a flat lens with improved bandwidth and gain. Cheng *et al.* [33] achieved a broadband planar Luneburg lens using complementary metamaterials, bridging the gap between gradient-index lenses and discrete phased architectures.

2.4 Mechanically and Electronically Steerable Lens Antennas

Before the adoption of reconfigurable electronics, beam steering in transmitarrays and lens antennas was primarily achieved through mechanical translation or rotation of the feed as illustrated in Fig. 2.4. Costa *et al.* [34] and Fernandes *et al.* [35, 36] demonstrated compact 60-GHz mecha-

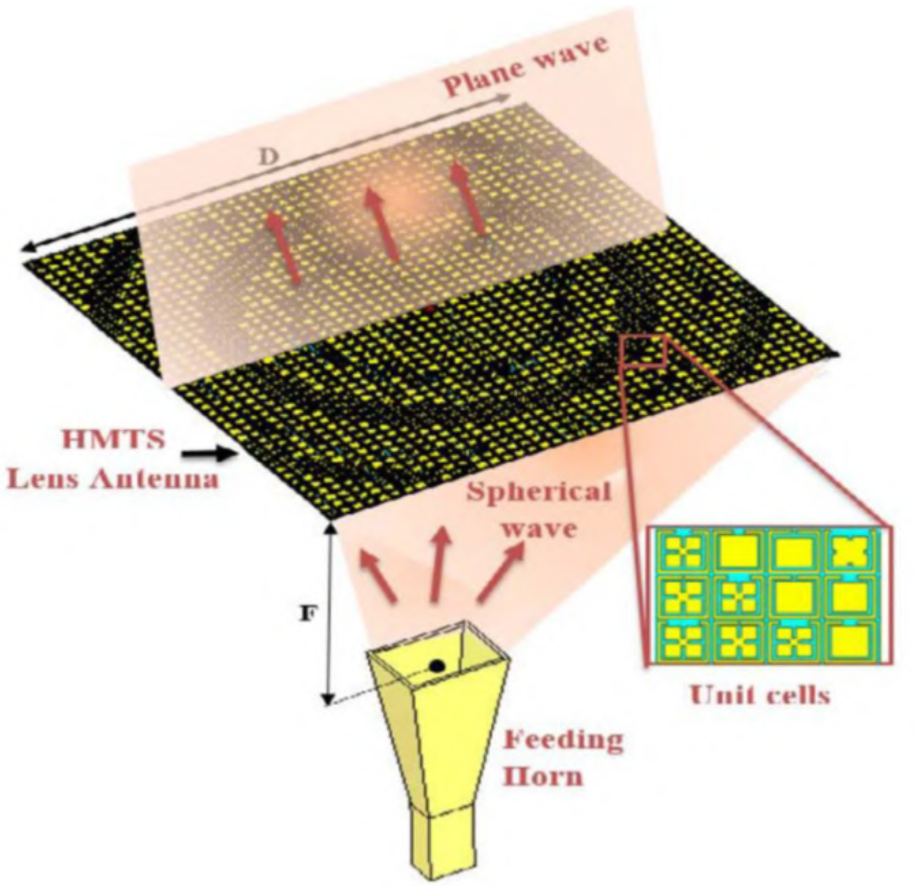

FIGURE 2.3 : Typical Huygens' metasurface element enabling broadband transmission [31].

nically steerable lens systems for indoor LANs, offering a practical approach to adaptive beam coverage albeit at the expense of mechanical complexity and slow response.

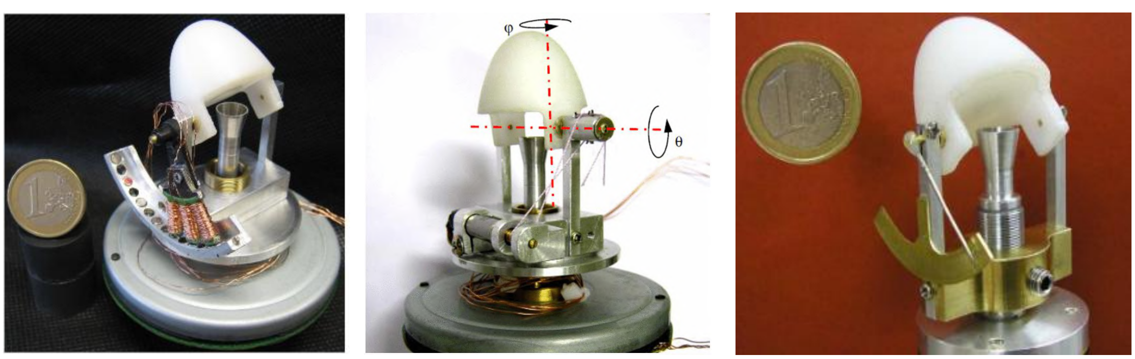

(a) (b) (c)

FIGURE 2.4 : Manufactured three lens antennas for mechanically beamsteering (a) [35], (b) [34] and (c) [36].

Zarb-Adami *et al.* [37] and Gholam *et al.* [38] compared analog and digital beamforming techniques for large-N apertures, highlighting the trade-offs between hardware simplicity and phase accuracy. Steyskal [39] earlier defined the fundamentals of digital beamforming, laying the groundwork for hybrid analog-digital control in modern arrays.

Artemenko *et al.* [40] extended the concept to millimeter-wave WLAN/WPAN systems through electronically steerable integrated lens antennas, paving the way for planar feed integration. More recently, Romeu *et al.* [41] introduced a lens-based switched-beam antenna for 5G smart repeaters, demonstrating multi-beam functionality with compact architecture.

2.5 Reconfigurable and Active Transmitarray Architectures

The introduction of electronically tunable components such as PIN diodes, varactors, MEMS, and tunable materials has enabled real-time control of the transmission phase of individual elements. Clemente *et al.* [42] reported one of the earliest wideband electronically reconfigurable transmitarrays at X-band, comprising 400 elements controlled through dual-mode resonators and PIN diodes (Fig. 2.5). Subsequent studies by Diaby *et al.* [19, 43, 44] extended this concept to Ka-band 1-bit and 2-bit unit cells, validating both simulated and measured broadband beam steering. Ali *et al.* [45] and Rana *et al.* [46] reviewed the state of beam-steerable transmitarrays, summarizing emerging challenges in insertion loss, phase quantization, and control complexity.

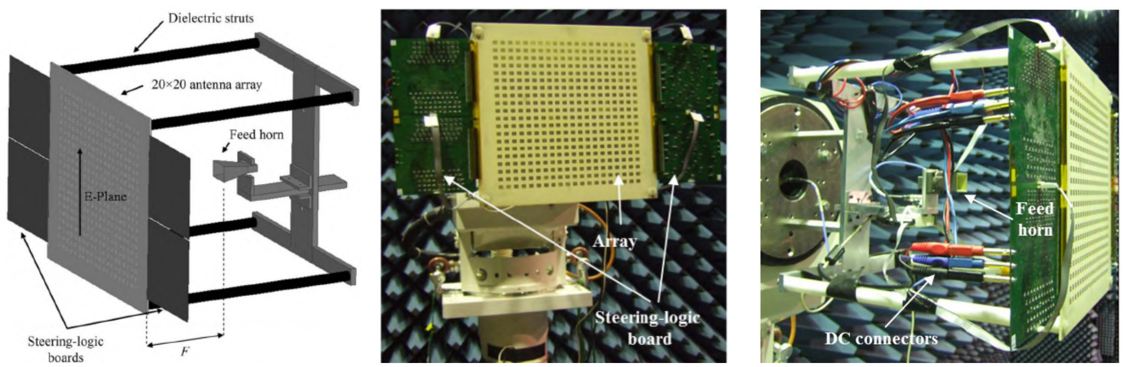

FIGURE 2.5 : Electronically reconfigurable transmitarray [42].

Melouki *et al.* [47] introduced a multi-bit wideband transmitarray offering independent phase and amplitude control for millimeter-wave applications, demonstrating improved sidelobe suppression and gain uniformity. Luo *et al.* [48] proposed a wideband 1-bit reconfigurable transmitarray based on polarization-rotation elements, simplifying biasing and fabrication. Diaby *et al.* [44] later refined the dual-bit Ka-band unit-cell design to realize fine phase quantization and electronically steerable radiation patterns.

2.6 Active and Tunable Metasurfaces

Recent developments have incorporated new active materials such as graphene [49], vanadium-dioxide (VO_2) [50], and semiconductor inclusions [51] to achieve dynamic electromagnetic control across wide frequency bands. Graphene-based metasurfaces provide voltage-tunable surface conductivity, enabling dynamic phase and polarization control at terahertz frequencies [49]. Yang *et al.* [50]

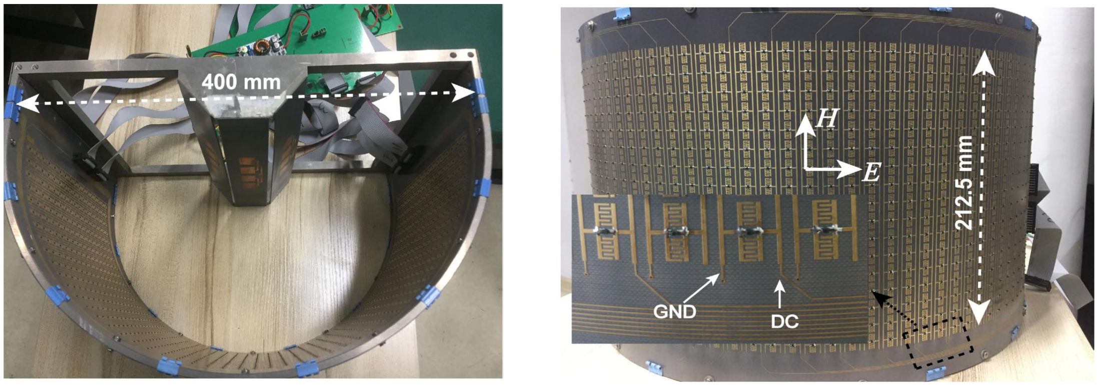

FIGURE 2.6 : Fabricated metasurface cylindrical lens antenna [18].

demonstrated a programmable VO_2 metasurface capable of beam steering via thermal or electrical stimuli. You *et al.* [51] provided an extensive tutorial on transmissive metasurfaces for terahertz wavefront manipulation, highlighting opportunities for broadband adaptive lenses.

Although these approaches reveal powerful reconfigurability, their integration within high-power Ka-band systems remains constrained by fabrication cost and biasing complexity.

2.7 Transmitarrays for Satellite and Vehicular Communications

Transmitarray antennas have gained particular importance in high-frequency satellite and vehicular communication systems requiring compact, steerable apertures with robust environmental performance. Hasani *et al.* [52] introduced a dual-band circularly polarized transmitarray operating at 20/30 GHz for satellite links, demonstrating polarization isolation better than 20 dB. Iqbal *et al.* [53] achieved a compact Ku-band transmitarray optimized for gain and footprint. Kausar *et al.* [54] designed a multi-beam steerable transmitarray lens suitable for both satellite and 5G mm-wave systems.

Yeap *et al.* [55] realized a 77-GHz dual-layer transmitarray for automotive radar, and Greco *et al.* [56] recently advanced this concept into an in-package solution for vehicular radars. Melouki *et al.* [57] extended transmitarray functionality to dual-purpose vehicular sensing and communications. Similarly, Ganie and Saurav [58] demonstrated a two-dimensional switchable-beam transmitarray for vehicular base stations.

2.8 Emerging Applications : UAVs and Conformal Apertures

Beyond ground and satellite terminals, reconfigurable transmitarrays are increasingly considered for airborne and conformal platforms. Vaquero *et al.* [59] evaluated a millimeter-wave transmitarray base station in the Fresnel region. PourMohammadi *et al.* [60] reported a wideband beam-steering Ka-band transmitarray suitable for aeronautical payloads as illustrated in Fig 2.9, while

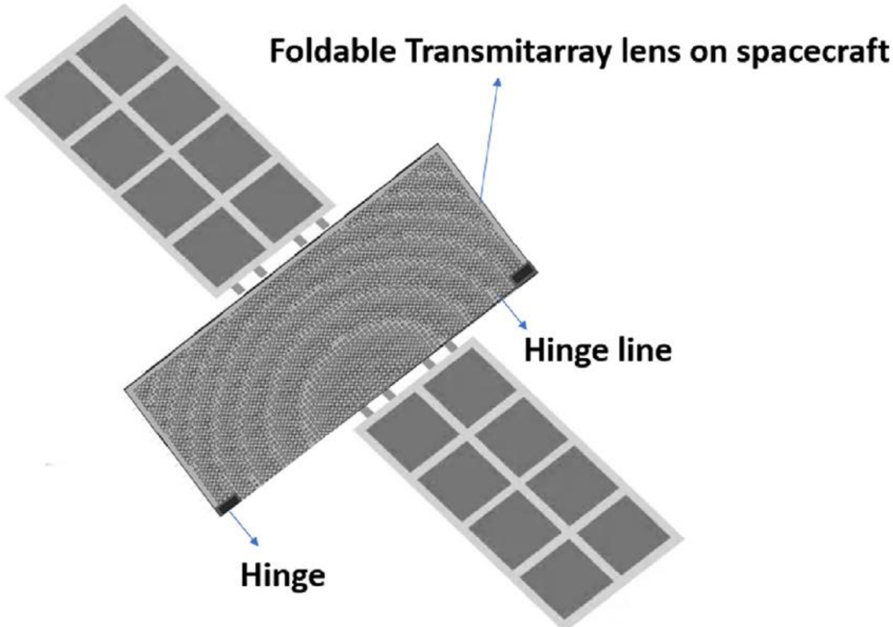

FIGURE 2.7 : Depiction of transmitarray lens mounted on satellite [54].

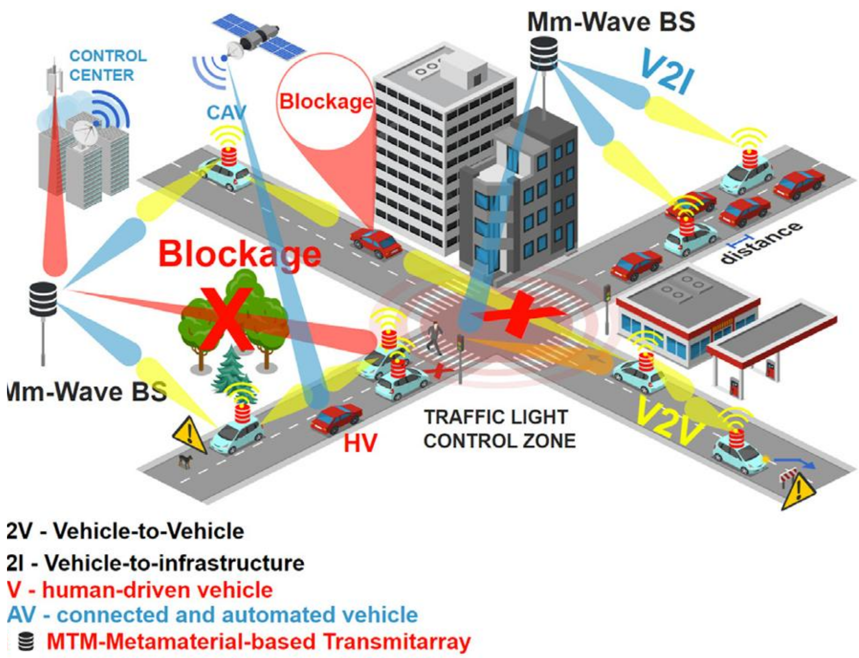

FIGURE 2.8 : Transmitarray antenna in vehicular sensing and communication [57].

Fu *et al.* [61] proposed a low-cost conformal transmit-reflect-array for UAV relay communications. Nguyen *et al.* [62] realized a C-band 1-bit reconfigurable unit cell optimized for airborne platforms, and Qin *et al.* [63] discussed conformal transmitarrays as integral components of 6G UAV-aided networks as can be seen in Fig. 2.10.

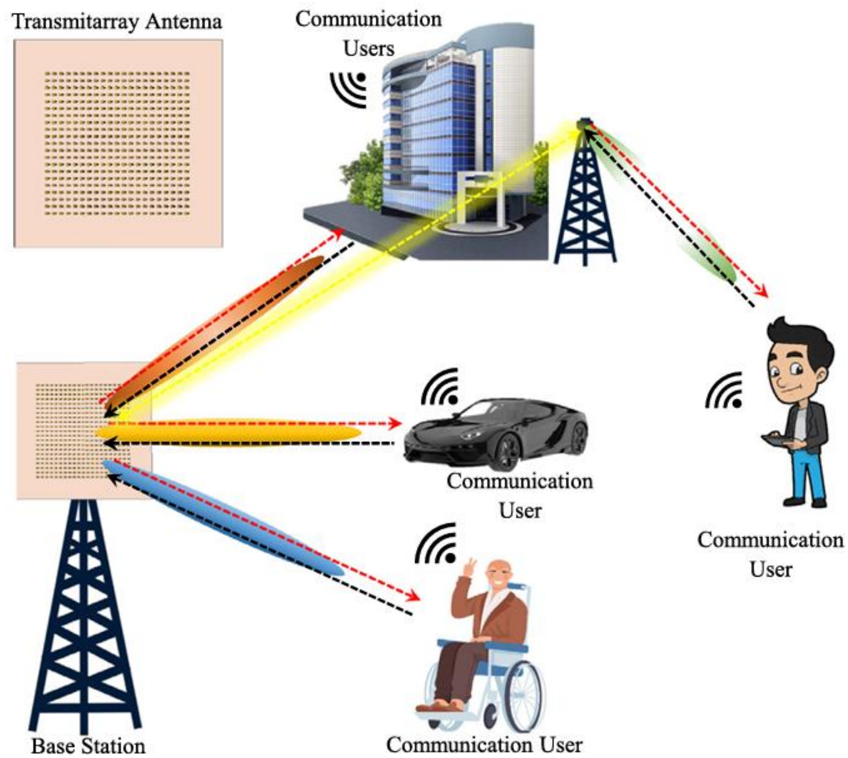

FIGURE 2.9 : Conceptual illustration of a transmit array antenna in base stations [60].

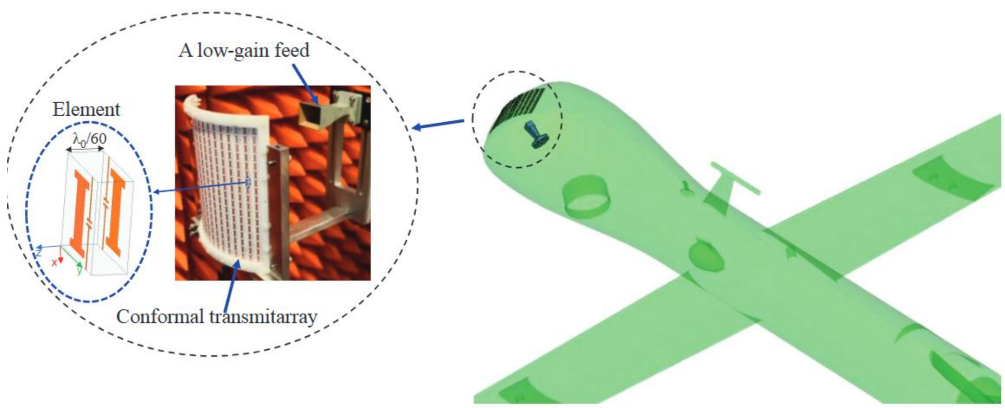

FIGURE 2.10 : Schematics of a conformal transmitarray integrated with an UAV [63].

2.9 Synthesis, Efficiency, and Design Challenges

Despite significant progress, several persistent challenges hinder the widespread adoption of reconfigurable transmitarrays at millimeter-wave frequencies :

- **Insertion loss and bandwidth limitations** — multilayer substrates and reactive loading introduce dielectric and conductor losses, particularly at Ka-band.
- **Biasing complexity** — integrating extensive DC networks without disturbing RF performance is non-trivial.

— **Phase quantization** — limited-bit discretization constrains beam-scanning range and uniformity.
— **Fabrication and scalability** — via-dense multilayer topologies complicate production and introduce alignment tolerances critical at high frequencies.

Existing architectures relying on patch-based resonators or multilayer cascades remain susceptible to surface-wave coupling and limited phase linearity within 26–32 GHz.

2.10 Research Gap and Motivation

From the surveyed literature, it is evident that transmitarray research has transitioned from static multilayer apertures to actively reconfigurable metasurface-based systems. Nevertheless, a unified solution that simultaneously ensures wideband operation, low insertion loss, compact form factor, and simplified biasing at Ka-band remains elusive.

These limitations reveal a clear research gap : the need for a **uniplanar, broadband reconfigurable transmitarray architecture** capable of binary or multi-bit phase control with minimal amplitude variation and reduced parasitic coupling. Such an approach would bridge the performance divide between multilayer and narrowband designs, enabling efficient, electronically steerable Ka-band front-ends for 5G backhaul, satellite gateways, and vehicular radar systems.

3 DEVELOPMENT OF A MULTI-BIT WIDEBAND TRANSMITARRAY WITH INDEPENDENT PHASE AND AMPLITUDE CONTROL FOR MM-WAVE APPLICATIONS

This chapter presents the full development process of a multi-bit wideband transmitarray (TA) for millimeter-wave applications, showcasing two key contributions. The initial concept, introduced in a conference paper, proposed the idea of independently controlling both phase and amplitude using a novel unit cell architecture. This foundational work was later extended in a journal publication, which refined the unit cell design for wideband performance, introduced genetic algorithm (GA) optimization, and validated the structure with fabricated prototypes tailored for vehicular communication systems.

3.1 Introduction

Millimeter-wave (mm-wave) technology has gained significant attention in recent years due to its ability to support high data rates and its applicability in next-generation communication systems, such as 5G and the Internet of Vehicles (IoV) [64, 65]. However, mm-wave signals suffer from high atmospheric attenuation, necessitating the use of high-gain antennas to compensate for path loss. Traditional antenna arrays, while capable of achieving high gain, often suffer from complex feeding networks, high losses, and increased costs [66, 67].

Reflectarray antennas have long held a significant position in the world of high-gain, planar aperture antenna designs. By combining the focusing capability of parabolic reflectors with the thin profile of phased arrays, reflectarrays enable the redirection of electromagnetic waves through engineered phase shifts at discrete unit cells across a surface. Their promise of low profile, reduced mass, and ease of fabrication has spurred extensive research and deployment in satellite communications, radar systems, and terrestrial backhaul links [68].

However, despite these advantages, reflectarrays suffer from notable intrinsic limitations. The most pressing among these is feed blockage : a horn antenna must sit in front of the aperture, obstructing part of the radiated field and degrading aperture efficiency. Precise placement of the feed further complicates mechanical integration in compact platforms. Reflectarrays also exhibit limited operational bandwidths due to the resonant nature of their reflective elements, and they suffer from beam squint when steered to wide angles [69].

Transmitarrays offer several compelling advantages, including the elimination of aperture blockage by positioning the feed horn behind the array, enhanced bandwidth through tailored multilayer unit-cell designs, seamless integration with curved or conformal platforms, and superior beam-steering capability essential for mm-Wave vehicular sensing and communication [70].

The fundamental operation of a transmitarray parallels that of a conventional lens, realized through sub-wavelength electromagnetic structures rather than bulk dielectric materials. An incident wave from a feed source is first captured by a receiving layer, phase-shifted to equalize path lengths across the aperture, and then re-radiated by a transmitting layer. The resulting wavefront is coherent and directed to the target beam direction.

Structurally, a transmitarray comprises three key components : (1) a receiving layer that couples incident fields into the aperture, (2) a phase-shifting mechanism imparting the necessary phase compensation at each unit cell, and (3) a transmitting layer that re-radiates the modified wave [71,72]. Unlike reflectarrays, transmitarrays suffer no front-surface blockage and inherently support broader bandwidths, as they avoid surface-wave propagation constraints. This architecture also facilitates streamlined integration into vehicles, satellites, and UAVs.

At mm-Wave frequencies-where free-space path loss is severe and high gain is critical- Transmitarrays become especially attractive. However, most existing TAs, particularly passive ones, are limited to phase-only control, which restricts their ability to achieve both high gain and low sidelobe levels (SLL)-a critical requirement for mm-wave applications [73, 74].

To address these limitations, our initial work, presented in the conference paper [47], introduced a novel metamaterial-based TA capable of independent phase and amplitude control. This design leveraged polarization twisting and current-reversal techniques to achieve 1-bit phase resolution (0° and 180°) while incorporating a rotating transmitting layer for amplitude tuning. Building upon these findings, the subsequent journal paper [57] expanded the scope to vehicular sensing and communication, integrating Genetic Algorithm (GA) optimization to further enhance performance.

This chapter is structured as follows : Sections 2 and 3 detail the initial phase/amplitude controlled TA design and its performance limitations. Sections 4, 5 and 6 introduce the novel GA optimized independent phase and amplitude control design, for vehicular sensing applications, and Section 7 concludes with the key contributions and future directions.

Finally, the limitations imposed by PCB fabrication techniques at high frequencies are discussed, paving the way toward next-generation 3D printed Transmitarrays, which will be addressed in the subsequent chapter.

3.2 Initial design with Phase and Amplitude Control

To address the aforementioned limitations, we introduce a novel TA unit cell design that has the ability to independently manipulate both phase and amplitude. This is achieved through the utilization of various Taylor excitation schemes with distinct configurations. We employ a 1-bit phase-controlled unit cell, incorporating techniques such as current-reversal and polarization twisting. Additionally, we introduce a new method that entails rotating the transmitting layer, resulting in 1- and 2-bit amplitude-controlled systems designed to reduce side lobe levels. Our simulation results unequivocally demonstrate the effectiveness of this innovative structure in shaping beams at different angles, specifically at 0° and 30°, with high gain and minimal sidelobe levels. This proposed design can be further utilized to perform diverse beam manipulation techniques in both azimuth and elevation planes.

3.3 Unit cells : geometry and characteristics

The proposed unit cell designs relies on the principle of polarization twisting (current-reversal method). Its structural dimensions are optimized separately, to achieve both a phase-only and independent phase/amplitude control for side-lobe level reduction. All simulations tasks were carried out using Floquet ports and periodic boundary conditions in CST Microwave Studio, while assuming a normal incidence illumination.

3.3.1 Phase only Unit cell-based TA

In this section, a linearly polarized unit cell based on both the Receiver-to-transmitter structure, and the current reversal technique is proposed. This kind of structure gives a 1-Bit resolution with two states (0 and 180 degrees).

This was achieved by rotating the receiver layer by 180 degrees, around the metallized via that connects both the receiving and transmitting parts of the unit cell. This via acts as the reference point for the electric field. As a result, the incoming wave from the receiving part is redirected accordingly, and the current will flip its direction, hence the 0-to-180 degrees phase shift. Moreover, the transmitting layer is rotated by 90 degrees to mitigate the issue of spill-over radiation on the co-polarization pattern, by flipping the field polarization.

Fig. 3.1 depicts the geometry of the proposed unit cell element, where a 5 x 5 mm^2 (i.e. half free-space wavelength at 30 GHz) in size unit cell is designed to work in the band of interest ranging from 26 to 32 GHz. It consists of simple dipoles printed on both the transmitting and receiving layers. Two identical Rogers RO3003 dielectric mediums (ε_r =3, and $tan\delta$ =0.001), with a thickness of 0.762 mm are used. Both conducting are connected by the metalized via with a diameter of 200 μm. In addition, a circular aperture (diameter of 800 μm) is etched on the ground plane, to isolate the via from the ground. All other dimensions are depicted in Fig. 3.1(b & c).

Fig. 3.2 shows unit cell simulation setup, alongside the transmission magnitude and phase results of this unit cell. It can be noted that in Fig. 3.2(b) that the transmission magnitude for both phase states is the same, and the -3dB transmission bandwidth covers the frequency band ranging

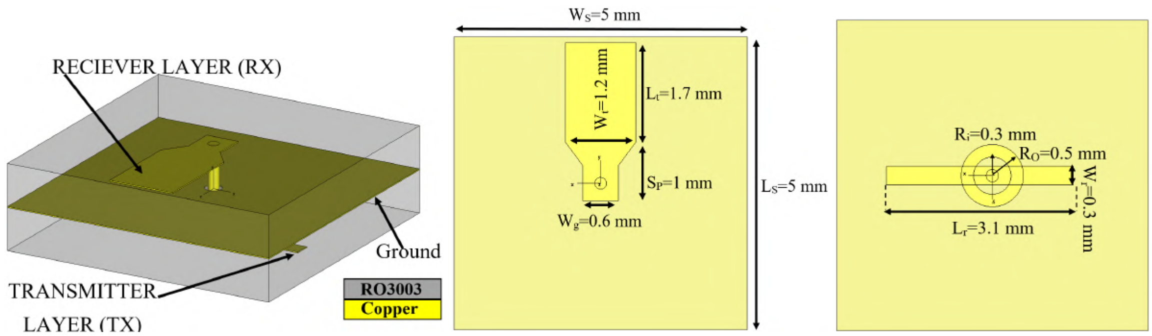

(a) **(b)** **(c)**

FIGURE 3.1 : Geometry of the proposed unit cell element. (a) Perspective view, (b) Top view, and (c) Bottom view.

from 26.7 GHz to 31.6 GHz (4.9 GHz), corresponding to 17% at 29 GHz. Moreover, the achieved insertion loss is as low as 0.17 dB at 28.3 GHz. Furthermore, the proposed unit cell exhibits a perfect 180 degrees phase shift over the whole band of interest, and this can be seen in Fig. 3.2(b).

These very attractive features lead to a simplified design procedure because only two phase states need to be considered, e.g. the 0° and 180° phase states will be presented as unit cell-10 (MA-10) and unit cell-01 (MA-01), respectively.

To verify the feasibility of the proposed design, a 20 x 20 (400 elements) full TA is constructed on Rogers RO3003, with a total size of 100 x 100 mm, and then illuminated by a TM-polarized probe antenna. A focal distance of 60 mm (F/D = 0.42) was set alongside other important parameters, in our own beam-steering software, to generate specific phase distributions, for two different beam-steering angles of 0, and 30°.

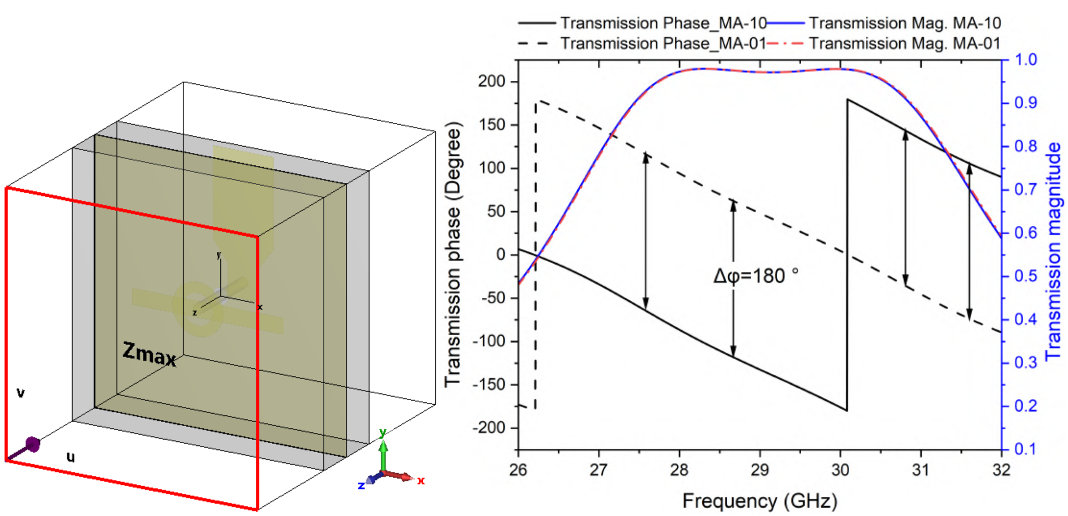

(a) **(b)**

FIGURE 3.2 : (a) unit cell simulation setup, and (b) its simulated transmission results.

Fig. 3.3 illustrates the results, where it is clearly seen that, this unit cell was able to achieve accurate beam-steering angles, with only a 1-Bit resolution, on the expense of loosing some gain and higher Side-lobe-levels, due to the quantization loss. More precisely, The maximum achieved gain for both the 0 and 30 degrees was 20.1 and 17.6 dBi, respectively. As for the side-lobe levels, at 0 degree the TA exhibited -12.3 dB, where as in the case of the 30 degrees beam-deflection angle, the side-lobe level was -10.1 dB, which is further degraded if larger deflection angles are desired. To get around this, the transmission amplitude should also be considered, when designing Transmitarrays, as it is vital to reducing high side-lobe levels, associated with the use of 1-bit phase-only controlled TAs.

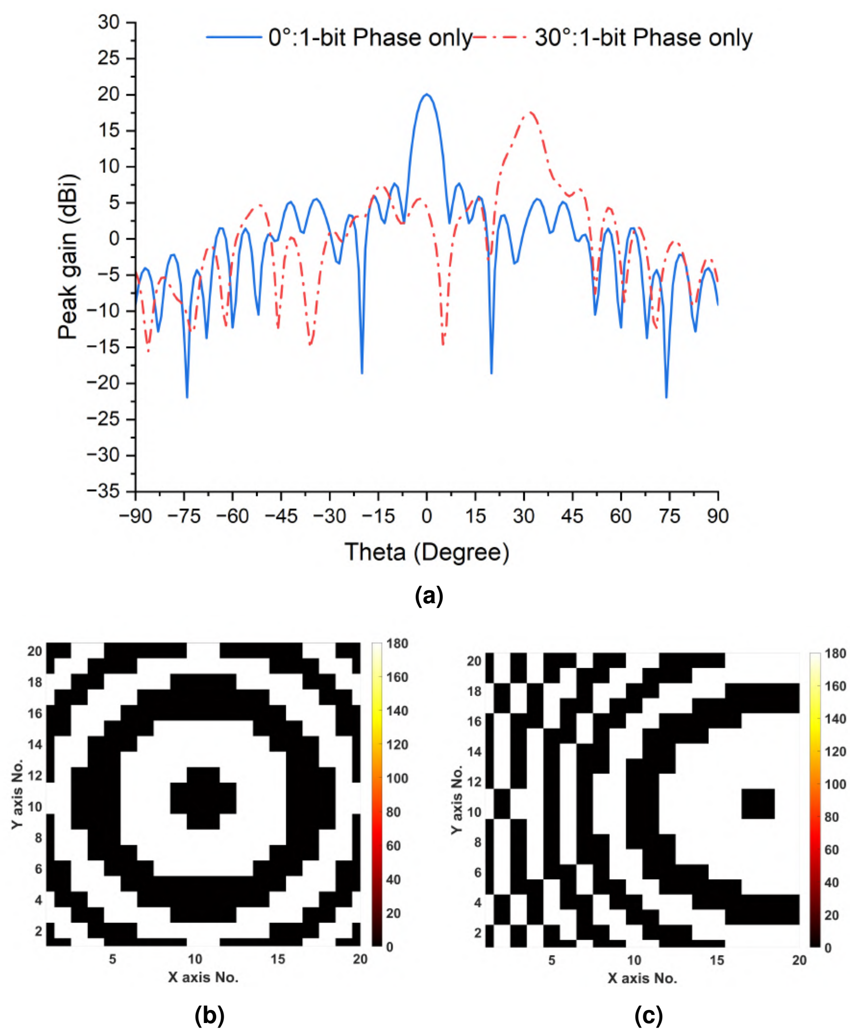

FIGURE 3.3 : (a) Beam steering performance at 0, and 30°; (b) and (c) their corresponding phase distributions, operating at 29 GHz.

3.3.2 Phase & Amplitude Unit cell-based TA

To get around the aforementioned drawbacks of using phase-only TAs, we propose a novel unit cell, based on the previous design in terms of achieving the two phases of 0 and 180 degrees, in addition to the ability to dynamically change the transmission magnitude of the unit cell, while maintaining a stable phase response (± 2.3°), giving rise to a novel 1-bit unit cell with independent phase and amplitude tunability.

In the previous design, the transmitting layer is kept fixed at 90° orientation, in relation to the direction of the receiving part. This would give the maximum achieved cross-polarization transmission magnitude, and the idea is to have different levels, and this can be done by simply rotating the transmitting layer. To that end, the previous orientation of the transmitting part is set as the reference line (as 0°), and it is then rotated by angle α (see Fig. 3.4(a & b) ranging from 0 to 90°, and -90 to 0° for MA-01 and MA-10 unit cells, respectively.

To better understand this, let's consider a y-polarized EM wave that incidents on the receiving layer, when α = 90° the EM wave is then transformed into an x-polarized one, when it passes through the coupling via and then finally through the transmitting part. When α = 0°, the y-polarized EM wave coming from the receiving element keeps its polarization traveling through the via and transmitting layer, meaning the co-polarized component is fully transmitted while the cross-polarized one is totally reflected, with almost no transmission, and since in our design we seek the reduction of the co-polarization spill-over effect on the TA, the 0° is set as the reference for 0 cross-polarized transmission amplitude. Thus, when α varies between 0 and 90°, the EM wave is partially reflected and partially passing through the element.

Table 3.1 and Fig. 3.4(c) summarize all angles and their corresponding transmission coefficients and phases, for both MA-10 and MA-01.

Similar to the phase only TA, a 20 x 20 structure is constructed based on the novel unit cell, where α is set as a new parameter in our own beam-steering software, to generate both phase and amplitude distributions.

Two different amplitude distribution schemes based on the Taylor excitation pattern are used [75], to achieve low side-lobe levels while maintaining high gain performance.

TABLEAU 3.1 : Simulated results for all angles of α and their corresponding transmission coefficients and phases, for both MA-10 and MA-01

MA-01	**0°**	**22.5°**	**45°**	**60°**	**70°**	**90°**
Amplitude	0.97/-0.24 dB	0.9/-1dB	0.7/-3dB	0.5/-6dB	0.35/-9dB	0/ -100dB
Phase variation	0°	+0.4°	+1°	+1.1°	+1.8°	+2.3°
MA-10	**0°**	**-22.5°**	**-45°**	**-60°**	**-70°**	**-90°**
Amplitude	0.97/-0.24 dB	0.9/-1dB	0.7/-3dB	0.5/-6dB	0.35/-9dB	0/ -100dB
Phase variation	180°	-0.4°	-1.3°	-1.6°	-1.54°	-2.2°

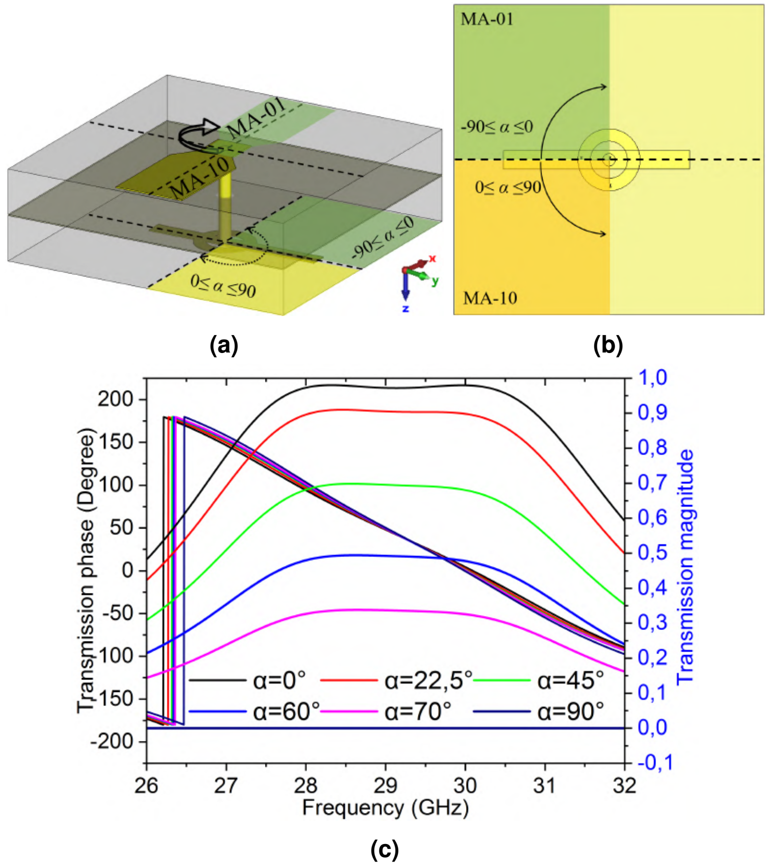

FIGURE 3.4 : Initial phase/amplitude controlled unit cell, (a) Perspective view, (b) Bottom view, and (c) its simulated transmission magnitude and phase response.

First, high focused beam at 29 GHz is simulated, using 1-bit transmission phase/amplitude scheme, based on two orientation angles α of 0 and 45 degrees. These later give two states of amplitude, 0.97 and 0.7 (in linear scale), hence the 1-bit resolution in magnitude. The previous phase distribution illustrated in Fig. 3.3(b) is used here, alongside a 1-bit Taylor-based distribution scheme as shown in Fig. 3.5(a). Nonetheless, the resulted radiation pattern of the focused beam is depicted in Fig. 3.5(c), where it is clearly seen that the new TA achieved higher gain and lower side-lobe level of 23.3 dBi and -14.5 dB, respectively. Thus, an enhancement of 3.2 and -2.2 dB in gain and SLL.

Moreover, a 2-bit (0.97, 0.7, 0.5 and 0.35) Taylor-based distribution scheme is then utilized to further improve both peak gain and SLL. This can be seen in Fig. 3.5(c) where the maximum achieved gain was 25 dBi, and the Side-lobe level was also reduced attaining -20.4 dB which is remarkable for a transmitarray with only 1-bit in phase.

To further prove the feasibility of the proposed approach, three radiation patterns steered to 30 degrees were simulated, and the results are depicted in Fig. 3.5(d). Starting from a phase only 1-bit system, and going through two more new schemes with both phase and amplitude control (1-bit and 2-bits), the peak gain improved drastically. The phase only system exhibited a peak gain of 17.6 dBi, whereas in the case of the new phase/amplitude based-TA, the peak gain improved from 19.8 to 23.4 dBi, when employing the 1- and 2-bit Taylor excitation patters, respectively. As for the case of the SLL, at first it was -10.1 dB, and after applying the aforementioned amplitude distribution schemes, it was reduced from -12.6 to -16.4 dB, yielding interesting results.

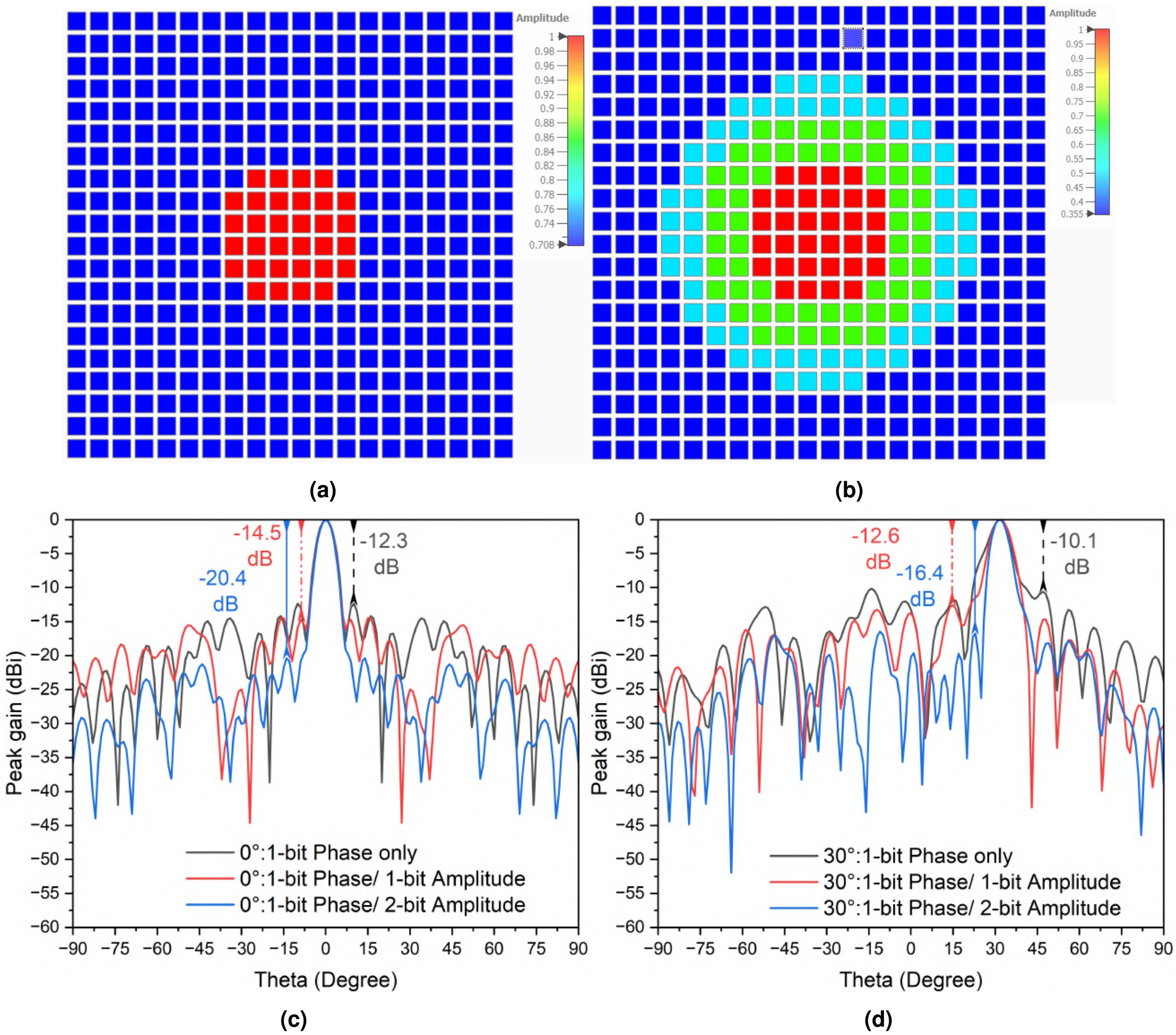

FIGURE 3.5 : Taylor amplitude distribution : (a)1-bit, (b) 2-bit schemes. (c) high focused beam at 0°, and (d) beam steering at 30°, for different techniques, at 29 GHz.

For the sake of simplicity, all beam steering schemes are only implemented at the azimuth plane, and this can be extended to a 2D beam steering environment. These attractive features make the proposed concept, a potential candidate for mm-wave applications, where low SLL and high gain performances are required.

In this work, a multi-bit transmitarray has been proposed, where its core component namely the dual-layer unit cell provided wideband 1-bit phase compensation in the band of interest, with a maximum transmission amplitude of 0.97. This was achieved by using both current-reversal and polarization twisting techniques. Additionally, the presented structure has another interesting feature, where the amplitude can be adjusted independently from phase states, with 1- and 2-bit schemes of Taylor excitation patterns. Then it has been used to realize two unique beam-steering systems at 29 GHz. The obtained results have shown excellent performance in terms of beam scanning with both high gain and low side lobe levels. Due to its lower cost and adaptability, the proposed structure can be a potential candidate for high-gain with low side lobe levels beam-shaping system for future Mm-wave applications, as clearly seen in the following sections.

3.4 Advanced Design and Optimization for Millimeter-Wave Vehicular Sensing and Communication

The Internet of Vehicles (IoV) has recently transformed the traditional automotive industry, significantly improving transportation efficiency. A key technology in IoV is the development of a reliable high-speed communication system. This system enables vehicles to exchange data with various devices and networks, such as satellites and mobile wireless communications [76, 77]. This includes interactions between intelligent cars through Vehicle-to-Vehicle (V2V) and Vehicle-to-Infrastructure (V2I) networks [78], as illustrated in Fig. 3.6.

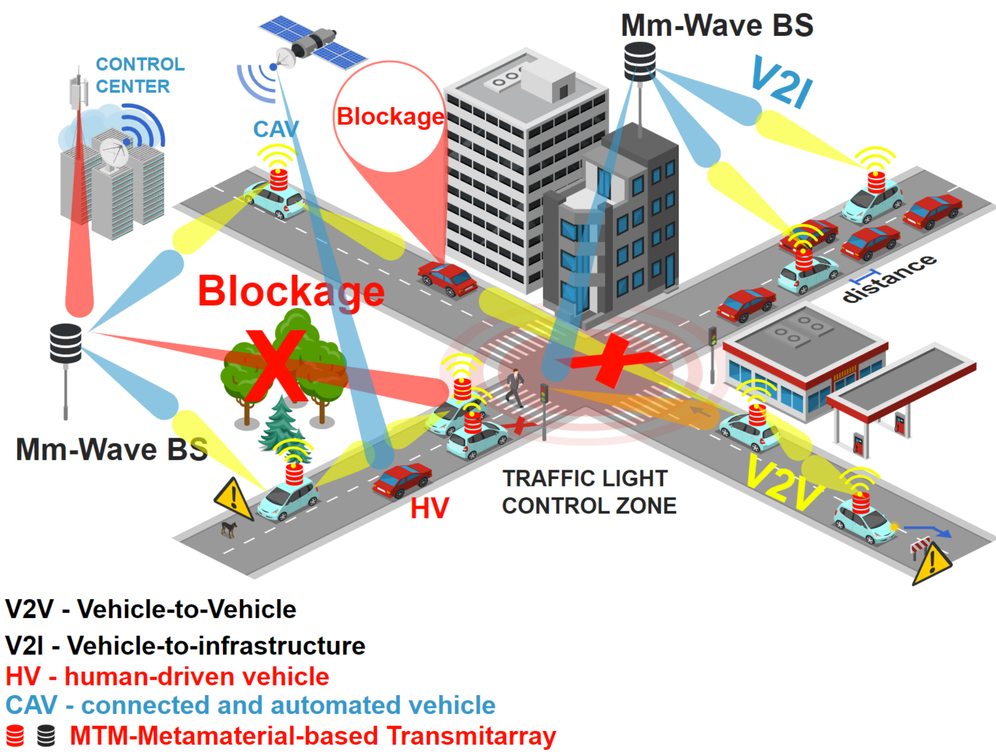

FIGURE 3.6 : Overview of wideband high-gain antenna applications in vehicular sensing and communication.

An intelligent car needs to exchange a large amounts of real-time data, including multimedia, navigation, and intelligent transportation information [79]. Achieving this requires a data transfer rate in the Gbps range, which poses a significant challenge for the microwave band due to its limited bandwidth. On the other hand, Millimeter-Wave (mm-Wave) technology is gaining attention because it offers abundant spectrum resources and faster data rates, making it a promising option to support Gbps-level IoV [80, 81].

In the mm-Wave band, high-gain antennas are needed to offset the significant atmospheric attenuation and to simplify the design challenges of power amplifiers (PAs). Therefore, a compact, wideband, high-gain mm-Wave antenna is ideal for vehicular communication [64, 65, 82].

Numerous studies have focused on vehicular antennas for millimeter-wave bands. For instance, the authors of [83] proposed a 32 × 64-slot array antenna with equal spacing, using a non-uniform corporate-feed network for excitation. However, its complex structure requires high-precision manufacturing. In contrast, in the case of [84], a slow-wave structure with metallized blind via-holes in the horn's flare region was utilized to reduce phase velocity and balance the large phase difference between the center and edge of the aperture.

Using an antenna array is a traditional approach to achieve wideband, high-gain antennas [66, 67, 85]. However, it often faces issues like complexity, high loss, and high cost due to the feeding network.

With the spatial feeding mechanism, both transmitarray (TA) and reflectarray (RA) can overcome these challenges by eliminating complex feeding networks, thereby enhancing performance and simplifying design. While several reflectarray antennas have been developed for IoV applications, they tend to suffer from feed horn blockage and integration challenges within vehicles [68,69]. In contrast, transmitarray antenna designs position the feed horn below the radiation aperture, eliminating blockage and making them more practical and appealing for real-world applications.

Transmitarrays (TAs) exhibit significant potential for diverse applications within the millimeter-wave frequency range [24, 70]. Successful implementation of a TA relies on unit-cells providing complete transmission within the desired frequency range while allowing precise control over the transmission phase [86]. Due to their high-gain, wide bandwidth, efficiency, and cost-effectiveness-leveraging standard printed circuit technology for fabrication-TAs can find applications in various long-distance systems, such as satellite-terrestrial links, mobile communication, and radar systems [87–89].

Multilayer metamaterial-based TAs not only exhibit high-gain characteristics but also contribute to expanding the bandwidth of the TA aperture and achieving the necessary 360° phase range [90]. Moreover, for the attainment of wideband and high-efficiency attributes, a five-layer structure with varying element thicknesses has been proposed for the TA aperture in [75], resulting in a remarkable bandwidth of 97.7%, a maximum gain of 22.3 dBi, and an efficiency of 62%. In [91], the authors have explored an innovative design employing dual layers, featuring a dual-layer metasurface lens based on novel split dipole elements. This design accomplishes a phase range of 396° with a transmission coefficient exceeding -1 dB.

The previously mentioned research investigates approaches to achieve a phase range of at least 360° to fulfill phase compensation needs while maintaining an acceptable transmission coefficient. This is done to attain features such as high gain, wide bandwidth, and a thin profile. It is evident that controlling the transmission amplitude and phase independently is challenging, restricting the freedom in structural design.

Nevertheless, the majority of existing TAs, particularly passive ones, have been constrained to utilizing phase-only control [73, 74]. This limitation makes them less suitable for applications in the millimeter-wave spectrum, where the demand is for high gain and low side-lobe levels.

With this aim in mind, we present a novel metamaterial-based design capable of independently manipulating both phase and amplitude, similar to the initial design, where it was realized through the utilization of various Taylor excitation schemes with distinct configurations, for amplitude control, and both the current reversal and polarization twisting techniques, to attain the required phase shifts. Moreover, genetic algorithm (GA) optimization is employed to address gain reduction during amplitude tapering, ensuring robust performance. Our simulation and measurement results unequivocally demonstrate the effectiveness of this innovative structure in shaping beams at different angles, specifically at 0° and 30°, with high gain and minimal side-lobe levels. This proposed design can be further employed to execute diverse beam manipulation techniques in both azimuth and elevation planes.

In short, the key novelty of this work lies in the combination of multi-bit amplitude control, phase manipulation, and GA optimization, which together enable superior beam-steering accuracy and side-lobe suppression. Our approach significantly outperforms traditional designs, providing a versatile and high-performance solution for next-generation mm-wave vehicular communication systems.

3.5 Wideband Unit cells : geometry and characteristics

The proposed unit cells rely on the concept of polarization twisting through the current-reversal method. Their structural dimensions are individually fine-tuned to attain both phase-only control and independent control of phase and amplitude. All simulation procedures are conducted in CST Microwave Studio using Floquet ports and periodic boundary conditions, assuming normal incidence illumination.

3.5.1 Wideband Phase only unit cell-based TA

This section presents a linearly polarized unit cell with a 1-bit resolution (0° and 180°) achieved through the receiver-to-transmitter structure and current-reversal technique. The unit cell employs a 180° rotation of the receiver layer around a via, serving as the electric field's reference point. This rotation alters the current direction, causing a 0° to 180° phase shift. Additionally, a 90° rotation of the transmitting layer addresses spill-over radiation issues in the co-polarization pattern by flipping the field polarization.

Fig. 3.7 shows the proposed unit cell's geometry with a 5 $\times$ 5 mm^2 unit cell intended for operation within the 26 to 32 GHz band. Comprising simple dipoles, arcs with a specific opening angle β = 225°. This design is implemented on both the transmitting and receiving layers. It employs two identical Rogers RO3003 dielectric mediums (ε_r = 3, $tan\delta$ = 0.001) with a thickness h_{sub} = 0.762 mm.

The conducting layers are connected by a 200 μm diameter metalized via, while a 600 μm diameter circular aperture is etched on the ground plane, isolating the latter from the coupling via. Additional dimensions can be found in Table 3.2.

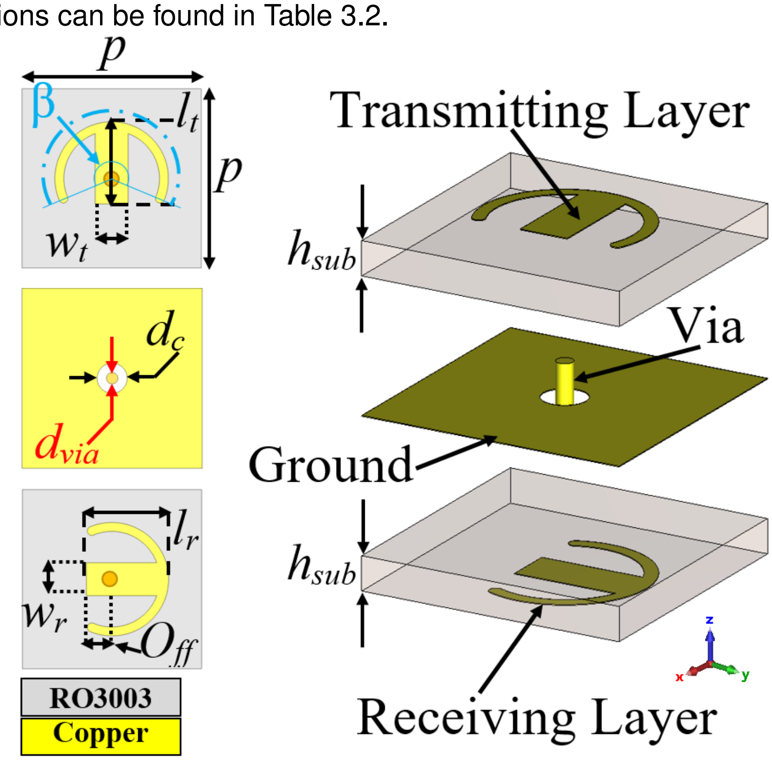

FIGURE 3.7 : Geometry of the proposed unit cell.

Fig. 3.8 illustrates the simulation configuration for the unit cell, showing the transmission magnitude and phase results. In Fig. 3.8(b), the transmission magnitude remains consistent for both phase states, with a -1dB bandwidth from 26 GHz to 32.1 GHz (6.1 GHz), equivalent to 21.78% at 28 GHz. The proposed arcs with dipoles topology contribute to this bandwidth performance, achieving a minimal insertion loss of 0.17 dB at 28 GHz. Moreover, the unit cell exhibits a consistent 180° phase shift across the entire frequency range of interest, as highlighted in Fig. 3.8(b). These appealing characteristics simplify the design process, as it involves only two phase states : 0° and 180°, denoted as unit cell-0 (MA-0) and unit cell-180 (MA-180), respectively.

TABLEAU 3.2 : **Proposed unit cell design parameters.**

Parameter	P	h_{sub}	l_t=l_r	w_t=w_r	Off	d_c	d_{via}
Value (mm)	5	0.76	2.6	1.1	0.85	0.6	0.2

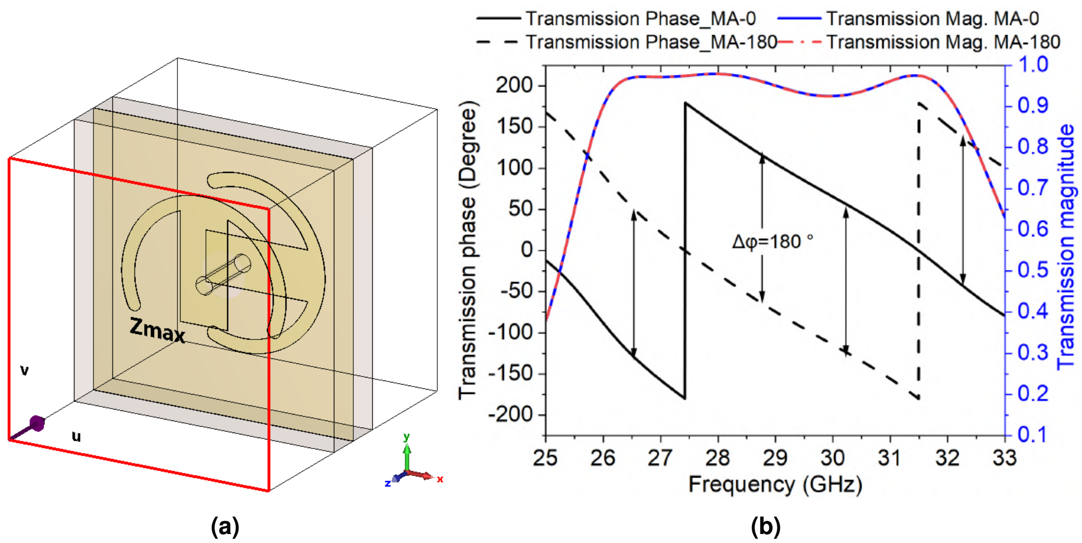

FIGURE 3.8 : **(a) unit cell simulation setup, and (b) its simulated transmission results.**

To validate the proposed design's feasibility, a 20 × 20 (100 × 100 mm) complete TA is created using Rogers RO3003, illuminated by a TM-polarized WR-28 horn antenna with a focal distance of 60 mm (F/D = 0.6). Specific phase distributions are generated for beam-steering angles of 0 and 30° using custom beam-steering software (Fig. 3.9(a & b)).

In Fig. 3.9, the results demonstrate the unit cell's ability to achieve precise beam-steering angles despite its 1-bit resolution. However, this comes at the expense of reduced gain and increased side-lobe levels due to quantization loss. The maximum gain achieved was 22.3 dBi for 0° and 20.8 dBi for 30°. Side-lobe levels were -15.7/-14.1 dB at 0° and -12.4/-13.4 dB at 30° for H-/E-planes, respectively, with potential degradation at larger deflection angles. To address this, designing the TA with consideration for transmission amplitude is crucial to mitigate high side-lobe levels associated with 1-bit phase-only control.

3.5.2 Wideband Phase & Amplitude-unit cell-based TA

To address limitations of phase-only TAs, an innovative unit cell is introduced that achieves two phases (0° and 180°) while enabling dynamic tuning of the transmission magnitude with a consistent phase response (within ± 4°). This advancement results in a novel 1-bit unit cell with independent control over the phase and amplitude adjustments.

In the previous design, the transmitting layer's fixed orientation at 90° maximizes cross-polarization transmission magnitude. For this purpose, the initial orientation of the transmitting part is designa-

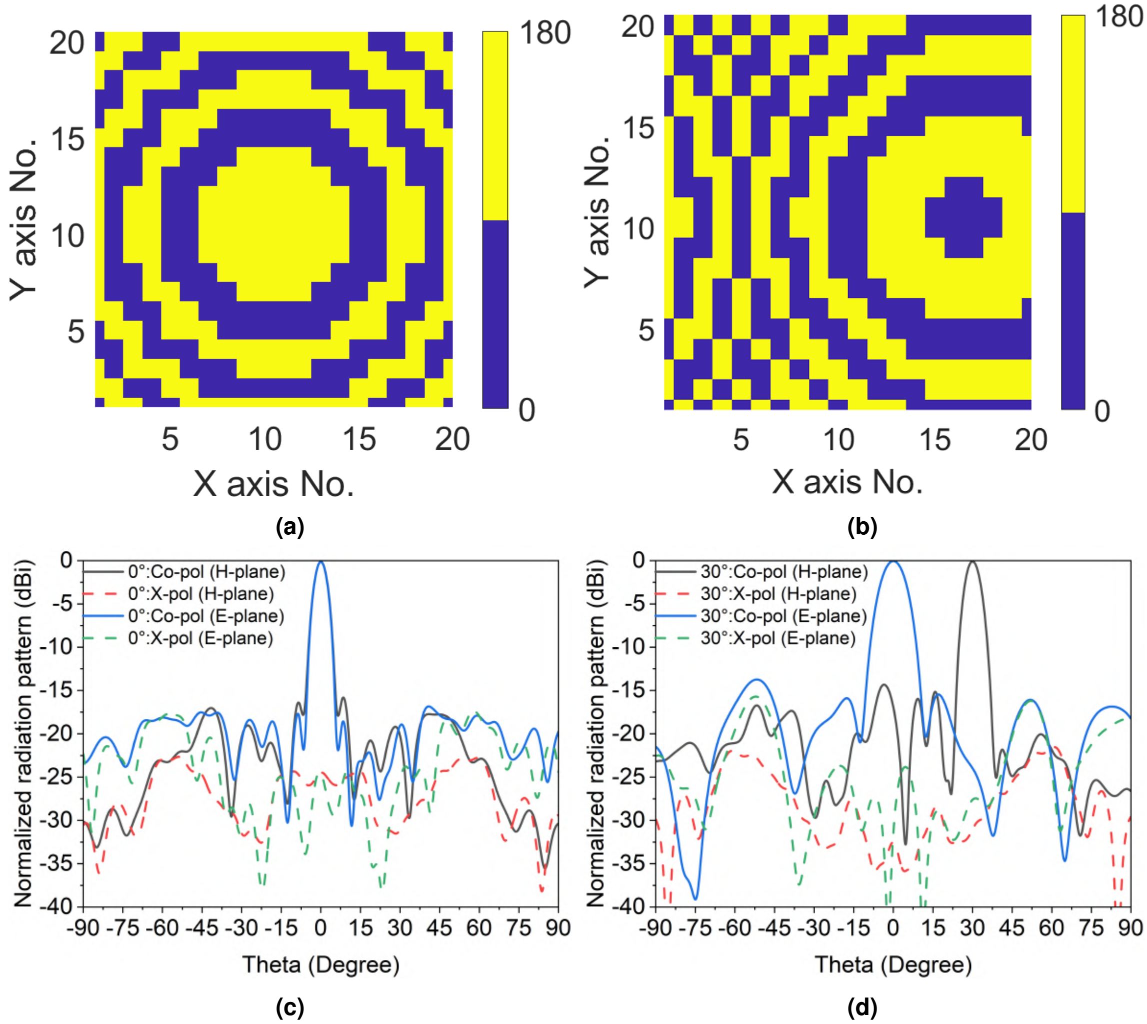

FIGURE 3.9 : (a) and (b) Initial phase distributions at 0 and 30°; (c) and (d) their corresponding beam-steered normalized radiation patterns at 28 GHz, respectively.

ted as the reference line (α = 0°). The new unit cell introduces dynamic adjustment by rotating the transmitting layer from 0° to 45° for MA-180 and from -45° to 0° for MA-0 unit cells, as shown in Fig. 3.10(a & b).

Analyzing an incident y-polarized electromagnetic wave on the receiving layer, at α = 0°, the wave changes to an x-polarized wave, while at α = 90°, the initial y-polarized wave retains its polarization. Choosing 0° as the reference for maximum cross-polarized transmission, as α varies between 0 and 45°, the wave undergoes partial reflection and transmission through the element.

Table 3.3 and Fig. 3.10(c) summarize the different angles, their respective transmission coefficients, and phases for both MA-0 and MA-180 configurations.

Similar to the phase-only TA, a 20 $\times$ 20 structure is created using the innovative unit cell, incorporating α as a new parameter in our beam-steering software to generate phase and amplitude distributions. To attain low side-lobe levels with high gain, two amplitude distribution schemes based on the Taylor excitation pattern are utilized [47]. A simulation is conducted at 28 GHz, focusing

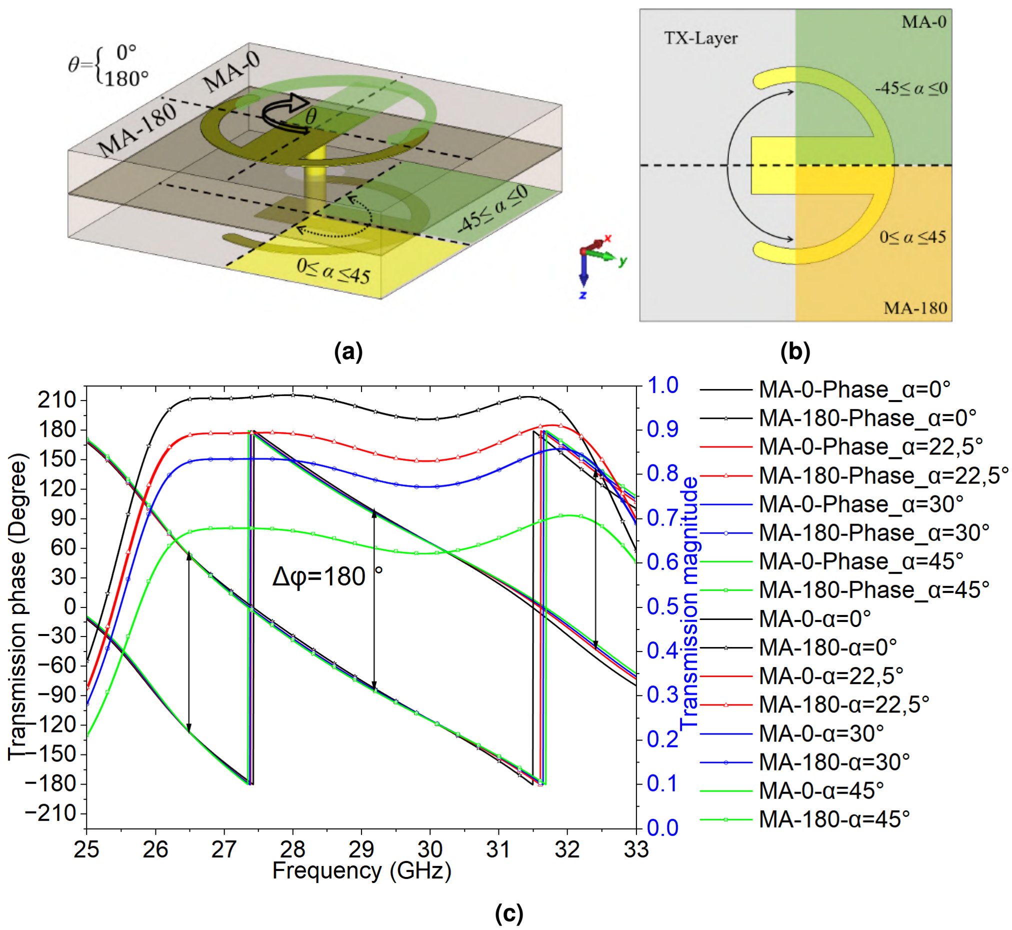

FIGURE 3.10 : Proposed phase/amplitude controlled unit cell, (a) perspective view, (b) bottom view (Tx-layer), and (c) its simulated transmission magnitude and phase response.

on a highly directed beam using a 1-bit transmission phase/amplitude approach. Two α angles (0 and 45°) are employed, representing amplitude states of 0.98 and 0.7 in linear scale. These configurations result in a 1-bit resolution in magnitude. By incorporating a 1-bit Taylor-based distribution scheme with the same phase distribution as in Fig. 3.9(a), the simulation achieves a peak gain of 21.1 dBi and lower SLLs of -16.9/-15.8 dB for both H-/E-planes, respectively. This enhancement reflects a side-lobe level reduction of -1.2/-1.7 dB for the H-/E-planes, along with a decrease in the peak gain of 1.2 dB.

TABLEAU 3.3 : Simulated results for all angles of α, along with their corresponding transmission coefficients and phases, for both MA-0 and MA-180 at 28 GHz.

MA-0	**0°**	**22.5°**	**30°**	**45°**
Amplitude	0.98/-0.17 dB	0.9/-1dB	0.8/-2dB	0.7/-3dB
Phase variation	0°	1°	2°	3.8°
MA-180	**0°**	**22.5°**	**30°**	**45°**
Amplitude	0.98/-0.17 dB	0.9/-1dB	0.8/-2dB	0.7/-3dB
Phase variation	180°	-2°	-2.7°	-4°

Additionally, a 2-bit Taylor-based distribution scheme (0.98, 0.9, 0.8, and 0.7) is implemented to further enhance the SLL, where the peak gain reaches 22 dBi, and the SLL notably decreases to -18.4/-17 dB for both the H-/ E-planes, respectively, leading to interesting achievement for a 1-bit phase TA.

To validate the proposed method's feasibility, simulations of three radiation patterns steered to 30° were conducted. Starting with a phase-only 1-bit system and progressing to new schemes involving phase and amplitude control (1-bit and 2-bits), the SLL initially stood at -12.4/-13.4 dB. Applying the mentioned amplitude distribution schemes reduces the SLL from -14.5 to -15.7 dB for both H-/E-planes, indicating promising outcomes. A similar observation is noted for peak gain, where a decrease is observed. The initial phase-only system exhibits a peak gain of 20.8 dBi, while the new phase/amplitude-based TA demonstrates peak gains of 19.7 and 20.1 dBi using the 1- and 2-bit Taylor excitation patterns, respectively.

Nevertheless, the proposed amplitude tapering technique showed significant enhancement in SLL levels at the expense of some overall gain. This trade-off is expected since utilizing an amplitude tapering technique generally leads to a decrease in peak gain, presenting a challenge in designing TAs with both high gain and low side-lobe levels.

3.5.3 Genetic Algorithm (GA) optimized Phase & Amplitude TA

To address challenges associated with amplitude tapering and achieve improved TA performance, a Genetic Algorithm (GA)-based system is proposed for optimizing the TA's aperture. Genetic algorithms have demonstrated significant potential in solving electromagnetic challenges, as seen in previous studies optimizing structures like electromagnetic band gap (EBG) and artificial magnetic conductor (AMC) [92, 93].

The proposed system utilizes a Visual Basic for Applications (VBA) link between CST Microwave Studio and MATLAB's embedded GA. In this optimization process, binary encoded words generated by the GA represent potential solutions, involving 0° and 180° phases. These solutions undergo analysis and assessment using a predefined fitness function, initially defined as the sum of all values surpassing 22.3 dBi (the initial peak gain at 28 GHz) within the frequency range of 26 to 32 GHz. This formulation aims to create an optimized phase-only TA characterized by increased gain and a broader -3dB bandwidth.

Initially $G_{TA}(fi)$ is defined as the peak gain of the TA structure, where the peak gain is taken at equal frequencies f_i, with the total number of N = 13 frequency points, within the designated overlapping frequency band of interest ($f_{min=26} \leq f_i \leq f_{max=32}$).

In order to maximize the function $G_{TA}(fi)$ using GA optimization technique, the fitness function Fit_{Phase} should be defined as below :

$$Fit_{Phase} = \frac{1}{G_{TA}(f_i)} \tag{3.1}$$

Then the GA algorithm will try to minimize the function Fit_{Phase}, and this will give the maximum value of function $G_{TA}(fi)$.

The optimization procedure aims to manipulate the phase of each unit cell in the frequency band of interest (26 to 32 GHz) using a genetic algorithm. The algorithm utilizes a uniform mutation rate of 0.001, a single-point crossover, and tournament selection with a population size of 50 randomly selected binary strings representing specific phase distributions. The process involves 20 iterations, and the top-performing structures undergo crossover and mutation until the desired fitness value ($Fit_{Phase} < \frac{1}{22.3}$) is achieved or the maximum iterations are reached.

The optimal TA design is achieved in the 7th iteration, reaching a maximum peak gain of 26.21 dBi at 31 GHz with a -3dB bandwidth of 28.57% at 28 GHz. In comparison, the unoptimized phase-only TA has a -3dB gain bandwidth of 17.85% around 28 GHz, with the initial peak gain enhanced from 22.3 to 25.6 dBi.

Regarding the SLLs, the original levels are -15.7/-14.1 dB, and after optimization, they become -16.1/-14.8 dB for H-/E-planes, representing a marginal enhancement of -0.4/-0.7 dB for both plane cuts. A trade-off between the maximum gain and SLL is evident, prompting consideration of a novel fitness function.

To address limitations, a new fitness function is employed in the final optimization process (see Fig. 3.11), targeting both the receiving and transmitting layers of the TA. This involves considering both phase and amplitude states (0 and 180° for phase; 0, 22.5, 30, and 45° for amplitude transmission magnitude). These variables are the inputs of the GA-based system to achieve a balanced optimization.

The optimization process sets two main objectives : maximizing the peak gain and broadening the -3dB bandwidth while minimizing SLL.

Recognizing the conflicting nature of these objectives, they are combined into a unified single-objective function. To manage this integration, weighting coefficients are assigned to the partial criteria within the aggregated objective function [94]. The formulation is expressed as follows :

$$Fit_{Ph.\&Amp.} = c_1 \cdot \frac{1}{G_{TA}(f_i)} + c_2 \cdot SLL(f_i) \tag{3.2}$$

c_1 and c_2 are the weighting coefficients for both peak gain and SLL objectives, respectively, and are set equally to 0.5. The final GA-optimized phase distributions at 28 GHz for 0 and 30°, with their

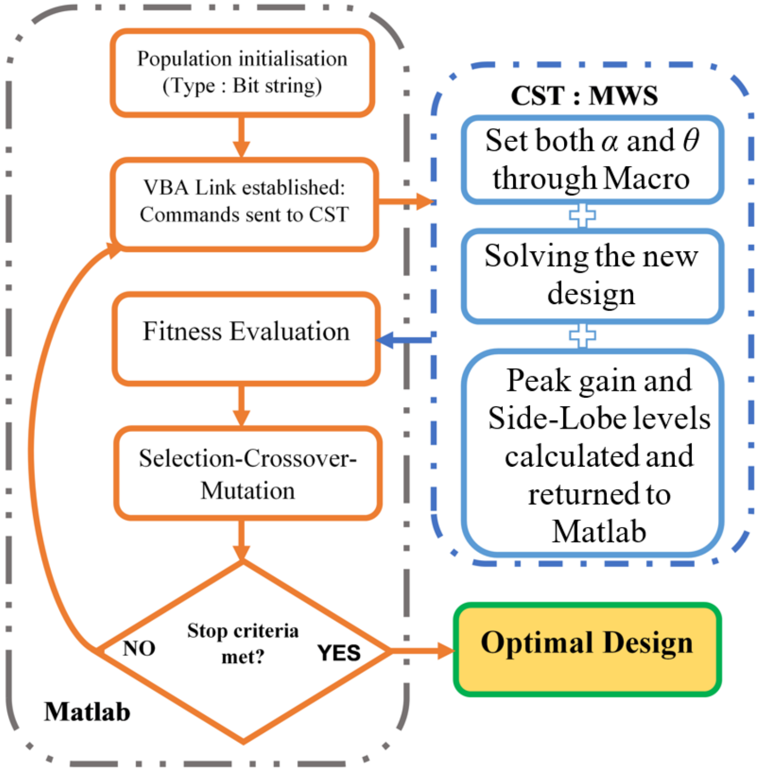

FIGURE 3.11 : The Proposed flowchart of the GA optimization process for high gain with low SLL TA.

corresponding amplitude distributions, are achieved after the 12th iteration when the stop criterion is met, and are depicted in Fig. 3.12.

In the optimized phase and amplitude-controlled TA, the maximum peak gain reaches 27.6 dBi at 29 GHz with a corresponding -3dB bandwidth of 26.8% at 28 GHz, spanning from 26.5 to 34 GHz. This represents only a 1.77% decrease in bandwidth compared to the optimized phase-only TA, which is considered negligible given the substantial enhancement in the peak gain. In contrast, the unoptimized phase-only TA exhibits a -3dB gain bandwidth of 17.85% around 28 GHz, with the initial peak gain at 28 GHz improved from 22.3 to 27.2 dBi, indicating an 8.95% improvement in -3dB bandwidth and a 4.8 dBi enhancement in the peak gain.

Regarding the side-lobe levels, the original levels were -15.7/-14.1 dB, and after the GA optimization process considering both phase and amplitude, the side-lobe levels become -22.9/-19.4 dB for H-/E-planes, respectively. This represents a significant enhancement of -7.2/-5.3 dB for both plane cuts.

For a 30° beam deflection, a maximum peak gain of 24.9 dBi is achieved at 28 GHz, compared to the initial phase-only configuration where the maximum gain reaches 20.8 dBi. The proposed GA-based optimization system results in a notable increase of 4.1 dBi. The initial side-lobe levels, initially at -12.4/-13.4 dB, are decreased in the final design, reaching SLL levels of -16.8/-19.5 dB for both H-/E-plane cuts. Additionally, the simulations have been extended to evaluate the performance of the proposed structure for a larger beam steering angle of 50°. At 50°, the peak gain is 20.1

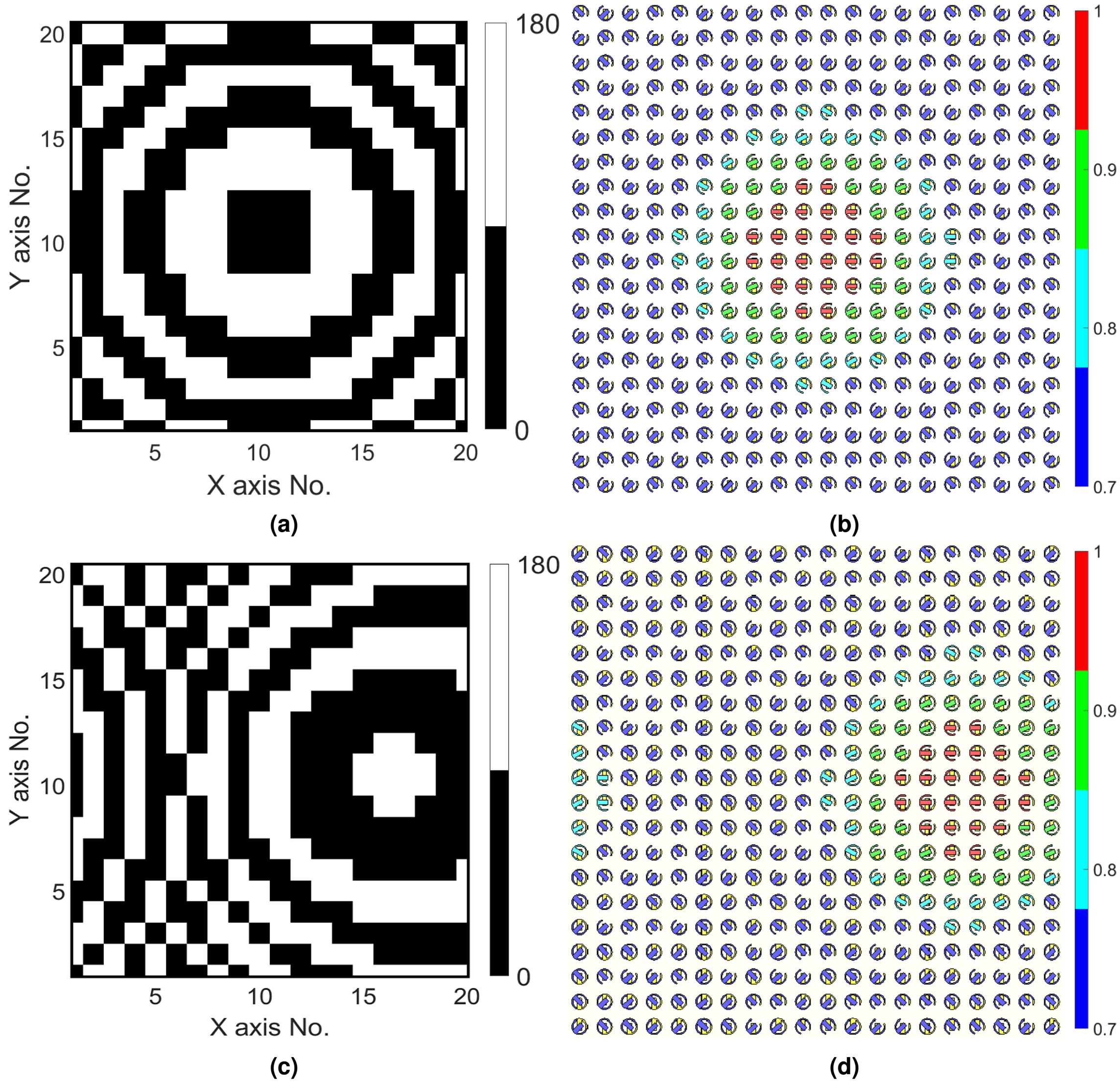

FIGURE 3.12 : (a) and (c) GA-optimized phase distributions at 0 and 30°; (b) and (d) their corresponding optimized Taylor amplitude distributions at 28 GHz, respectively.

dBi, with SLL of -13.7 dB in the H-plane and SLL of -14.2 dB in the E-plane. The results indicate that the structure maintains a good and acceptable performance for vehicle sensing applications. To facilitate a clearer understanding, Table 3.4 summarizes the simulation results at 0°, 30°, and 50°.

TABLEAU 3.4 : Performance comparison for different beam steering angles.

Beam Angle	Peak Gain (dBi)	SLL H-plane (dB)	SLL E-plane (dB)
0°	27.2	-22.1	-19.4
30°	24.9	-16.8	-19.5
50°	20.1	-13.7	-14.2

It should be pointed out that in practical automotive radar systems, beam steering angles typically range from ± 30° to ± 60°, depending on the specific application (e.g., long-range, mediumrange, or corner radar). While some systems target wider beam steering, many mid-range sensing applications operate effectively within this range [95] and [96]. These findings demonstrate the effectiveness and feasibility of the proposed GA-based system incorporating both phase and amplitude tapering techniques.

3.6 Fabrication and measurement results

Two 20 $\times$ 20 prototypes of the previously proposed phase/amplitude TAs, designed for 0° and 30° beam steering, were optimized and fabricated on Rogers RO3003 substrates using multi-layer printed circuit board (PCB) technology. The effective aperture of the TA is 100 $\times$ 100 mm, comprising 400 unit cell elements, and includes a 5 mm extension along the edges for mounting support. A linear-polarized horn antenna serves as a source to illuminate the aperture, with an F/D ratio of 0.6. The fabricated TAs underwent measurements for peak gain and radiation patterns in the far-field region. The measurements were conducted in an anechoic chamber setup, as depicted in Fig. 3.13(b).

First, the simulated and measured main beam direction (0°) gains of the proposed TA with both phase and amplitude tailoring are presented in Fig. 3.14. A very good agreement between

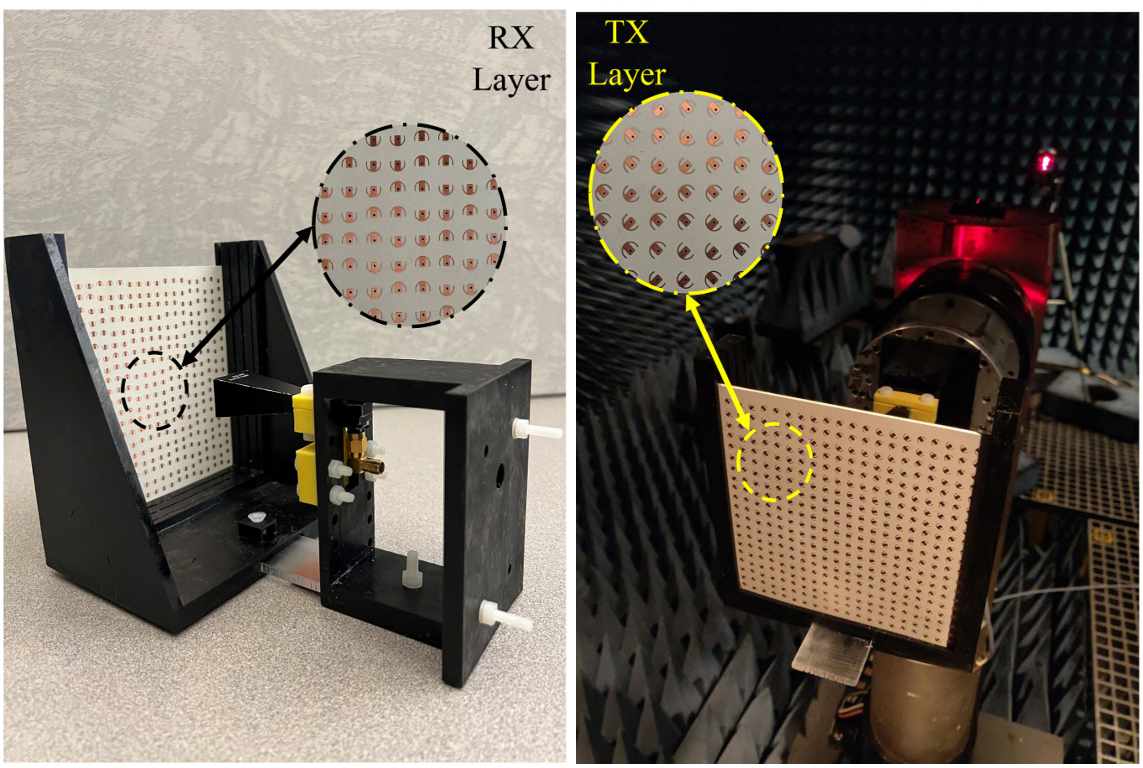

(a) **(b)**

FIGURE 3.13 : (a) Fabricated prototype with mounting block, and (b) the measurement setup in the anechoic chamber.

simulation and measurement results is observed over the whole bandwidth, both for the gain (Fig. 3.14) and radiation patterns Fig. 3.15).

The maximum achievable peak gain (main beam direction) is about 27.6 dBi at 29 GHz in simulation, whereas in the case of measurement, it reaches a peak gain of 27.4 dBi (see Fig. 3.14). The -3dB bandwidths span from 26.5 to 34 GHz (7.5 GHz) and from 26 to 32 GHz (8 GHz), equivalent to 26.8% and 28.6% -3dB bandwidth around 28 GHz, for both simulation and measurement results, respectively. The maximum measured peak gain at 28 GHz for both the 0 and 30° beam-deflection angles are 27.2 and 24.5 dBi, respectively. Moreover, the measured side-lobe and cross-polarization levels remain lower than -22.1/-19.4 dB and -44/-35.7 dB, for 0°; -16.3/-19.6 dB and -29.7/-29.05 dB for 30° in H-/E-planes, respectively.

Furthermore, the aperture efficiency for the proposed TA is also provided, and it can be determined through the following calculation :

$$\varepsilon_{ap} = \frac{G\lambda_0^2}{4\pi Ap} \tag{3.3}$$

Here, G represents the gain, and AP denotes the physical aperture area [97]. The study reports aperture efficiencies achieved through simulation and measurement, with values of 46.25% and 47.87% at 28 GHz for 0° beam steering, and 28.2% and 25.71% for a 30° beam deflection angle. These results highlight excellent effective radiation performance. The simulation and measurement outcomes align well, with minor discrepancies attributed to fabrication and substrate tolerance errors.

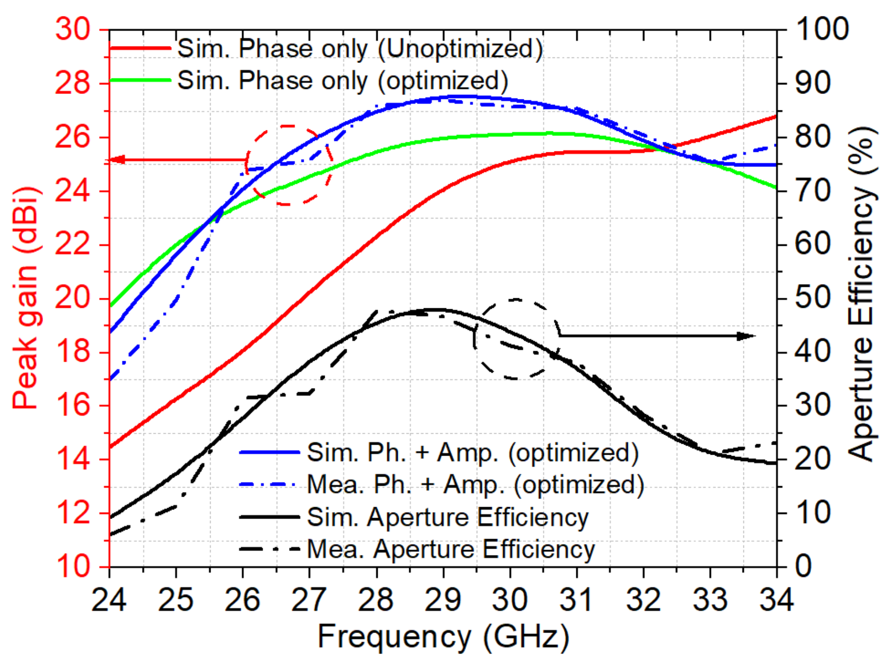

FIGURE 3.14 : Simulated and measured peak gains and the corresponding aperture efficiencies for the TAs with phase only, and GA-optimized phase with 2-bit Amp. controls at different frequencies.

For simplicity and brevity, beam steering schemes are applied exclusively to the azimuth plane, with potential extension to a 2D beam steering environment. The comparison in Table 3.5 highlights the superior performance of the proposed TA, even with just 1-bit phase compensation. These results position the proposed design as a promising candidate for mm-Wave vehicular communications, effectively meeting the demands for low SLL and high gain.

This study has introduced a novel TA with multiple bits, featuring a dual-layer unit cell that provides wideband 1-bit phase compensation. The unit cell has achieved a maximum transmission amplitude of 0.98 through current-reversal and polarization-twisting techniques. The proposed structure allows independent adjustment of amplitude from phase states using 1- and 2-bit Taylor excitation patterns. Genetic algorithm optimization has been used to address gain reduction during amplitude tapering, ensuring robust performance. Demonstrated at 28 GHz, the TA has achieved two distinct beam-steering angles (0 and 30°) with exceptional beam scanning performance, characterized by high gain and low side lobe levels.

The structure's cost-effectiveness and adaptability position it as a promising solution for future mm-Wave vehicular communication systems requiring high-gain, low side lobe levels, and beam-shaping capabilities.

Although PCB technology is cost-effective, it imposes performance limits at mm-Wave :

— **Copper losses :** Skin effect and surface roughness elevate ohmic loss.
— **Dielectric loss :** Even low-loss substrates exhibit non-negligible tangents.
— **Fabrication tolerances :** Sub-millimeter misalignment degrades phase/amplitude accuracy.
— **Thermo-mechanical stability :** Harsh vehicular environments increases delamination and warping risks.

These challenges limit peak efficiency and highlight the need for alternative manufacturing methods. Additive manufacturing and 3D printing technologies emerge as a promising path, with important traits and performances such as :

— **Low-loss materials :** High-purity polymers and composites reduce dielectric and conduction losses.

TABLEAU 3.5 : Performance comparison between the proposed GA-optimized TA and Related Works.

Ref.	Phase distibution range	Amplitude distribution technique	Operating Frequency (GHz)	Realized gain (dBi)	SLLs (dB) @ operating frequency (H-/ E-plane)	N°. of layers/ TA thickness (λ_L)	Aperture efficiency (%)	-3dB bandwidth (%)	Beam steering capability?
[98]	2-bit	N/A	28	25.2	-21/-21	3/0.1	13.8	18	No
[99]	360°	Cassegrain reflectarray	12	22.8	-17/-15	3/1.53	36.9	9.5	No
[100]	360°	Particle Swarm	28	27	-30/-30	2/0.14	28	11.2	No
[101]	360°	N/A	30	25	-10/-10	3/0.16	13	Not Given	Yes
[102]	1-bit	N/A	28	20.8	Not Given	3/0.08	28.4	16.5	Yes
[60]	1-bit	N/A	28	25.5	-15.2/-14.1	3/0.14	41.6	33.3	Yes
This work	1-bit	**GA-optimized Taylor**	**28**	**27.2**	**-22.1/-19.4**	**3/0.12**	**47.8**	**28.6**	**Yes**

λ_L = free space wavelength at the lowest frequency.

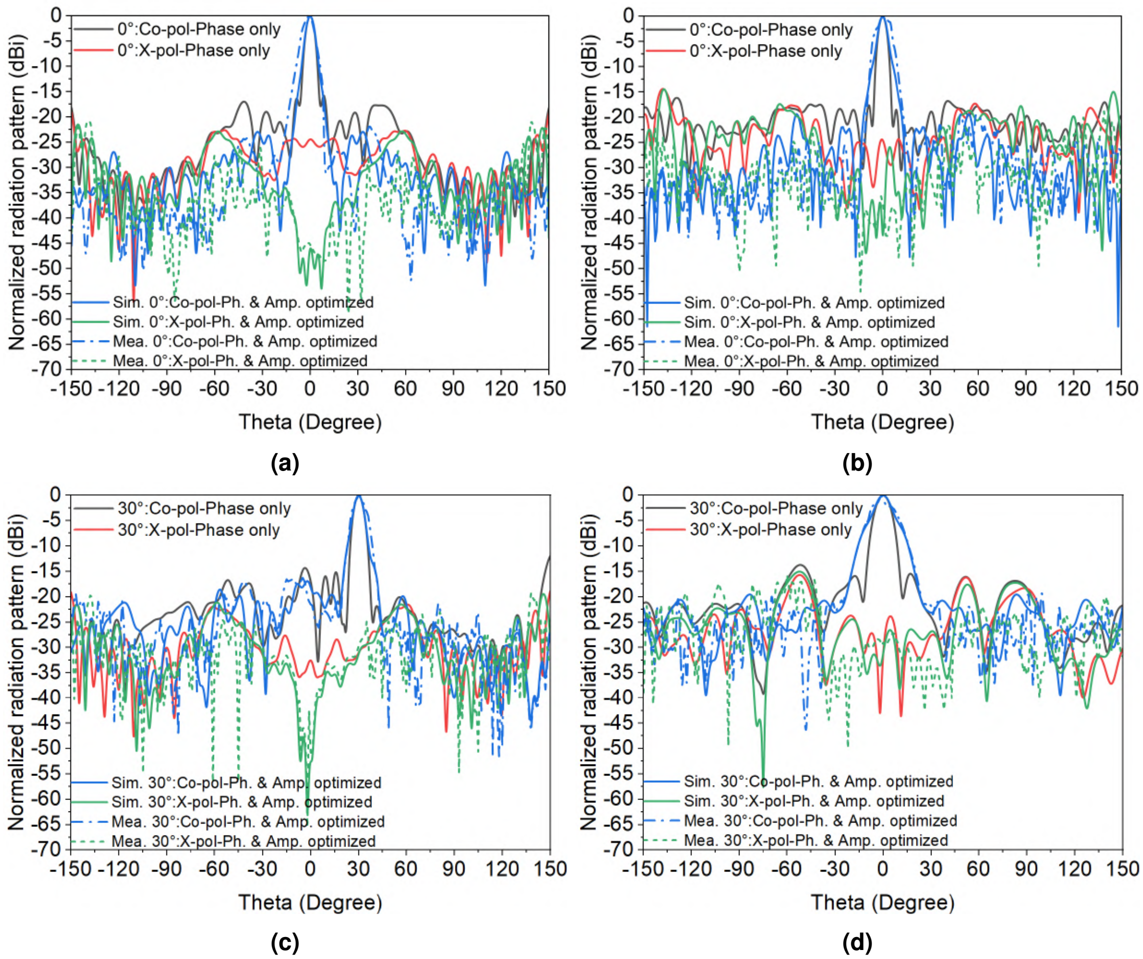

FIGURE 3.15 : Simulated and measured normalized radiation patterns of the proposed TA versus the initial designs, at 28 GHz. (a) & (b) : H- and E-planes for 0°(main beam direction) . (c) & (d) : H- and E-planes for 30° beam deflection, respectively.

- **Complex geometries :** Fully 3D unit-cell topologies enable multi-resonant, broadband designs.
- **Conformal integration :** Antennas can be printed directly onto curved vehicle surfaces.
- **Reduced assembly :** Monolithic prints eliminate via-related losses and misalignment.

The next chapter will delve into the design and realization of 3D printed metamaterial transmitarrays for next-generation mm-Wave systems.

3.7 Conclusion

This chapter traced the evolution from reflectarrays to high-performance transmitarrays, culminating in multi-bit, wideband architectures with independent phase and amplitude control. Through innovative unit-cell design and GA-based optimization, transmitarrays were demonstrated with record-breaking gains, exceptional sidelobe suppression, and broad bandwidth. Yet, PCB fabrication challenges motivate the transition to 3D printed solutions, which promise to further enhance efficiency, bandwidth, and integration for future mm-Wave vehicular applications.

4 3D-PRINTED CONFORMAL LENS DESIGN FOR ADVANCED BEAM-SHAPING IN MM-WAVE APPLICATIONS

4.1 Introduction

The increasing bandwidth demands of wireless systems have pushed the operating frequency of modern communication infrastructures into the millimeter-wave (mm-wave) spectrum. This frequency band offers wide channels and supports high-speed data links but suffers from challenges such as high free-space attenuation, susceptibility to blockage, and limited beam coverage. To counter these limitations, highly directive and reconfigurable antennas are crucial.

Traditionally, beam steering in mm-wave systems has been achieved using phased arrays, electronically steerable reflectarrays, or transmitarrays. While these approaches provide robust beam-forming capabilities, they involve complex feed networks, power-hungry control circuits, and high manufacturing costs, particularly when wide-angle steering or multiple beam generation is required.

A promising alternative that has emerged in recent years is the use of 3D-printed conformal transmissive lenses. These structures, made of passive dielectric materials shaped through additive manufacturing, exploit the principle of height-to-phase conversion. Unlike phased arrays, which rely on active elements to achieve phase shifts, 3-D lenses impose a spatial phase profile on the incident wavefront by varying the optical path length through each subwavelength segment of the lens. This provides a fully passive and low-loss solution to beam manipulation.

This chapter presents a comprehensive overview of the theoretical foundations, experimental validations, and practical implementations of 3D-printed conformal lenses for mm-wave applications. Drawing on three peer-reviewed conference papers and a recent journal article, we demonstrate the progression from basic beam steering to advanced orbital angular momentum (OAM) generation and mechanically assisted 360° scanning. The culmination of this work is an optimized and fabricated design validated through simulation and measurement.

4.2 Theoretical Foundations of 3D Conformal Lenses

4.2.1 Height-to-Phase Principle

At the core of a transmissive 3-D printed lens is the ability to tailor the phase of an outgoing electromagnetic wave by controlling the thickness—or height—of individual unit cells. When a plane wave illuminates a dielectric slab, the wave experiences a phase delay proportional to the slab's refractive index and physical thickness. By spatially varying the thickness across the lens surface, a desired phase profile can be imposed.

Fig. 4.1 illustrates both the OAM generation and beam steering principles of a conformal cylindrical lens antenna. The lens is segmented into M $\times$ N sub-wavelength segments with an inner radius (R) and thickness (h_s). Using the geometric-optics method, a cylindrical wave front can be transformed into a planar wave front with a specified deflection angle, assuming individual control over the transmission phase of each segment (achieved in this work by adjusting the height of dielectric-based unit cells). The reference ray $\vec{r}_f$ represents the shortest ray traveling in the desired direction, and the phase difference between vector rays $\vec{r}_{mn}$ and $\vec{r}_f$ is expressed as [18, 103] :

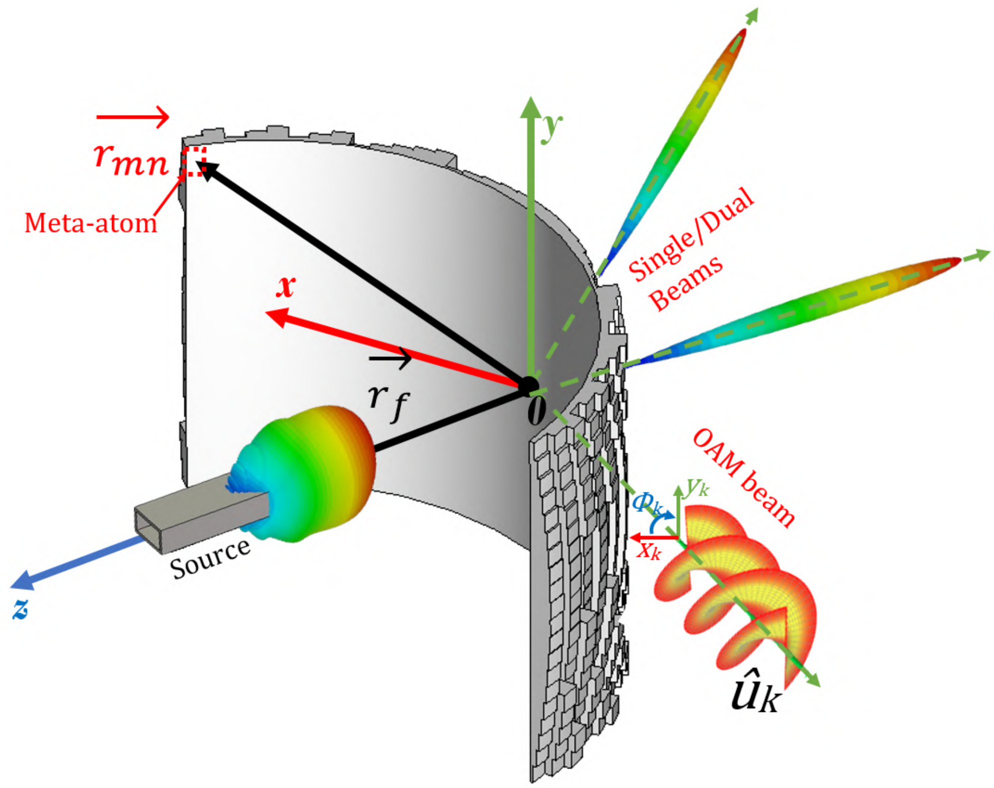

FIGURE 4.1 : Proposed conformal 3D lens with multiple Beam-shaping capabilities.

$$\phi_{mn}^{c} = -k_0 \left| \vec{r}_{mn} - \vec{r}_f \right| + \arg\left\{ \sum_k \exp\left[j\left(k_0 \vec{r}_{mn} \cdot \hat{u}_k \pm l_k \Phi_k \right) \right] \right\} \tag{4.1}$$

where, k_0 represents the free-space wave vector. ϕ_{mn}^{c} denotes the required phase of the mnth element of the lens, while $\vec{r}_{mn}$ and $\vec{r}_f$ represent the vector positions of each unit cell and the feed antenna, respectively. Additionally, l_k is the OAM mode number, and Φ_k is the azimuth angle of each unit cell in the normal plane of the proposed structure. Through compensating phase differences, the outgoing wave can be collimated to the predefined desired beam-steering direction.

The simulation considers each sub-wavelength segment as a homogeneous substrate, and the phase shift is controlled by adjusting the segment's refractive index. The relationship between the required phase difference (Δ_φ) and the refractive index difference (Δ_n) is established as follows :

$$\Delta_\varphi = k_0.h_s.\Delta_n \tag{4.2}$$

where h_s is the thickness of the dielectric unit cell.

Eq. 4.2 establishes a correlation between the thickness of the element and the phase of transmission. Leveraging previously computed phases, this relationship is established assuming a known and consistent refractive index (n). Consequently, it becomes feasible to fabricate the proposed lens using a single dielectric slab with varying unit-cell thicknesses. This methodology facilitates the incorporation of various predetermined schemes for manipulating beams, expressed as follows :

$$\Delta_{h_s} = \Delta_\varphi / k_0 \Delta_n \tag{4.3}$$

As $n = \sqrt{\varepsilon_r.\mu_r}$, having information about the dielectric constant of the substrate is sufficient for the design and fabrication of a 3D lens using available dielectric materials.

If the material is homogeneous, such as polylactic acid (PLA) or any other dielectric slab, the refractive index remains constant, and only the height needs to be tuned. This technique provides several benefits :

- Full 360° phase coverage can be achieved without electronic tuning.
- The fabrication process is simplified by using a single-material, monolithic lens.
- The absence of metal traces eliminates ohmic losses.

4.2.2 Unit Cell Simulation and Performance

The simulation configuration for examining the transmission properties, both magnitude and phase, of both the refractive-based dielectric unit cell and the proposed height-to-phase based unit-cell involves utilizing periodic unit cell boundary conditions and Floquet ports, with normal incidence as illustrated in Fig. 4.2(a). The thickness of the dielectric within the unit-cell serves as a parameter in the simulation setup, providing a practical avenue for designing a 3D-based lens [86].

Furthermore, a dielectric unit cell based on Polylactic Acid (PLA) filament ((ϵ_r = 2.72, tan δ = 0.08)) is characterized in terms of height-to-phase variation, and the results are shown in Fig. 4.2(b), where is clearly seen, that the proposed unit cell exhibits high transmission amplitude, while achieving the full 360° required phase shift to almost perfectly manipulate the incident wave on the lens, with various functionalities.

A good unit-cell should offer high transmission (>90%) across the desired phase range as clearly seen in Fig. 4.2(b). These studies have shown that with proper dielectric selection (PLA in this case), a unit-cell thickness variation from 0.2 mm to 7 mm is sufficient to span the entire 0-360°

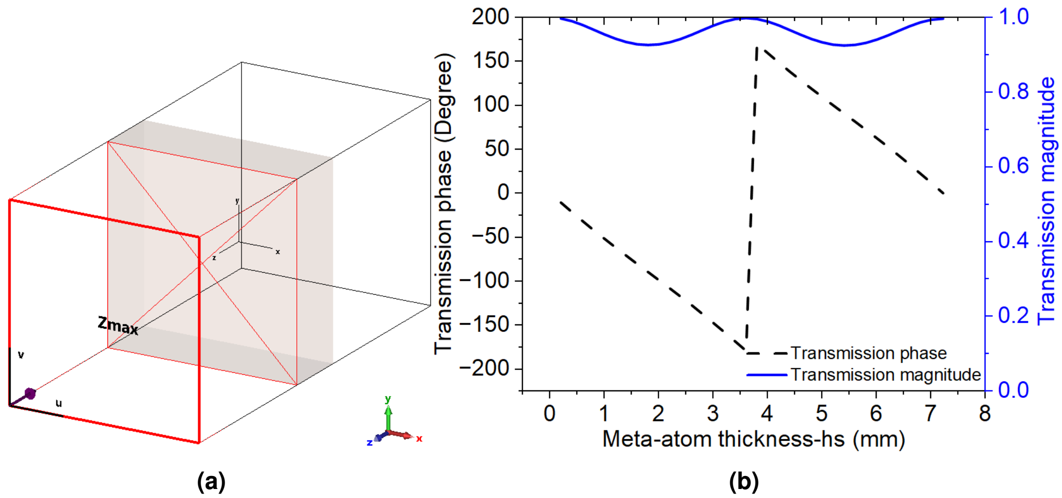

FIGURE 4.2 : (a) unit-cell simulation setup, and (b) its simulated transmission results at 28 GHz.

phase range at 28 GHz. This foundation sets the stage for practical implementation across several distinct applications.

4.3 Application Demonstrations

4.3.1 Beam Steering via Dielectric Height Modulation

In the proposed 3-D printed lens, Polylactic Acid (PLA) filament ((ϵ_r = 2.72, tan δ = 0.08)) is used to form the cylindrical conformal lens. For the sake of simplicity, all simulations are performed at 28 GHz, with a phase tunability of 360° (see Fig. 4.2(b)), which can provide full phase compensation. Two unique functionalities are designed, validated and explained briefly in the following sections.

4.3.1.1 Single beam with beam-steering functionality

First, three beam deflections of 0°, 15°, and 30°, respectively, are simulated using the proposed technique, and illustrated in Fig. 4.3(a), where it is noted that the gains are 21.8, 21.8, and 21.6 dBi at 0°, 15°, and 30°, so almost invariant with the beam scanning, with only 0.2 dBi loss at 30°. Moreover, the side lobe level at 0° is -20.4 dB, however, it increased with the beam steering by 6.1 and 5 dB at 15° and 30°, respectively.

4.3.1.2 Dual beam with beam-steering functionality

Another interesting beam manipulating scheme is also designed, where the main beam is split into two beams steered simultaneously at different predefined angles. Fig. 4.3(b) illustrates the beam steering results at three different angles of 15°, 30°, and 45°, respectively.

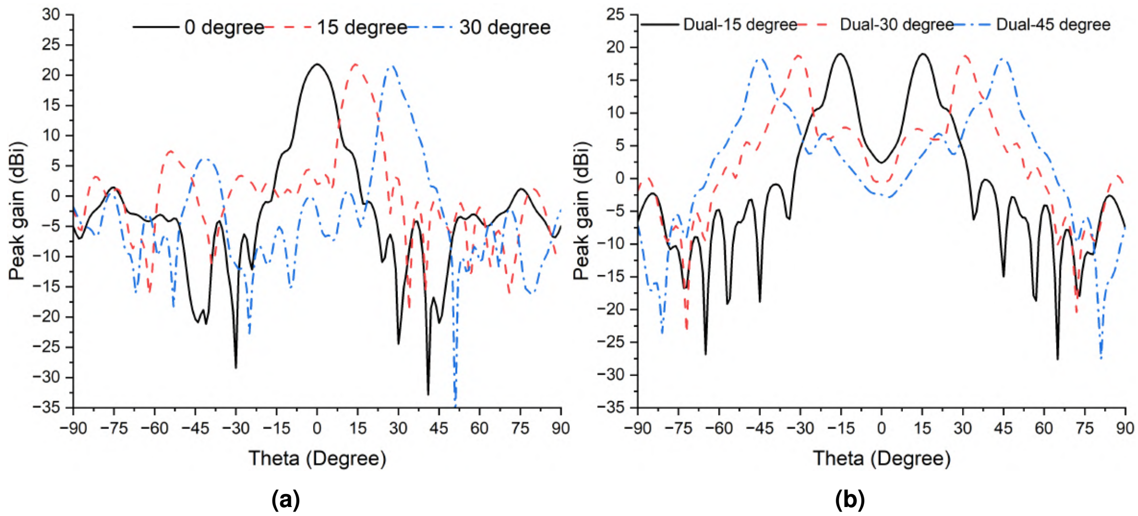

FIGURE 4.3 : Beam steering performance at 28 GHz (a) single and (b) dual-beam schemes.

This work confirmed that this passive lens structure could achieve effective directional control while maintaining high radiation efficiency and low-profile integration.

4.3.2 Multi-Mode OAM Beam Generation and Steering

Building on the initial success, the next milestone was to demonstrate Orbital Angular Momentum (OAM) beam generation. OAM beams carry helical phase fronts and can be used to multiplex signals spatially.

In the proposed 3-D lens, a Polylactic Acid (PLA) filament (ϵ_r = 2.72, tan δ = 0.08) shapes the cylindrical conformal lens. Simulations at 28 GHz focus on the azimuth plane for simplicity. Two distinct functionalities are designed, validated, and briefly explained in the following sections.

4.3.2.1 Single OAM beam with beam-steering functionality

Initially, three OAM beams with the mode l =+1 are directed to 0°, 15°, and 30° using the proposed method, as shown in Fig. 4.4(a). Notably, the gains remain consistent at 20.4, 19.5, and 19.4 dBi at 0°, 15°, and 30°, demonstrating minimal loss with only a 1 dBi decrease at 30°.

Additionally, Fig. 4.4(a) illustrates the phase front and amplitude response of the 3-D lens, revealing a null with a helical phase corresponding to mode l =+1.

4.3.2.2 Dual OAM beams with beam-steering functionality

Another unique beam manipulation scheme involves splitting the main beam into two distinct OAM beams (l=+1, +2) independently steered at predefined angles. In Fig. 4.4(b), the results of beam steering at $\pm 30^{\circ}$ for both modes and independent steering at -45° and +30° for l =+1 and l =+2 are illustrated.

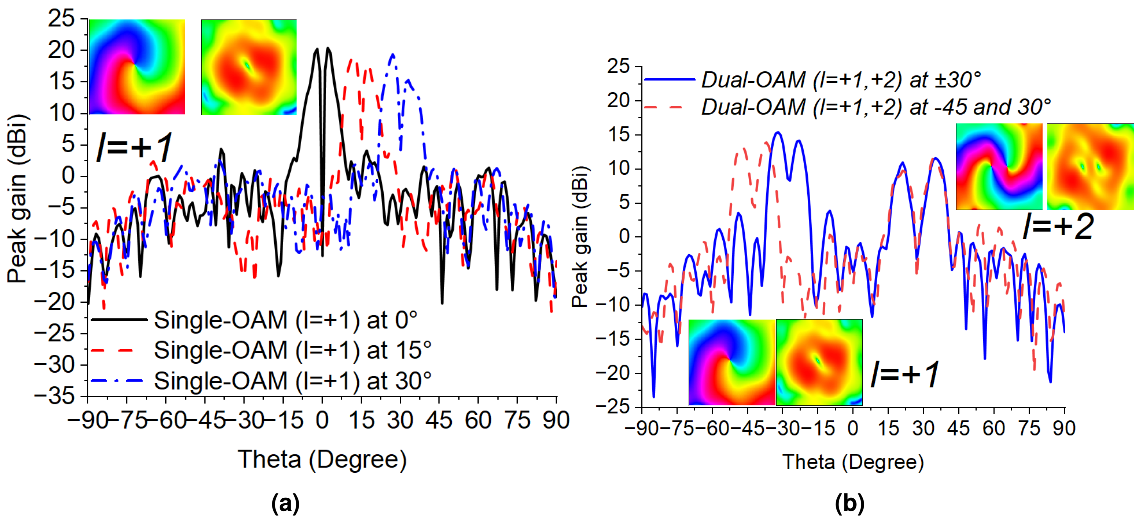

FIGURE 4.4 : Beam steering performance at 28 GHz (a) single and (b) dual-OAM modes beam schemes.

To maintain simplicity, all beam steering schemes were implemented solely in the azimuth plane. However, these concepts can be extended to a 2D beam steering environment with independent mode generation and steering functionalities, showcasing the versatility of the presented 3-D lens. This advancement unlocked new degrees of freedom for wavefront shaping, offering compatibility with multiplexed communications and spatial encoding.

4.3.3 Hybrid UAV System with Mechanical Steering

In real-world scenarios, particularly for UAV-based platforms, 360° beam coverage and vertical connectivity are essential. Two novel hybrid antenna systems for UAV-assisted communication networks, combining a 3D-printed cylindrical lens with a monopole dielectric resonator antenna (MDRA) were proposed. The first system achieves dual-pattern coverage with high-gain omnidirectional radiation in the azimuth plane and conical coverage for the lower hemisphere, ensuring seamless device-to-device (D2D) and UAV-to-base-station (D2B) communication. The second system introduces a high-gain pencil beam with 360° beam-steering capability enabled by a mechanical rotary mechanism, maintaining constant gain and low side lobe levels. To that extent, two system configurations were studied :

— An omnidirectional/conical radiation lens for general area coverage.

— A pencil beam lens mounted on a mechanical rotary platform.

In this study, all 3D-printed lenses are designed using a Polylactic Acid (PLA) filament (ϵ_r = 2.72, tan δ = 0.08). All designs and simulation outcomes, were obtained at 28 GHz while focusing only on the azimuth plane for the sake of simplicity. Two unique beam-shaping functionalities are designed, validated and explained briefly in the following sections.

4.3.3.1 High gain omni-directional/conical pattern antenna

In this section, we propose a novel 3D-printed cylindrical lens designed to achieve dual-pattern coverage essential for UAV-assisted communication networks. By integrating the lens with the MDRA, the system achieves a high-gain omnidirectional radiation pattern in the azimuth plane, complemented by a conical pattern to cover the bottom hemisphere (see Fig. 4.5). This configuration ensures seamless device-to-device (D2D) communication among UAVs and reliable UAV-to-base-station (D2B) links, making it particularly suited for search and rescue (SAR) missions.

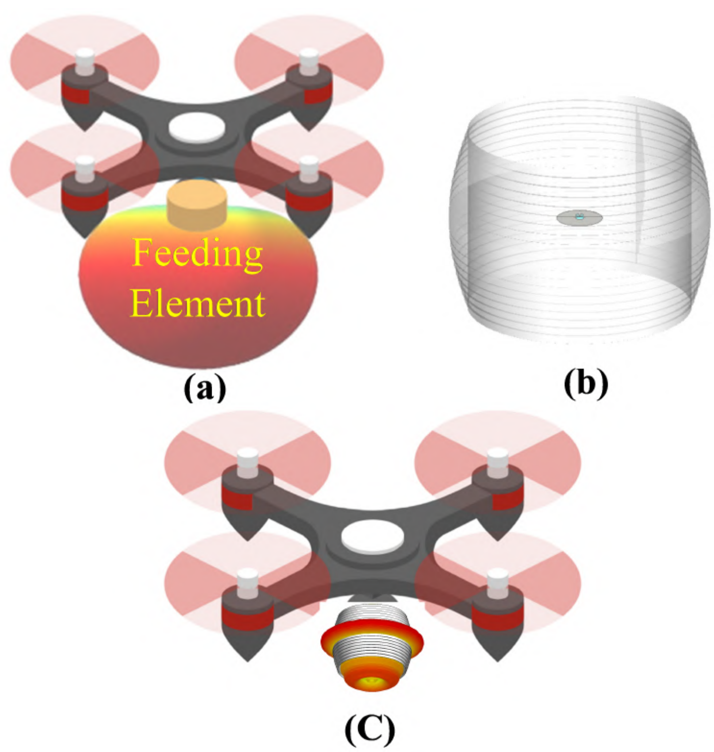

FIGURE 4.5 : (a) UAV with the standalone MDRA, (b) the proposed high gain omndi-directional/conical 3D-lens, and (c) the proposed 3D-lens based UAV communication system.

Simulation results at 28 GHz demonstrate the effectiveness of the proposed system. Fig. 4.6(a), depicts the H-plane cut fo the proposed system, confirming the uniform high-gain omnidirectional coverage, with a maximum peak gain of 8.63 dBi in elevation, and constant omnidirectional pattern with negligible gain variation of less than 0.4 dB (see Fig. 4.6(b)). Fig. 4.6(c) illustrates the E-plane cut, with a consistent conical radiation characteristics, ensuring robust communication in both lateral and vertical planes. These results validate the proposed design's ability to maintain a coherent mesh network, facilitating reliable connectivity in dynamic UAV operations.

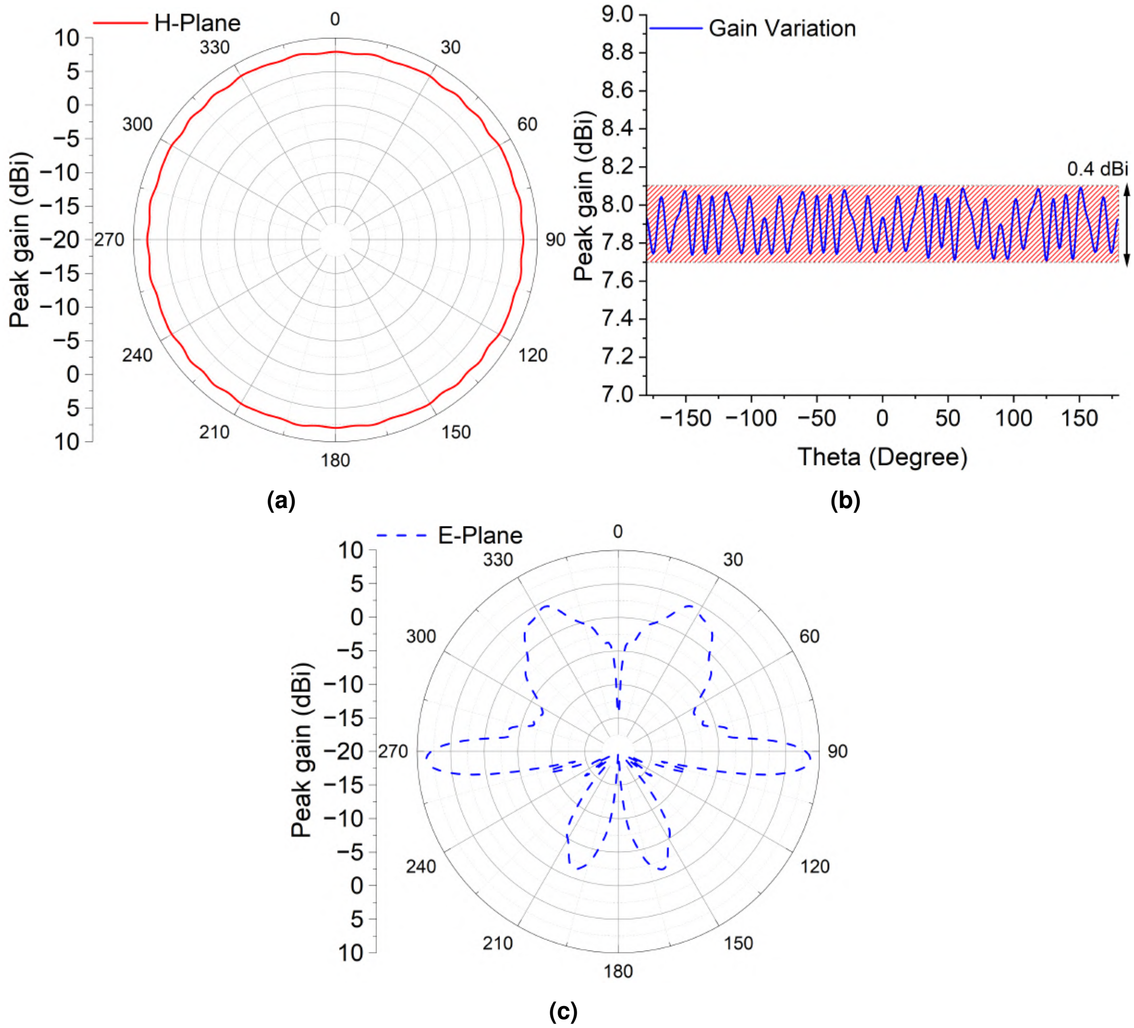

FIGURE 4.6 : Radiation pattern results in : (a) H-plane (omnidirectional pattern), (b) its gain variation, and (c) E-plane cut (both omnidirectional and conical patterns).

4.3.3.2 Mechanically-driven 3D-lens with beam-steering functionality

In this section, another interesting beam manipulating scheme is proposed, where a 3D-printed cylindrical lens is designed to produce a high-gain pencil-like beam when combined with the MDRA antenna as the source. This system achieves a sharp, focused radiation pattern with consistent peak gain and controlled side lobe levels. To enable dynamic beam steering across 360° in the azimuth plane, we incorporate a mechanical rotary system that rotates the 3D-printed lens (see Fig. 4.7), directing the pencil beam to predefined angles for seamless communication with other UAVs or infrastructure.

The integration of the mechanical rotary system ensures that the lens can steer the electromagnetic (EM) waves with precision while maintaining constant gain and uniform side lobe levels across the azimuth plane. This hybrid approach effectively mitigates the common challenges faced by traditional phased arrays and electronically reconfigurable planar transmitarrays [104], such as high side lobe levels and inconsistent peak gain during beam steering, especially at high deflection angles.

The simulation results at 28 GHz were carried out to validate the performance of the system, and they are illustrated in Fig. 4.8. The pencil beam exhibits high peak gain of 18.2 dBi with a minimal side lobe levels (SLL) of less than -15.6 dB at 0°. Similar results, were obtained at 30, 60, and 90° with peak gain values ranging from 18.2 to 18.4 dBi, and SLL values of -15.6 to -

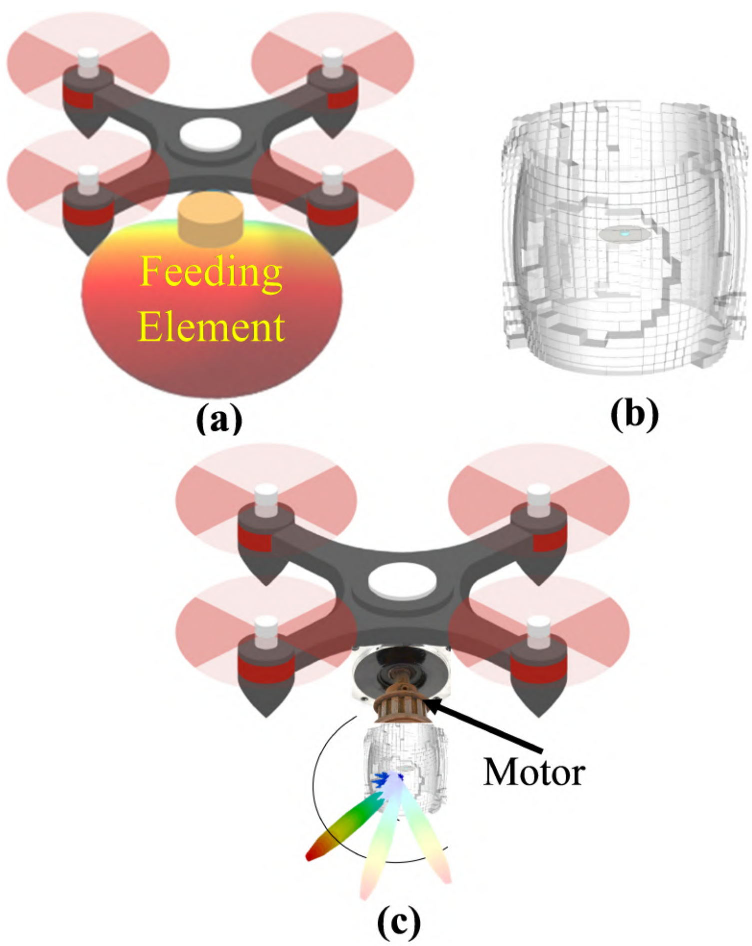

FIGURE 4.7 : (a) UAV with the standalone MDRA, (b) the proposed pencil-beam 3D-lens, and (c) the proposed hybrid mechanical/3D-printed lens based UAV communication system.

15.7 dB, respectively. These performances will ensure efficient energy concentration and reduced interference.

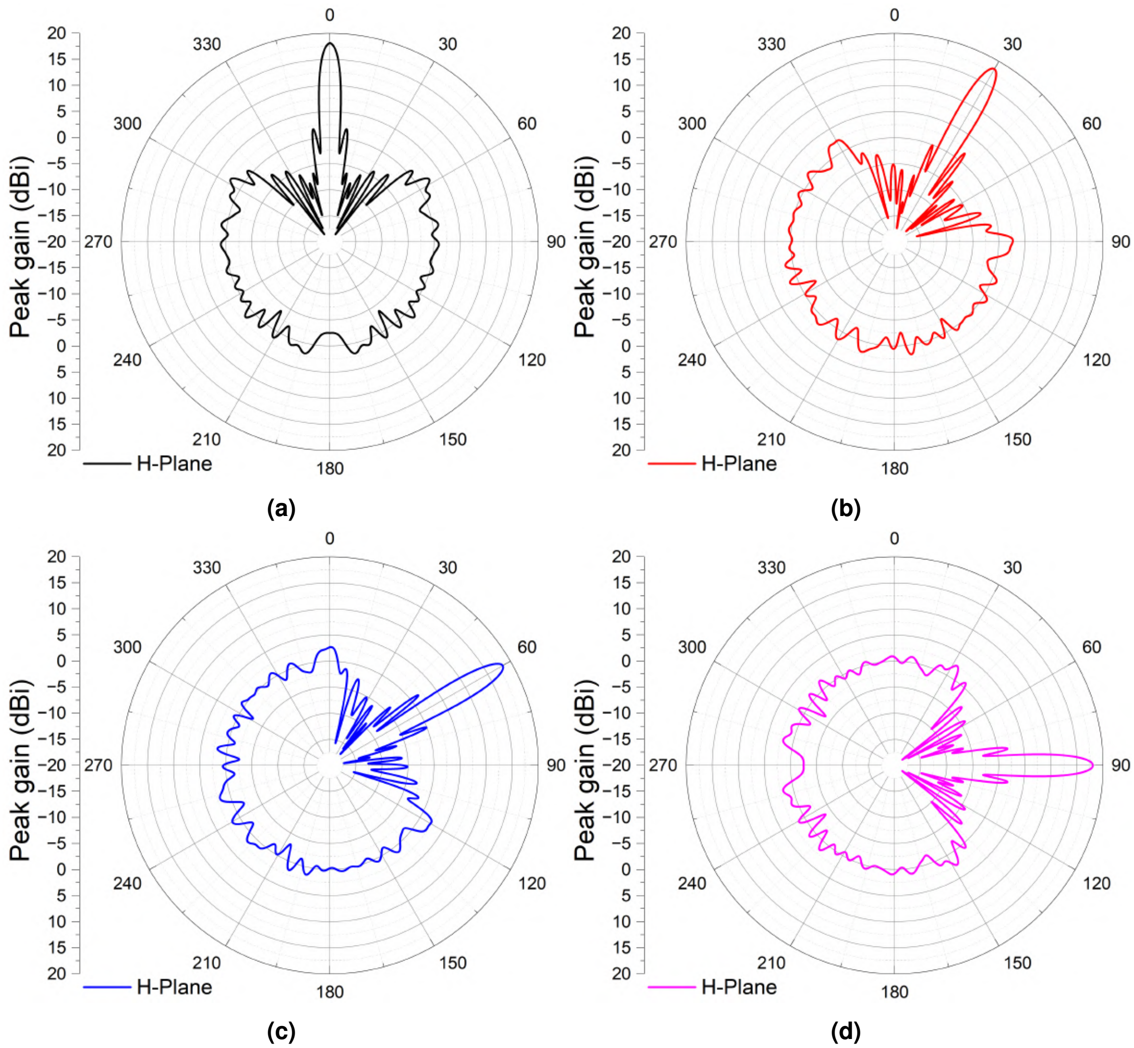

FIGURE 4.8 : Radiation pattern results in H-plane at : (a) 0°, (b) 30°, (c) 60° and (d) 90°.

The mechanical steering mechanism ensures smooth 360° coverage without compromising the system's radiation performance, making it a promising solution for UAV-assisted communication networks requiring precise, high-gain, and reliable beam-steering capabilities.

From the reported simulation results, the proposed concept demonstrated superior performance in both systems, addressing the limitations of traditional phased arrays and planar transmitarrays. These designs offer a reliable and efficient solution for UAV-assisted search and rescue (SAR) missions and other dynamic communication applications.

Moreover,this implementation demonstrated that a mechanically actuated system can complement the passive 3-D lens to achieve cost-effective dynamic beam control.

4.4 Experimental Validation and Optimization of 3D-Printed Conformal Lenses

Building upon the theoretical foundations and simulation studies presented earlier, this section details the experimental realization and validation of 3D-printed conformal lenses designed for millimeter-wave (mm-wave) beam shaping applications. The focus is on the implementation of an Automatic Synthesizing Method (ASM) integrated with a Genetic Algorithm (GA) for optimizing the phase distribution across the lens surface, facilitating functionalities such as single-beam steering, dual-beam generation, and orbital angular momentum (OAM) beam formation.

4.4.1 Conformal 3-D printed lens setup

The overall proposed system consists of two main parts : the feeding source and the 3D-printed lens. First, a pyramidal horn antenna with a maximum peak gain of 14.2 dBi, operating at the band of interest (26 to 32 GHz), is utilized here, to illuminate the lens. Fig. 4.9 illustrates the feeding element and it's corresponding s-parameters and peak gain performances, where it is clearly seen that this kind of feeding is suitable for the proposed 3-D printed lens.

In the proposed lens, a PLA filament (ϵ_r = 2.72, tan δ = 0.08) shapes the cylindrical conformal lens with a radius (R) of 68.1 mm. This lens is composed of 40 $\times$ 20 array of unit cells based on the previously discussed dielectric-based structure, with 360° phase shift ability. Each unit cell has a size (P) of 5.35 mm, corresponding to half of the wavelength ($\lambda_0/2$) at 28 GHz.

All simulations were performed using both MATLAB and CST Microwave studio, and are mainly performed at 28 GHz. They are focused on the azimuth plane only for simplicity sake. Three distinct functionalities are designed, validated, and briefly explained in the following sections.

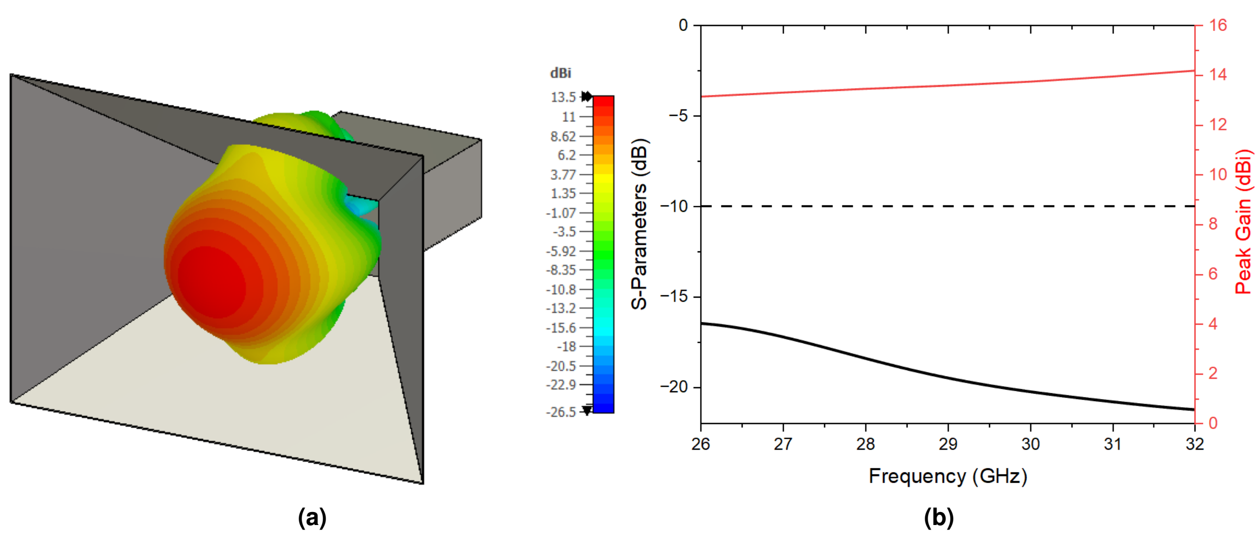

FIGURE 4.9 : (a) Feeding element, and (b) its simulated reflection coefficient and peak gain results.

4.4.1.1 Single beam with beam-steering functionality

First, three beam deflections of 0°, 15°, and 30°, respectively, are simulated using the proposed technique, and are based on the previously proposed cylindrical lens, with 40 $\times$ 20 array. The corresponding phase distributions of the aforementioned beam-deflection angles, were calculated using MATLAB and latter on applied as input parameters for our CST Microwave studio-based automatic synthesizing system [105, 106], to generate the proper 3D-patterns.

Initially, the required phase profiles for the beam-manipulating schemes, were calculated using Eq. 4.1, and the preliminary results were not that optimal in terms of peak gain and Side-lobe levels, and to get around this, a Genetic Algorithm (GA)-based system is proposed for optimizing the 3-D lens aperture. Previous research has shown that genetic algorithms hold considerable promise for tackling electromagnetic problems, exemplified by their effectiveness in optimizing structures such as electromagnetic band gaps (EBGs), artificial magnetic conductors (AMCs), and Partially reflective surfaces (PRS) [92, 93, 106].

The system under consideration employs a Visual Basic for Applications (VBA) connection between CST Microwave Studio and MATLAB's embedded Genetic Algorithm (GA) (see Fig. 4.10). Within this optimization framework, the GA generates binary encoded words that represent potential solutions, encompassing various compensation phases. These solutions are subjected to analysis and evaluation using a predefined fitness function, initially devised to aggregate all values exceeding 21 dBi (the initial peak gain at 28 GHz) across the frequency spectrum ranging from 26 to 32 GHz. The objective of this formulation is to design an optimized lens characterized by enhanced gain with low side-lobe levels (less than -15 dB) while performing beam-steering functionality.

At first, $G_{lens}(f_i)$ and $SLL(f_i)$ are denoted as the peak gain and Side-lobe level, respectively, of the 3-D lens structure. These values are taken at frequencies f_i, with a total of N = 13 frequency points falling within the specified overlapping frequency range of interest ($f_{min=26} \leq f_i \leq f_{max=32}$).

The optimization procedure aims to achieve two primary goals : maximizing the peak gain and minimizing SLL. These objectives are unified into a single-objective function. To facilitate this integration, weighting coefficients are allocated to the individual criteria within the main objective function [94]. The formulation is as follows :

$$Fit_{lens} = k_1 \cdot \frac{1}{G_{lens}(f_i)} + k_2 \cdot SLL(f_i) \tag{4.4}$$

k_1 and k_2 are the weighting coefficients for both peak gain and SLL objectives respectively, and are set equally to 0.5.

The optimization procedure aims to manipulate the phase of each unit cell within the frequency range of interest (26 to 32 GHz) using a genetic algorithm. The algorithm employs a uniform mu-

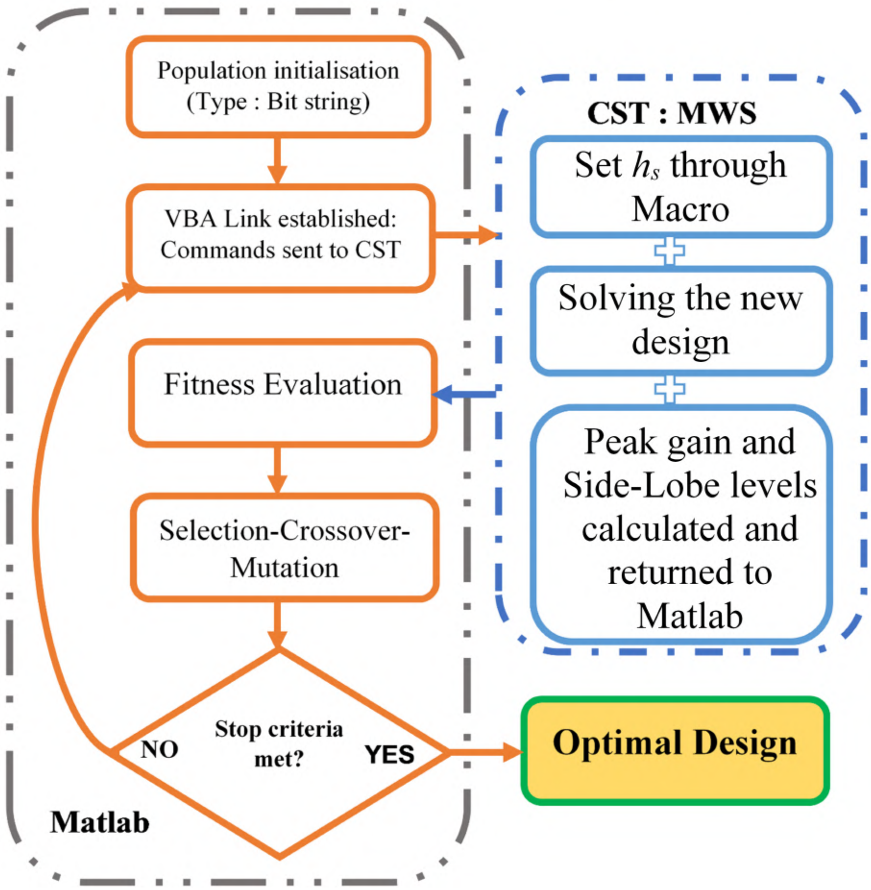

FIGURE 4.10 : The Proposed flowchart of the GA optimization process for high gain with low SLL 3-D lens.

tation rate of 0.001, single-point crossover, and tournament selection with a population size of 100 randomly selected binary strings representing specific phase distributions. The process involves 30 iterations, during which the top-performing structures undergo crossover and mutation until reaching the desired fitness value or reaching the maximum iteration limit.

The final phase distributions optimized by the genetic algorithm at 28 GHz for 0°, 15°, and 30° are attained after the 15th iteration when the termination criterion is met.

Fig. 4.11 depicts the generated phase distribution for the targeted angles. Full wave simulation were carried out with the final optimized designs for three different beam deflection angles, and the results are illustrated in Fig. 4.12. Maximum peak gains of 25.9, 25.5 and 23.8 dBi for the 0°, 15°, and 30° at 28 GHz, so almost invariant with the beam scanning, with only 2.1 dBi loss at 30°. Moreover, the side lobe level at 0° was -24.6 dB, however, it increased with the beam steering by 2.7 and 6.7 dB at 15° and 30°, respectively.

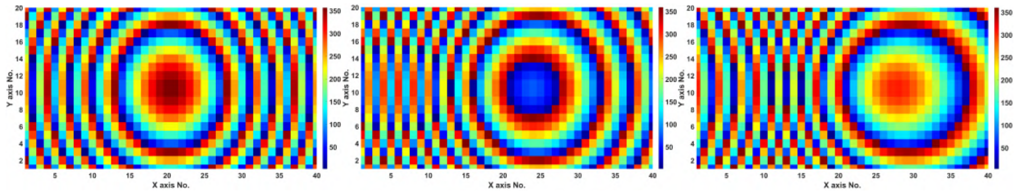

(a) (b) (c)

FIGURE 4.11 : Beam steering phase distribution at 28 GHz : (a) 0°, (b) 15° and (c) 30° schemes.

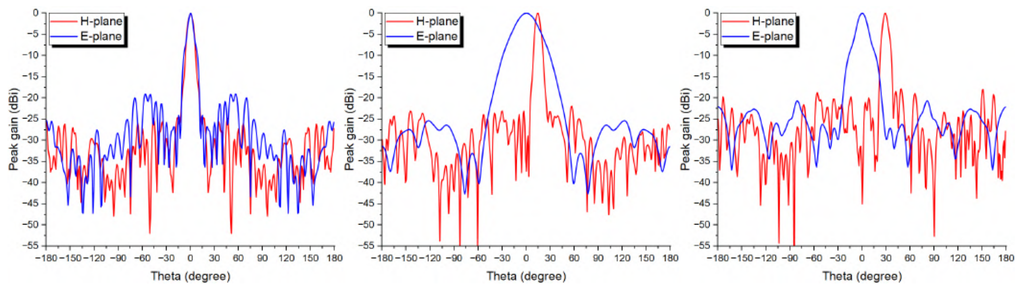

(a) (b) (c)

FIGURE 4.12 : Beam steering performance at 28 GHz (a) 0°, (b) 15° and (c) 30° in both H-/E-planes.

4.4.1.2 OAM vortex Generation

As is widely known, the current communication systems have certain limitations in terms bandwidth (BW) and signal-to-noise ratio (SNR), which hinder the ability of existing antennas to meet the escalating data rate requirements for today's users. As a result, there is a critical necessity for the development of alternative approaches that can fulfill users' expectations for connectivity. Orbital Angular Momentum (OAM) antennas have emerged as promising candidates to address these challenges.

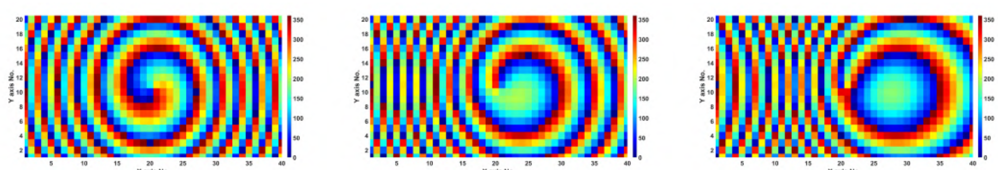

(a) (b) (c)

FIGURE 4.13 : OAM Mode l=+1 phase distributions at 28 GHz, for (a) 0°, (b) 15° and (c) 30° beamsteering schemes.

In contrast to conventional antennas, OAM antennas operate by transmitting signals through their phase fronts. Each mode of an OAM antenna possesses a distinct helical phase front that is orthogonal to other modes, facilitating the independent transmission of multiple data streams. Unlike the conventional method where multiple signals necessitate dividing the available bandwidth into separate sections, OAM antennas offer a unique advantage. They have the capability to generate multiple modes from a single aperture, leveraging this characteristic to enhance channel

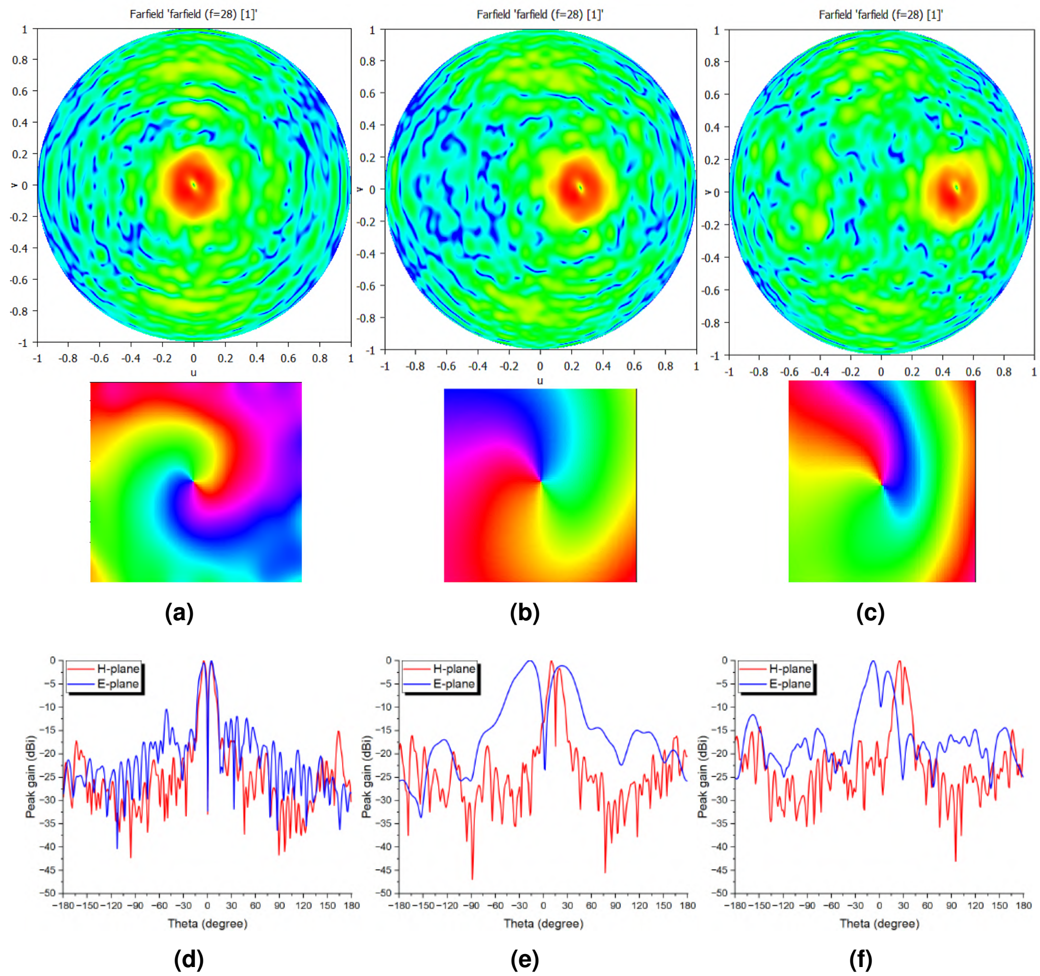

FIGURE 4.14 : OAM Mode l=+1 amplitude and phase responses at 28 GHz, for (a) 0°, (b) 15° and (c) 30°; (d), (e) and (f) their corresponding normalized radiation patterns in both H-/E-planes.

capacity and consequently boost data rates. This distinctive feature underscores the potential of OAM antennas in meeting the evolving demands of wireless communication systems.

To that extent, another unique beam manipulation scheme involves converting the main beam into an OAM beam of arbitrary mode (in this case l=+1) and steered later on to any predefined angles. In Fig. 4.14, three beam-steered OAM waves at 0°, 15° and 30° are illustrated.

Similar to the previous feature, the required phase distributions for both generating the OAM mode and also steering it, are calculated using the same MATLAB-to-CST Microwave synthesizing system, and are depicted in Fig. 4.13. Both amplitude and phase response of these three OAM beams are presented, with both OAM null and spiral phase are seen in Fig. 4.14(a),(b) and (c), proving the feasibility of the proposed 3D-printed lens in both generating and steering OAM waves.

The maximum achieved peak gain at 28 GHz, for 0°, 15° and 30°, are 20.2, 19.9, and 19.8 dBi, so almost invariant with the beam scanning, with only 0.4 dBi loss when 30° deflection is chosen.

4.4.1.3 Dual beam with beam-steering functionality

Another interesting beam manipulating scheme is also designed, where the main beam is split into two beams steered simultaneously at different predefined angles. Fig. 4.15, depicts the calculated required phase distributions for three different beam deflection angles of 10°, 25°, and 45°, respectively. The resulted normalized radiation patterns are illustrated in Fig. 4.16, where both H and E-planes are considered, at 28 GHz. It can be noted that the beams are almost perfectly in accordance with the desired beam-steering angles. This kind of feature can be useful for Point to Multi point communication applications, without the need of two transmitters or more, and can simultaneously broadcast in different directions with dual or even more beams, depending on the required links between the transmitting device and the receiving counterparts. Moreover, independent beam steering for different beams can be attained using the proposed method, and can also be extended to work in both azimuth and elevation planes as per the application's requirements.

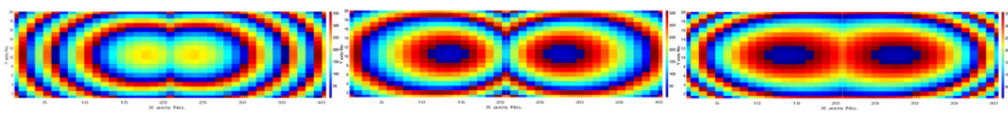

(a) (b) (c)

FIGURE 4.15 : Beam splitting (dual-Beams) phase distributions at 28 GHz : (a) 10°, (b) 25° and (c) 45° schemes.

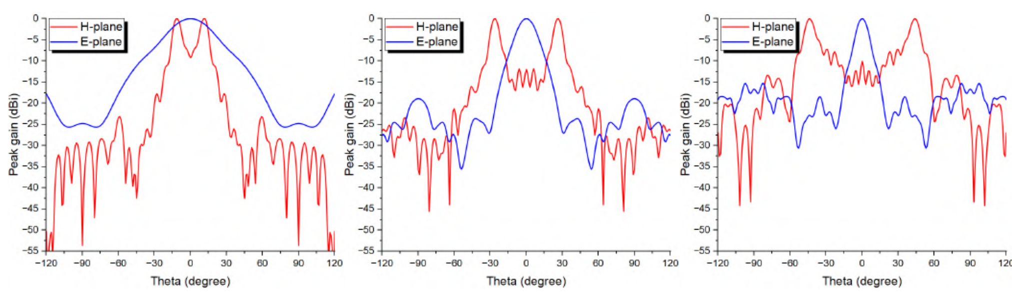

(a) (b) (c)

FIGURE 4.16 : Beam splitting (dual-Beams) normalized radiation patterns at 28 GHz, for (a) 10°, (b) 25° and (c) 45° schemes, for both H-/E-plane cuts.

4.5 Fabrication and measurements results

A 40 × 20 array of unit cells that construct a conformal prototype of the previously proposed dual-beam lens, designed for -45° and 45° angles, was optimized and fabricated on PLA filament (ϵ_r = 2.72, tan δ = 0.08) using 3-D printing technology. The effective aperture of the lens comprises 800 unit-cell elements. A linear-polarized horn antenna serves as a source to illuminate the aperture, with a focal distance of F= 68.1 mm.

First, the reflection coefficient evaluation of the proposed antenna, with and without the 3-D conformal lens structure, is carried out using an Agilent 8722ES Vector Network Analyzer (VNA) as shown in FFig. 4.17(a). The measurement results show that the proposed 3-D lens antenna covers the band of interest, spanning from 26 to 32 GHz, with less than -15 dB in reflection coefficient.

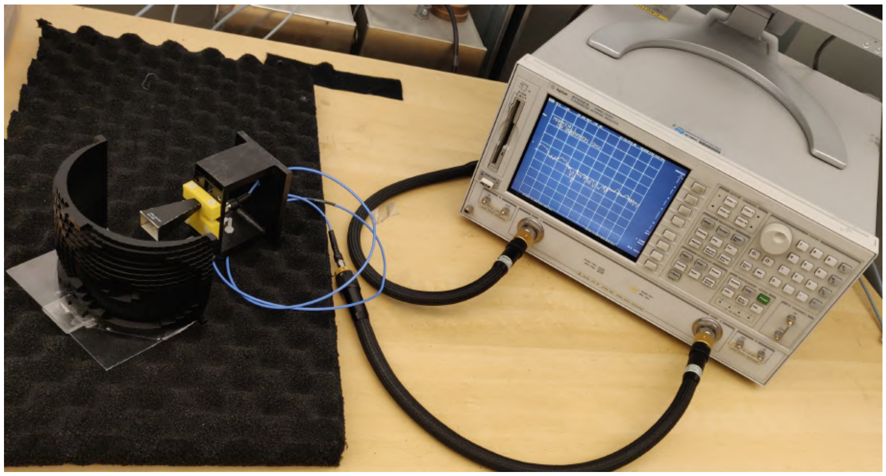

(a)

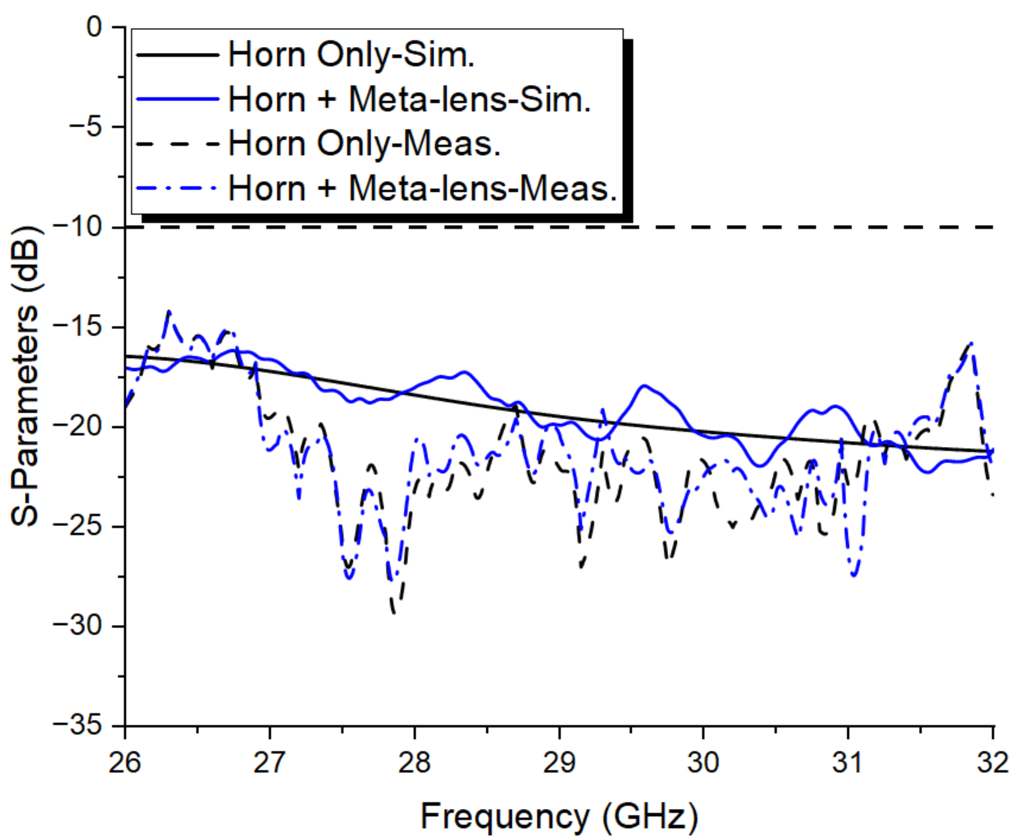

(b)

FIGURE 4.17 : (a) Proposed 3D printed lens for dual-beam shaping with its VNA measurement setup; (b) Simulated versus measured reflection coefficient results, for with and without the lens.

It is also compared to the simulated results, where the proposed antenna operates at the same band of frequencies. Therefore, both simulation and measurement results are in good agreement, despite the slight discrepancies between them, which are probably due to assembly and fabrication errors. Moreover, by using dielectric based lens, the reflection coefficient is not affected much, as seen in Fig. 4.17(b), which is another advantage compared to copper/dielectric based transmitarray.

For further analysis, the fabricated lens underwent measurements for peak gain and radiation patterns in the far-field region. The measurements were conducted in an anechoic chamber setup, as depicted in Fig. 4.18(b).

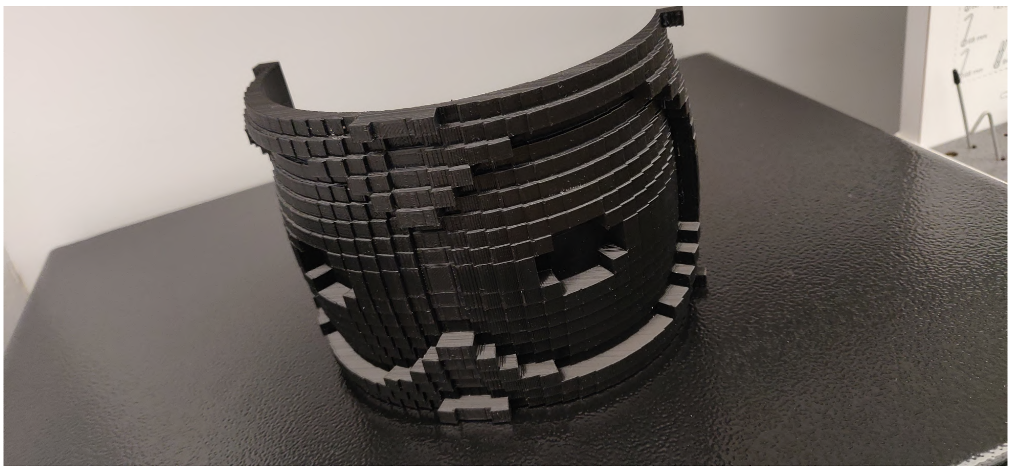

(a)

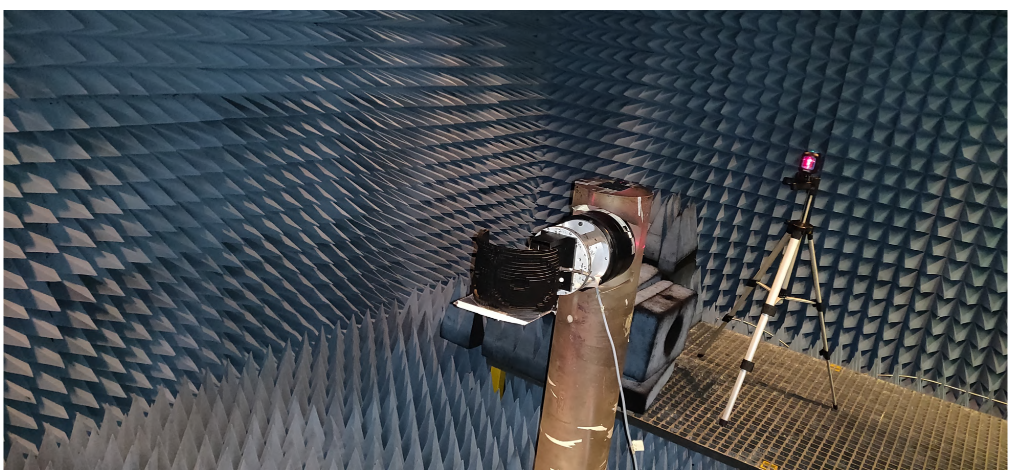

(b)

FIGURE 4.18 : (a) Proposed 3D printed lens for dual-beam shaping, and (b) its measurement setup in the anechoic chamber.

The simulated versus measured normalized radiation patterns in both plane cuts, are depicted in Fig. 4.19, where it is clearly seen that both simulation and measurement results agree well, with slight discrepancies, due to fabrication errors and lower resolution, during the 3-D printing process, which effected the overall performance of the fabricated prototype. Moreover, the simulated peak gain was 18.5 dBi, where as in the case of measurement, the maximum attained peak gain was 15.1 dBi, so a loss of almost 3.4 dBi is noted.

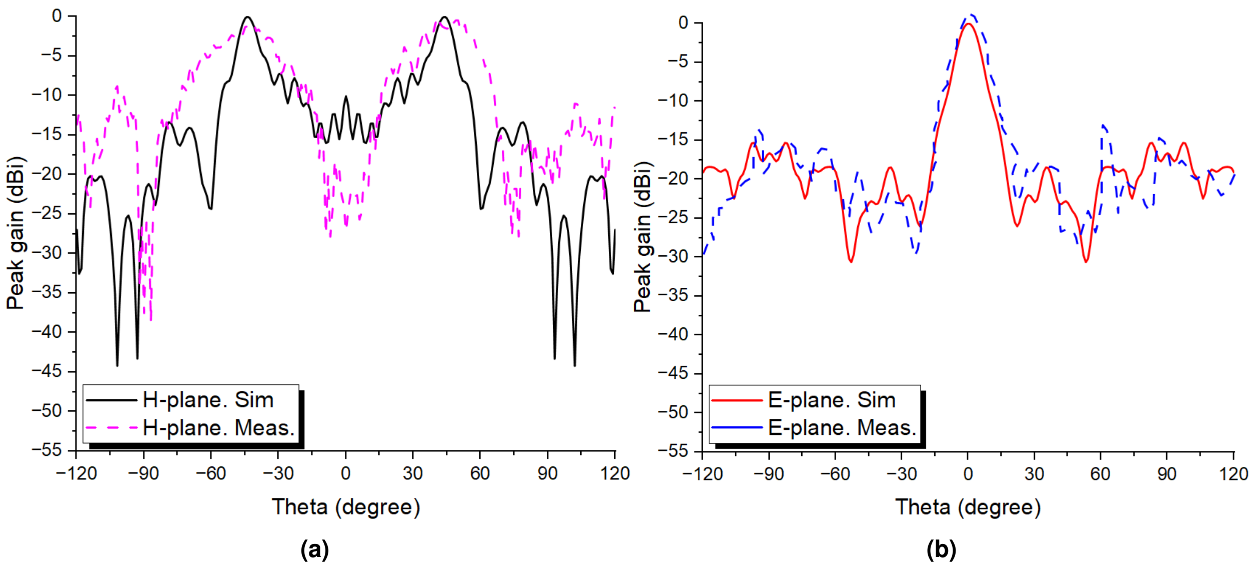

FIGURE 4.19 : Simulated versus measured normalized radiation patterns for the dual-beam prototype, in both H-/E-plane cuts at 28 GHz.

Despite these discrepancies, the proposed automatic synthesizing system proved to be effective in designing 3-D printed lens with versatile features and capabilities, with lower cost and practically easier in fabrication, compared to other technologies. Furthermore, there is no cooper or conductor losses associated with 3-D printing technology, and if combined with the emerging RF 3-D printable materials, such as Radix Printable Dielectric [107], more efficient and way performing lens can be designed at higher mm-wave frequencies.

For the sake of simplicity, all beam steering schemes are only implemented at the azimuth plane, and this can be extended to a 2D beam steering environment, with independent dual-beam steering functionalities, proving the versatility of the presented conformal 3-D printed lens for future mm-wave applications.

4.6 Conclusion

This chapter has presented the development of 3D-printed conformal meta-lenses as a practical and effective approach for shaping electromagnetic beams at millimeter-wave frequencies. Using the concept of height-to-phase control, we examined how changing the thickness of small dielectric elements across a curved surface can redirect waves in specific directions or form complex beam patterns.

Throughout the chapter, we explored several ways this lens technology can be applied. The lens was shown to steer a single beam, create two independent beams, and even generate beams with orbital angular momentum (OAM), which have twisted wavefronts useful for advanced communication methods. All of this was achieved using a single-layer dielectric structure made with 3D printing, without needing any active electronics or complicated manufacturing processes. Because of its simple design, low cost, and compatibility with curved surfaces, this type of lens is especially useful for mobile or lightweight systems such as those mounted on drones or vehicles.

However, as powerful as these passive lenses are, they have one important limitation : they cannot change their beam direction once they are built. This makes them less suitable for situations where the direction of communication needs to change quickly—such as in crowded networks, moving vehicles, or environments with a lot of interference. In these cases, systems need to react and adapt in real time.

To address this need, we turn to a different type of technology : electronically reconfigurable transmitarrays. These systems allow us to change the phase of each unit cell using components like PIN diodes or varactors controlled by voltage. Although these systems are more complex, harder to manufacture, and consume more power—especially when built using printed circuit board (PCB) technology—they offer one major advantage : speed. They can steer beams quickly and adjust to different communication scenarios as they happen.

In the next chapters, we will focus on these electronically tunable systems. We will see how fast and flexible beamforming can be achieved using reconfigurable unit cells, and how this technology can support modern communication demands such as 5G networks, satellite links, and intelligent transportation systems. Despite the challenges, electronically controlled transmitarrays offer an important solution where fast response and adaptability are required.

5 RECONFIGURABLE TRANSMITARRAY BASED ON A NOVEL CPW-TO-SLOTLINE TRANSITION

5.1 Introduction

Transmitarray antennas (TAs) have emerged as an efficient solution for realizing high–gain, low–profile, beam–steerable apertures at millimeter–wave frequencies. Unlike phased arrays, which rely on complex active front–ends with distributed phase shifters, or reflectarrays, which suffer from feed blockage and phase nonlinearity, transmitarrays offer a passive or semi–passive architecture in which directive radiation is achieved by controlling the transmission phase of subwavelength unit cells across a planar aperture. The phase assigned to each element compensates the feed path difference between the radiating source and the aperture, enabling beam steering with minimal feeding losses.

At Ka–band (26–32 GHz), electronically reconfigurable transmitarrays face well–known constraints : insertion loss introduced by active switches, bias–network parasitics, and the difficulty of implementing compact, wideband phase control. Conventional 1–bit cells often rely on resonant microstrip/patch topologies with lumped loading, which narrows the operational bandwidth and increases sensitivity to fabrication tolerances; when bias lines are integrated, parasitic coupling can degrade the transmission magnitude and compress the usable phase range.

To address these limitations, this chapter introduces a *novel uni–planar transmitarray architecture* that performs *mode conversion* and *phase control* within a single metallization layer using a coplanar–waveguide (CPW)–to–slotline transition. The key idea is to realize the CPW odd–mode to slotline odd–mode conversion in–plane, following the physical principle of asymmetrically delaying one CPW branch by approximately $\lambda_s/2$ so that the two CPW slot fields excite a pure slotline mode with a controlled phase reference [23]. In its most compact form, this mechanism produces a binary ($0^\circ/180^\circ$) phase response without requiring multilayer apertures, vias, or external hybrids.

Relative to prior art, dual-layer Huygens/transmitarray elements and PIN-loaded phase shifters can offer broad control but typically incur multilayer alignment, via/bias routing, and resonant-mode dispersion penalties that complicate wideband operation and amplitude balance [9, 24, 42, 108]. By contrast, the present uni-planar topology collapses the feed, mode conversion, and phase control into a single metal layer, thereby mitigating bias-line parasitics and maintaining a nearly constant transmission magnitude across phase states while preserving Ka-band bandwidth.

Building on this mechanism, we propose and study two realizations. First, a **1–bit uni–planar passive unit cell** is modeled under periodic boundary conditions with Floquet–port excitation in a three–dimensional *CST Microwave Studio* framework. The cell integrates the transition and radiating section on a single layer of Rogers RO3006 ($h = 0.254$ mm, $\varepsilon_r \approx 6.5$) with a lattice period of

$p = 4.8$ mm. The simulated transmission magnitude of both binary states remains above 0.9 across 26–32 GHz while maintaining an inter–state phase difference close to $180°$, confirming broadband, low–loss phase inversion within the uni–planar geometry. A 3D model of a 20×20 array illuminated by a printed Vivaldi feed at a focal distance of $F = 53$ mm (chosen from the feed's -10 dB beamwidth) verifies array–level performance in CST, yielding peak gains near 21 dBi with side–lobe levels below -14 dB over 26–30 GHz.

Second, the concept is **fabricated and measured in a 3–bit passive form** by exploiting a purely geometric degree of freedom : the dielectric path length L_s after the transition. Incrementing L_s by approximately 1.1 mm produces $\sim 45°$ phase steps, enabling the full $\{0°, 45°, \ldots, 315°\}$ set while preserving the nearly constant transmission magnitude and an almost identical phase slope among states. The aperture is assembled modularly from panels of twenty cells each, all on single–layer RO3006, and measured in an anechoic chamber with the same Vivaldi feed at $F = 53$ mm. The resulting 3–bit transmitarray achieves peak gains of 21.1, 22.4, and 22.5 dBi at 26, 28, and 30 GHz, respectively, with corresponding side–lobe levels of -17.2, -19.4, and -17.1 dB. These measurements confirm the expected improvement over the 1–bit case—consistent with the reduction in quantization loss from approximately 1.96 dB (1–bit) to 0.27 dB (3–bit)—while demonstrating that the uni–planar topology maintains high transmission magnitude across all phase states.

An important aspect of this work is that the present uni–planar designs are *passive prototypes*. Nonetheless, the copper layout explicitly reserves pads and isolation gaps for future PIN–diode integration directly across the CPW slots, which would enable real–time electronic reconfigurability without altering the RF geometry. In that active incarnation, the same in–plane transition would act as a binary phase shifter by toggling the differential path electrically rather than geometrically. Thus, the chapter proceeds from first principles of CPW–to–slotline conversion to validated arrays—first through CST–based 1–bit studies and then through a fabricated 3–bit prototype—establishing a single–layer, fabrication–friendly path toward broadband, low–loss, and ultimately electronically steerable Ka–band transmitarrays.

5.2 P-i-n Diode Characterization

To provide electrical control of the transmitarray (TA) unit cells, commercially available off-the-shelf p-i-n diodes (MACOM MADP-000907-14020) were employed. These devices were selected due to their low-loss characteristics and stable performance in the millimeter-wave frequency range. The biasing voltages applied to the diode correspond to $1.35\,\mathrm{V}$ in the ON state and $0\,\mathrm{V}$ in the OFF state, ensuring reliable switching between conductive and non-conductive conditions. The geometrical configuration and flip-chip packaging of the diode are illustrated in Fig. 5.1, where the physical dimensions (in millimetres) of the MACOM MADP-000907-14020 are reported.

In order to accurately extract the equivalent circuit parameters of the diode, two complementary characterization techniques were adopted, following the methodology presented in [109]. The first

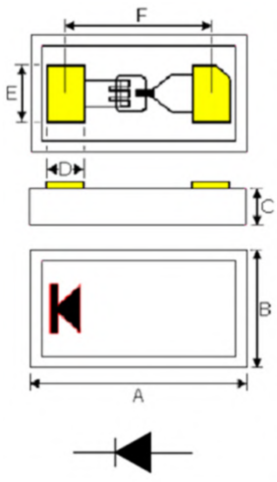

Outline Dimension

DIM	INCHES		MM	
	Min.	Max.	Min.	Max.
A	0.029	0.030	0.750	0.765
B	0.015	0.016	0.380	0.395
C	0.007	0.008	0.175	0.195
D	0.004	0.005	0.101	0.127
E	0.007	0.0073	0.177	0.185
F	0.018	0.019	0.457	0.482

FIGURE 5.1 : Schematic and geometrical dimensions (in millimetres) of the MACOM MADP-000907-14020 p-i-n diode flip-chip package.

step involved a *Through-Reflect-Line (TRL)* calibration, which was conducted using a microstrip-based calibration setup. This approach allowed the initial estimation of the equivalent circuit elements by compensating for systematic measurement errors introduced by the test fixture. Subsequently, a *waveguide simulator (WGS)* measurement was performed to further refine and validate the extracted parameters. The combination of these two techniques enabled the iterative adjustment of the circuit model through comparison between experimental data and full-wave electromagnetic simulations, leading to an accurate representation of the diode's electrical behavior under various biasing conditions [9].

The experimental setup used for the characterization is shown in Fig. 5.2, where the diode was mounted in a TRL-calibrated test fixture and measured using a VNA. The measured scattering parameters obtained from the calibration are presented in Fig. 5.4. These results correspond to the forward- and reverse-biased conditions, revealing the diode's frequency-dependent performance in the $24.0\,\mathrm{GHz}$–$32.0\,\mathrm{GHz}$ range. In the forward-biased condition (with a bias current of $I_{\text{bias}} = 10\,\mathrm{mA}$), the diode exhibits a low-resistance conductive path, and its behavior can be effectively modeled by a **series L–R circuit** characterized by

$$R_{\text{ON}} = 4\,\Omega, \quad L_{\text{ON}} = 0.12\,\mathrm{nH} \tag{5.1}$$

Conversely, in the reverse-biased condition (with $V_{\text{bias}} = 1.35\,\mathrm{V}$), the device presents high impedance, and its response is accurately represented by a **shunt R–C circuit** defined by

$$R_{\text{OFF}} = 20\,\mathrm{k\Omega}, \quad C_{\text{OFF}} = 35\,\mathrm{fF} \tag{5.2}$$

These circuit models, extracted from the de-embedded TRL structure, are schematically depicted in Fig. 5.3 for both the ON and OFF states.

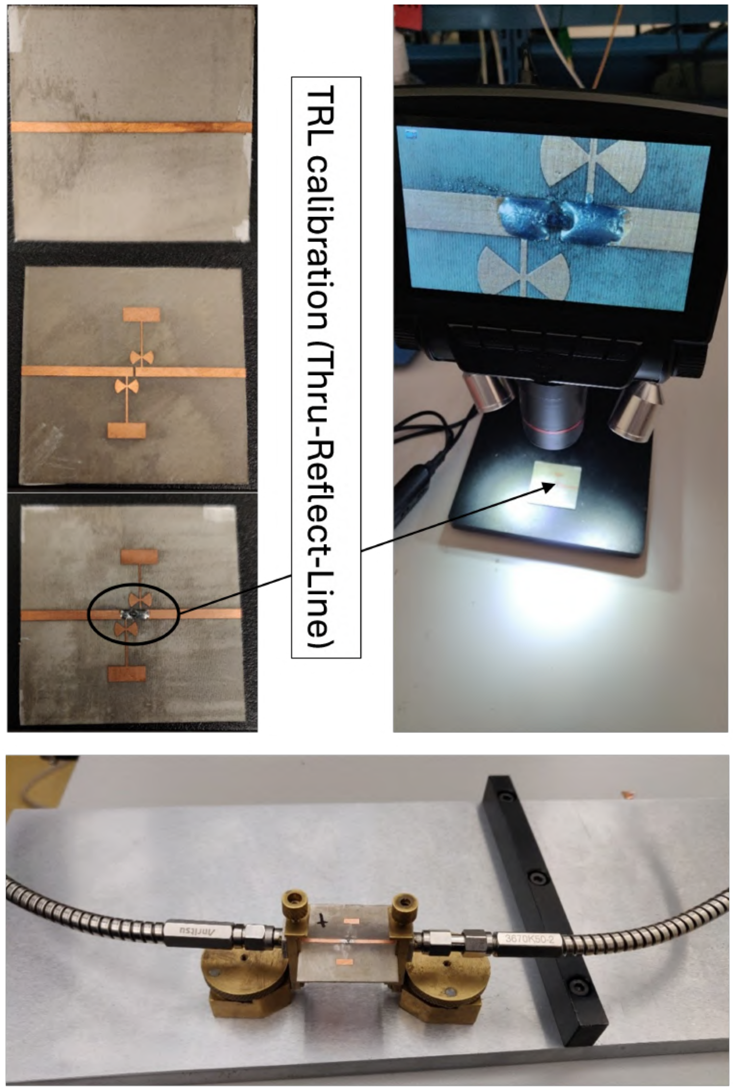

FIGURE 5.2 : Photograph of the experimental setup used for p-i-n diode characterization using the TRL calibration method.

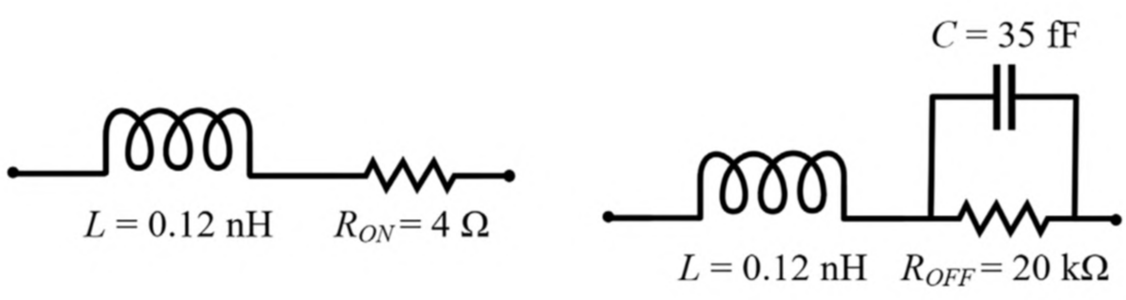

(a) **(b)**

FIGURE 5.3 : Equivalent circuit representations of the p-i-n diode in (a) ON state and (b) OFF state.

The measured insertion loss varies between $1.0\,\mathrm{dB}$ and $3.0\,\mathrm{dB}$ across the $24.0\,\mathrm{GHz}$–$32.0\,\mathrm{GHz}$ frequency band. It should be noted that a portion of these losses is attributed to the measurement configuration itself. In particular, the characteristic impedance of the test lines employed in the calibration setup deviates from the standard $50\,\Omega$ reference, leading to impedance mismatch and additional losses when interfacing with microwave probes calibrated at $50\,\Omega$. Moreover, a limited isolation level was observed in the same frequency range, which is an inherent characteristic of the diode package and biasing configuration. This limitation will be addressed in the subsequent design of the TA unit cell, where a phase-shifting mechanism independent of the active device isolation will be introduced. This approach ensures robust and predictable phase control across the aperture without relying on the intrinsic isolation performance of the switching element.

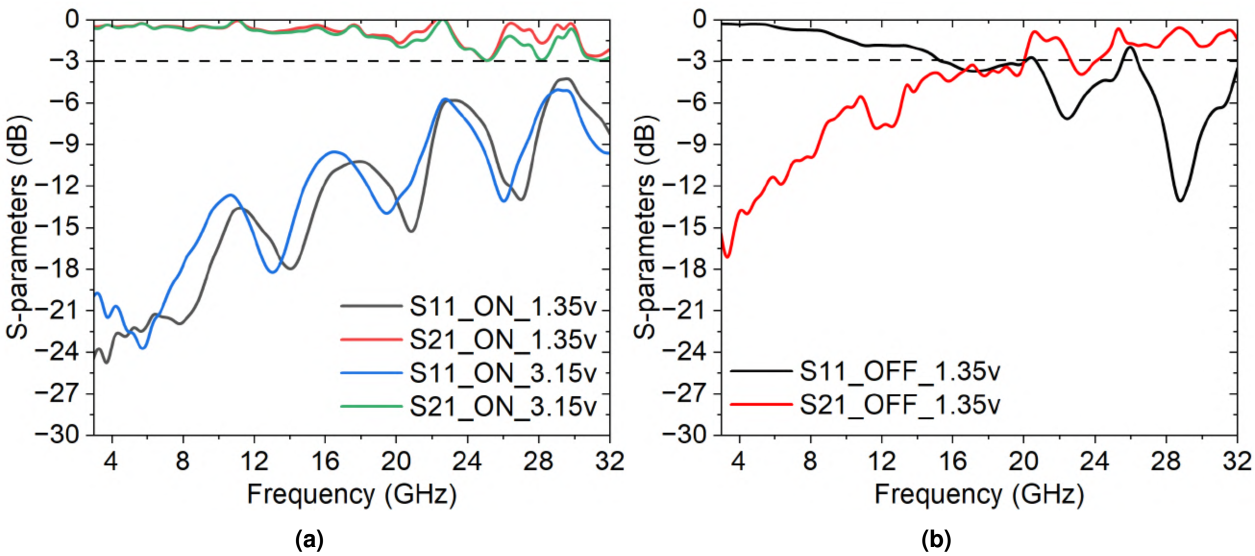

FIGURE 5.4 : Measured S-parameters of the p-i-n diode under (a) forward bias and (b) reverse bias conditions.

The validated equivalent circuit models obtained for both the ON and OFF states serve as the foundation for the **transmission-line (TL) model** adopted in the design of the proposed unit cell. By incorporating these parameterized models into the TL representation, the electromagnetic response of each state can be analytically described, allowing accurate prediction of the reflection and transmission phases. This integration not only enables precise control of the phase distribution across the array but also facilitates the optimization of the overall aperture performance in terms of bandwidth, insertion loss, and beam-steering capability. The following section will detail the implementation of this TL-based modeling framework and its role in the development of the proposed reconfigurable transmitarray.

5.3 Transmissive tunable active Transmitarray unit cell

In the previous section, a dielectric slab with different refractive indices and heights, were are able to steer and manipulate the incident wave coming from a simple horn antenna. The beam-steering was achieved by compensating the required phases for each unit cell.

Similarly, in this section we proposed a unit cell based on both a planar quasi-Yagi antenna, acting as a receiver, and a printed dipole antenna, as the transmitter counterpart. They were connected by a novel CPW-to-slot-line transition forming a Receiver-to-Transmitter structure.

5.3.1 1-Bit RTA Unit Cell Design

Fig. 5.5 13 shows the geometry of the proposed unit cell, with the dimensions of 4.5 and 20 mm in width and length, respectively. The unit cell was constructed on a Rogers RO3006 with a thickness of 0.254 mm and backed by a 0.4 mm FR-4 substrate for biasing lines. Two Macom-MADP-000907-14020P P-i-n diodes where used for switching, between the two states.

CPW/Slotline modal picture

Let $V_L(z)$ and $V_R(z)$ be the CPW left/right slot voltages (referenced to the center strip). Define

$$V_{\text{even}} = \tfrac{1}{2}(V_L + V_R), \qquad V_{\text{odd}} = \tfrac{1}{2}(V_L - V_R). \tag{5.3}$$

Single-ended CPW excitation enforces $V_L = -V_R \Rightarrow V_{\text{even}} = 0$, so the CPW carries the *odd* mode. The slotline's dominant mode is also *odd* (equal/opposite charges on slot edges). Thus the CPW odd mode couples efficiently into the slotline odd mode.

Two-branch TL model (core novelty)

Treat the CPW edges as two *slotlike branches* of equal characteristic impedance Z_s and electrical lengths $\ell_{L,R}$ that recombine at the slot port. Each branch is terminated by a diode impedance

$$Z_d^{\text{ON}} = R_s + j\omega L_s, \qquad Z_d^{\text{OFF}} = \frac{1}{j\omega C_j}, \qquad \Gamma = \frac{Z_d - Z_s}{Z_d + Z_s}.$$

Summing forward and round-trip contributions gives the exact branch factor

$$T(\ell, \Gamma) = \frac{e^{-j\beta_s \ell}}{1 - \Gamma\, e^{-j2\beta_s \ell}}, \qquad \beta_s = \frac{2\pi f}{c}\sqrt{\varepsilon_{\text{eff}}}. \tag{5.4}$$

Because the CPW odd mode imposes opposite polarities at the two edges, the slot port sees a *difference* of phasors :

$$S_{21} = T(\ell_L, \Gamma_L) - T(\ell_R, \Gamma_R). \tag{5.5}$$

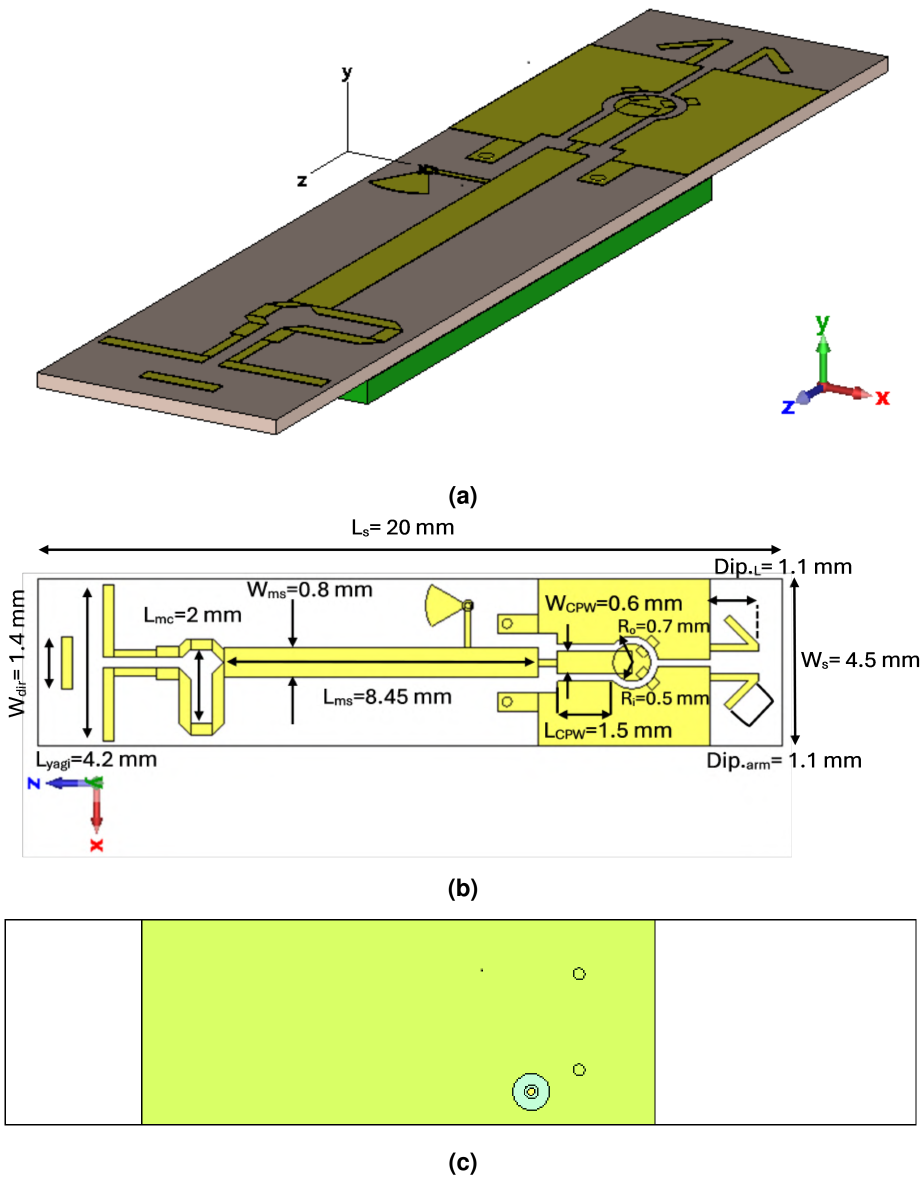

FIGURE 5.5 : Geometry of the proposed Meta-atom element. (a) Perspective view, (b) Top view, and (c) Bottom view.

Binary states :

$$\text{State A } (0°): \quad (\Gamma_L, \Gamma_R) = (\Gamma_{\text{ON}}, \Gamma_{\text{OFF}}), \tag{5.6}$$

$$\text{State B } (180°): \quad (\Gamma_L, \Gamma_R) = (\Gamma_{\text{OFF}}, \Gamma_{\text{ON}}). \tag{5.7}$$

If $\ell_L = \ell_R = \ell$,

$$S_{21}^B = -S_{21}^A \quad \Rightarrow \quad \Delta\phi = \angle\left(\frac{S_{21}^B}{S_{21}^A}\right) = 180°. \tag{5.8}$$

Eq. (5.8) is *exact* by symmetry : swapping the diode states flips the differential sign at the transition itself. This is the novelty—**phase inversion occurs *inside* the CPW–slot converter**, not in an external hybrid/stub.

Unequal lengths and tolerance

Let $\ell_R = \ell_L + \delta\ell$ with $|\beta_s \delta\ell| \ll 1$. Using

$$\frac{\partial T}{\partial \ell} = T\left[-j\beta_s + \frac{2j\beta_s\,\Gamma e^{-j2\beta_s\ell}}{1-\Gamma e^{-j2\beta_s\ell}}\right], \qquad \frac{\partial T}{\partial \Gamma} = \frac{e^{-j\beta_s\ell}\,e^{-j2\beta_s\ell}}{(1-\Gamma e^{-j2\beta_s\ell})^2},$$

the first-order state-difference phase error is

$$\delta\Delta\phi \approx 2\,\Im\left\{\frac{1}{F_A}\left[\frac{\partial T(\ell,\Gamma_{\mathrm{ON}})}{\partial \ell} - \frac{\partial T(\ell,\Gamma_{\mathrm{OFF}})}{\partial \ell}\right]\right\}\delta\ell, \qquad F_A = T(\ell,\Gamma_{\mathrm{ON}}) - T(\ell,\Gamma_{\mathrm{OFF}}). \tag{5.9}$$

Hence small $\delta\ell$ and strong diode contrast keep $\Delta\phi$ near $180°$ across band.

Junction S-matrix view (odd/even modal ports)

Model the junction as ports $\{L, R, S\}$. Transform to $\{D, C, S\}$ with $D = (L - R)/\sqrt{2}$ (odd), $C = (L + R)/\sqrt{2}$ (even). Geometric symmetry decouples C from S, leaving a coupled $\{D, S\}$ 2-port. The scattering from $D \to S$ is proportional to $T_L - T_R$, reproducing (5.5). Swapping diodes enforces $S_{SD} \mapsto -S_{SD} \Rightarrow 180°$.

Design rules

1. $\ell_L \approx \ell_R$ (symmetry).
2. $|\Gamma_{\mathrm{ON}}| \ll 1$, $|\Gamma_{\mathrm{OFF}}| \approx 1$ (contrast).
3. compact $\ell\lambda_g/4$ (broader band).
4. bias symmetry at RF-cold points.

This kind of structure gives a 1-Bit resolution with two states (0 and 180 degrees). This was achieved by incorporating two P-i-n diodes, redirecting the incoming wave from receiving part to the transmitting one, and by flipping the on/off states of the P-i-n diodes, the current will flip its direction at the slot-line end, hence the 0-to-180 degrees phase shift.

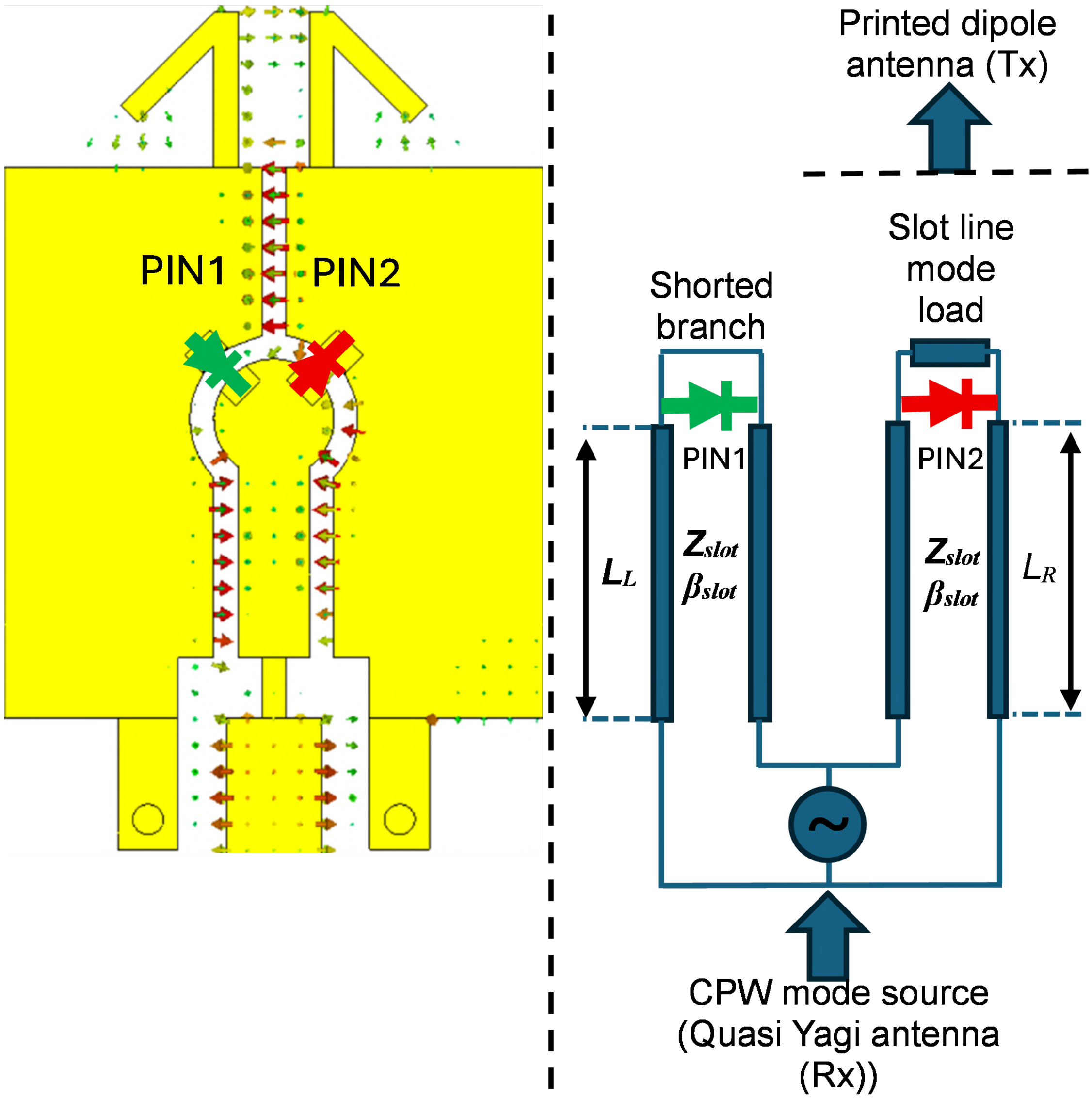

FIGURE 5.6 : TL-model, State A (Left ON/Right OFF).

5.3.2 Biasing Network and RF Choke Design

To enable dynamic phase reconfiguration within the proposed transmitarray (TA) unit cell, a carefully engineered DC biasing network is integrated to independently control the two PIN diodes (PIN_1 and PIN_2) embedded across the CPW-slotline transition. The design ensures stable forward and reverse biasing conditions while maintaining negligible perturbation to the RF performance across the Ka-band (26–32 GHz). The complete biasing structure and vertical interconnection scheme are illustrated in Fig. 5.8 and Fig. 5.9, respectively.

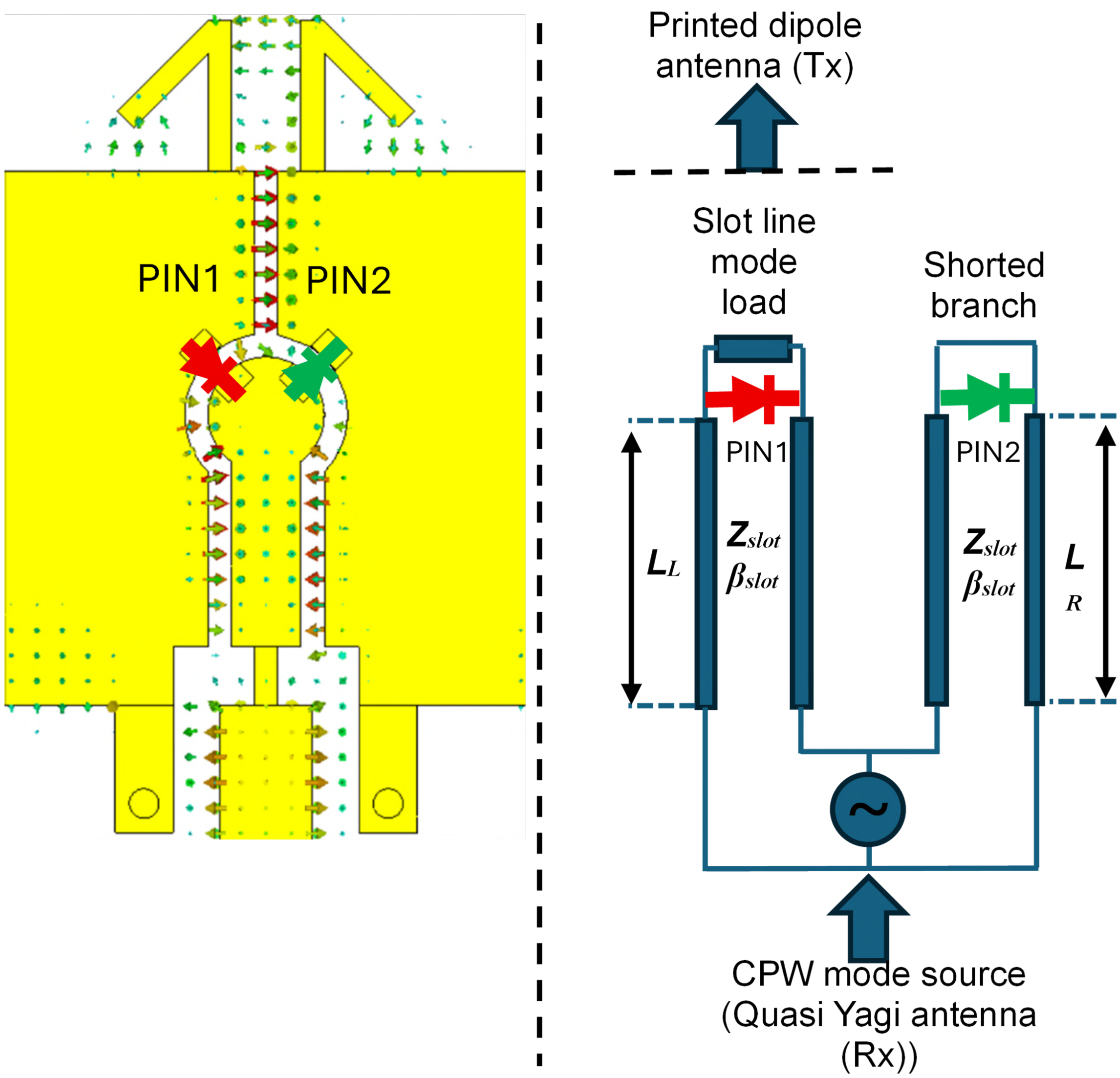

FIGURE 5.7 : TL-model, State B (Left OFF/Right ON).

5.3.2.1 Biasing Topology and Routing Strategy

The biasing network is realized on the lower FR-4 substrate layer, which serves as the DC routing and interface board. Thin microstrip bias lines (highlighted in green in Fig. 5.8) are used to distribute the control voltages to each unit cell, ensuring compact integration and modular scalability across the entire TA aperture. Each control line is connected to the active CPW layer through metallized vias, enabling vertical DC transitions between layers.

To prevent undesired coupling between the RF and DC paths, the biasing lines are carefully routed away from the high-field regions of the CPW-slotline junction. Furthermore, decoupling capacitors and isolation resistors can be incorporated near the bias feed points to stabilize the DC potential and suppress low-frequency oscillations. The modular layout allows each column of unit cells to be addressed independently, thus enabling beam steering by electronically controlling the ON/OFF states of the PIN diodes.

5.3.2.2 Radial Stub RF Choke Implementation

A critical component of the biasing design is the incorporation of a *radial stub RF choke* at the interface between the RF transition and the DC feed line, as shown in Fig. 5.8. The radial stub acts as a high-impedance termination at the operating frequency band, effectively isolating the RF signal from leaking into the DC bias network. The radial stub can be modeled as a short-circuited

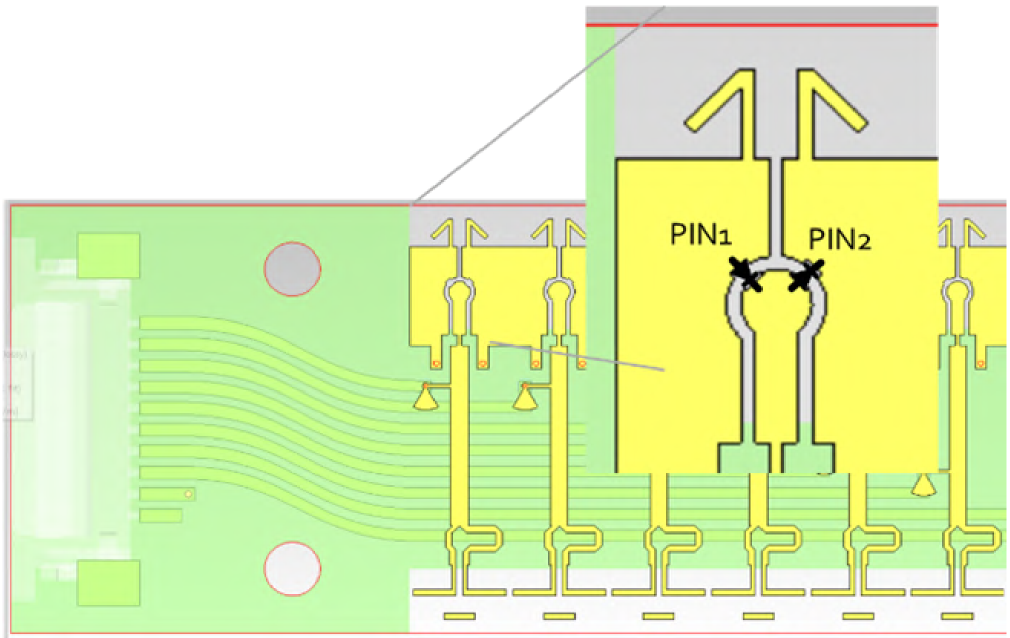

FIGURE 5.8 : Top-view layout of the proposed biasing network with zoomed-in view of the PIN-diode section and integrated radial stub RF choke (radius = 1.13 mm, angle = 60°).

transmission line with a flare angle θ and radius R, designed such that its input impedance presents an open circuit at the operating frequency :

$$Z_{\text{in}} = -jZ_0 \cot(\beta L_{\text{eff}}), \tag{5.10}$$

where Z_0 is the characteristic impedance, β is the propagation constant, and L_{eff} is the effective electrical length determined by the stub geometry. The design condition $\beta L_{\text{eff}} = \pi/2$ ensures that the stub input behaves as an open circuit ($Z_{\text{in}} \to \infty$) at the target frequency, thus presenting a strong RF choke to the bias line.

In the proposed design, the radial stub is optimized with a **radius of 1.13 mm** and a **flare angle of 60**°, yielding an effective electrical length close to $\lambda_g/4$ at 29 GHz (the center of the Ka-band). This geometry ensures broadband high impedance across 26–32 GHz while maintaining a compact footprint. The gradual impedance taper offered by the radial profile provides smoother transition characteristics and enhanced bandwidth compared to conventional $\lambda/4$ linear stubs.

Consequently, the DC bias path remains electromagnetically decoupled from the RF transition, guaranteeing minimal insertion loss and preserving the amplitude balance and phase difference of the two diode states (0°/180°).

5.3.2.3 Vertical Interconnection and Layered Assembly

As illustrated in Fig. 5.9, the multilayer stack-up comprises four primary layers :

1. The top CPW metallization layer hosting the active CPW-slotline transition and quasi-Yagi radiator.
2. An intermediate bonding layer for mechanical stability and alignment.
3. A middle bias layer fabricated on FR-4, dedicated to routing the DC control lines and housing the bias vias.
4. The bottom control interface layer containing the connector and driver interface (e.g., pin header for the control module).

Metallized vias (red and yellow traces in Fig. 5.9) establish the vertical connections between the active diodes and their respective bias sources. Each via is strategically placed to minimize parasitic inductance and to avoid disturbing the CPW ground symmetry. The radial stubs and DC vias are positioned symmetrically on both sides of the CPW-slotline junction to preserve field balance and maintain consistent phase performance in both diode states.

Full-wave electromagnetic simulations confirm that the inclusion of the radial stub choke introduces negligible degradation to the transmission amplitude, while preserving the desired $0°/180°$ phase states. Moreover, the choke provides over 25 dB isolation between the RF path and DC network across the entire 26–32 GHz band. This high isolation ensures that bias switching does not alter the effective impedance of the CPW transition, enabling accurate and repeatable reconfiguration.

5.3.3 Unit Cell Performance : Scattering parameters

Fig. 5.10 shows the full-wave simulation model in CST Microwave studio. It was designed and optimized in a periodic condition with two floquet ports. The periodic dimension of the simulation setup is 4.5 mm × 4.5 mm in the xoy plane. The polarization of the dipole element is in the xoz plane along the x-axis (TM polarized). The substrate of the unit cell is Rogers RO3006 (ϵ_r = 6.5, h = 0.254 mm). To leave enough space for the layout of the bias line which is placed under the ground of the Microstrip line, the length of the unit cell along the z-axis was 20 mm, corresponding to 1.73 λ_0 at 26 GHz.

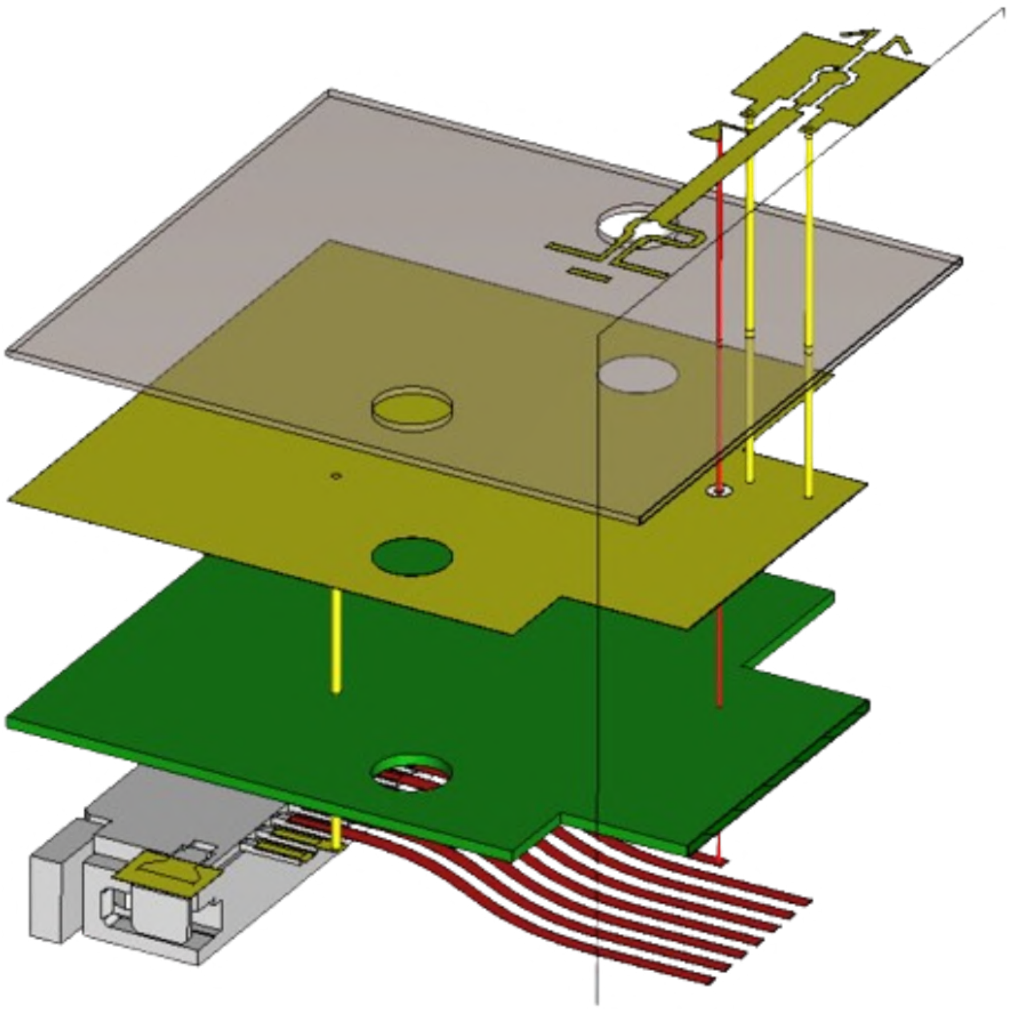

FIGURE 5.9 : Exploded view of the multilayer assembly showing the vertical interconnections and DC routing between layers.

The unit cell is designed to work in the band of interest ranging from 26 to 32 GHz, and the simulated results of the transmission magnitude and phase of the *final optimized unit cell* at two states, are illustrated in Fig. 5.10.

The full-wave optimization was carried out to ensure accurate integration of the characterized diode behavior with the CPW-to-slotline transition and the overall radiating structure.

The results demonstrate an excellent amplitude balance between the two operating states (*UC-0* and *UC-180*), with transmission magnitudes remaining above 0.8 across the entire 26–32 GHz band. More importantly, a consistent and broadband phase difference of approximately $\Delta\varphi = 180^\circ$ is observed, confirming that the proposed topology achieves true binary phase switching with minimal amplitude variation.

Unlike patch-based approaches that rely on mirrored reactive loading, the proposed unit cell operates through a hybrid-mode field reversal mechanism within the CPW-to-slotline transition. The quasi-printed Yagi antenna serves as the receiving element, converting the incident wave into

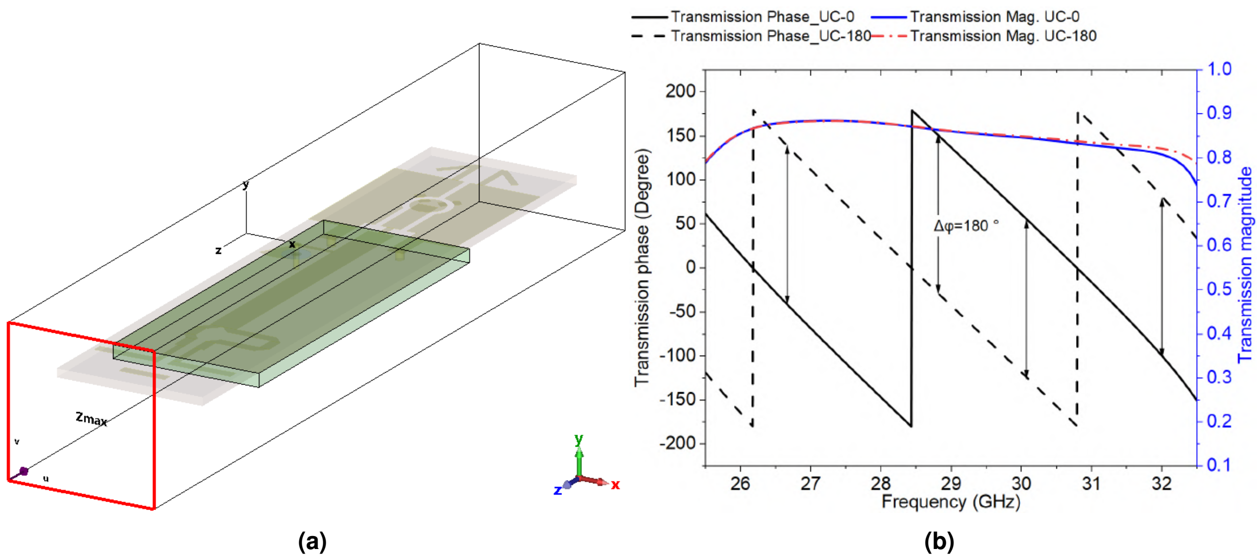

FIGURE 5.10 : (a) meta-atom simulation setup, and (b) its simulated transmission results.

a CPW mode that propagates towards the dual-diode transition. Depending on the diode biasing state, one of the two PIN diodes (PIN_1 or PIN_2) is forward-biased while the other remains reverse-biased.

This asymmetric biasing modifies the boundary conditions of the CPW-slotline junction and consequently excites complementary field configurations :

— In the **UC-0 state** (PIN_1 ON, PIN_2 OFF), the CPW mode couples predominantly to a slotline mode with a given polarity.

— In the **UC-180 state** (PIN_1 OFF, PIN_2 ON), the complementary bias configuration mirrors the electromagnetic field distribution across the slot, effectively reversing the transverse current flow and flipping the sign of the radiated/transmitted electric field.

Because this transformation is governed by the structural symmetry of the transition rather than by the absolute impedance contrast of the diodes, the mechanism is inherently robust to limited isolation. Even though the TRL-extracted parameters indicate residual coupling in both bias states, the geometric field inversion enforces a deterministic $180°$ phase reversal while preserving nearly identical amplitude levels.

The combination of broadband CPW-slotline mode conversion and amplitude-equalized reactive states ensures that the unit cell operates efficiently across the full Ka-band. The quasi-Yagi receiver and printed dipole transmitter provide smooth impedance transitions at both ends, while the integrated radial stub RF choke (see Section 5.3.2) effectively decouples the DC bias paths from the RF fields. As a result, the final structure achieves :

1. Broadband **phase switching** with $\Delta\varphi \approx 180°$ from 26–32 GHz,

2. **Low insertion loss** ($|S_{21}| > -1$ dB), and

3. **Stable amplitude response** suitable for beamforming applications.

This confirms that the proposed dual-diode CPW-slotline transition enables a compact, wideband, and high-fidelity binary phase-shifting element compatible with modular transmitarray integration.

It is important to highlight that, despite the limited isolation and non-negligible insertion loss exhibited by the characterized PIN diodes under both forward and reverse bias conditions, the proposed unit cell maintains excellent transmission characteristics and a robust 180° phase shift across the entire Ka-band. This apparently counterintuitive behavior can be explained by the underlying electromagnetic mechanism governing the CPW-to-slotline transition, which decouples the phase-shifting function from the absolute isolation level of the diodes.

In conventional switching topologies, strong isolation between ON and OFF states is required to ensure distinct transmission paths and amplitude contrast. In contrast, the present design leverages a **reactive-symmetry-based phase inversion**, in which the phase shift is dictated primarily by the *polarity of the excited mode* rather than by the magnitude of the diode impedance. Specifically :

- In the **forward-biased state**, the conducting diode introduces a slightly inductive perturbation to the CPW-slotline junction, guiding the energy through a specific field orientation.
- In the **reverse-biased state**, the diode behaves as a capacitive discontinuity, redirecting the field distribution into a complementary configuration that is spatially mirrored with respect to the transition axis.

Because these two states correspond to *conjugate reactive loads* applied at symmetric locations, their electromagnetic fields are also conjugate. The resulting slotline modes therefore possess identical amplitudes but opposite phases, yielding a near-ideal $\Delta\varphi = 180^\circ$ differential response. The key outcome is that **the phase transition is geometrically enforced by the mode symmetry**, rather than being reliant on the diodes' impedance contrast or isolation. This field-mirroring mechanism has also been observed in other reconfigurable unit cells based on inductive/capacitive reactive loading at symmetric positions [110–113].

Moreover, the optimized CPW-slotline impedance environment equalizes the insertion loss under both bias conditions. Even though the intrinsic R_{ON} and C_j of the diodes cause moderate losses in isolation measurements, these effects are absorbed and balanced within the broadband matching network and the quasi-Yagi/dipole coupling scheme. As a result, the final unit cell sustains high transmission ($|S_{21}| > 0.8$) and stable amplitude across the band, while the reactive inversion ensures a consistent binary phase shift.

The equivalent RLC parameters used in the transmission-line model were obtained via a (TRL) calibration process, enabling accurate bias-dependent de-embedding of the diode parasiticsThis characterization confirms that even with finite impedance contrast, the broadband 180° phase switching can be achieved through the proposed symmetric CPW-slotline transition and dual-diode configuration.

5.4 Waveguide-Based Characterization of the Proposed Unit Cell

5.4.1 Measurement Setup

To experimentally validate the electromagnetic behavior of the proposed reconfigurable transmitarray (RTA) unit cell, a dedicated WR-34 waveguide simulator (see Figure 5.11) was designed and fabricated. The measurement fixture reproduces the boundary conditions of a periodically excited unit cell under normal incidence, while maintaining the same dominant-mode propagation as in free-space operation. Unlike conventional reflectarray or multilayer patch configurations, the present architecture employs a **coplanar-waveguide (CPW) to slotline transition** implemented on a dual-substrate stack. This topology required the development of a customized dual-layer metallic enclosure capable of supporting the hybrid CPW–slotline excitation within the waveguide environment.

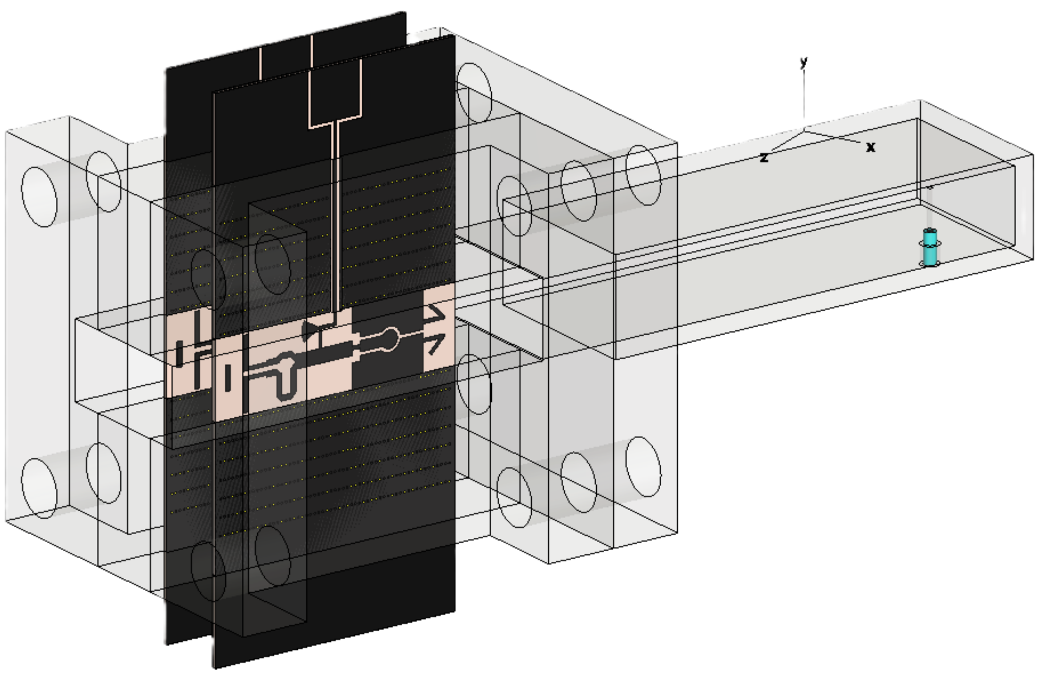

FIGURE 5.11 : Perspective view of the designed 4.5 x 8.63 mm waveguide simulator.

The resulting cavity has internal dimensions of approximately $8.636\,\mathrm{mm} \times 4.5\,\mathrm{mm}$, corresponding to the equivalent of two periodic elements along the E-plane of the waveguide. Metallized via fences were incorporated along both lateral walls to suppress parasitic substrate modes and ensure field confinement. Small openings were also introduced on the top metallic wall to accommodate the dc-bias feedthroughs connected to the two integrated **MACOM MADP-000907-14020P PIN diodes** as seen in Figure 5.12. The fixture was interfaced through precision coax-to-waveguide transitions at both ports and calibrated using a full **TRL (Thru–Reflect–Line)** standard to remove connector and transition losses.

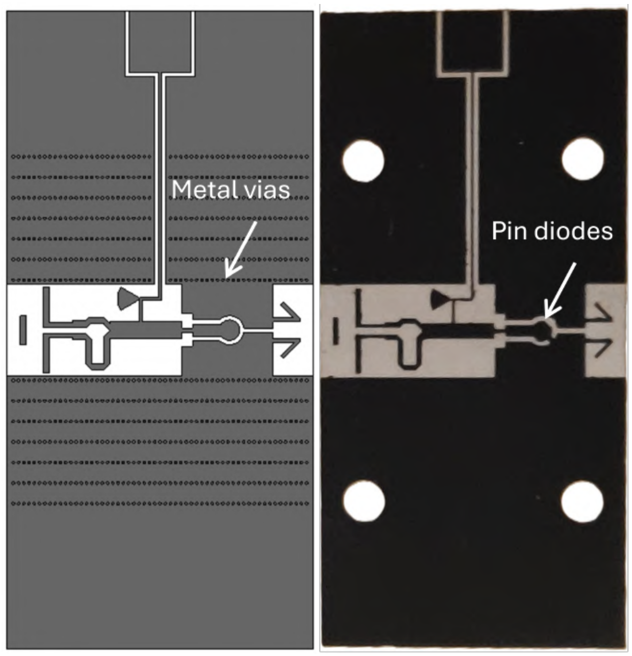

(a) (b)

FIGURE 5.12 : Proposed waveguide-based transmitarray unit cell. (a) 3D model. (b) Fabricated prototype.

Fig. 5.13 illustrates the fabricated cavity and the mounted unit cell under test, showing the bias feedthroughs and the modular integration within the WR-34 flange.

5.4.2 Simulated and Measured S-Parameter Results

The performance of the element was evaluated for both diode biasing configurations corresponding to the $0°$ and $180°$ phase states. Fig. 5.14 and Fig. 5.15 present the comparison between simulated and measured reflection and transmission coefficients across the 24–34 GHz frequency range.

For the reflection response, the simulated $|S_{11}|$ results indicate that the unit cell maintains excellent impedance matching throughout the Ka-band. In the **first state** $(0°)$, $|S_{11}|$ remains below $-10\,\mathrm{dB}$ from $24.24\,\mathrm{GHz}$ to $32.56\,\mathrm{GHz}$, corresponding to a continuous matched bandwidth of approximately $8.32\,\mathrm{GHz}$. The best simulated return loss reaches $-26.3\,\mathrm{dB}$ at $25.46\,\mathrm{GHz}$, and the average level remains better than $-18\,\mathrm{dB}$ between 26 and $30\,\mathrm{GHz}$, gradually relaxing to around $-15.6\,\mathrm{dB}$ beyond $30\,\mathrm{GHz}$. The **second state** $(180°)$ exhibits nearly identical behavior, with the $-10\,\mathrm{dB}$ bandwidth extending from $24.28\,\mathrm{GHz}$ to $32.53\,\mathrm{GHz}$ (about $8.25\,\mathrm{GHz}$) and a minimum reflection of $-26.7\,\mathrm{dB}$ at $25.56\,\mathrm{GHz}$.

The measured reflection curves confirm the simulation results with minor deviations. For the **first state**, $|S_{11}|$ remains below $-10\,\mathrm{dB}$ between $24.38\,\mathrm{GHz}$ and $32.19\,\mathrm{GHz}$, yielding a $7.8\,\mathrm{GHz}$ effective bandwidth. The minimum reflection is $-23.6\,\mathrm{dB}$ at $25.37\,\mathrm{GHz}$, with an average of $-13.8\,\mathrm{dB}$

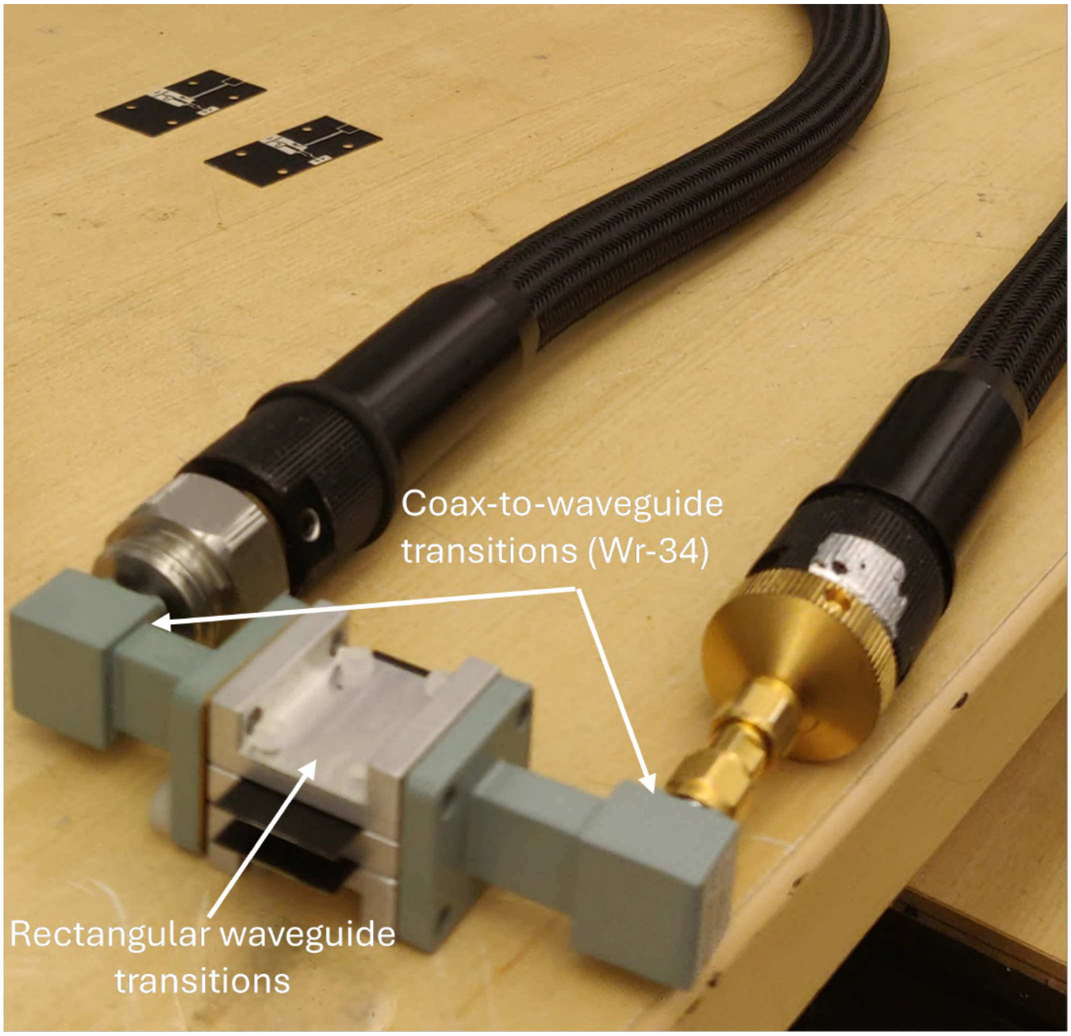

FIGURE 5.13 : Fabricated WR-34 waveguide simulator and integrated reconfigurable unit cell.

within the 26–$30\,\mathrm{GHz}$ region and $-13.2\,\mathrm{dB}$ from 30–$34\,\mathrm{GHz}$. The **second state** shows a similar trend, with a continuous $-10\,\mathrm{dB}$ bandwidth from $24.43\,\mathrm{GHz}$ to $32.19\,\mathrm{GHz}$, a minimum reflection of $-24.3\,\mathrm{dB}$ at $25.62\,\mathrm{GHz}$, and average levels of $-14.4\,\mathrm{dB}$ and $-12.9\,\mathrm{dB}$ in the 26–30 GHz and 30–34 GHz ranges, respectively. The measured curves thus confirm a robust impedance match with only a slight upward shift of approximately $70\,\mathrm{MHz}$ and an expected 1–2 dB degradation due to fabrication tolerances and connector repeatability typical of millimeter-wave measurement environments.

The transmission response further validates the correct operation of the CPW-to-slotline transition and the overall unit-cell topology. The simulated transmission magnitude exhibits an insertion loss ranging from $1.4\,\mathrm{dB}$ to $1.6\,\mathrm{dB}$ across 26–$30\,\mathrm{GHz}$ for both diode configurations, with nearly identical amplitude levels and a constant $180°$ phase difference between the two states. The measured $|S_{21}|$ response follows this trend, showing slightly higher losses (about $1.6\,\mathrm{dB}$ to $1.9\,\mathrm{dB}$) due to additional conductor losses and the finite precision of the waveguide fixture alignment.

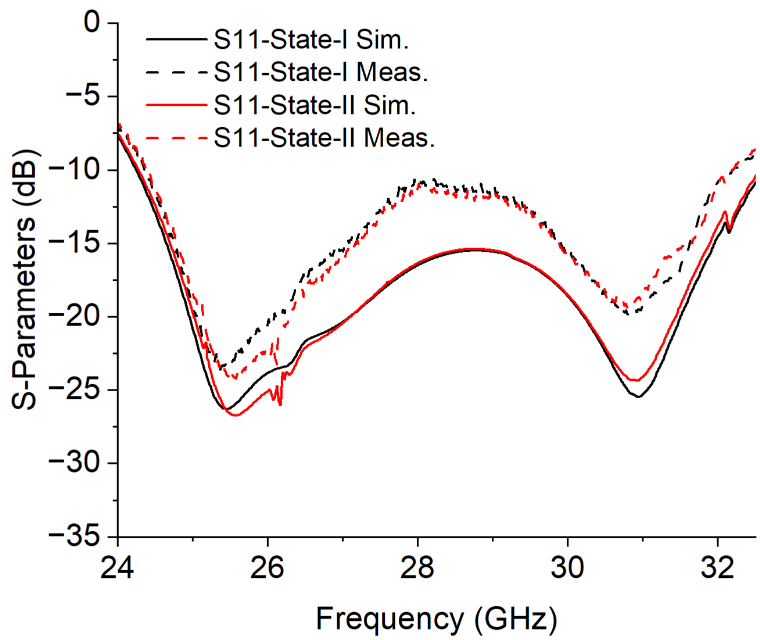

FIGURE 5.14 : Simulated and measured reflection coefficient $|S_{11}|$ for the two diode biasing states.

The measured phase of the transmission coefficient also agrees well with the simulated behavior. The phase difference between the two biasing states remains essentially constant at $\Delta\phi \approx 179° \pm 3°$ across the 26–$30\,\mathrm{GHz}$ range, validating the desired binary $0°/180°$ phase-switching functionality. Beyond $30\,\mathrm{GHz}$, a slight divergence appears (within approximately $\pm 8°$), coinciding with the minor degradation of $|S_{11}|$ and attributable to the emergence of weak parasitic slotline resonances.

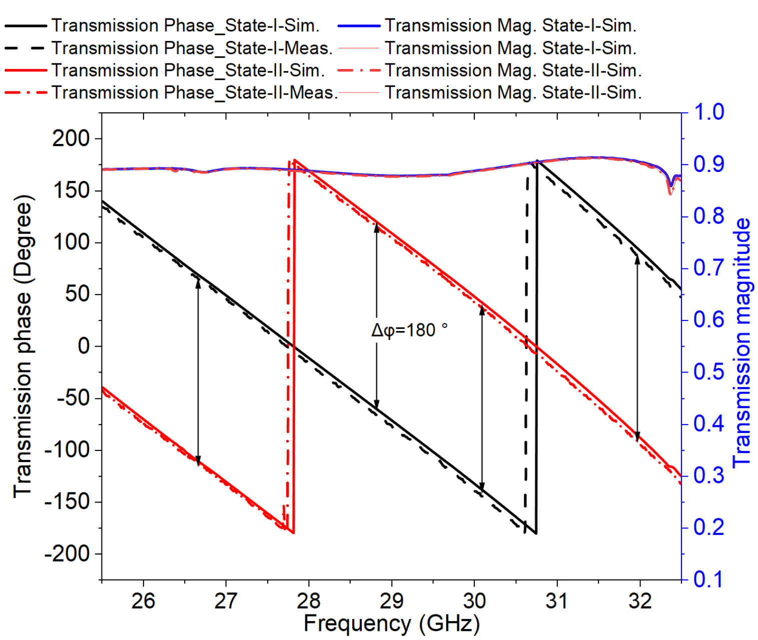

FIGURE 5.15 : Simulated and measured transmission coefficient S_{21} magnitude and phase for both diode states.

5.4.3 Performance Discussion

The comprehensive agreement between simulation and measurement demonstrates the robustness of the proposed **dual-PIN-diode CPW-to-slotline unit-cell** architecture. The element achieves a broad impedance-matched bandwidth of approximately $8\,\mathrm{GHz}$, extending well beyond the intended 26–$30\,\mathrm{GHz}$ operational window, while preserving low transmission loss and a stable binary phase control. The measured characteristics confirm efficient operation over the entire Ka-band, with negligible amplitude imbalance and a nearly perfect 180° differential phase response.

These results validate the proposed topology as a reliable building block for high-gain, beam-steerable transmitarray antennas. The combination of broadband impedance matching, low insertion loss, and compact geometry ($4.5\,\mathrm{mm} \times 4.5\,\mathrm{mm}$) ensures that the unit cell can be seamlessly integrated within larger modular panels. The measured results conclusively verify that the CPW-to-slotline transition effectively translates the simulated electromagnetic behavior into experimentally stable transmission, offering the required phase agility and transmission efficiency for next-generation Ka-band reconfigurable transmitarray applications.

5.5 Proposed Transmitarray Design

The proposed transmitarray (TA) is a modular reconfigurable aperture composed of fourteen identical panels, each incorporating sixteen 1-bit unit cells based on the CPW-to-slotline transition architecture presented in Section 5.4. Each cell integrates two MACOM MADP-000907-14020P PIN diodes that provide binary phase control (0°/180°) through the internal field-reversal mechanism of the transition itself. This modularity facilitates array scalability, simplifies bias routing, and enables precise fault isolation during prototyping and measurement.

Each panel is fabricated on a dual-layer stack of Rogers RO3006 ($h = 0.254$ mm) and FR-4 ($h = 0.4$ mm) and measures $108\,\mathrm{mm}{\times}20\,\mathrm{mm}$. The element periodicity is $4.5\,\mathrm{mm}$ in both x and y directions, corresponding to $p/\lambda_0 \approx 0.42$ at 30 GHz—adequately below the visible-mode threshold for $\pm 30^\circ$ scanning. Each panel connects to the control board through two 10-pin connectors that distribute bias voltages to 32 diodes (two per unit cell) in two groups of eight cells.

5.5.1 Array Topology and Illumination Geometry

The complete 16×14 aperture is assembled from fourteen such panels, forming a total area of $108\,\mathrm{mm}{\times}63\,\mathrm{mm}$. As illustrated in Fig. 5.17, the transmitarray is illuminated by a TM-polarized Vivaldi feed placed at a focal distance of $F = 52\,\mathrm{mm}$, corresponding to an F/D ratio of approximately 0.8. This configuration offers a balanced compromise between spillover and phase curvature while

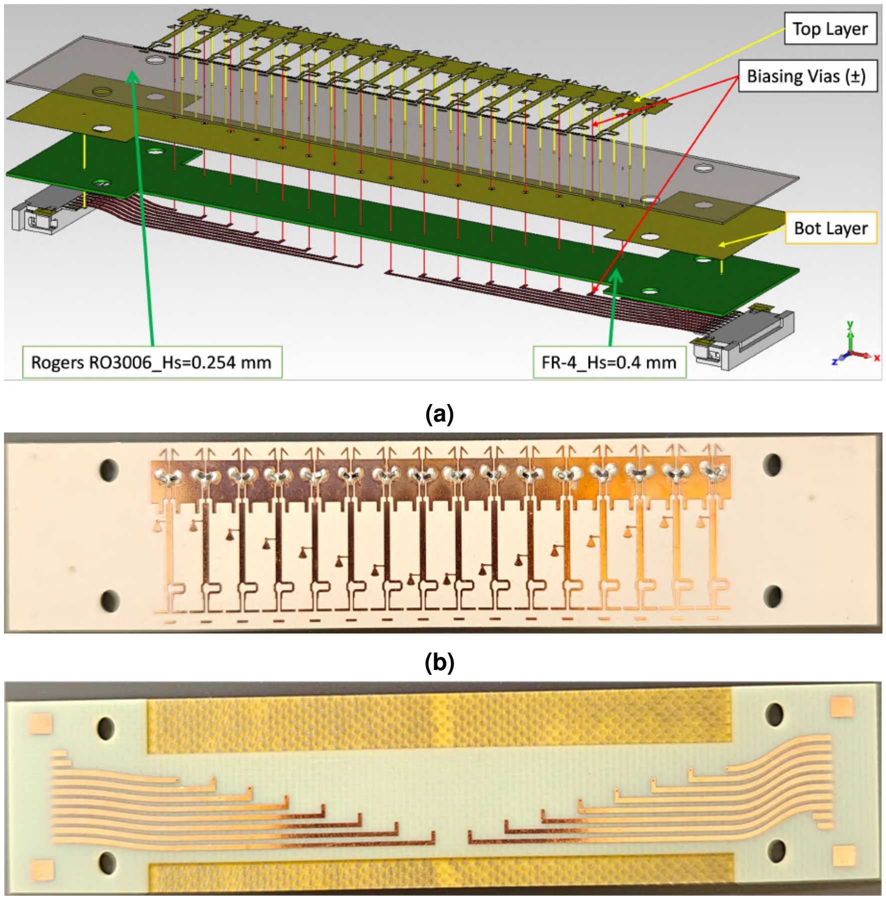

(a)

(b)

(c)

FIGURE 5.16 : Geometry of the proposed TA panel. (a) Perspective view. Fabricated panel : (b) Top layer, and (c) Bottom layer.

maintaining low blockage. The feed's polarization matches the quasi-Yagi receiving element within each cell, maximizing coupling efficiency and minimizing cross-polarization across the aperture.

5.5.2 Effect of the Biasing Network on the Transmitarray Panel

To investigate the influence of the integrated dc-biasing network on the electromagnetic performance of the proposed transmitarray (TA), a full-wave simulation was carried out on a complete panel comprising sixteen reconfigurable unit cells arranged in a 16×1 configuration. Each element integrates two PIN diodes that are individually controlled through a distributed biasing network implemented on the upper FR-4 control layer, as illustrated in Fig. 5.18. The dc traces were routed orthogonally to the radiating dipoles and connected through high-impedance microstrip feedthroughs to minimize their interaction with the RF current paths. In addition, the routing geometry was optimized to avoid the formation of resonant stubs or unwanted capacitive coupling between adjacent lines.

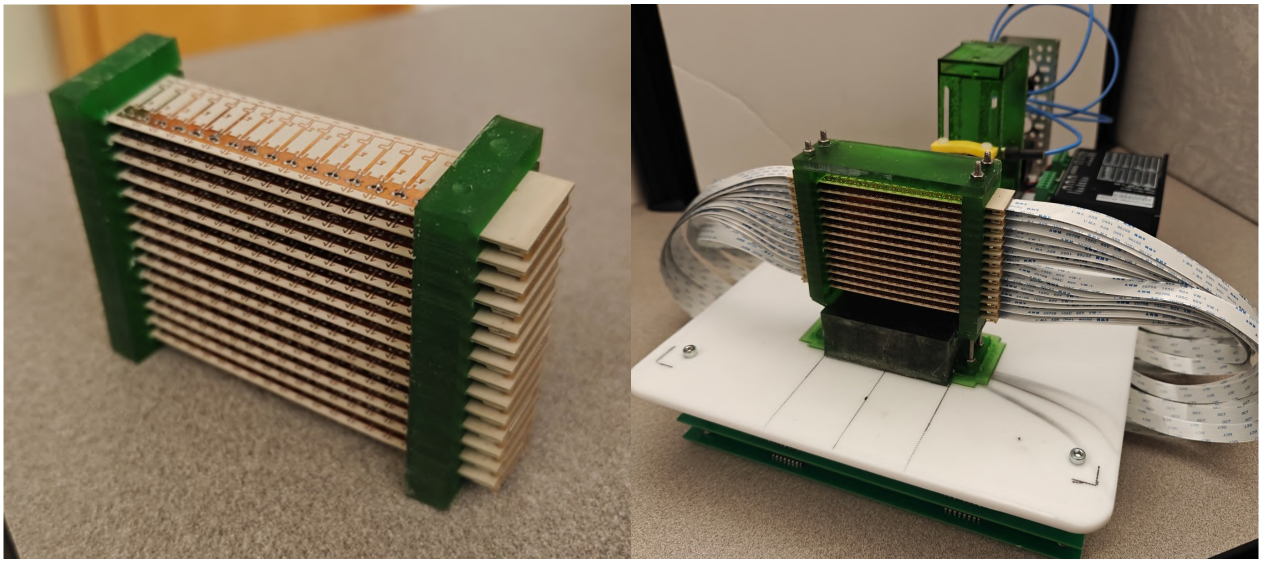

(a) **(b)**

FIGURE 5.17 : The proposed full transmitarray. (a) 14 panels assembly, and (b) Fully assembled TA with feeding element.

The purpose of this analysis was to verify that the introduction of the bias network does not perturb the transmission magnitude or phase of the array elements compared to the standalone unit cell. Eight representative unit cells (UC1–UC8) distributed along the panel width were simulated under identical boundary conditions, with the complete bias line configuration activated. The simulated transmission magnitude and phase of these selected cells are shown in Figs. 5.19 and 5.20.

Across the Ka-band (24–34 GHz), all the analyzed elements exhibit very similar transmission characteristics. The amplitude response remains practically invariant over the operational band of 26–30 GHz, with deviations between the edge and central cells remaining below $\pm$0.15 dB. The average insertion loss across the main operating band lies between 1.5 and 1.8 dB, which is in close agreement with the isolated unit-cell response. This result confirms that the distributed dc-bias lines do not introduce any significant additional ohmic or dielectric losses.

The phase distribution across the eight analyzed unit cells also demonstrates excellent uniformity. The maximum phase deviation between adjacent elements does not exceed $\pm 4^{\circ}$, confirming that the parasitic coupling between the bias traces and the CPW–slotline transition is effectively suppressed. The slight frequency-dependent phase drift that appears beyond 31 GHz originates mainly from the finite boundary truncation of the simulation model rather than the biasing network itself. The strong correlation of the magnitude and phase responses among the various cells therefore validates that the adopted bias-line topology provides reliable dc control while preserving the electromagnetic transparency of the array surface.

A comparison of the transmission characteristics across all cells further indicates that the dc routing strategy—consisting of narrow (< 0.2 mm) FR-4 microstrip traces placed orthogonally to the polarization of the radiating field—prevents any perturbation to the effective impedance or modal propagation. The bias vias were positioned within low-field regions of the CPW–slotline junction, ensuring that no parasitic loading occurs in the active transmission path. Consequently, the proposed bias integration method guarantees that all sixteen unit cells of the panel maintain uniform transmission amplitude and a consistent binary phase response.

These results conclusively demonstrate that the inclusion of the bias network has a negligible effect on both transmission magnitude and phase, thereby confirming the electromagnetic transparency and reliability of the integrated control system. The optimized layout successfully enables large-aperture reconfigurable panels without compromising the array's transmission efficiency or phase uniformity.

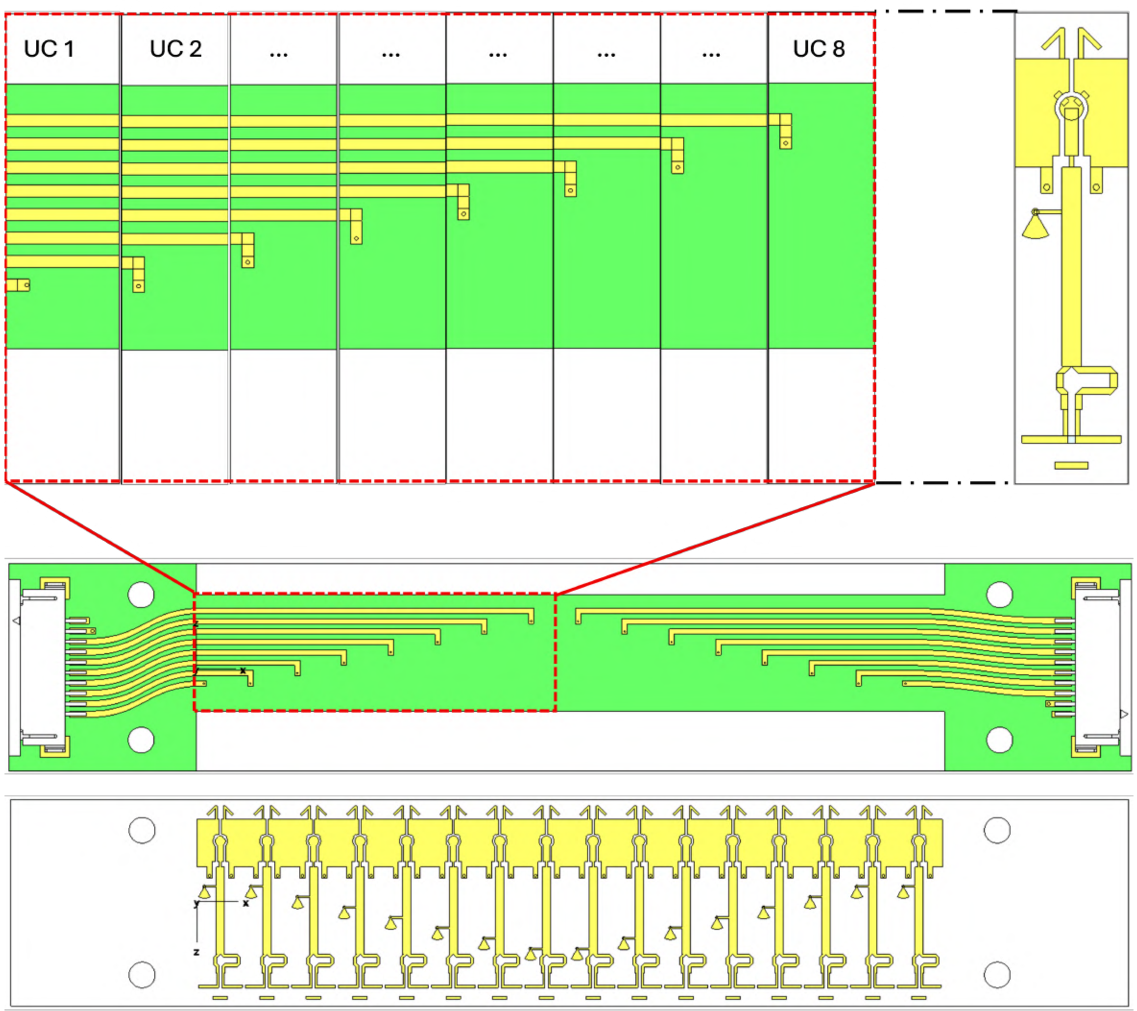

FIGURE 5.18 : Layout of the 16-cell transmitarray panel showing the dc-bias network distribution on the FR-4 control layer.

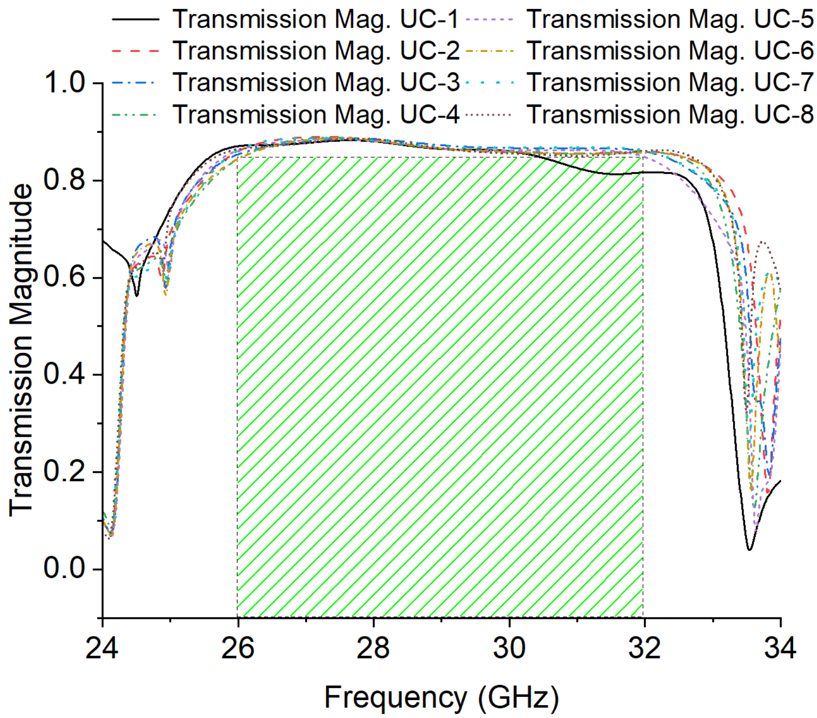

FIGURE 5.19 : Simulated transmission magnitude $|S_{21}|$ for representative unit cells (UC1–UC8) across 24–34 GHz, confirming the negligible effect of the bias lines on transmission amplitude.

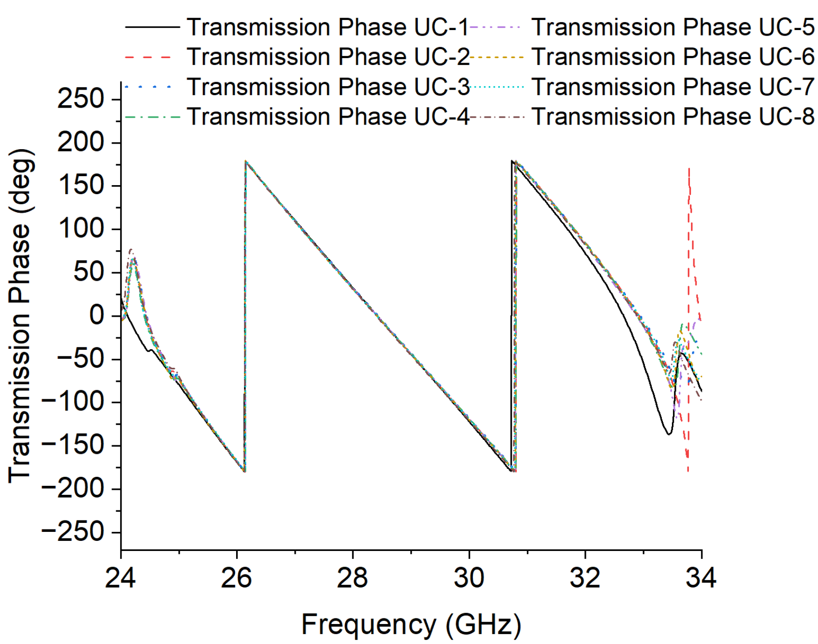

FIGURE 5.20 : Simulated transmission phase of representative unit cells (UC1–UC8) showing excellent phase uniformity across the Ka-band.

5.5.3 Phase Distribution and Quantization Efficiency

The desired transmission phase distribution for the (m,n)-th element follows the geometric-optics compensation law :

$$\phi_{mn}^{\text{(ideal)}} = k_0 \left(|\mathbf{r}_{mn} - \mathbf{r}_F| + \mathbf{r}_{mn} \cdot \hat{\mathbf{s}} \right), \tag{5.11}$$

where $k_0 = 2\pi/\lambda_0$ is the free-space wave-number, $\mathbf{r}_{mn}$ is the element position, $\mathbf{r}_F$ denotes the feed phase center, and $\hat{\mathrm{s}}(\theta_0, \phi_0)$ is the desired beam direction. Since each unit cell supports only two transmission phases (0° and 180°), the phase distribution is quantized as

$$\phi_{mn}^{\text{(applied)}} = \begin{cases} 0^\circ, & \text{if } \phi_{mn}^{\text{(ideal)}} \bmod 2\pi < \pi, \\ 180^\circ, & \text{otherwise.} \end{cases} \tag{5.12}$$

The theoretical phase quantization efficiency for a 1-bit system is given by

$$\eta_{\text{q}} \approx \left(\frac{2}{\pi}\right)^2 \approx 0.405, \tag{5.13}$$

which defines the upper limit for directivity degradation due to binary phase discretization. The experimentally measured peak gains (18.5–18.9 dBi at 28 GHz) are consistent with this theoretical bound when insertion loss and illumination taper are included.

5.5.4 Aperture Efficiency and Performance Budget

The overall aperture efficiency η_{ap} of the transmitarray can be expressed as :

$$\eta_{\text{ap}} = \eta_{\text{q}} \times \eta_{\text{IL}} \times \eta_{\text{m}} \times \eta_{\text{sp}} \times \eta_{\text{tap}} \times \eta_{\text{misc}}, \tag{5.14}$$

where the factors correspond respectively to phase quantization, transmission loss, impedance matching, spillover, amplitude taper, and residual losses. Table 5.1 summarizes the estimated contributions at 28 GHz.

TABLEAU 5.1 : Estimated Aperture Efficiency Breakdown at 28 GHz

Parameter	Symbol	Estimated Value
Phase Quantization (1-bit)	η_{q}	0.405
Transmission (Insertion Loss ≈ 1.7 dB)	η_{IL}	0.67
Impedance Matching ($\lvert S_{11}\rvert < -10$ dB)	η_{m}	0.95
Spillover Efficiency ($F/D = 0.8$)	η_{sp}	0.90
Amplitude Taper Efficiency	η_{tap}	0.92
Polarization & Miscellaneous	η_{misc}	0.97
Total Aperture Efficiency	η_{ap}	**0.40**

The calculated total efficiency ($\eta_{\text{ap}} \approx 0.40$) matches the experimentally achieved broadside gain of 18.9 dBi, validating that the measured performance is primarily limited by the inherent 1-bit quantization and dielectric losses, rather than by the bias network or diode parasitics.

5.5.5 Measurement Results and Discussion

The radiation characteristics of the proposed transmitarray were evaluated in an anechoic chamber using the setup shown in Fig. 5.21. The feed antenna was aligned along the array's optical axis, and the structure was mounted on a precision rotational stage to measure the far-field patterns for several beam-steering configurations. The measurements were conducted over the 26–32 GHz band using a calibrated VNA network analyzer.

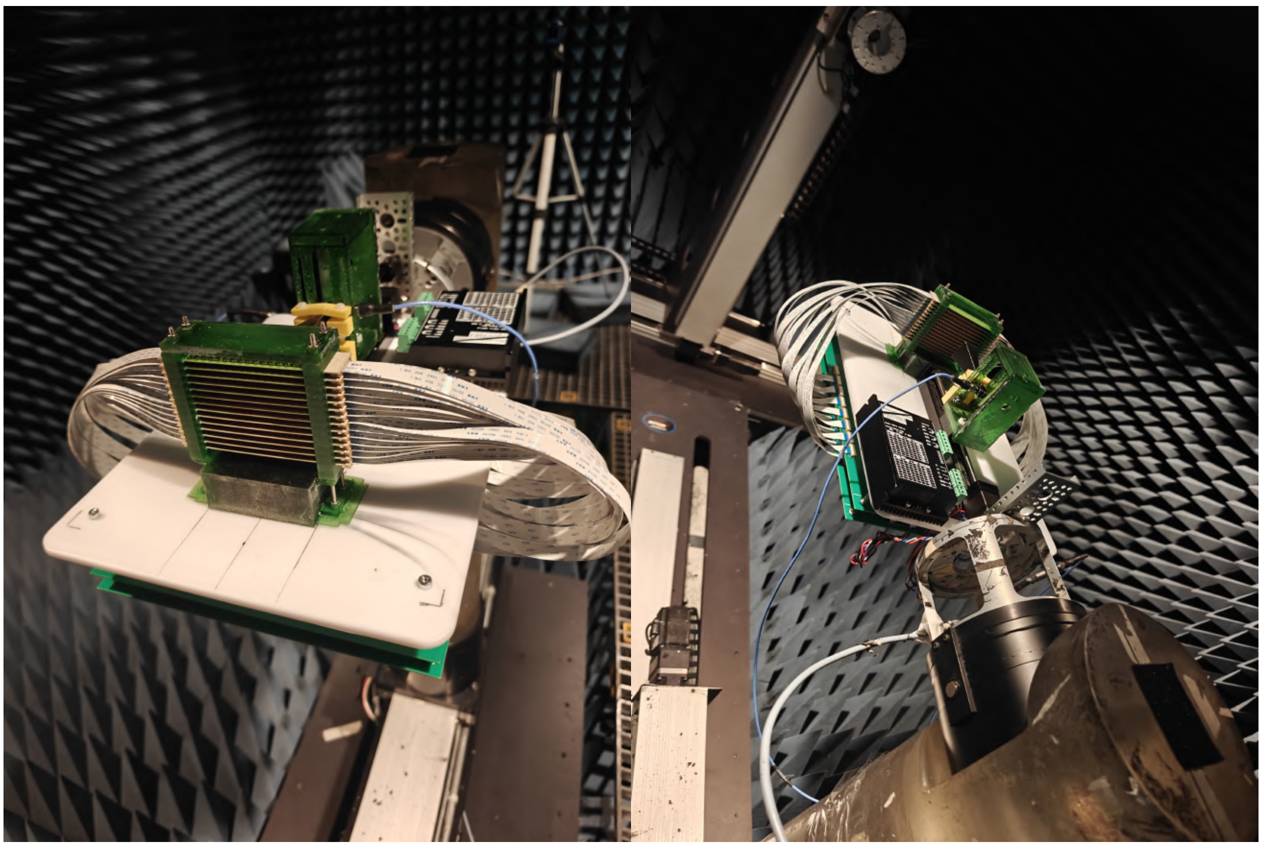

(a) (b)

FIGURE 5.21 : Radiation pattern measurement setup in the anechoic chamber.

Figure 5.22 compares the simulated and measured radiation patterns for beam-steering angles of 0° and 30° at different operating frequencies (26, 28, and 30 GHz). Excellent agreement is observed between simulations and measurements, confirming the accuracy of the phase synthesis and the negligible influence of the bias lines on the radiating performance.

At 28 GHz, the measured broadside peak gain reaches 18.87 dBi (see Fig. 5.23), in excellent agreement with the simulated 18.54 dBi value. Across the 26–32 GHz band, the side-lobe levels (SLL) remain below -11 dB, with a minimum value of -14.7 dB at 29 GHz.

For the 30° beam-steered case, the measured gain is approximately 18.0 dBi at 29 GHz, with a side-lobe degradation of about 3.3 dB, consistent with the expected quantization loss of binary

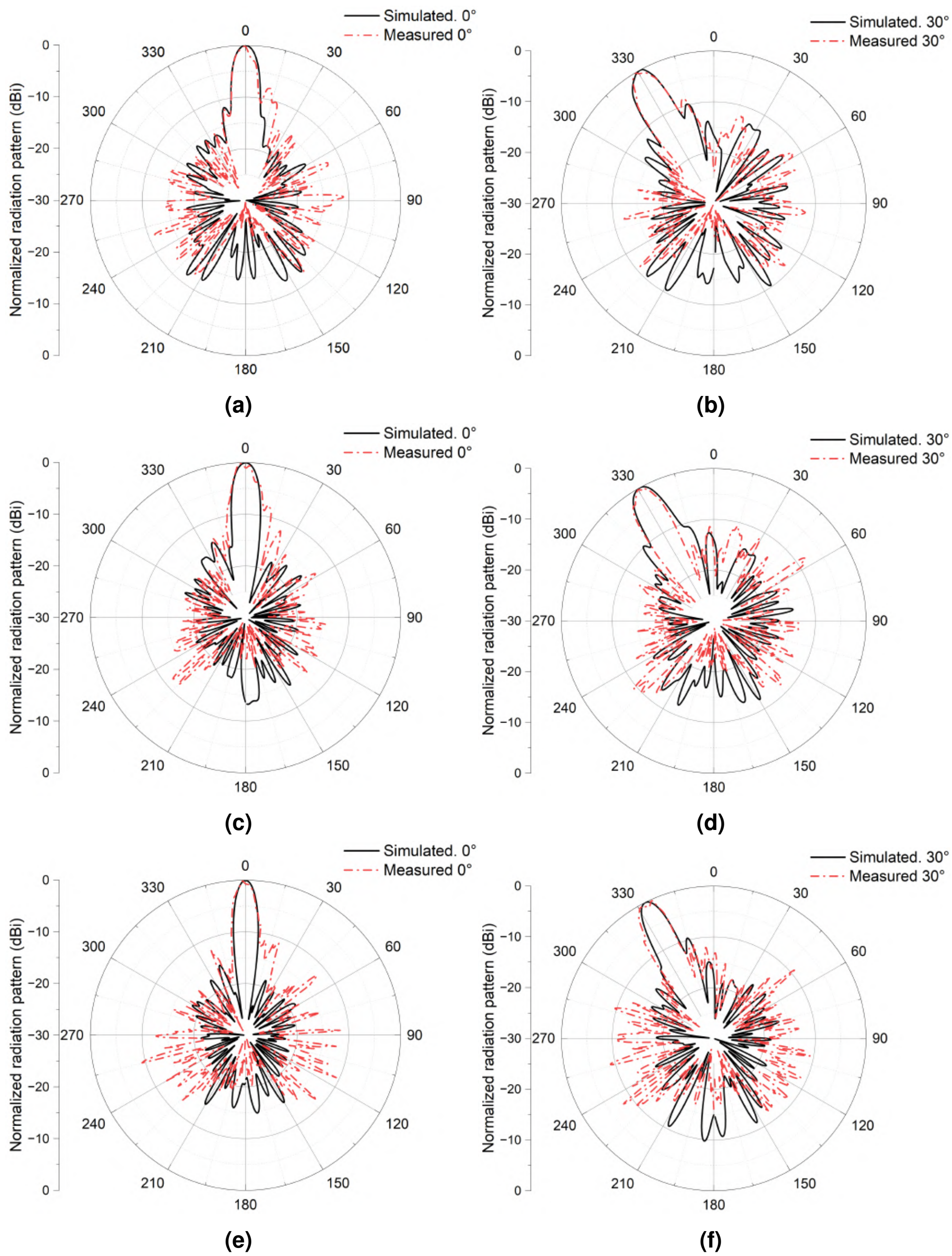

FIGURE 5.22 : Beam steering performance at two different angles of 0, and 30°, operating at (a ,b) 26, (c, d) 28 and (e, f) 30 GHz.

phase control. The small discrepancies between simulation and measurement (1–1.5 dB) arise mainly from fabrication tolerances and diode soldering variations across the large aperture.

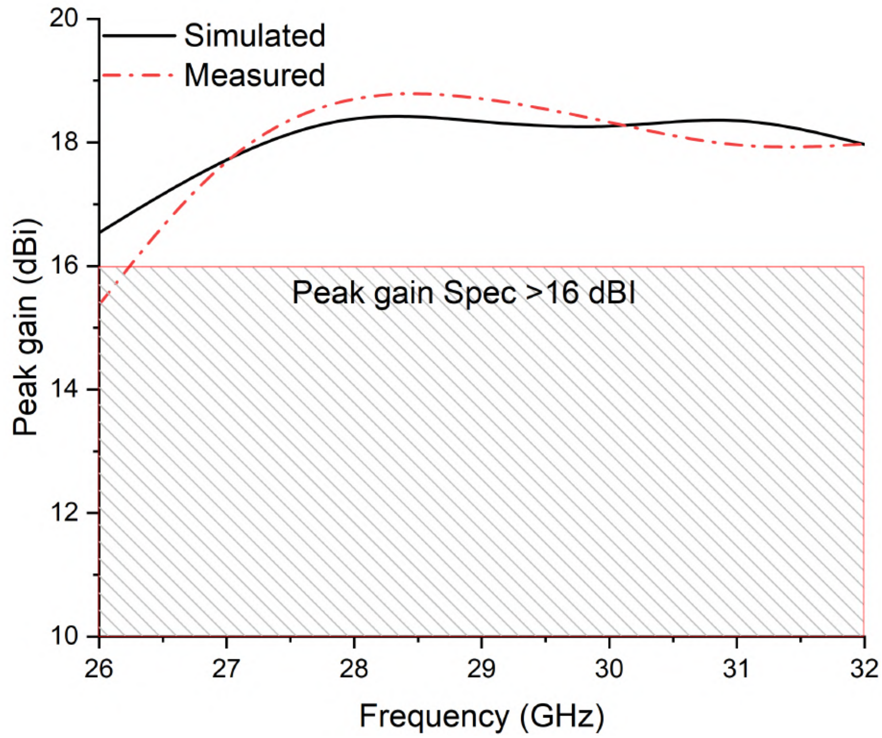

FIGURE 5.23 : Simulated and measured peak gain over the band of interest.

To further demonstrate the versatility of the system, a dual-beam configuration was tested by applying mirrored phase distributions along the aperture, as illustrated in Fig. 5.24. Two identical beams were generated, tilted at $\pm 20°$ from broadside, confirming the feasibility of multi-beam generation using the same 1-bit control architecture.

TABLEAU 5.2 : Performance Summary of the Proposed Reconfigurable Transmitarray at 28 GHz

Parameter	Measured Value	Notes
Operating Bandwidth	26–32 GHz	Ka-band
Phase States	0° / 180°	1-bit reconfiguration
Peak Gain (Broadside)	18.9 dBi	@ 28 GHz
Beam-Steering Range	$\pm 30°$	stable across band
Sidelobe Level (SLL)	< -11 dB	-14.7 dB @ 29 GHz
Insertion Loss per Cell	≈ 1.7 dB	simulated and measured
Aperture Efficiency	40%	including quantization loss
Dual-Beam Capability	Verified ($\pm 20°$)	mirrored phase law

Overall, the experimental results confirm that the proposed reconfigurable transmitarray exhibits excellent beam-steering accuracy, stable gain performance across the Ka-band, and robust dual-beam functionality. The combination of compact geometry, low insertion loss, and transpa-

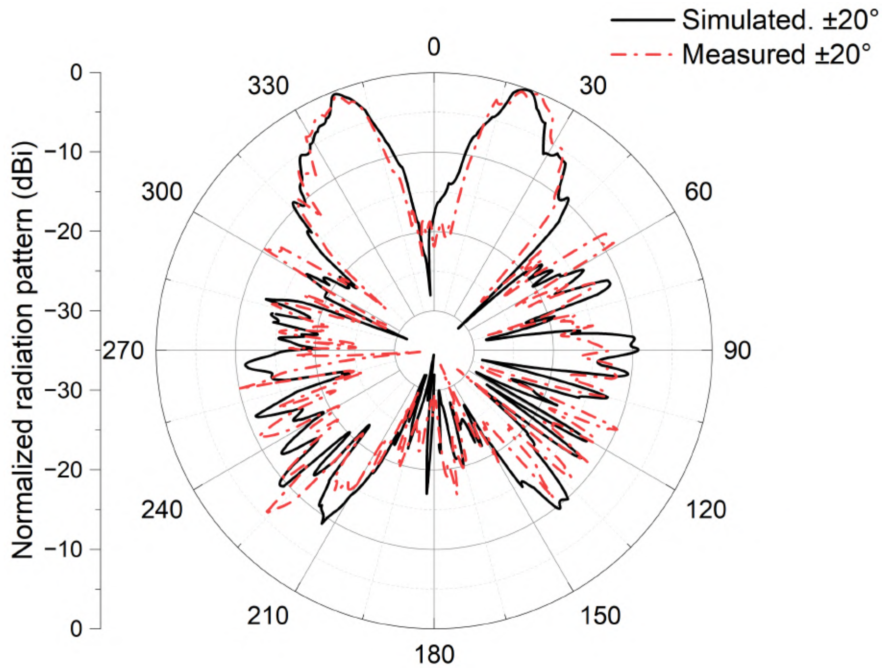

FIGURE 5.24 : Simulated versus measured radiation pattern for the dual-beam feature at 28 GHz.

rent bias integration makes the design suitable for high-efficiency beamforming at millimeter-wave frequencies.

5.6 Uni–planar Passive Transmitarray Based on a CPW–to–Slotline Transition

The uni–planar transmitarray developed in this work represents a significant step toward a fully planar, low-profile, and broadband aperture that can be extended to future electronically reconfigurable designs. It originates from the previously demonstrated dual-layer CPW–to–slotline concept but has been re-engineered into a single-layer passive architecture that maintains the same electromagnetic behavior while drastically simplifying fabrication. In this new design, both the coplanar waveguide (CPW) and the slotline are defined on the same metallization layer over a Rogers RO3006 substrate ($h = 0.254$ mm, $\varepsilon_r \approx 6.5$), eliminating the need for via transitions, multilayer alignment, or bonding processes. The transition between the CPW and slotline modes is achieved through a carefully optimized coplanar junction that allows the odd CPW mode to directly excite the odd slotline mode without vertical coupling. This configuration preserves the broadband impedance matching and field confinement properties of the previous two-layer architecture but achieves them entirely within a single metallization plane.

The uni–planar unit cell, illustrated in Fig. 5.25, incorporates two printed dipole-like structures that appear geometrically similar but serve distinct electromagnetic functions. The upper dipole operates as the radiating element that re-radiates the transmitted energy into free space, while the lower dipole, together with the extended CPW line, forms the feeding transition that excites

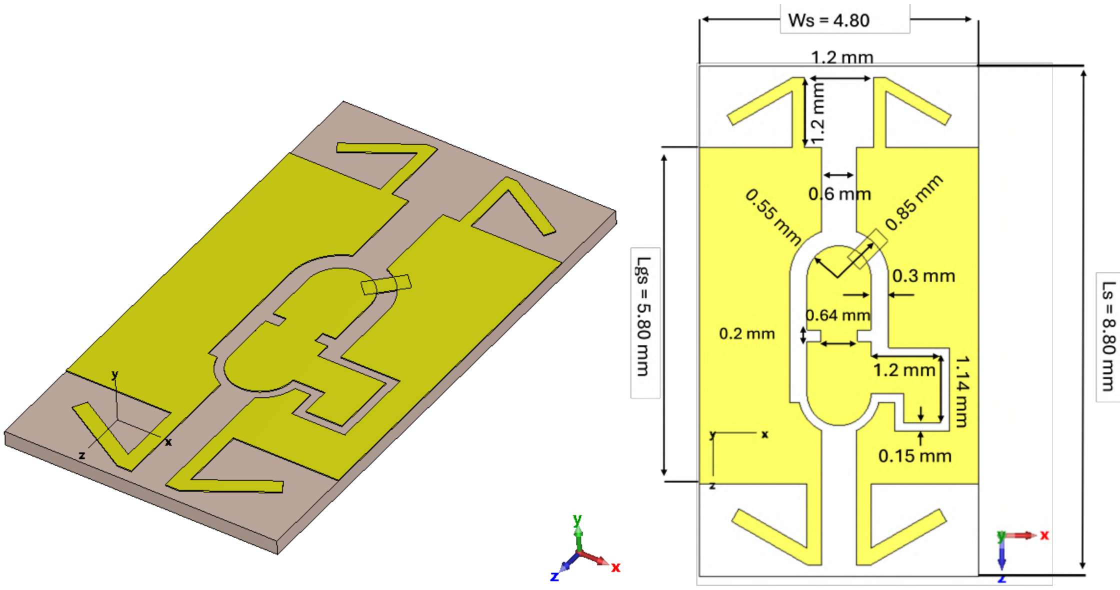

(a) **(b)**

FIGURE 5.25 : Geometry of the proposed uni–planar unit cell : (a) Perspective view, and (b) Top view.

the radiating section through a CPW–to–slotline conversion. This mechanism follows the same physical principle reported in [23], where a CPW line is asymmetrically extended to introduce a half-guided-wavelength ($\lambda_s/2$) delay between its two branches. When one branch is lengthened by this amount, the two CPW slot fields arrive at the junction with a $180°$ phase difference, combining constructively into a pure odd slotline mode. The proposed uni–planar cell reproduces this effect in a single metallization layer : the extended CPW arm beneath the coupling region generates the required phase delay, ensuring efficient CPW-to-slotline conversion without multilayer vias or apertures. Consequently, the lower dipole region acts as a broadband mode converter, while the upper dipole serves as the radiating aperture. This integrated single-layer transition preserves high transmission magnitude, stable phase behavior, and broadband impedance matching across the Ka-band range.

5.6.1 1-bit Uni–planar Passive Unit Cell and Array Design

The foundation of the uni–planar architecture is a passive 1-bit unit cell that integrates this transition and the radiating section within a single metal layer. A differential electrical path of approximately $\lambda_{SL}/2$ is introduced between the two CPW branches, creating a $180°$ phase inversion in the transmitted slotline field. Although this configuration is entirely passive, the layout reserves planar area and DC-isolation gaps that can accommodate two PIN diodes in future active versions, allowing for real-time electronic phase control without modifying the RF geometry.

All electromagnetic simulations of the unit cell were carried out using the frequency-domain solver of *CST Microwave Studio*. A three-dimensional (3-D) periodic model with Floquet ports and unit-cell boundaries was employed to extract the transmission magnitude and phase under normal-incidence excitation. This setup accurately represents the CPW–to–slotline transition and ensures convergence across the 26–32 GHz frequency band. Fig. 5.26 shows the periodic simulation environment, and the simulated transmission response for the two passive configurations corresponding to $0°$ and $180°$ states. A nearly constant transmission magnitude of more than 0.9 and a differential phase of approximately $180°$ are maintained across the band, confirming efficient mode conversion and broadband performance within the single-layer geometry.

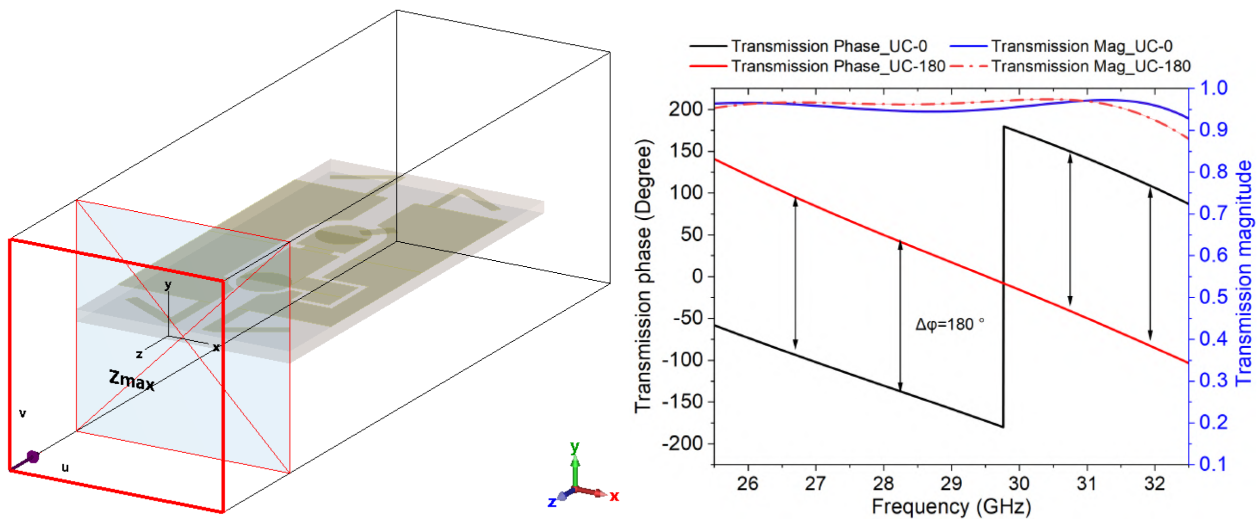

(a) (b)

FIGURE 5.26 : (a) 1-bit Uni-planar unit cell simulation setup, and (b) its simulated transmission results.

To verify the array-level performance, a three-dimensional full-wave model of the 1-bit transmitarray was also developed in *CST Microwave Studio*. All simulations in this work, including both unit-cell and array-level analyses, were conducted in CST to ensure consistency in boundary conditions and solver precision. The array consisted of 20 panels (see Fig. 5.29 (a)) with 20 elements in each one of them (400 cells) illuminated by a printed Vivaldi feed located at a focal distance of 53 mm.

This focal distance was selected according to the -10 dB beamwidth of the feed radiation pattern to provide balanced illumination across the aperture while minimizing spillover. The resulting far-field performance obtained from the CST 3-D model is summarized in Table 5.3. The simulated peak gain remains approximately 21 dBi over the 26–30 GHz band, with side-lobe levels below –14 dB. These results confirm that the uni–planar passive concept can support an efficient high-gain aperture even without active switching or bias control.

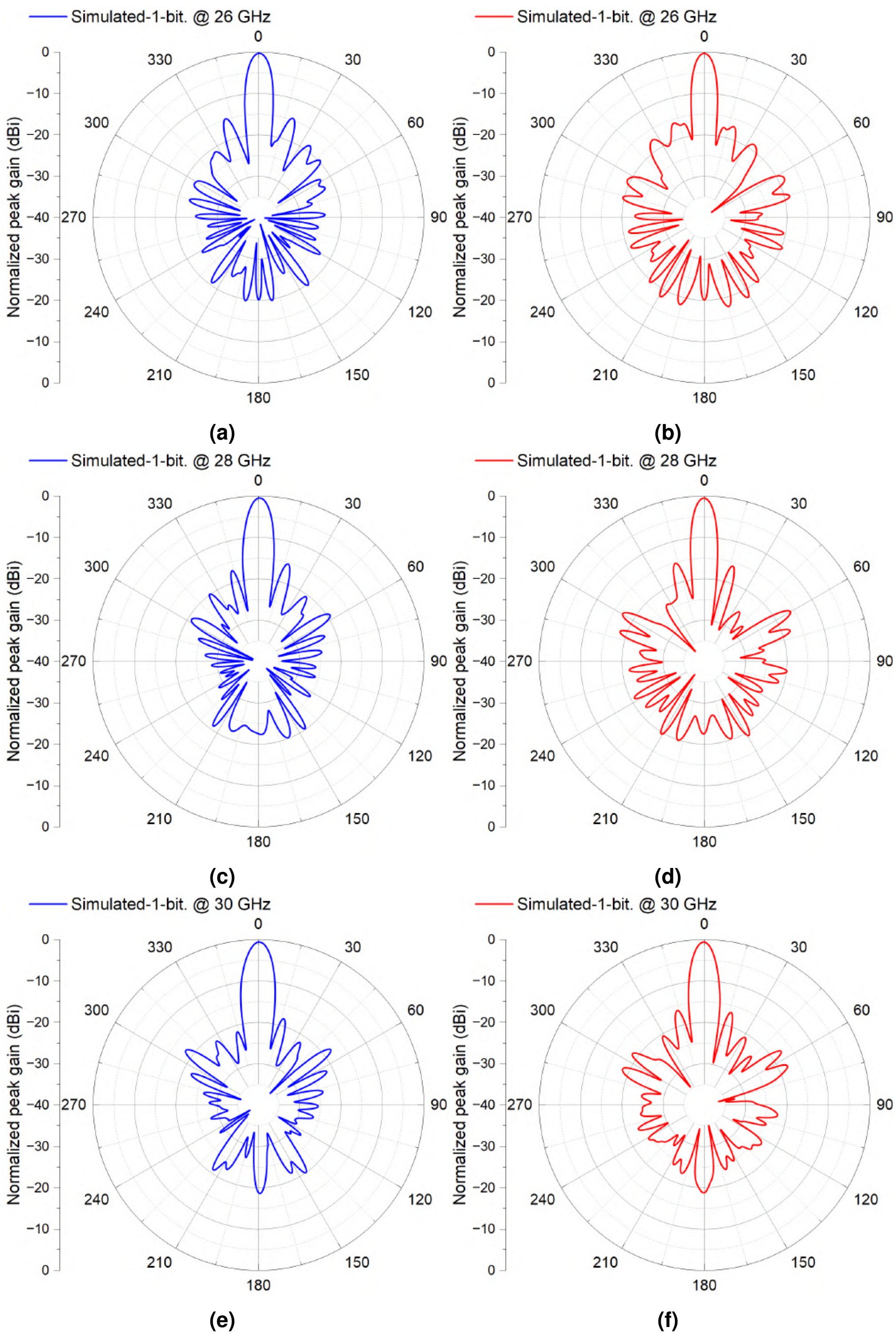

FIGURE 5.27 : Normalized peak gain patterns at 0° for both H- and E-planes, operating at (a ,b) 26, (c, d) 28 and (e, f) 30 GHz for the 1-bit uni-planar structure.

TABLEAU 5.3 : Simulated radiation performance of the 1-bit uni–planar passive transmitarray.

Frequency (GHz)	Peak gain (dBi)	Side-lobe level (dB)
26	20.7	-14.2
28	20.9	-14.8
30	20.8	-17.4

5.6.2 Fabricated 3-bit Uni–planar Passive Transmitarray

Following the numerical validation of the 1-bit configuration, a 3-bit version of the uni–planar design was fabricated and experimentally characterized to demonstrate the scalability and broadband capability of the proposed transition. The 3-bit concept extends the same single-layer CPW–slotline topology by varying the dielectric path length L_s after the transition region. Each incremental extension of approximately 1.1 mm introduces an additional $45°$ phase shift, allowing the realization of eight discrete phase states from $0°$ to $315°$ in $45°$ increments. This purely geometric phase-control approach avoids the use of resonant elements, ensuring low dispersion and nearly constant transmission magnitude across all states.

All 3-bit unit-cell simulations were performed in *CST Microwave Studio* under the same conditions as the 1-bit analysis. Figs. 5.28 (a) and (b) present the simulated transmission magnitude and phase for the eight configurations. The results show a negligible variation in transmission magnitude (within ± 0.5) and an almost identical slope among the phase curves, indicating a uniform delay response with frequency and validating the accuracy of the dielectric-length tuning method.

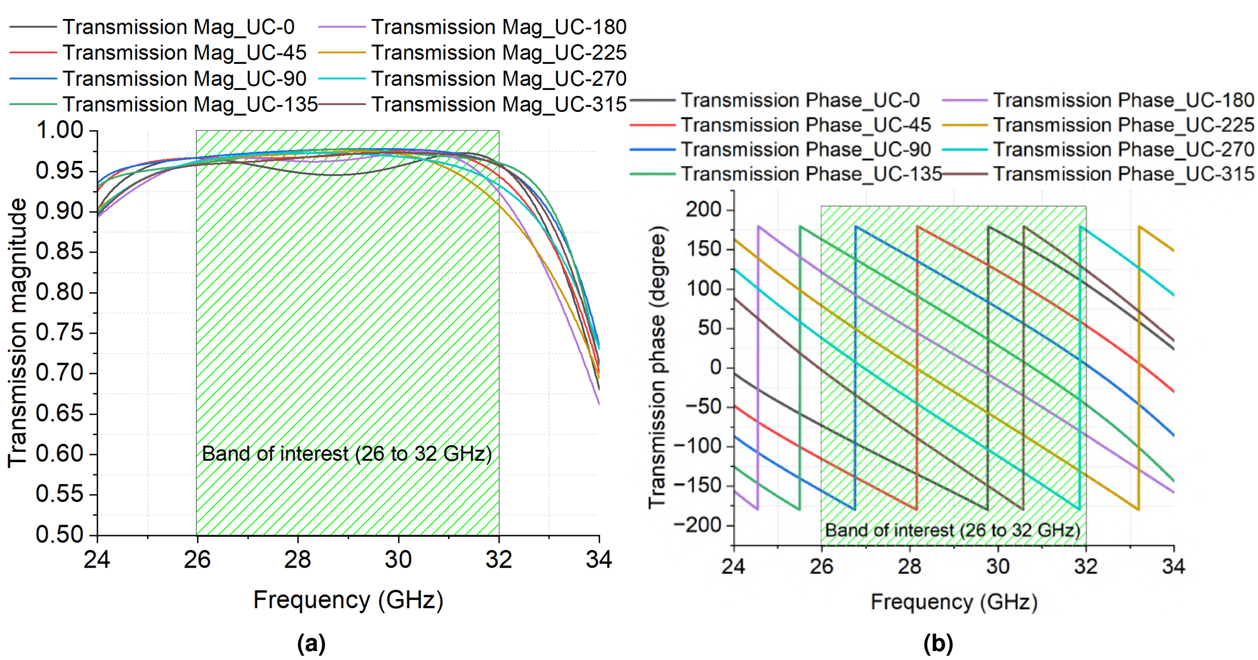

FIGURE 5.28 : Simulated transmission magnitude and phase $|S_{21}|$ for the unit cells (UC0–UC315) across 24–34 GHz.

A single 3-bit panel containing 20 uni–planar cells with incremental dielectric lengths was fabricated on Rogers RO3006 using standard photo-lithography, as shown in Fig. 5.29 (c). Multiple identical panels were assembled to form the complete transmitarray aperture. The array was tested in an anechoic chamber using a printed Vivaldi feed located at a focal distance of 53 mm, as illustrated in Fig. 5.30. Table 5.4 summarizes the measured radiation performance of the fabricated 3-bit transmitarray.

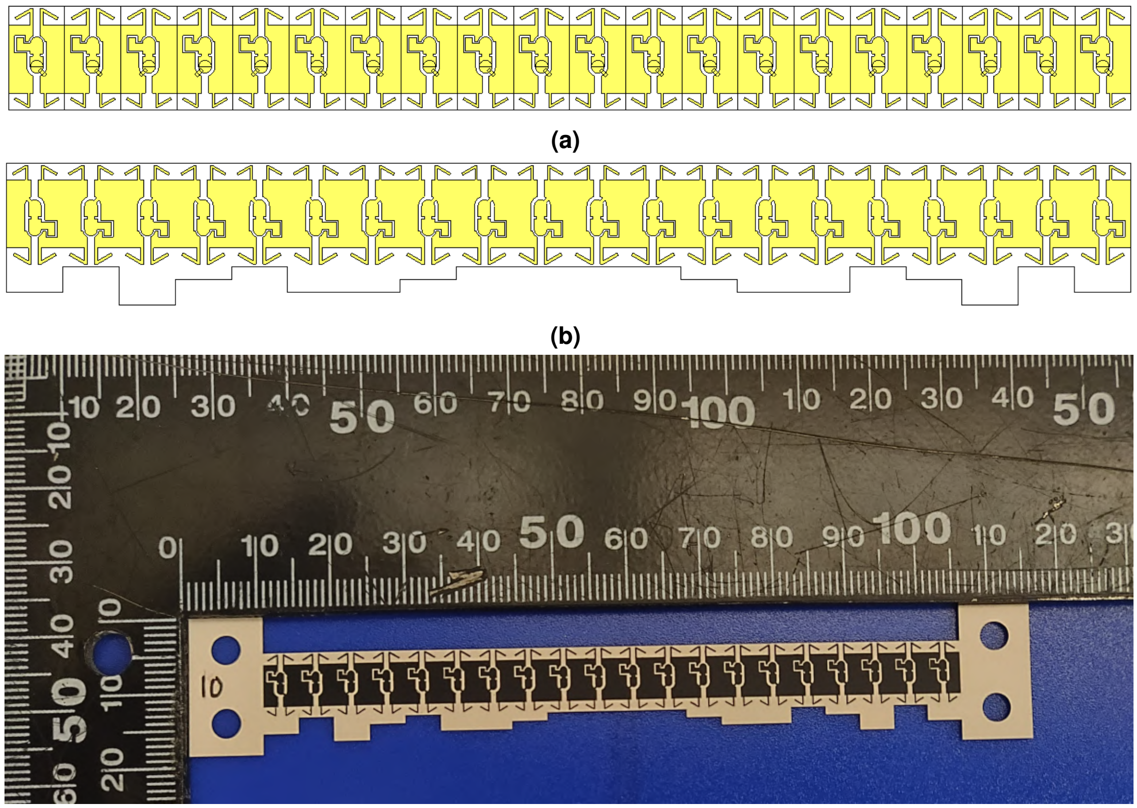

(a)

(b)

(c)

FIGURE 5.29 : Geometry of the proposed TA panels. (a) 1-bit panel (3D-model). 3-bit panels : (b) 3D-model, and (c) fabricated panel.

The measured peak gain reaches 22.4–22.5 dBi across 28–30 GHz with side-lobe levels as low as –19.4 dB at 28 GHz, representing a gain improvement of approximately 1.5–1.7 dB and a 3–5 dB side-lobe reduction compared to the simulated 1-bit case. The corresponding aperture efficiency, calculated from the measured 22.4 dBi gain at 28 GHz, is about 63%, compared to roughly 50% for the 1-bit design. This improvement is consistent with the theoretical reduction in phase-quantization loss from 1.96 dB to 0.27 dB when increasing the number of phase states from one to three bits.

The excellent agreement between simulated and measured results confirms the robustness of the uni–planar CPW–to–slotline transition and validates its potential for high-efficiency broadband transmitarrays. Although the present prototype operates entirely passively, the metallization layout already includes reserved pads and isolation regions for the future integration of PIN diodes. This

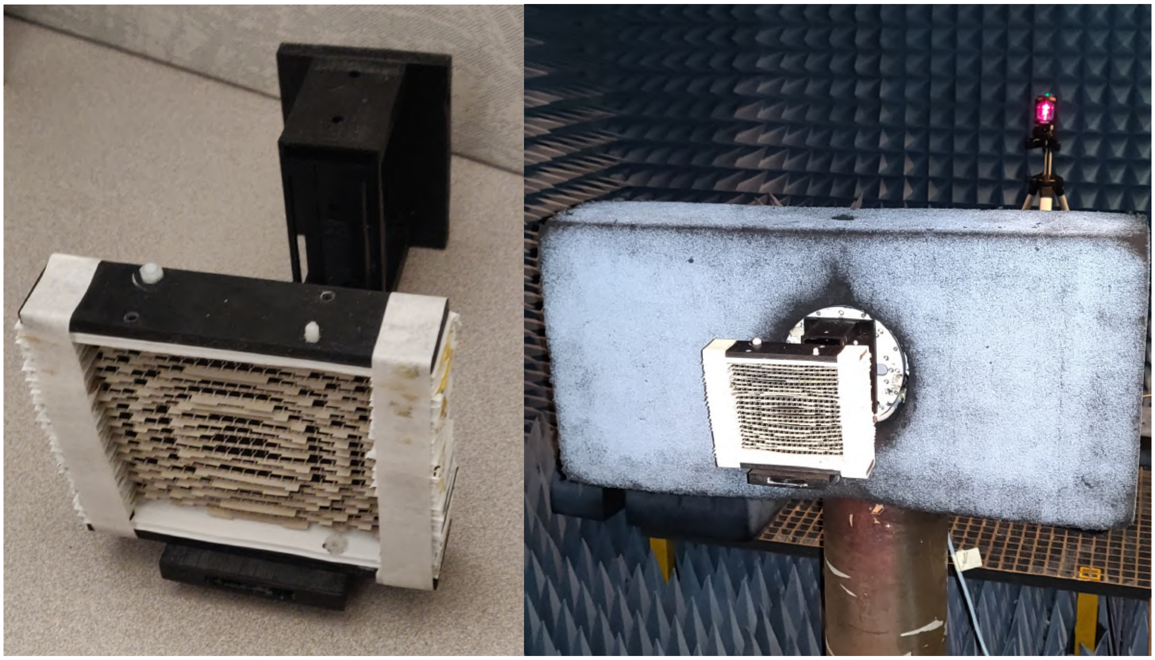

(a) (b)

FIGURE 5.30 : The proposed full 3-bit transmitarray. (a) 20 panels assembly, and (b) Fully assembled TA in the anechoic chamber.

TABLEAU 5.4 : Comparison between simulated and measured peak gain and side-lobe levels of the fabricated 3-bit uni–planar passive transmitarray.

Frequency (GHz)	Simulated		Measured	
	Peak gain (dBi)	SLL (dB)	Peak gain (dBi)	SLL (dB)
26	21.1	-17.2	20.4	-17.0
28	22.4	-19.4	21.9	-18.7
30	22.5	-17.1	21.4	-16.7

will enable real-time electronic phase control while preserving the same single-layer geometry. By achieving high gain, low side-lobe levels, and wideband operation within a simple planar structure, the proposed uni–planar architecture establishes a scalable foundation for next-generation reconfigurable Ka-band transmitarrays.

5.7 Conclusion

This chapter presented the complete development, simulation, and experimental validation of a new class of transmitarray antennas for Ka–band applications. The work began with the formulation of a reconfigurable 1–bit unit cell concept in which two PIN diodes are integrated directly across the coplanar slots, enabling in–plane *mode conversion* and binary *phase inversion* within a single compact transition. A rigorous transmission–line model and full–wave electromagnetic simulations in *CST Microwave Studio* confirmed that the differential switching of the two diodes generates a

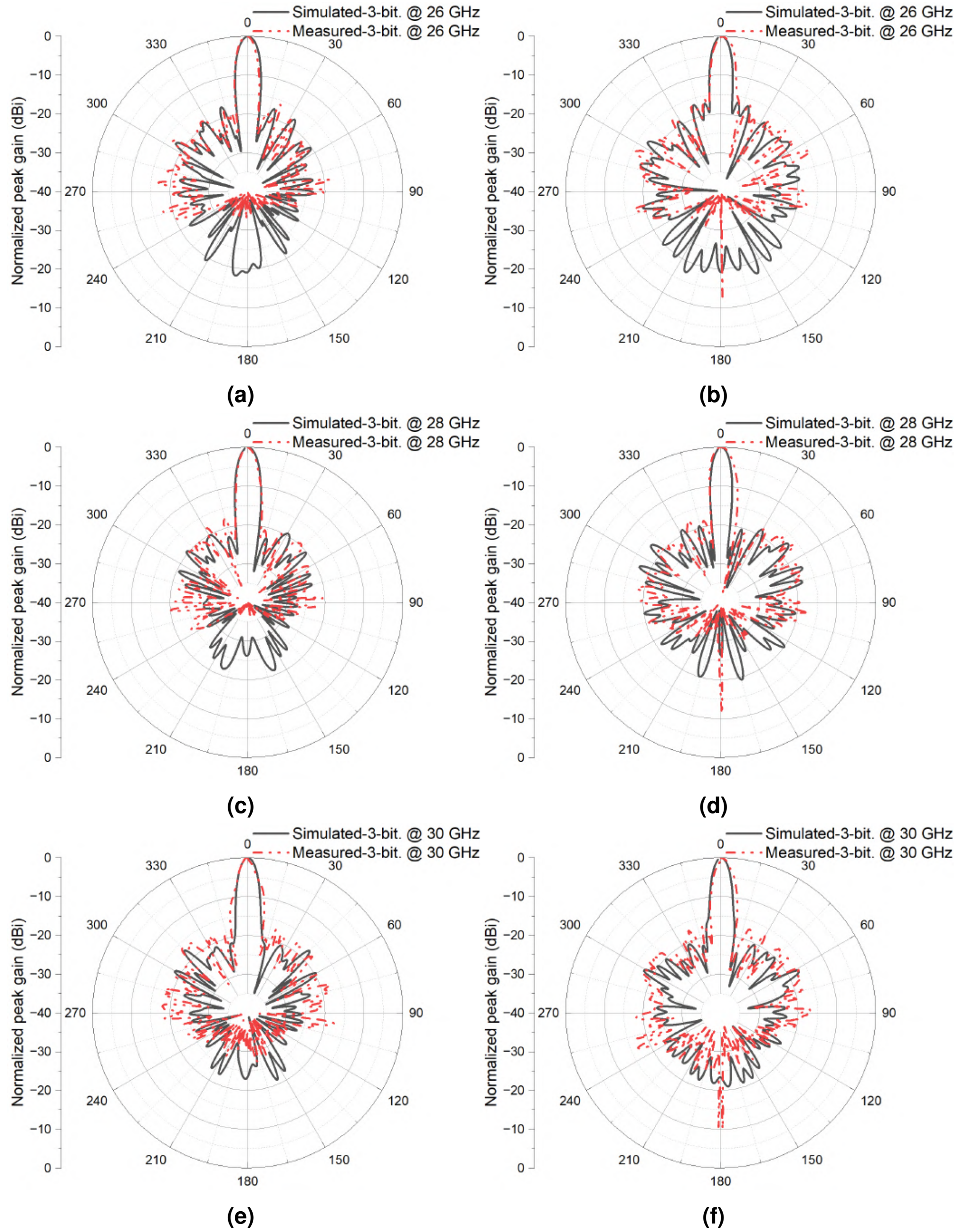

FIGURE 5.31 : Normalized peak gain patterns at 0° for both H- and E-planes, operating at (a ,b) 26, (c, d) 28 and (e, f) 30 GHz, for the 3-bit uni-planar structure.

broadband 180° phase reversal while maintaining low insertion loss and high transmission magnitude.

Building on these findings, a simplified **uni–planar passive implementation** was conceived and experimentally realized. In this single–layer version, the CPW–to–slotline transition and the radiating dipole are printed on the same metallization layer, eliminating the need for vias, multi-layer bonding, or vertical transitions. The uni–planar concept was first validated through a 1–bit full–wave model, demonstrating efficient mode conversion and broadband 0°/180° operation with

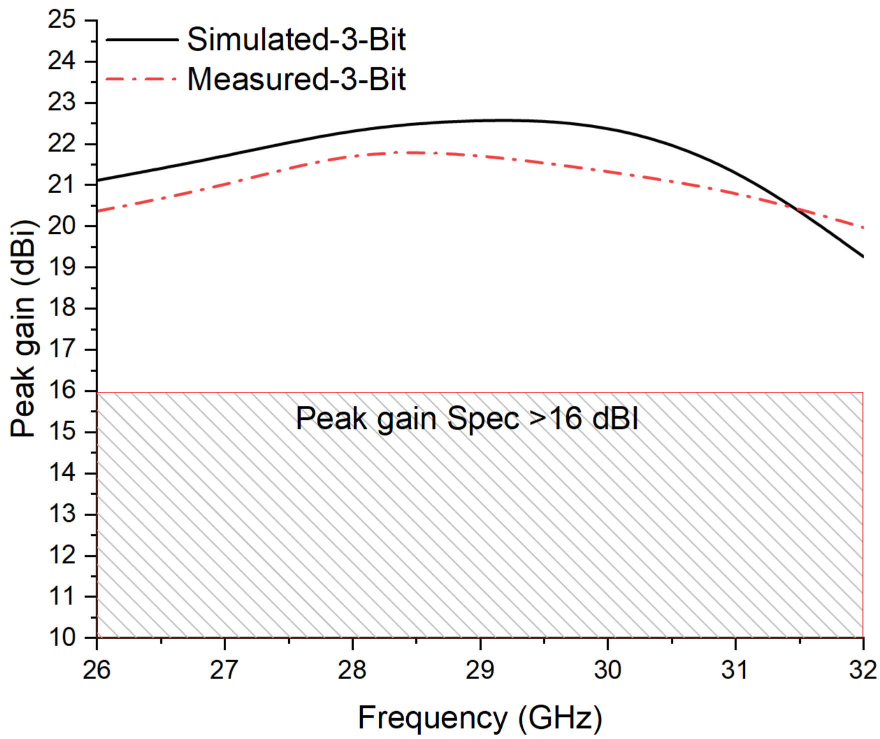

FIGURE 5.32 : Simulated and measured peak gain over the band of interest for the 3-bit uni-planar structure.

transmission above 0.9 across 26–32 GHz. To further verify scalability, a 3–bit passive prototype was fabricated by extending the slotline path length in discrete steps of 1.1 mm, achieving approximately 45° incremental phase shifts while preserving nearly constant amplitude and linear phase progression between states.

The fabricated 3–bit transmitarray exhibited excellent agreement between simulation and measurement, with peak gains of 21.1, 22.4, and 22.5 dBi at 26, 28, and 30 GHz, respectively, and side–lobe levels better than –17 dB. These results represent a clear performance improvement over the simulated 1–bit configuration, validating both the scalability and amplitude–stability of the uni–planar approach. Importantly, the measured data confirmed that extending the dielectric length for phase control introduces only negligible variation in transmission magnitude—a key feature enabling higher phase resolution without compromising efficiency.

In summary, the proposed uni–planar CPW–to–slotline architecture offers a compact, low–loss, and fabrication–friendly platform for broadband transmitarrays at Ka–band. The passive 3–bit prototype experimentally demonstrates the viability of achieving fine phase quantization entirely within a single metallization layer. Moreover, the layout naturally accommodates future integration of PIN diodes for real–time electronic beam steering without altering the RF geometry. This establishes a direct technological bridge between passive geometric phase control and fully reconfigurable transmitarray front–ends, paving the way toward lightweight, high–efficiency, and electronically steerable Ka–band apertures for next–generation satellite and 5G backhaul systems.

6 CONCLUSION AND FUTURE WORK

6.1 Conclusions

This thesis has presented a unified research effort toward the development of high-performance, reconfigurable, and low-cost **transmitarray (TA) and lens antennas** operating in the Ka-band for millimeter-wave (mm-wave) beamforming applications. The proposed systems address key limitations of conventional antenna architectures by combining electromagnetic design innovation, algorithmic optimization, and advanced fabrication techniques, enabling compact, efficient, and reconfigurable front-ends for next-generation communication and sensing platforms.

The research began with a **comprehensive literature review** of metasurface-based reconfigurable antennas, where the limitations of traditional phased arrays, mechanical beamformers, and reflectarray systems were examined. This review established the motivation for reconfigurable TAs as a promising solution, capable of achieving high gain and wide-angle beam steering without the drawbacks of complex feed networks or aperture blockage. The fundamental operating principles of TAs, including transmission phase compensation, polarization control, and spatial feeding mechanisms, were detailed as a basis for the developments that followed.

Building on this foundation, a **multi-bit wideband TA** with independent phase and amplitude control was designed, optimized, and validated. The concept introduced a novel dual-layer unit cell architecture leveraging **polarization twisting and current-reversal techniques** to achieve binary (1-bit) phase states, while a **rotating transmitting layer** enabled independent amplitude tuning. A **Genetic Algorithm (GA)-based optimization framework** was developed to refine amplitude tapering and phase distribution, resulting in wideband operation, suppressed sidelobe levels, and high gain verified through the fabrication and measurement of 20×20 prototypes. The measured results confirmed the accuracy of the simulation-based optimization, marking an important step toward practical, algorithmically optimized TA systems.

The thesis then expanded the TA concept into three-dimensional, continuous-aperture realizations through the development of **3D-printed conformal dielectric lenses**. Exploiting the **height-to-phase conversion principle**, these lenses demonstrated passive beam steering, dual-beam formation, and orbital angular momentum (OAM) generation using lightweight, low-loss PLA substrates. The ability to fabricate conformal, wide-aperture lenses with tailored phase distributions validated the potential of **additive manufacturing** as a complementary pathway to planar metasurface technologies. This stage bridged the gap between traditional PCB fabrication and future conformal mm-wave systems suitable for UAV, automotive, and satellite applications.

Finally, the research culminated in the development of an **electrically reconfigurable CPW-to-slotline transmitarray architecture** using **dual-PIN-diode integration per unit cell**. The proposed topology achieved 1-bit phase control (0°/180°) using intrinsic mode symmetry rather than external matching networks, resulting in a compact, uni-planar, and scalable structure. A 16-cell modular panel design demonstrated the feasibility of multi-panel integration for higher aperture gain and flexible beam steering. This architecture unites simplicity, broadband matching, and reconfigurability, forming the foundation for scalable electronically steerable arrays.

Overall, the work presented in this thesis provides several key contributions to the field of mm-wave antenna design :

— A complete framework for **multi-bit amplitude and phase control** in transmitarrays using GA-based optimization, enabling high gain and low sidelobe levels.
— The introduction of **3D-printed conformal dielectric lenses** for low-cost, passive beam steering and OAM generation.
— The design and demonstration of a novel **CPW-to-slotline unit cell** enabling binary phase control without external networks, suitable for PIN-diode integration.
— Experimental validation of compact wideband prototypes that bridge the gap between simulation-based optimization and practical implementation.
— A comprehensive synthesis connecting electromagnetic modeling, optimization, additive manufacturing, and reconfigurable integration in a single coherent framework.

Collectively, this research advances the state-of-the-art in high-gain, reconfigurable, and compact mm-wave antennas. The results demonstrate practical pathways toward scalable, efficient, and intelligent beamforming architectures for emerging applications such as 5G/6G communications, vehicular sensing, and satellite links.

6.2 Future Work

The results and methodologies presented in this thesis establish a strong foundation for the continued evolution of transmitarray and lens antenna technologies. Several research directions can be pursued to further enhance performance, scalability, and integration.

— **Fabrication and Measurement of Reconfigurable Panels :** The immediate next step is the realization and experimental validation of the electronically reconfigurable CPW-slotline transmitarray. This includes hardware integration of the biasing network, modular interconnection of 16-cell panels, and far-field radiation measurements to validate electronic beam steering and reconfigurable operation.
— **Multi-bit Reconfigurability :** Extending the current binary (1-bit) architecture to 2-bit or 3-bit phase resolution will improve beam precision and dynamic range, enabling smoother beam scanning and reduced quantization loss.

- **Integration of Intelligent Control :** Incorporating **machine learning and adaptive control algorithms** could enable autonomous beam management, environmental adaptation, and real-time optimization of array states, particularly for mobile or dynamic platforms.
- **Advanced Materials and Fabrication :** The use of **low-loss 3D printable composites**, liquid crystal polymers (LCP), or tunable dielectrics such as VO_2 and BST can further improve efficiency and speed. Additive manufacturing of hybrid dielectric–metallic metasurfaces can also reduce losses and support conformal integration.
- **Hybrid Transmitarray–Lens Architectures :** Future systems may integrate 3D-printed dielectric lenses with electronically reconfigurable metasurfaces, combining passive shaping with active tuning for multi-mode or hybrid beam control.
- **Energy-Efficient Biasing and Power Management :** Low-power biasing strategies, pulse-driven diode control, or energy-harvesting subsystems can enhance suitability for UAV and IoT platforms where autonomy and power efficiency are critical.
- **System-Level Integration :** Co-designing the reconfigurable TA with RF front-end circuits (amplifiers, mixers, and phase shifters) will enable compact, fully functional antenna modules compatible with 5G/6G systems.
- **Conformal and Multi-Panel Arrays :** The modular transmitarray concept can be scaled into large, conformal surfaces for vehicular and aerospace platforms, where multiple panels cooperate to achieve dynamic 3D beam coverage.
- **Multi-Functional Operation :** Beyond communications, the proposed platforms can be extended for joint radar–communication systems, OAM multiplexing, or adaptive sensing with programmable beam coding.
- **Field Testing and Deployment :** Real-world evaluation in dynamic vehicular or UAV environments will be essential to assess robustness under multipath, thermal, and mechanical stress conditions.

By pursuing these research avenues, the presented work can evolve into a fully integrated, intelligent, and energy-efficient beamforming platform. The convergence of **electromagnetic design, additive manufacturing, and smart control** will pave the way for practical, reconfigurable mm-wave front-ends that serve as key enablers for next-generation 5G, 6G, and beyond communication ecosystems.

7 APPENDIX A

7.1 Proposed SIW H-Horn Antenna

The proposed feeding element design procedure is described briefly in this section, starting by simply designing a conventional parallel plat H-horn antenna (PP-H-horn), and going through both SIW and leaky-wave technologies, we managed to get an outstanding results, in terms of impedance matching, radiation efficiency, peak gain and low side-lobe levels. Since the desired final design should be compact and easy to fabricate, PCB technology is used here to attain those objectives. By first replacing the conventional PP-H-horn with its SIW-based counterpart, yielding acceptable results, but far from the desired performances, due to the poor impedance matching and radiation characteristic of thin SIW substrates. To get around these issues, periodic leaky-wave strips with end-fire radiation [114] are used, where parallel periodic strips are printed on both top and bottom planes of the substrate.

First, the poor matching is resolved by using a certain number of parallel strips, with a width tapering technique, and the idea behind it is, that the two reflected waves by both the first and the second strips will nearly cancel each other, when there is a phase difference of 180° between those two waves. The total reflected wave will be as follow :

$$E_r = E_{r1} + E_{r2} = a_1.e^{-j\varphi_0} + a_2.e^{-j\varphi_0}.e^{\frac{-j4\pi L}{\lambda_g}} \tag{7.1}$$

If the strip width $L = \lambda_g/4$ and the spacing between the two adjacent strips is very small, then $a_1 \simeq a_2$, and Eq. (7.1) becomes as the following :

$$E_r = (a_1 - a_2).e^{-j\varphi_0} \simeq 0 \tag{7.2}$$

To put it simply, n pairs of tapered strip-to-slot were defined with the parameters of slot width w_{si}, and total pair width w_{pi}, in addition to the total length of the strip-to-slot pairs L_a.

A parametric study was conducted, to explore the effect of the total numbers of strip-to-slot pairs, on the impedance matching, where it was noticed that by increasing it, the impedance bandwidth was enhanced, achieving 28 % fractional bandwidth at the center frequency of 28 GHz, with a total of 18 pairs, and this was set to be the maximum, as our goal is to have both compactness and better impedance matching. The detailed procedure for calculating the dimensions of each strip-to-slot pairs is shown in Eq. (7.3). where w_{pi} was taken as $\lambda_g/4$ at the lower end frequency,

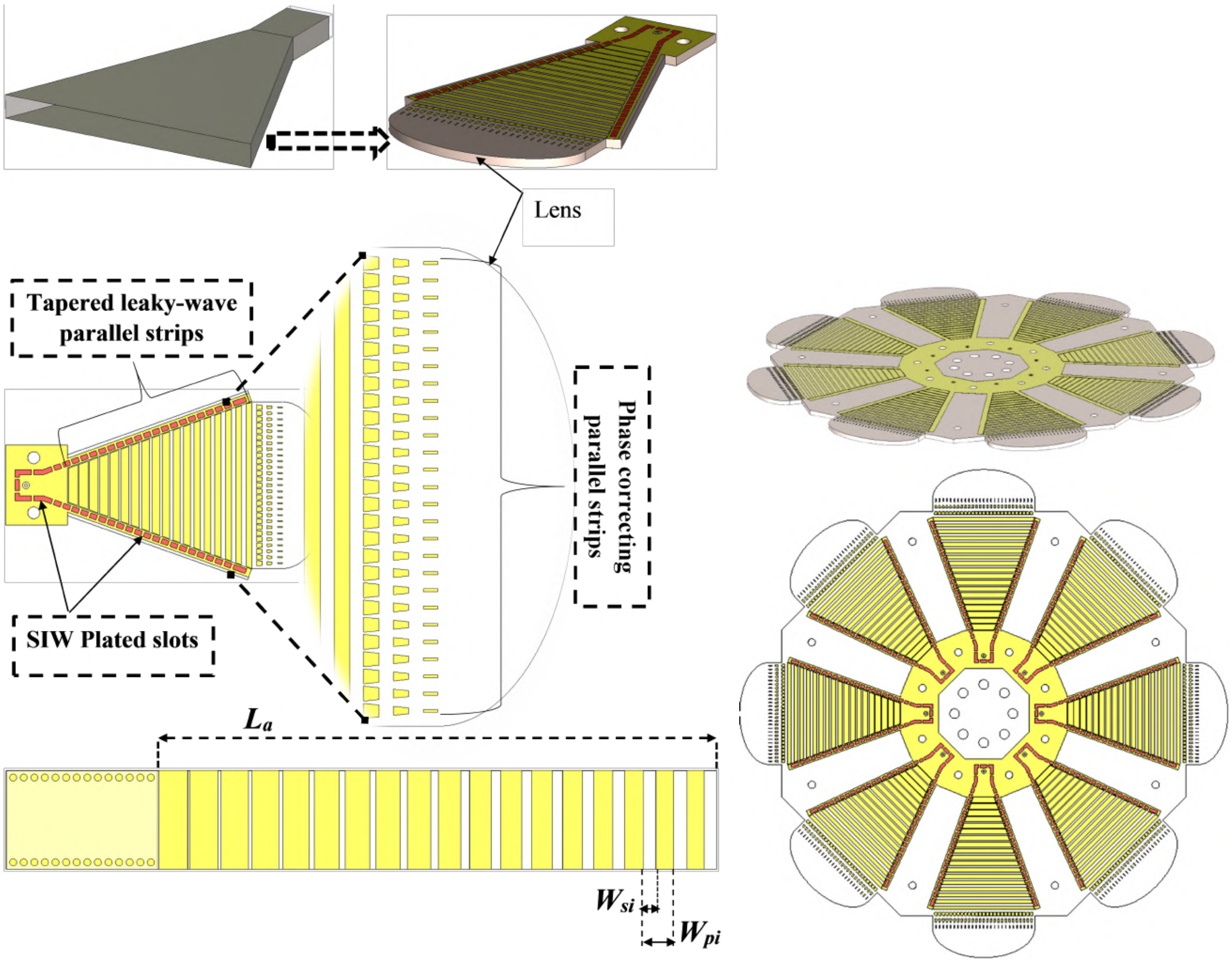

(a) **(b)**

FIGURE 7.1 : Design process for the proposed feeding antenna, (a) single element, and (b) octagonal-shaped one.

and the tapered step was 0.05 mm.

$$\begin{cases} w_{pi} = 2.2 \\ w_{si} = 0.1 + 0.05(i-1) \quad ; where \rightarrow i = 1, 2, ..., n \end{cases} \tag{7.3}$$

To that end, by using this tapering technique, an end fire leaky-wave pattern is achieved, as the wave was moving forward, with much less energy reflected back to the SIW-based waveguide.

In addition, three more parallel strip lines were added with triangular tapering, alongside a simple dielectric lens, for phase distribution correction, before launching the EM wave into the free space, leading to an increase in gain and efficiency.

All this design consideration, gave rise to an outstanding performances, in terms of impedance bandwidth, peak gain, and especially very low side lobe levels. This latter was then put into an octagonal-shaped formation, for 360° coverage, and both designs were fabricated using Rogers

RO3003 dielectric slab, with a thickness of 1.524 mm. In addition, a 2.92 mm waveguide type K-connectors were used to feed the antennas.

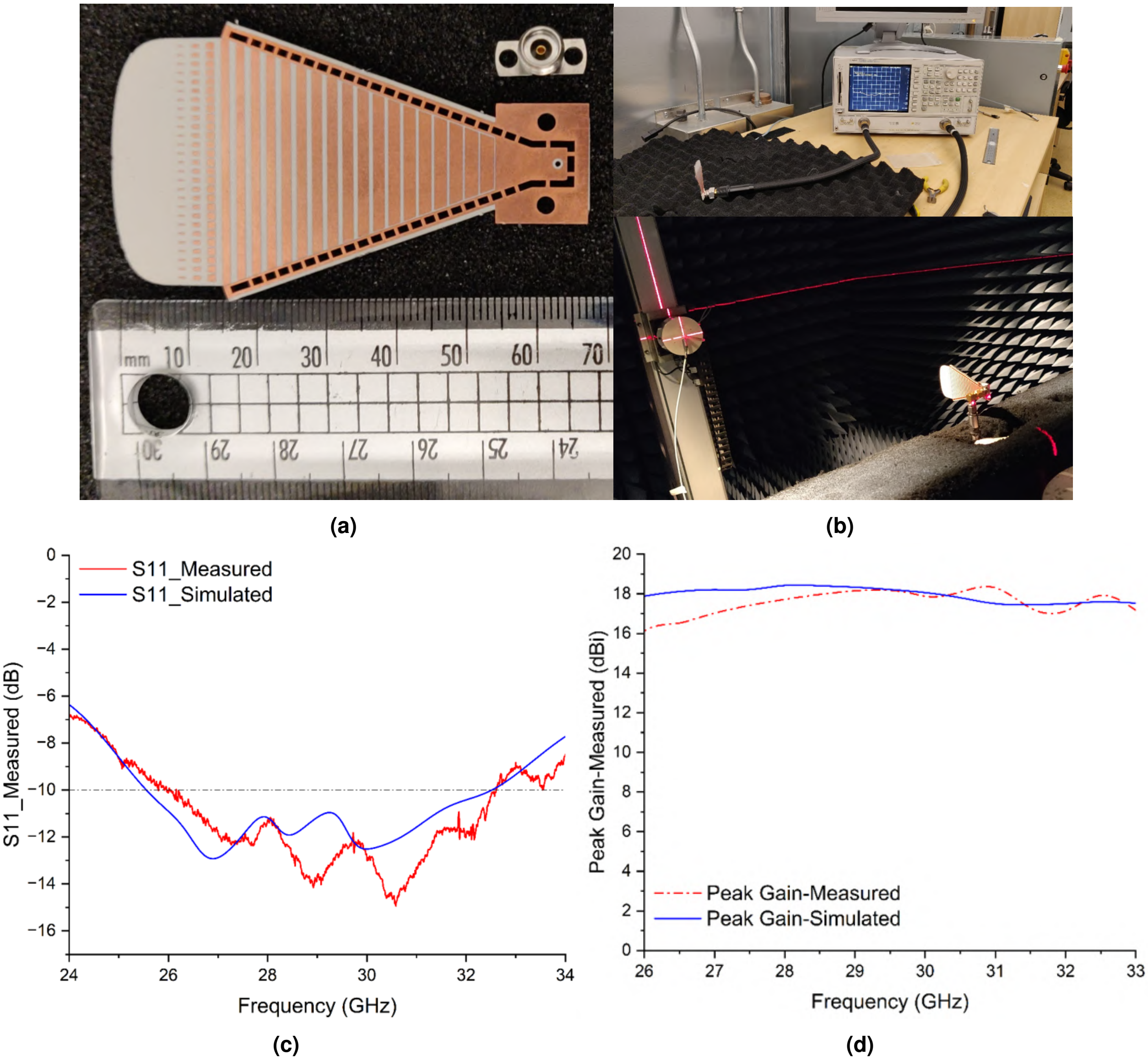

FIGURE 7.2 : (a) Fabricated single element prototype, (b) measurement setup, (c) and (d) its reflection coefficient and peak gain results.

The S-parameters of both designs were measured using Agilent 8722ES Vector Network Analyzer, and in the anechoic chamber, their radiation characteristics were assessed, and the results are illustrated in the following figures.

Fig. 7.2, shows the performance of the single element, where both the reflection coefficient and peak gain, were simulated and measured, and both are in good agreement. The proposed design achieved the required impedance bandwidth, where the desired operation range was set to be from 26 to 32 GHz. In addition, the maximum achieved peak gain was 18.68 dBi in measurement,

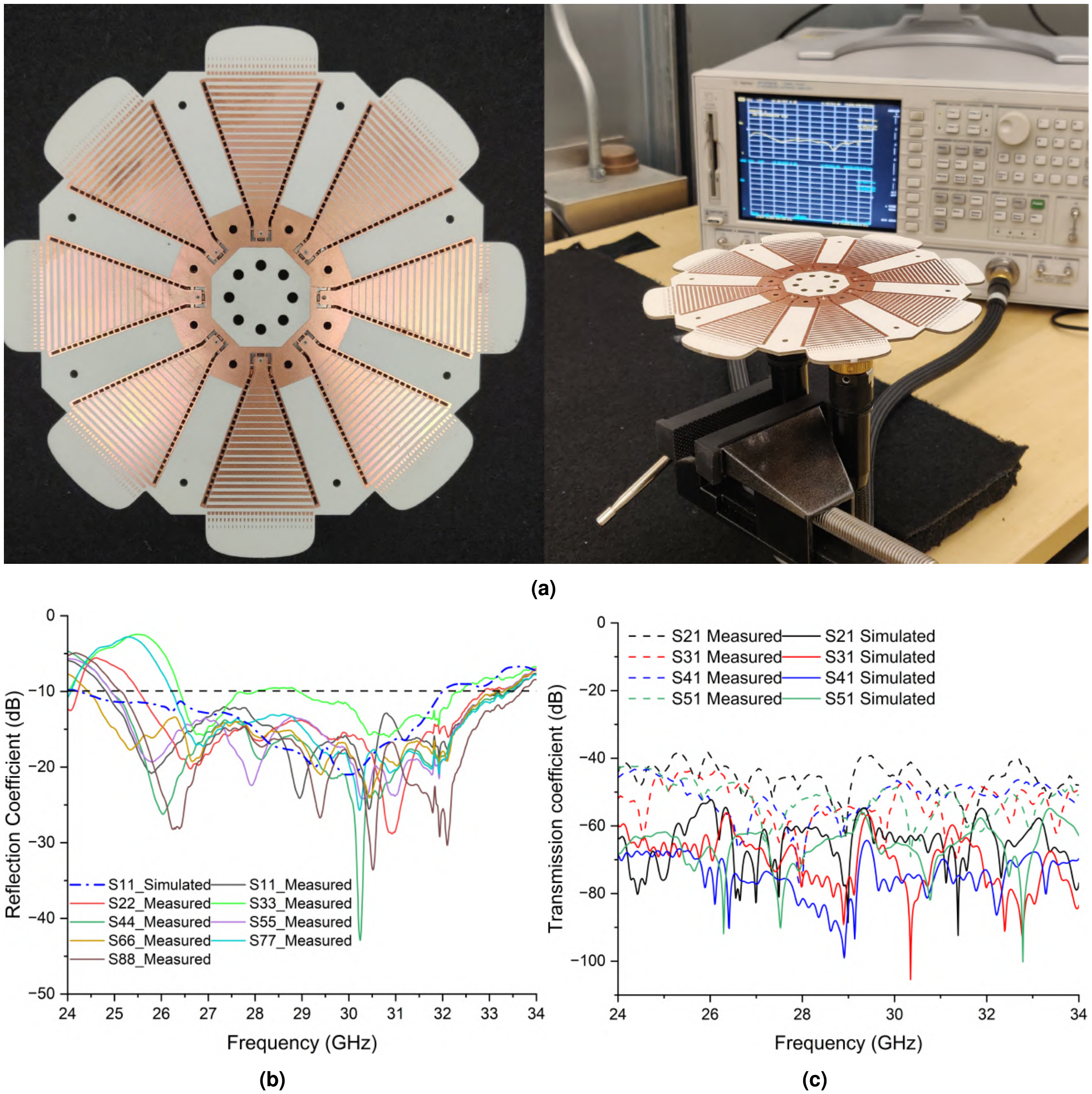

FIGURE 7.3 : (a) Fabricated Octagonal-shaped prototype with the measurement setup, (b) and (c) its reflection and transmission coefficient results, respectively.

and 18.5 dBi in simulation. So, both are in accordance with the project's specification, with almost unvaried peak gain.

As for the case of the octagonal-shaped antenna, Fig. 7.3 illustrates the fabricated prototype, alongside its simulated and measured S-parameters (reflection and transmission coefficients) results. It can be noted that two sub-antenna elements didn't perform well, compared to the other six, due to fabrication errors, but still both of them almost covered the desired band of interest. As for the isolation levels, here we only presented half of the results due to the imposed symmetry of the design, where an outstanding isolation levels were achieved, between 40 to 70 dB.

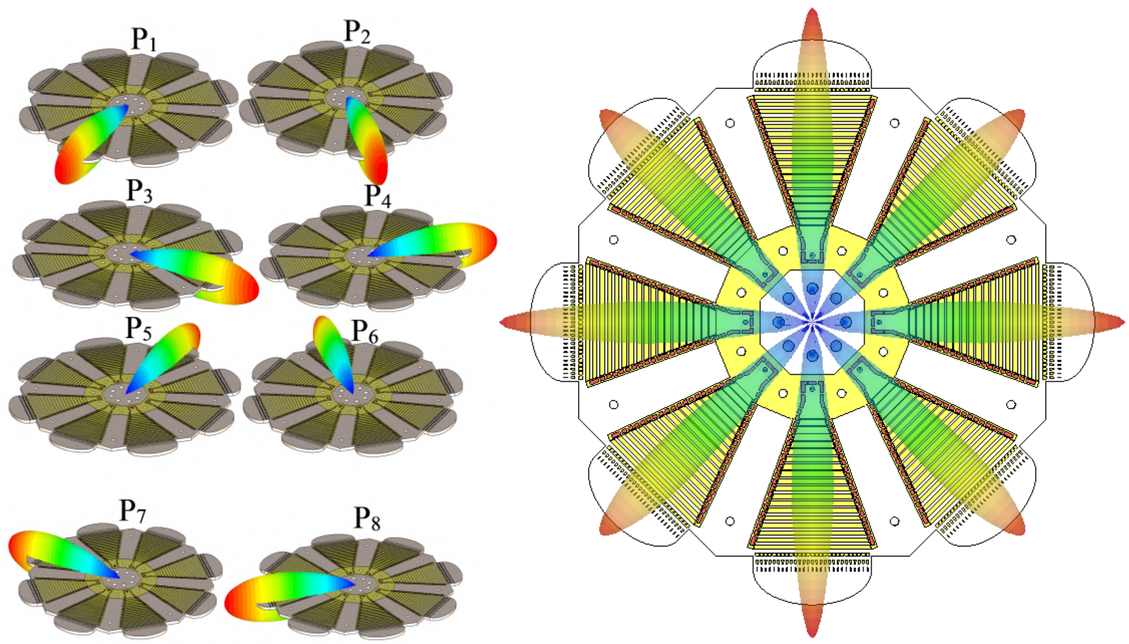

(a) **(b)**

FIGURE 7.4 : Radiation patterns of the proposed antenna for different excitation ports.

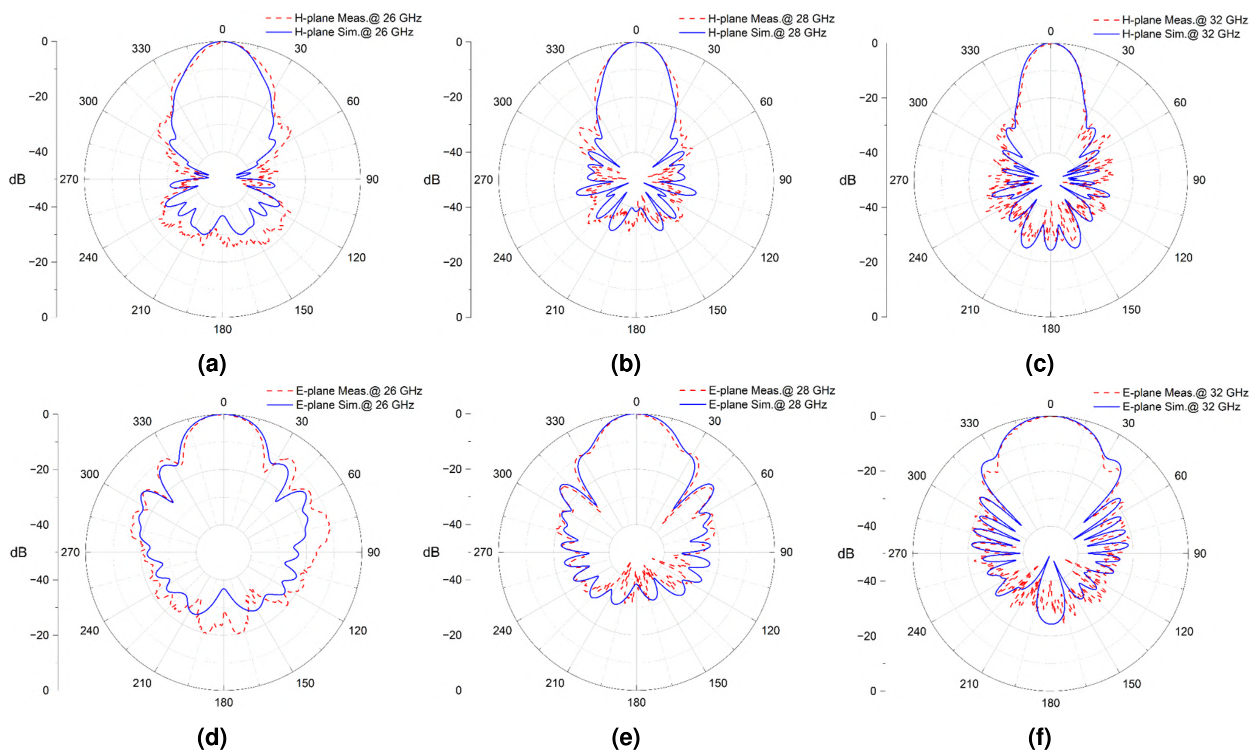

FIGURE 7.5 : Radiation Patterns at three different frequencies : 26, 28 and 32 GHz.

In both Figs. 7.2 and 7.5, the radiation patterns of the proposed antenna, were evaluated in simulation and measurements, and the results are in good agreement. It can be noted that the antenna has very narrow beam-width in the H-plane cut, where as in the E-plane one, the beam is much larger, hence the Fan-like beam shape for the elevation plane. Meaning, when the system is doing the beam-sweeping in the azimuth plane, the Fan-like beam will make sure that all users are covered, without the need to beam-sweep in the elevation plane too. And this is one of the features that this design provided, alongside the achieved low side-lobe levels of -28 dB. and being also low in profile and easy to fabricate, making it a potential candidate for a 360° beam-steering system, at Mm-wave band.

8 APPENDIX B

8.1 Logic Control Board

In this section, and as the final third piece of the work packages, a beam-steering logic board is designed, fabricated and validated using a test bench board, made of green and red LEDs, mimicking the operation principle of switching between two PIN diodes states (forward, and reverse biasing), corresponding to 0 and 180° phases.

This section documents the complete design and development process of a custom logic control board intended to manage the forward and reverse biasing of 256 pairs of PIN diodes. The system is constructed using ESP32 micro controllers, 74HC595 shift registers, CD4053 analog multiplexers, and a dual +5V/-5V power supply. Two identical control boards are connected in a daisy chain to enable scalability and synchronized control.

8.1.1 System Architecture and Components

The system is engineered to selectively control the state (on/off) of 256 PIN diode pairs by applying either a positive or negative bias voltage. This function is critical for applications like RF switching networks, phased array antennas, and signal routing systems.

The key components used are :
— ESP32 Micro controller
— 74HC595 Serial-In, Parallel-Out Shift Registers.
— CD4053 Triple 2-Channel Analog Switches.
— Dual +5V/-5V Regulated Power Supply.
— Two identical logic boards handling 128 diode pairs .
— Daisy chain connection between the two boards.

8.1.2 Shift Register Architecture (74HC595)

The 74HC595 is an 8-bit shift register with a storage register. It receives serial data from the ESP32 and converts it into parallel output to control the CD4053 switches. Each shift register controls 8 diode pairs.

Important Pins :
— SER : Serial data input
— SRCLK : Shift register clock

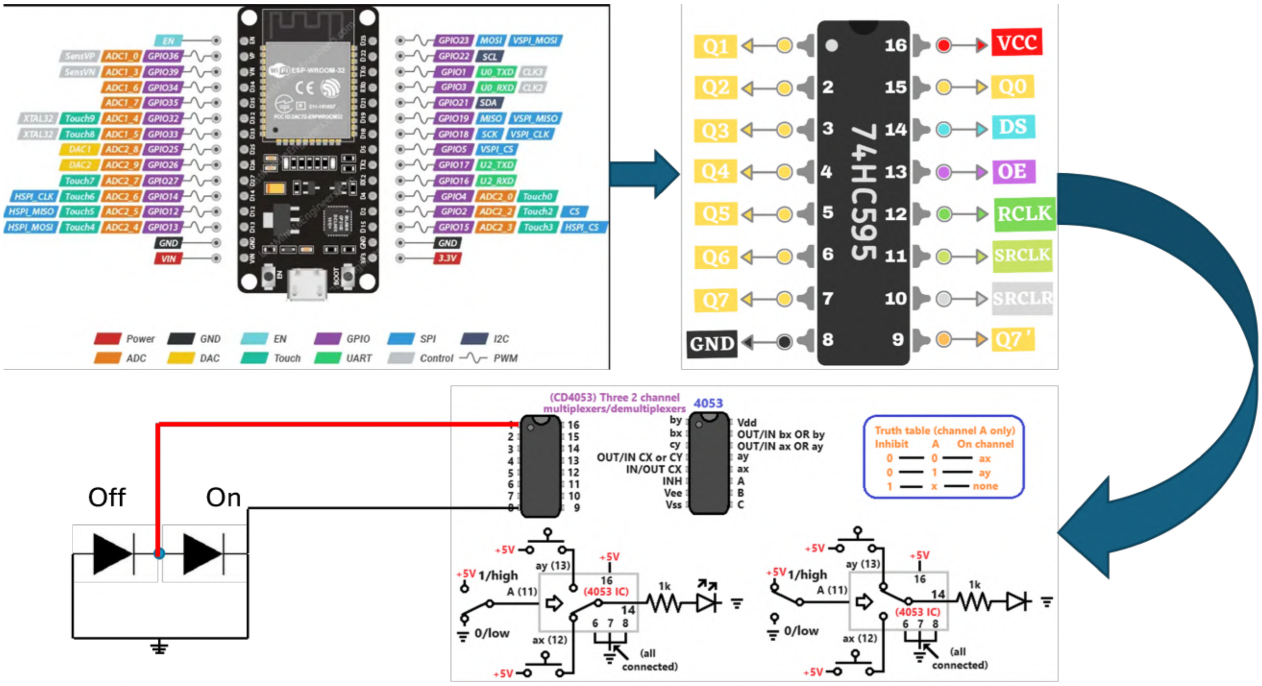

FIGURE 8.1 : Proposed ESP32-Based control unit board.

— RCLK : Latch clock
— Q0–Q7 : Parallel outputs
— Q7' : Serial output for cascading

Using only 3 GPIO pins (SER, SRCLK, RCLK), the ESP32 can control 256 outputs by chaining 32 shift registers. Each 8-bit segment in the 256-bit sequence sets the bias state for one CD4053 switch.

8.1.3 Analog Multiplexers (CD4053)

The CD4053 contains three SPDT analog switches. It can switch between two inputs (typically +5V and -5V) to apply the correct bias voltage to a PIN diode pair. The control signal for each switch comes from a shift register output.

Switching Logic :

— Logic LOW (0) : Connects -5V to the diode (reverse bias)
— Logic HIGH (1) : Connects +5V to the diode (forward bias)

Each CD4053 supports three diode pairs. The x, y inputs of each switch are connected to –5V and +5V respectively, while the common z output connects to the diode via a current-limiting resistor.

8.1.4 Daisy Chain Configuration

To scale the system, two identical control boards are built and connected in series. Each board has 16 shift registers, thus controlling 128 diode pairs. The Q7' (serial output) of the last register on Board 1 connects to the SER input of the first register on Board 2.

This configuration allows streaming a 256-bit control sequence from the ESP32, ensuring simultaneous and synchronized biasing of all diodes across both boards.

8.1.5 ESP32 Control and Timing

The ESP32 micro controller is responsible for generating the 256-bit binary sequence and controlling the shift register timing. The control sequence is shifted in serially using SRCLK and then latched simultaneously using RCLK to ensure glitch-free updates.

The ESP32 also serves a web interface where the user can input sequences manually or via UI. A graphical representation displays the state of each diode pair (1 = Forward Bias, 0 = Reverse Bias).

8.1.6 Power Supply Design

A dual power supply is used to generate regulated +5V and –5V rails. These voltages are fed into the CD4053 multiplexers to provide correct diode biasing. Current-limiting resistors are added between the CD4053 outputs and diode pairs to prevent over-current.

Each PIN diode typically draws 10 mA, and the power supply must support the maximum expected current load for simultaneously active diodes.

8.1.7 PCB Layout and Design

The PCB layout was created using DipTrace software. Components are organized in a modular format to simplify manufacturing and troubleshooting. The board layout accommodates :

- 16 shift registers per board
- 6 CD4053 chips (each controls 3 diode pairs)
- Input/output headers for ESP32 GPIO connections and power rails
- Daisy-chain connectors for serial data

High-current traces for power lines and appropriate ground planes ensure noise reduction and stability.

Below in Fig. 8.2, is the final fabricated boards, alongside the dummy led testing bench, used to validate the proper operation of the beam-steering logic board.

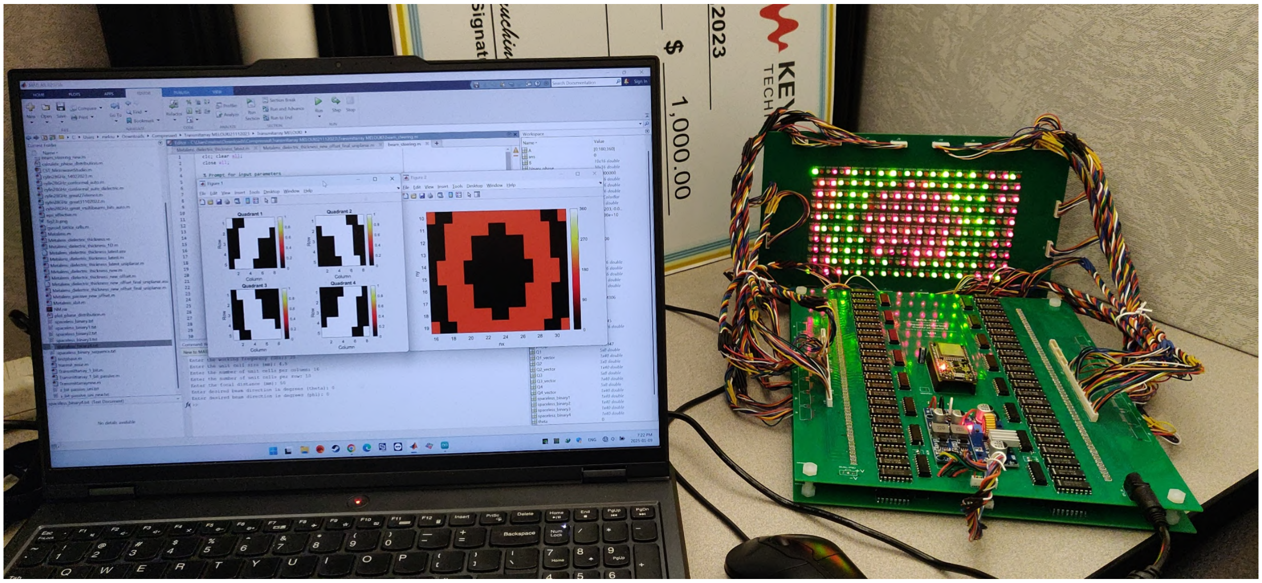

FIGURE 8.2 : ESP32-Based control unit board with the LED testing bench.

This proposed architecture demonstrates a scalable and efficient logic control system capable of managing 256 PIN diode pairs using standard digital and analog components. The use of shift registers minimizes GPIO usage while maintaining fast and synchronized updates. Daisy-chaining and modular design provide flexibility for larger systems. The ESP32-based web interface adds usability and visualization, making the system ideal for RF and switching applications.

BIBLIOGRAPHIE

[1] T. S. Rappaport, S. Sun, R. Mayzus, H. Zhao, Y. Azar, K. Wang, G. N. Wong, J. K. Schulz, M. Samimi, and F. Gutierrez, "Millimeter wave mobile communications for 5g cellular : It will work!" *IEEE access*, vol. 1, pp. 335–349, 2013.

[2] B. Ratni, A. de Lustrac, G.-P. Piau, and S. Burokur, "Planar metasurface for parabolic reflector antenna : Frequency agility and beam steering," in *2017 IEEE International Symposium on Antennas and Propagation & USNC/URSI National Radio Science Meeting*. IEEE, 2017, pp. 2073–2074.

[3] M. M. Tahseen, T. A. Denidni, and A. A. Kishk, "Proof of concept low-loss reconfigurable reflectarray for beam steering," in *2018 18th International Symposium on Antenna Technology and Applied Electromagnetics (ANTEM)*. IEEE, 2018, pp. 1–2.

[4] G. H. Elzwawi, H. H. Elzwawi, M. M. Tahseen, and T. A. Denidni, "Frequency selective surface-based switched-beamforming antenna," *IEEE Access*, vol. 6, pp. 48 042–48 050, 2018.

[5] J. C. Gallagher and M. E. DeVine, "Fifth-generation (5g) telecommunications technologies : issues for congress," *Congressional Research Service*, vol. 1, no. 30, pp. 1–39, 2019.

[6] J. R. Hoehn, K. M. Sayler, and J. C. Gallagher, "Overview of department of defense use of the electromagnetic spectrum," 2021.

[7] M. Series, "Minimum requirements related to technical performance for imt-2020 radio interface (s)," *Report*, pp. 2410–0, 2017.

[8] B. Ai, K. Guan, M. Rupp, T. Kurner, X. Cheng, X.-F. Yin, Q. Wang, G.-Y. Ma, Y. Li, L. Xiong *et al.*, "Future railway services-oriented mobile communications network," *IEEE Communications Magazine*, vol. 53, no. 10, pp. 78–85, 2015.

[9] L. Di Palma, A. Clemente, L. Dussopt, R. Sauleau, P. Potier, and P. Pouliguen, "1-bit reconfigurable unit cell for ka-band transmitarrays," *IEEE Antennas and Wireless Propagation Letters*, vol. 15, pp. 560–563, 2016.

[10] A. Hakkarainen, J. Werner, N. Gulati, D. Patron, D. Pfeil, H. Paaso, A. Mämmelä, K. Dandekar, and M. Valkama, "Reconfigurable antenna based doa estimation and localization in cognitive radios : Low complexity algorithms and practical measurements," in *2014 9th International Conference on Cognitive Radio Oriented Wireless Networks and Communications (CROWNCOM)*. IEEE, 2014, pp. 454–459.

[11] A. Mozharovskiy, A. Artemenko, A. Sevastyanov, V. Ssorin, and R. Maslennikov, "Beam-steerable integrated lens antenna with waveguide feeding system for 71–76/81–86 ghz point-to-point applications," in *2016 10th European Conference on Antennas and Propagation (EuCAP)*. IEEE, 2016, pp. 1–5.

[12] A. Abbaspour-Tamijani, L. Zhang, G. Pan, H. K. Pan, and H. Alavi, "Lens-enhanced phased array antenna system for high directivity beam-steering," in *2011 IEEE International Symposium on Antennas and Propagation (APSURSI)*. IEEE, 2011, pp. 3275–3278.

[13] T. Ueda, S. Yamamoto, Y. Kado, and T. Itoh, "Pseudo-traveling-wave resonator with magnetically tunable phase gradient of fields and its applications to beam-steering antennas," *IEEE transactions on microwave theory and techniques*, vol. 60, no. 10, pp. 3043–3054, 2012.

[14] Y. Yokohama and T. Kodera, “Voltage beam-steerable leaky-wave antenna using magnet-less non-reciprocal metamaterial (mnm),” in *2015 International Symposium on Antennas and Propagation (ISAP)*. IEEE, 2015, pp. 1–3.

[15] T. A. Denidni and G. Y. Delisle, “A nonlinear algorithm for output power maximization of an indoor adaptive phased array,” *IEEE transactions on electromagnetic compatibility*, vol. 37, no. 2, pp. 201–209, 1995.

[16] V. S. Rao, V. Srinivasan, and S. Pal, “Generation of dual beams from spherical phased array antenna,” *Electronics letters*, vol. 45, no. 9, p. 1, 2009.

[17] G. Poilasne, P. Pouliguen, K. Mahdjoubi, L. Desclos, and C. Terret, “Active metallic photonic band-gap materials (mpbg) : Experimental results on beam shaper,” *Ieee Transactions on antennas and propagation*, vol. 48, no. 1, pp. 117–119, 2000.

[18] H. Li, C. Ma, F. Shen, K. Xu, D. Ye, J. Huangfu, C. Li, L. Ran, and T. A. Denidni, “Wide-angle beam steering based on an active conformal metasurface lens,” *IEEE Access*, vol. 7, pp. 185 264–185 272, 2019.

[19] A. Clemente, F. Diaby, L. Di Palma, L. Dussopt, and R. Sauleau, “Experimental validation of a 2-bit reconfigurable unit-cell for transmitarrays at ka-band,” *IEEE Access*, vol. 8, pp. 114 991–114 997, 2020.

[20] D. Kong, H. Li, Q. Luo, and S. Gao, “Electronically beam-scanning antenna with active slot frequency selective surface for 5g base stations,” in *2020 IEEE MTT-S International Wireless Symposium (IWS)*. IEEE, 2020, pp. 1–3.

[21] L. Han, G. Cheng, G. Han, R. Ma, and W. Zhang, “Electronically beam-steering antenna with active frequency-selective surface,” *IEEE Antennas and Wireless Propagation Letters*, vol. 18, no. 1, pp. 108–112, 2018.

[22] C. Gu, S. Gao, B. Sanz-Izquierdo, E. A. Parker, F. Qin, H. Xu, J. C. Batchelor, X. Yang, and Z. Cheng, “3-d coverage beam-scanning antenna using feed array and active frequency-selective surface,” *IEEE transactions on antennas and propagation*, vol. 65, no. 11, pp. 5862–5870, 2017.

[23] T.-G. Lim, H.-N. Ang, I. D. Robertson, and B. L. Weiss, “Ka-band cpw-to-slotline transition in photoimageable thick film technology for tapered slot antenna applications,” *Microwave and Optical Technology Letters*, vol. 48, no. 10, pp. 2032–2034, 2006.

[24] H. Kaouach, L. Dussopt, J. Lanteri, T. Koleck, and R. Sauleau, “Wideband low-loss linear and circular polarization transmit-arrays in v-band,” *IEEE Transactions on Antennas and Propagation*, vol. 59, no. 7, pp. 2513–2523, 2011.

[25] J. Li, Q. Zeng, R. Liu, and T. A. Denidni, “A compact dual-band beam-sweeping antenna based on active frequency selective surfaces,” *IEEE Transactions on Antennas and Propagation*, vol. 65, no. 4, pp. 1542–1549, 2017.

[26] A. H. Abdelrahman, F. Yang, A. Z. Elsherbeni, P. Nayeri, and C. A. Balanis, “Analysis and design of transmitarray antennas,” 2017.

[27] Y. J. Guo and R. W. Ziolkowski, *Advanced antenna array engineering for 6G and beyond wireless communications*. John Wiley & Sons, 2021.

[28] C. G. Ryan, M. R. Chaharmir, J. Shaker, J. R. Bray, Y. M. Antar, and A. Ittipiboon, “A wideband transmitarray using dual-resonant double square rings,” *IEEE Transactions on antennas and propagation*, vol. 58, no. 5, pp. 1486–1493, 2010.

[29] C. Pfeiffer and A. Grbic, “Metamaterial huygens’ surfaces : tailoring wave fronts with reflectionless sheets,” *Physical review letters*, vol. 110, no. 19, p. 197401, 2013.

[30] G. V. Eleftheriades, M. Kim, V. G. Ataloglou, and A. H. Dorrah, “Prospects of huygens’ metasurfaces for antenna applications,” *Engineering*, vol. 11, pp. 21–26, 2022.

[31] Z. Pourgholamhossein, M. N. Jazi, and T. A. Denidni, “Broadband flat-lens antenna design using ultrathin huygens’ metasurface for millimeter-wave applications,” *IEEE Transactions on Antennas and Propagation*, vol. 71, no. 12, pp. 9914–9919, 2022.

[32] Y. Cao, M. Zhang, C. Fan, and J.-X. Chen, “A broadband transmitarray antenna using a metasurface-based element for millimeter-wave applications,” *Micromachines*, vol. 15, no. 3, p. 383, 2024.

[33] Q. Cheng, H. F. Ma, and T. J. Cui, “Broadband planar luneburg lens based on complementary metamaterials,” *Applied Physics Letters*, vol. 95, no. 18, 2009.

[34] J. R. Costa, E. B. Lima, and C. A. Fernandes, “Compact beam-steerable lens antenna for 60-ghz wireless communications,” *IEEE Transactions on Antennas and Propagation*, vol. 57, no. 10, pp. 2926–2933, 2009.

[35] C. A. Fernandes, R. C. Martins, T. Radil, P. M. Ramos, E. B. Lima, C. R. Medeiros, and J. R. Costa, “Low-cost mechanically steered millimeter-wave lens antenna system for indoor lans,” in *2010 International Workshop on Antenna Technology (iWAT)*. IEEE, 2010, pp. 1–4.

[36] J. R. Costa, E. B. Lima, C. R. Medeiros, T. Radil, R. C. Martins, P. M. Ramos, and C. A. Fernandes, “Development of an indoor wireless personal area network based on mechanically steered millimeter-wave lens antenna,” in *2010 IEEE Instrumentation & Measurement Technology Conference Proceedings*. IEEE, 2010, pp. 1202–1206.

[37] K. Zarb-Adami, A. Faulkner, J. B. De Vaate, G. Kant, and P. Picard, “Beamforming techniques for large-n aperture arrays,” in *2010 IEEE International Symposium on Phased Array Systems and Technology*. IEEE, 2010, pp. 883–890.

[38] F. Gholam, J. Vía, and I. Santamaría, “Beamforming design for simplified analog antenna combining architectures,” *IEEE Transactions on Vehicular Technology*, vol. 60, no. 5, pp. 2373–2378, 2011.

[39] H. Steyskal, “Digital beamforming,” in *1988 18th European Microwave Conference*. IEEE, 1988, pp. 49–57.

[40] A. Artemenko, A. Maltsev, A. Mozharovskiy, A. Sevastyanov, V. Ssorin, and R. Maslennikov, “Millimeter-wave electronically steerable integrated lens antennas for wlan/wpan applications,” *IEEE Transactions on Antennas and Propagation*, vol. 61, no. 4, pp. 1665–1671, 2012.

[41] J. Romeu, S. Blanch, L. Pradell, A. Barlabe, J.-M. Rius, M. Albert-Gali, L. Jofre-Roca, C. Mazzucco, and R. Flamini, “Lens-based switched-beam antenna for a 5g smart repeater,” *IEEE Antennas and Wireless Propagation Letters*, vol. 22, no. 10, pp. 2482–2486, 2023.

[42] A. Clemente, L. Dussopt, R. Sauleau, P. Potier, and P. Pouliguen, “Wideband 400-element electronically reconfigurable transmitarray in x band,” *IEEE Transactions on Antennas and Propagation*, vol. 61, no. 10, pp. 5017–5027, 2013.

[43] F. Diaby, A. Clemente, L. Di Palma, L. Dussopt, K. Pham, E. Fourn, and R. Sauleau, “Design of a 2-bit unit-cell for electronically reconfigurable transmitarrays at ka-band,” in *2017 47th European Microwave Conference (EuMC)*. IEEE, 2017, pp. 1321–1324.

[44] F. Diaby, A. Clemente, R. Sauleau, K. T. Pham, and L. Dussopt, “2 bit reconfigurable unit-cell and electronically steerable transmitarray at ka-band,” *IEEE Transactions on Antennas and Propagation*, vol. 68, no. 6, pp. 5003–5008, 2019.

[45] Q. Ali, W. Shahzad, I. Ahmad, S. Safiq, X. Bin, S. M. Abbas, and H. Sun, “Recent developments and challenges on beam steering characteristics of reconfigurable transmitarray antennas,” *Electronics*, vol. 11, no. 4, p. 587, 2022.

[46] B. Rana, I.-G. Lee, and I.-P. Hong, “Digitally reconfigurable transmitarray with beam-steering and polarization switching capabilities,” *Ieee Access*, vol. 9, pp. 144 140–144 148, 2021.

[47] N. Melouki, F. Ahmed, H. Nasseri, P. Pourmohammadi, A. Iqbal, and T. A. Denidni, “Multi-bit wideband transmitarray aperture with independent phase and amplitude control for high gain with low sidelobe mm-wave applications,” in *2024 18th European Conference on Antennas and Propagation (EuCAP)*. IEEE, 2024, pp. 01–04.

[48] C.-W. Luo, G. Zhao, Y.-C. Jiao, G.-T. Chen, and Y.-D. Yan, “Wideband 1 bit reconfigurable transmitarray antenna based on polarization rotation element,” *IEEE Antennas and Wireless Propagation Letters*, vol. 20, no. 5, pp. 798–802, 2021.

[49] V. S. Yadav, S. K. Ghosh, S. Bhattacharyya, and S. Das, “Graphene-based metasurface for a tunable broadband terahertz cross-polarization converter over a wide angle of incidence,” *Applied optics*, vol. 57, no. 29, pp. 8720–8726, 2018.

[50] D. Yang, W. Wang, E. Lv, H. Wang, B. Liu, Y. Hou, and J.-h. Chen, “Programmable vo2 metasurface for terahertz wave beam steering,” *IScience*, vol. 25, no. 8, 2022.

[51] X. You, C. Fumeaux, and W. Withayachumnankul, “Tutorial on broadband transmissive metasurfaces for wavefront and polarization control of terahertz waves,” *Journal of Applied Physics*, vol. 131, no. 6, 2022.

[52] H. Hasani, J. S. Silva, S. Capdevila, M. García-Vigueras, and J. R. Mosig, “Dual-band circularly polarized transmitarray antenna for satellite communications at (20, 30) ghz,” *IEEE Transactions on Antennas and Propagation*, vol. 67, no. 8, pp. 5325–5333, 2019.

[53] M. N. Iqbal, M. F. M. Yusoff, M. K. A. Rahim, M. R. Hamid, Z. Johari, and H. U. Rahman, “A high gain and compact transmitarray antenna for ku-band satellite communications,” *Electromagnetics*, vol. 41, no. 5, pp. 331–343, 2021.

[54] S. Kausar, A. Kausar, M. U. Hadi, and H. Mehrpouyan, “Multi-beam high gain steerable transmitarray lens for satellite communication and 5g mm-wave systems,” *AEU-International Journal of Electronics and Communications*, vol. 173, p. 154888, 2024.

[55] S. B. Yeap, X. Qing, and Z. N. Chen, “77-ghz dual-layer transmit-array for automotive radar applications,” *IEEE transactions on antennas and propagation*, vol. 63, no. 6, pp. 2833–2837, 2015.

[56] F. Greco, E. Arnieri, G. Amendola, R. De Marco, and L. Boccia, “A 77 ghz transmit array for in-package automotive radar applications,” in *Telecom*, vol. 5, no. 3. MDPI, 2024, pp. 792–803.

[57] N. Melouki, F. Ahmed, P. PourMohammadi, H. Naseri, and T. A. Denidni, “Wideband transmitarray with independent phase/amplitude control for millimeter-wave vehicular sensing and communication,” *AEU-International Journal of Electronics and Communications*, vol. 195, p. 155771, 2025.

[58] J. A. Ganie and K. Saurav, “Two-dimensional switchable beam transmitarray antenna for mm-wave base stations and vehicular networks,” *IEEE Access*, vol. 11, pp. 34 563–34 574, 2023.

[59] Á. F. Vaquero, M. R. Pino, and M. Arrebola, “Evaluation of a transmit-array base station for mm-wave communications in the fresnel region,” in *2022 IEEE International Symposium on Antennas and Propagation and USNC-URSI Radio Science Meeting (AP-S/URSI)*. IEEE, 2022, pp. 788–789.

[60] P. Pourmohammadi, H. Naseri, N. Melouki, F. Ahmed, Q. Zheng, A. Iqbal, and T. A. Denidni, “A wideband beam steering transmitarray antenna for ka-band applications,” *AEU-International Journal of Electronics and Communications*, vol. 193, p. 155720, 2025.

[61] Z.-H. Fu, X.-S. Yang, and B.-Z. Wang, “Low-cost conformal transmit-reflect-array antenna for unmanned aerial vehicle relay communications,” *IEEE Transactions on Antennas and Propagation*, 2024.

[62] T. B. Nguyen, T. T. Nguyen, M. L. Nguyen, and T. M. Nguyen, “A c-band 1-bit reconfigurable transmitarray unit-cell for airborne uav applications,” in *2024 IEEE International Symposium on Antennas and Propagation and INC/USNC-URSI Radio Science Meeting (AP-S/INC-USNC-URSI)*. IEEE, 2024, pp. 2295–2296.

[63] P.-Y. Qin, L.-Z. Song, and Y. J. Guo, “Conformal transmitarrays for unmanned aerial vehicles aided 6g networks,” *IEEE Communications Magazine*, vol. 60, no. 1, pp. 14–20, 2022.

[64] S. Virothu and M. S. Anuradha, “Flexible cp diversity antenna for 5g cellular vehicle-to-everything applications,” *AEU-International Journal of Electronics and Communications*, vol. 152, p. 154248, 2022.

[65] B. Madhav, T. Anilkumar, and S. K. Kotamraju, “Transparent and conformal wheel-shaped fractal antenna for vehicular communication applications,” *AEU-International Journal of Electronics and Communications*, vol. 91, pp. 1–10, 2018.

[66] A. Li and K.-M. Luk, “Single-layer wideband end-fire dual-polarized antenna array for device-to-device communication in 5g wireless systems,” *IEEE Transactions on Vehicular Technology*, vol. 69, no. 5, pp. 5142–5150, 2020.

[67] G.-W. Yang and S. Zhang, “A dual-band shared-aperture antenna with wide-angle scanning capability for mobile system applications,” *IEEE Transactions on Vehicular Technology*, vol. 70, no. 5, pp. 4088–4097, 2021.

[68] L. Zhang, J. Zhang, Y. He, C. Mao, W. Li, S.-W. Wong, P. Mei, and S. Gao, “A single-layer 10-30 ghz reflectarray antenna for the internet of vehicles,” *IEEE Transactions on Vehicular Technology*, vol. 71, no. 2, pp. 1480–1490, 2021.

[69] Q. Luo, S. Gao, W. Li, M. Sobhy, I. Bakaimi, C. K. de Groot, B. Hayden, I. Reaney, and X. Yang, “Multibeam dual-circularly polarized reflectarray for connected and autonomous vehicles,” *IEEE Transactions on Vehicular Technology*, vol. 68, no. 4, pp. 3574–3585, 2019.

[70] F. F. Manzillo, A. Clemente, and J. L. González-Jiménez, “High-gain d-band transmitarrays in standard pcb technology for beyond-5g communications,” *IEEE Transactions on Antennas and Propagation*, vol. 68, no. 1, pp. 587–592, 2019.

[71] Q. Xi, C. Ma, H. Li, B. Zhang, C. Li, and L. Ran, “A reconfigurable planar fresnel lens for millimeter-wave 5g frontends,” *IEEE Transactions on Microwave Theory and Techniques*, vol. 68, no. 11, pp. 4579–4588, 2020.

[72] A. Abbaspour-Tamijani, K. Sarabandi, and G. Rebeiz, “A millimetre-wave bandpass filter-lens array,” *IET Microwaves, Antennas & Propagation*, vol. 1, no. 2, pp. 388–395, 2007.

[73] B. J. Xiang, X. Dai, and K.-M. Luk, “A wideband 2-bit transmitarray antenna for millimeter-wave vehicular communication,” *IEEE Transactions on Vehicular Technology*, vol. 71, no. 9, pp. 9202–9211, 2022.

[74] C. Jouanlanne, A. Clemente, M. Huchard, J. Keignart, C. Barbier, T. Le Nadan, and L. Petit, “Wideband linearly polarized transmitarray antenna for 60 ghz backhauling,” *IEEE transactions on antennas and propagation*, vol. 65, no. 3, pp. 1440–1445, 2017.

[75] M. Feng, Y. Li, J. Wang, Q. Zheng, S. Sui, C. Wang, H. Chen, H. Ma, S. Qu, and J. Zhang, “Ultra-wideband and high-efficiency transparent coding metasurface,” *Applied Physics A*, vol. 124, pp. 1–8, 2018.

[76] Z. Tian, X. Gao, S. Su, J. Qiu, X. Du, and M. Guizani, “Evaluating reputation management schemes of internet of vehicles based on evolutionary game theory,” *IEEE Transactions on Vehicular Technology*, vol. 68, no. 6, pp. 5971–5980, 2019.

[77] L. Liang, H. Peng, G. Y. Li, and X. Shen, “Vehicular communications : A physical layer perspective,” *IEEE Transactions on Vehicular Technology*, vol. 66, no. 12, pp. 10 647–10 659, 2017.

[78] B. Feng, J. Chen, S. Yin, C.-Y.-D. Sim, and Z. Zhao, “A tri-polarized antenna with diverse radiation characteristics for 5g and v2x communications,” *IEEE Transactions on Vehicular Technology*, vol. 69, no. 9, pp. 10 115–10 126, 2020.

[79] A. K. Saurabh, R. Bharati, and M. K. Meshram, “Wideband 32-element 3d-mimo antenna for vehicular applications,” *AEU-International Journal of Electronics and Communications*, vol. 186, p. 155475, 2024.

[80] B. A. Esmail and S. Koziel, “High isolation metamaterial-based dual-band mimo antenna for 5g millimeter-wave applications,” *AEU-International Journal of Electronics and Communications*, vol. 158, p. 154470, 2023.

[81] V. Va, T. Shimizu, G. Bansal, R. W. Heath Jr *et al.*, “Millimeter wave vehicular communications : A survey,” *Foundations and Trends® in Networking*, vol. 10, no. 1, pp. 1–113, 2016.

[82] P. PourMohammadi, H. Naseri, N. Melouki, F. Ahmed, M. S. Bizan, A. Iqbal, and T. A. Denidni, “A fabry-perot antenna using a frequency selective surface layer with wideband and low rcs for mm-wave applications,” *AEU-International Journal of Electronics and Communications*, vol. 169, p. 154736, 2023.

[83] L. Qin, Y. Lu, Q. You, Y. Wang, J. Huang, and P. Gardner, “Millimeter-wave slotted waveguide array with unequal beamwidths and low sidelobe levels for vehicle radars and communications,” *IEEE Transactions on Vehicular Technology*, vol. 67, no. 11, pp. 10 574–10 582, 2018.

[84] Y. Zhang, J.-Y. Deng, D. Sun, J.-Y. Yin, and L.-X. Guo, “Compact slow-wave siw h-plane horn antenna with increased gain for vehicular millimeter wave communication,” *IEEE Transactions on Vehicular Technology*, vol. 70, no. 7, pp. 7289–7293, 2021.

[85] P. PourMohammadi, P. Fei, H. Nasseri, Q. Zheng, O. J. Babarinde, V. Volski, G. A. Vandenbosch, and T. A. Denidni, “A single-layer compact wideband circularly polarized patch array for 5g communications,” *IEEE Antennas and Wireless Propagation Letters*, vol. 22, no. 4, pp. 754–758, 2022.

[86] N. Melouki, F. Ahmed, P. PourMohammadi, H. Naseri, A. Iqbal, and T. Denidni, “3d-printed conformal metamaterial lens with multiple beam steering functionalities,” in *2023 IEEE International Symposium on Antennas and Propagation and USNC-URSI Radio Science Meeting (USNC-URSI)*. IEEE, 2023, pp. 791–792.

[87] R. Manikandan, P. K. Jawahar, and P. H. Rao, “Low sidelobe level csrr loaded weighted array antenna,” *IEEE Transactions on Antennas and Propagation*, vol. 66, no. 12, pp. 6893–6905, 2018.

[88] L.-Z. Song, P.-Y. Qin, and Y. J. Guo, “A high-efficiency conformal transmitarray antenna employing dual-layer ultrathin huygens element,” *IEEE Transactions on Antennas and Propagation*, vol. 69, no. 2, pp. 848–858, 2020.

[89] J. R. Reis, M. Vala, and R. F. Caldeirinha, “Review paper on transmitarray antennas,” *IEEE Access*, vol. 7, pp. 94 171–94 188, 2019.

[90] M.-Y. Li, Y.-L. Ban, and F.-Q. Yan, “Wideband low-profile ku-band transmitarray antenna,” *IEEE Access*, vol. 9, pp. 6683–6688, 2020.

[91] T. Li, J. Sun, H. Meng, Y. Shen, S. Hu, W. Dou, Z. N. Chen, and T. Zwick, “Characteristic mode inspired dual-polarized double-layer metasurface lens,” *IEEE Transactions on Antennas and Propagation*, vol. 69, no. 6, pp. 3144–3154, 2020.

[92] N. Melouki, A. Hocini, and T. A. Denidni, “Performance enhancement of a compact patch antenna using an optimized ebg structure,” *Chinese Journal of Physics*, vol. 69, pp. 219–229, 2021.

[93] A. Hocini, N. Melouki, and T. Denidni, “Modeling and simulation of an antenna with optimized amc reflecting layer for gain and front-to-back ratio enhancement for 5g applications,” in *Journal of Physics : Conference Series*, vol. 1492, no. 1. IOP Publishing, 2020, p. 012006.

[94] V. Sedenka and Z. Raida, “Critical comparison of multi-objective optimization methods : Genetic algorithms versus swarm intelligence,” 2010.

[95] Texas Instruments, “Beam steering for corner radar reference design,” https://www.ti.com/lit/pdf/tiduev0, 2020, online; accessed 11-May-2025.

[96] Keysight Technologies, “Automotive radar : Advanced technology for adas,” https://www.keysight.com/us/en/industries/automotive/automotive-radar.html, 2018, online; accessed 11-May-2025.

[97] P. Pourmohammadi, V. Volski, and G. A. Vandenbosch, “Medium-sized highly coupled planar arrays with maximum aperture efficiency,” *Sensors*, vol. 21, no. 17, p. 5925, 2021.

[98] Y. Ge, C. Lin, and Y. Liu, “Broadband folded transmitarray antenna based on an ultrathin transmission polarizer,” *IEEE Transactions on Antennas and Propagation*, vol. 66, no. 11, pp. 5974–5981, 2018.

[99] G.-B. Wu, S.-W. Qu, and S. Yang, “Low-profile transmitarray antenna with cassegrain reflectarray feed,” *IEEE Transactions on Antennas and Propagation*, vol. 67, no. 5, pp. 3079–3088, 2019.

[100] C. Song, L. Pan, Y. Jiao, and J. Jia, “A high-performance transmitarray antenna with thin metasurface for 5g communication based on pso (particle swarm optimization),” *Sensors*, vol. 20, no. 16, p. 4460, 2020.

[101] Á. F. Vaquero, J. Teixeira, S. A. Matos, M. Arrebola, J. R. Costa, J. M. Felício, C. A. Fernandes, and N. J. Fonseca, “Design of low-profile transmitarray antennas with wide mechanical beam steering at millimeter waves,” *IEEE Transactions on Antennas and Propagation*, vol. 71, no. 4, pp. 3713–3718, 2023.

[102] S. Tiwari, A. K. Singh, and A. Dubey, “Wide-band wide-angle beamsteerable meta-lens antenna for terrestrial/non-terrestrial 5g communication systems,” *IEEE Journal on Miniaturization for Air and Space Systems*, 2024.

[103] S. Yu, L. Li, G. Shi, C. Zhu, and Y. Shi, “Generating multiple orbital angular momentum vortex beams using a metasurface in radio frequency domain,” *Applied Physics Letters*, vol. 108, no. 24, 2016.

[104] L. Dai, B. Wang, M. Wang, X. Yang, J. Tan, S. Bi, S. Xu, F. Yang, Z. Chen, M. Di Renzo *et al.*, “Reconfigurable intelligent surface-based wireless communications : Antenna design, prototyping, and experimental results,” *IEEE access*, vol. 8, pp. 45 913–45 923, 2020.

[105] M. N. E. Temmar, A. Hocini, D. Khedrouche, and M. Zamani, “Analysis and design of a terahertz microstrip antenna based on a synthesized photonic bandgap substrate using bpso,” *Journal of Computational Electronics*, vol. 18, no. 1, pp. 231–240, 2019.

[106] N. Melouki, A. Hocini, and T. A. Denidni, “High gain and wideband fabry-perot resonator antenna based on a compact single prs layer,” *IEEE Access*, vol. 10, pp. 96 526–96 537, 2022.

[107] R. Corporation, “Radix printable dielectric,” https://www.rogerscorp.com/advanced-electronics-solutions/radix-printable-dielectric, 2025, accessed : 2025-09-20.

[108] X. Wang, P.-Y. Qin, A. T. Le, H. Zhang, R. Jin, and Y. J. Guo, "Beam scanning transmitarray employing reconfigurable dual-layer huygens element," *IEEE Transactions on Antennas and Propagation*, vol. 70, no. 9, pp. 7491–7500, 2022.

[109] A. R. Vilenskiy, M. N. Makurin, C. Lee, and M. V. Ivashina, "Reconfigurable transmitarray with near-field coupling to gap waveguide array antenna for efficient 2-d beam steering," *IEEE Transactions on Antennas and Propagation*, vol. 68, no. 12, pp. 7854–7865, 2020.

[110] X. Tian and L. Song, "A novel 1-bit reconfigurable transmitarray element using symmetric patch antennas," in *2022 International Conference on Microwave and Millimeter Wave Technology (ICMMT)*, 2022, pp. 1–3.

[111] A. Clemente, L. Dussopt, R. Sauleau, P. Potier, and P. Pouliguen, "Wideband reconfigurable reflectarray element based on dual-mode resonator and pin diodes," *IEEE Transactions on Antennas and Propagation*, vol. 61, no. 10, pp. 5017–5026, 2013.

[112] S. V. Hum, M. Okoniewski, and R. J. Davies, "Modeling and design of electronically tunable reflectarrays," *IEEE transactions on Antennas and Propagation*, vol. 55, no. 8, pp. 2200–2210, 2007.

[113] S. V. Hum and J. Perruisseau-Carrier, "Reconfigurable reflectarrays and array lenses for dynamic antenna beam control : A review," *IEEE transactions on antennas and propagation*, vol. 62, no. 1, pp. 183–198, 2013.

[114] J. Liu, D. R. Jackson, Y. Li, C. Zhang, and Y. Long, "Investigations of siw leaky-wave antenna for endfire-radiation with narrow beam and sidelobe suppression," *IEEE Transactions on Antennas and Propagation*, vol. 62, no. 9, pp. 4489–4497, 2014.